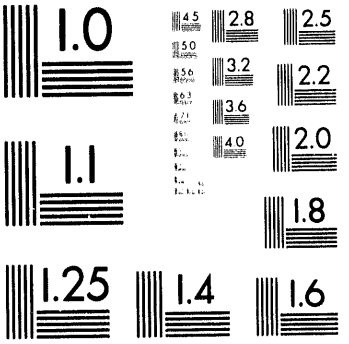
1.0
1.1
1.25
1.4
1.6
1.8
2.0
2.2
2.5
2.8
3.2
3.6
4.0
4.5
5.0
5.6
6.3

1 of 5

NUREG/CR-6056

A Framework for the Assessment of Severe Accident Management Strategies

Manuscript Completed: June 1993
Date Published: September 1993

Prepared by
W. E. Kastenberg, Editor
G. Apostolakis, V. K. Dhir, D. Okrent, M. Jae,
H. Lim, T. Milici, H. Park, J. Swider, L. Xing, D. Yu

Mechanical Aerospace and Nuclear Engineering Department
University of California
Los Angeles, CA 90024-1597

Prepared for
Division of Systems Research
Office of Nuclear Regulatory Research
U.S. Nuclear Regulatory Commission
Washington, DC 20555-0001
NRC FIN L1331

ABSTRACT

Severe accident management can be defined as the use of existing and/or alternative resources, systems and actions to prevent or mitigate a core-melt accident. For each accident sequence and each combination of severe accident management strategies, there may be several options available to the operator, and each involves phenomenological and operational considerations regarding uncertainty. Operational uncertainties include operator, system and instrumentation behavior during an accident. A framework based on decision trees and influence diagrams has been developed which incorporates such criteria as feasibility, effectiveness, and adverse effects, for evaluating potential severe accident management strategies. The framework is also capable of propagating both data and model uncertainty. It is applied to several potential strategies including PWR cavity flooding, BWR drywell flooding, PWR depressurization and PWR feed and bleed.

TABLE OF CONTENTS

LIST OF FIGURES

LIST OF TABLES

EXECUTIVE SUMMARY

Severe accident management can be defined as the innovative use of existing and/or alternative resources, systems and actions to prevent or mitigate a core melt accident. Such accident management strategies might include the use of alternative sources of air, power and water (resources), alternative pumps and generators (systems) and manual depressurization and manual injection (alternative actions). For each strategy or combination thereof, there exist operational and phenomenological uncertainties in the accident progression, including operator behavior, system availability and information.

This report describes a method for making decisions regarding the selection of severe accident management strategies, given the uncertainties mentioned above. The method is intended for use prior to any accident, i.e. it is not intended for use in real time. The method can be used to screen competing alternatives, sequential actions and multiple alternatives, and can be used to assess the uncertainty inherent in each strategy.

The method developed in this report is based on Decision Trees and Influence Diagrams. A Decision Tree is a pictorial diagram of events, namely decision events and chance events, arranged so as to depict the order in which they might occur. The chance events describe the degree of uncertainty in the accident progression, once a decision is made. Influence Diagrams are also pictorial diagrams of decision and chance events, but also contain a value node, against which the decisions are measured. The nodes in an Influence Diagram are connected by arcs. Arcs going into value and chance nodes are conditional and show probabilistic dependence, and arcs going into decision nodes represent the chronological order of events.

The method developed in this report is applied to several severe accident management strategies. It is shown that the method can be very useful when the conditional probabilities in the various chance nodes are known. Where they are not known very well, they can be obtained by expert opinion elicitation, and sensitivity and uncertainty analysis can be performed to obtain important insights into the decision making process.

The use of Influence Diagrams and Decision Trees has a second valuable benefit. It requires a systematic examination of the various potential factors which could affect the outcome of a particular strategy. These factors include feasibility, effectiveness and adverse effects. As a result, a more complete examination and evaluation of a candidate strategy may result, and factors sometimes overlooked may be identified and factored into the assessment.

In this report, data and models relied heavily on NUREG-1150, and on independent analyses by UCLA and other NRC contractors. This report does not

contain any new experimental findings in assessing uncertainties. The method is applied to the following cases: a) PWR cavity flooding, b) BWR drywell flooding, and c) PWR cavity flooding, depressurization and feed and bleed cooling if AC power is restored. Sensitivity studies for the key chance nodes are carried out in the first two cases, and an uncertainty propagation study is carried out for the latter case.

For the PWR cavity flooding case, the major uncertainties include the effectiveness of the water in removing decay heat and preventing vessel failure/penetration, the potential for steam generator tube rupture before surge line failure, and the potential adverse effect of an ex-vessel steam explosion. On balance, water in the cavity appears to reduce risk regardless of the uncertainty, except for the extreme cases (i.e. high probability) of a steam explosion or steam-generator tube rupture. Water in the cavity has the secondary mitigating effect of reducing the potential for early containment failure due to direct containment heating and late containment failure. Calculations presented for the probability of PWR vessel failure contain many uncertainties that need to be addressed.

For the BWR drywell flooding case, the major uncertainty is the effectiveness of the water in preventing vessel failure. The drywell must be vented before flooding can take place. Hence the major adverse effect is venting, followed by failure to flood (on time). On balance however, BWR drywell flooding is a preferred strategy. If the vessel should fail, isolation failure and linear failure are of concern even without a steam explosion. Steam explosions are not a key factor influencing the BWR drywell flooding strategy. Since the containment is vented, it is assumed to have failed already. Drywell flooding reduces the risk regardless of the conditional probability of early containment failure given a steam explosion. Calculations presented for the probability of BWR vessel failure also contain a number of uncertainties that need to be addressed.

As noted above, a combination of three strategies for a PWR was assessed; cavity flooding, depressurization and, feed-and-bleed cooling if AC power is restored. This study concludes that it is always better to initiate feed-and-bleed cooling of the core, regardless of other strategies initiated, and irrespective of the uncertainty in the key variables. In ranking these three strategies, taken singly or in combination, the major uncertainties include the potential for direct containment heating and the probability of an ex-vessel steam explosion.

The highest ranked strategy, with respect to minimizing the probability of early containment failure, is depressurization coupled with feed-and-bleed cooling if AC power is recovered. This is followed by cavity flooding coupled with feed-and-bleed cooling, and third ranked is feed-and-bleed cooling alone.

As noted above, a key uncertainty is whether or not water in the cavity or the drywell, up to the level of the top of the bottom head, is sufficiently effective in preventing vessel failure. A detailed set of thermal calculations was performed and is presented in Appendix I of this report. In this appendix, the effect of external

cooling on the thermal behavior of the vessel lower head containing molten core material was investigated using a two dimensional implicit finite difference scheme. Results were obtained for the vessel shell temperature, pool temperature and the crust thickness for both unsteady state (PWR) and steady state (PWR and BWR) conditions. For both cases, the thermal behavior of the vessel lower head was investigated by parametrically changing the emissivity of the pool free surface, the vessel wall, the baffle plate (BWR), the core shroud (BWR) and the upper structure, and the temperature of the upper structure. For a certain set of parameters, nucleate boiling on the outer surface of the vessel wall was found to be effective in lowering the temperature of the inner wall of the vessel below the melting temperature of the steel. It was found that some melting of the PWR vessel inner wall is predicted to occur, and that for most of the cases, melting of the BWR baffle plate would occur.

Some preliminary calculations were made regarding thermal stress and thermal creep. The thermal stresses across the PWR vessel shell are predicted to exceed the yield stress of the steel vessel, introducing the possibility of a large plastic deformation, in which case the survival of the vessel is in question. However, the stresses in the BWR vessel shell are predicted to be lower than the yield stress of steel. For a given system pressure, the creep rupture times after slumping of the core material into the vessel lower head were determined by using the relationship between the Larson-Miller parameter and the equivalent stress. A large uncertainty exists in the prediction of creep rupture times because of the large temperature gradients. Creep rupture times of only a few hours are predicted if the highest average wall temperature is used. However, rupture times are very long if the vessel outer wall temperature is used. Before any of these severe accident management strategies are adopted for use, the uncertainties regarding vessel failure need to be addressed.

For BWRs, consideration should be given to replacing the fire pumps with a new high capacity, independently powered low pressure pump. If the fire pump is used, the operator should foresee that AC power will not be recovered within 12 hours. In reality, the operators might be reluctant to flood early, because DC power and HPCI may still be available. Procedural changes have to be made if early flooding using the fire pumps is to be employed.

Some potential severe accident management strategies are inherently complex, involving both benefits and adverse aspects and subject to large uncertainties. Decision Trees and Influence Diagrams represent a valuable tool for examining and illuminating the various factors involved, and provide a tool for solving the various outcomes of the potential strategy. They can also give an estimate of the uncertainty inherent in such decision making.

ACKNOWLEDGMENTS

The authors wish to express their appreciation to Dr. Frank Odar for his guidance and support throughout this project. His comments and critiques of the early drafts of this report were invaluable, especially to the students. The research reported herein has formed the basis for no less than six Ph.D. dissertations (Jae, Lim, Milici, Park, Xing, and Yu). On behalf of these students, the faculty wish to thank the NRC for having the courage to support graduate student research, and the foresight in supporting basic and applied reactor safety research.

1. INTRODUCTION

1.1 Background

Severe accident management can be defined as the innovative use of existing and or alternative resources, systems and actions to prevent or mitigate a core melt accident. Together with risk management (changes in plant operation and/or addition of equipment) and emergency planning (off-site actions), severe accident management provides an extension of the defense-in-depth safety philosophy for core melt accidents.

A significant number of probabilistic safety assessments (PSA) have been completed which yield the principal plant vulnerabilities. These vulnerabilities can be categorized as, a) dominant sequences with respect to core melt frequency, b) dominant sequences with respect to various risk measures, c) dominant threats which challenge safety functions, and d) dominant threats with respect to failure of safety systems.

The goals of severe accident management are to:

1) prevent core damage,
2) prevent vessel failure,
3) prevent containment failure, and
4) mitigate fission product release to the environment.

These goals may be considered sequentially, as an accident progresses, or simultaneously, depending upon the resources available to the plant operators, and their effectiveness.

Severe accident management strategies can be generically classified as:

- the use of alternative resources (i.e., air, water, power),
- the use of alternative equipment (i.e., pumps, generators), and
- the use of alternative actions (i.e., manual depressurization, manual injection).

1.2 Key Uncertainties

For each sequence/threat and each combination of strategy there may be several options available to the operator. Each strategy/option involves phenomenological and operational considerations regarding uncertainty. These considerations include uncertainty in key phenomena, uncertainty in operator behavior, uncertainty in system availability and behavior, and uncertainty in available information (i.e., instrumentation).

In order to better scope the uncertainty associated with these strategies, two workshops were held at UCLA as follows:

- May 15-17, 1990 : Severe Accident Management for Pressurized Water Reactors (PWRs)

- Sept. 26-28, 1990 : Severe Accident Management for Boiling Water Reactors (BWRs).

The workshop participants included representatives from academia, industry, government and government contractors (national laboratories).

As a result of these two workshops a number of key uncertainties have been delineated, and several new accident management strategies were developed. The proceedings of these workshops were summarized in two NUREG/CR reports [1,2].

In general, the key uncertainties involve issues related to phenomena, operator actions, instrumentation and systems availability. The uncertainty in phenomena occur because operator actions change the progression of a severe accident, and introduce new physical regimes such as temperature or pressure, and new conditions such as the presence or absence of water. As a core–melt accident progresses, the geometry change will also contribute to uncertainty. Uncertainties in phenomena exist with respect to the occurrence of steam explosions (both in-vessel and ex-vessel), hydrogen generation, hydrogen combustion and detonation, and heat transfer in these new regimes and under these new conditions.

In addition to the traditional uncertainties in operator and system behavior regarding severe accidents, there is additional uncertainty in attempting to manage a severe accident using innovative means. This occurs because of the uncertain nature of the phenomena mentioned previously, a lack of knowledge regarding the state of the accident progression, and because the operators may not know whether or not their actions have been successful. Moreover, a lack of sufficient information due to damaged instrumentation may lead the operators to the wrong diagnosis and/or action.

1.3 Objectives

In order to include the various uncertainties mentioned above in assessing the viability of a potential severe accident management strategy, a framework has been developed using Decision Trees and Influence Diagrams. This framework is described in Section 2. The objective of this report is to develop this framework for assessing severe accident management strategies given the key uncertainties delineated at the workshops. Based on Decision Trees and Influence Diagrams, the framework is applied to two case studies:

- Cavity flooding in a PWR to prevent vessel penetration or vessel failure,
- Drywell flooding in a BWR to prevent vessel and/or containment failure.

Chapters 3 and 4 describe the application of this framework to the two case studies, respectively. Chapter 5 contains a tutorial on the direct evaluation of influence diagrams. Chapters 6 and 7 extend the framework to multiple decisions and the propagation of uncertainty, and apply it to the PWR cavity flooding strategy. Chapter 8 contains conclusions and recommendations. There are three appendices to the main report. The first deals with detailed phenomenological calculations regarding the effectiveness of both PWR cavity flooding and BWR drywell flooding. The second appendix deals with assessing the probability of steam explosions, and the third deals with obtaining probability distributions from expert opinion.

2. DEVELOPMENT OF A FRAMEWORK

2.1 Introduction

Consider a simple example in which a consumer is confronted with the option of whether or not to purchase an extended warranty for an electronic component. Suppose the extended warranty costs $100; on the other-hand should failure occur, the cost of repair is $500. The key uncertainty is whether or not the electronic component will fail during its lifetime. The decision can be graphically structured as shown in Figure 2.1. Suppose further that the consumer wishes to minimize his/her expected loss. The upper branch of the Decision Tree represents the purchase of insurance i.e., the extended warranty; the lower branch represents "self insurance". The square is a "Decision Node", and the circle is a "Chance Node" representing the uncertainty. If the chance of failure is estimated to be 10% (0.10), then the expected losses would be (EV = Expected Value):

$$EV_1 \text{ (Loss)} = - \$100 \qquad (2.1)$$

$$EV_2 \text{ (Loss)} = 0.9 (- \$0) + 0.1 (- \$500) = - \$50$$

If the consumer used this simple "Expected Value Rule", he/she would opt to self insure because EV in this case is -$50. If the consumer were more sophisticated, he/she could use an "Expected Utility Rule" in which a degree of risk aversion could be factored in.

An Influence Diagram for this type of decision is also shown in Figure 2.1. It is used primarily to show what influences the value of the decision (given by the diamond), and it can be used to help structure the decision tree.

Figure 2.2a - 2.2f shows the three possible cases associated with a decision problem. Each involves one node of each type: decision, chance, and value. In Figure 2.2a, the value depends on the random variable (chance node), which itself depends upon the decision. The equivalent decision tree, Figure 2.2b, shows that the decision node does not directly affect the value. For example, let D represent whether or not to purchase a new tire and C represent whether or not the tire

(new or old) will fail. The probability of tire failure depends on the mileage on the tire, hence $p_1 = p_2$. However, since R1 is assumed equal to R2 (the consequences of tire failure are the same, regardless of the mileage), the value node only depends on the chance node, C.

Figure 2.2c is similar, but here the value depends upon both the decision and the random variable (chance variable), which depends on the decision. The equivalent decision tree is also shown in Figure 2.2d. For example, let D represent whether or not to flood the reactor cavity and C represent whether the vessel fails or not. Since the probability of vessel failure depends on the decision and risk R1 is not equal to R2 (the risk of early fatalities), the value node depends on both the chance node C and the decision node D.

In Figure 2.2e, the value depends on both, the decision and the chance node, but the random variable is independent of the decision. Suppose that a consumer is confronted with the option of whether or not to purchase an extended warranty for an electronic component. Let node C represent whether or not the electronic component will fail during its lifetime. The decision can be graphically structured as shown in Figure 2.2e. The probability of failure is independent on whether or not one buys insurance, but the risk (cost) is dependent on the purchase of insurance and the probability of failure, as shown in Figure 2.2f. These three cases are generalized in Figure 2.3.

In many cases decision trees and influence diagrams will contain more than one decision. Figure 2.4a shows an influence diagram in which two decisions are modelled, i.e., whether or not to flood the reactor cavity and whether or not to depressurize the primary system. The equivalent decision tree is shown in Figure 2.4b. Since the two decision nodes in Figure 2.4a and 2.4b are not separated by a chance node, they can be collapsed into one decision having four outcomes, i.e., flood the cavity only, depressurize the primary system only, do both, and do neither, as shown in Figure 2.4c and Figure 2.4d.

As shown in Figure 2.4e, a sequential decision problem has chance nodes between the decision nodes. The two decision nodes cannot be collapsed into a single node, and still preserve the logic of the original diagram. The equivalent decision tree is also presented in Figure 2.4f.

If decision node D1 precedes decision node D2 in a regular influence diagram, then node D1 and all of its informational predecessors should be informational predecessors of node D2. Figure 2.4g shows the addition of an "no forgetting" arc. Informational arcs toward node D2 denote that the decision maker knows the outcome of node C when decision D2 is made, as well as decision D1 when decision D2 is made.

2.2 Accident Management

The Decision Tree and Influence Diagram shown in Figure 2.5 are simple examples of how a severe accident management strategy can be represented. The upper branch, "Do Nothing", means follow the normal emergency procedures contained in the Emergency Operating Procedures which are incorporated in a risk assessment such as NUREG-1150. The circle indicates a chance node with two outcomes. In the first outcome, the accident progression is stopped, and ends with risk R_1. This risk (R_1) might be zero (if there is no core damage or release) or may be economic (if there is core-damage). In the second outcome, the normal emergency procedures fail, and there is a risk, R_2 such as that calculated in NUREG-1150. The lower branch describes a severe accident management option for preventing vessel failure (e.g., Flooding the Cavity). This option can lead to success, but with risk R_3. The risk (R_3) might be economic with no radioactive release if the melt progression is stopped, as above. Failure of the strategy may lead to risk which may be greater or less than R_2, depending upon the physical and operational state of the system. For example, even though the vessel fails, the presence of water might scrub fission products, thereby reducing risk. Or it may lead to a steam explosion thereby increasing risk. This risk, R_4 represents an adverse effect.

The expected value (EV) for the two options, as depicted in Figure 2.5 are:

$$EV\ (\text{Do Nothing}) = P_1R_1 + (1-P_1)R_2 \qquad (2.2)$$

$$EV\ (\text{Flooding}) = P_2R_3+(1-P_2)R_4$$

The Influence Diagram for this example is also shown in Figure 2.5. In this case, the diagram is simple because the chance node represents simple failure or success.

2.3 Evaluation Criteria

When assessing a severe accident management strategy five criteria should be considered:

1. the feasibility of the strategy,
2. the effectiveness of the strategy,
3. the possibility of adverse effects,
4. information needs, and
5. compatibility with existing procedures

For the strategy considered in the example above, the **feasibility** is essentially a question of whether or not the operators will be able to fill the cavity up to the required level in sufficient time. The **effectiveness** has to do with whether or not there is sufficient heat transfer to keep the molten core in the vessel. A possible **adverse effect** is a steam explosion, should the strategy be feasible but not effective, i.e., the core penetrates the vessel, and finds water in the cavity, which otherwise would not be there. Information needs refers to instrumentation availability, and compatibility considers the impact on existing rules and procedures.

Figure 2.6 shows a case with adverse effects. The lower branch, "Do Nothing" is as before, the risk associated with employment of standard emergency operating procedures (the two branches in Figure 2.5 have been collapsed). The upper branch, flood the cavity, has three chance nodes. The first chance node C_1 represents the question of **feasibility**; whether or not the operators can fill the cavity to the required level on time. The second chance node C_2 represents **effectiveness**; whether or not the water will keep the vessel cool enough. The third chance node C_3 represents **adverse effects;** whether or not there will be a steam explosion if the strategy is not effective. Note that this last question can also apply to the feasibility issue as well. The branch "flooding not successful"

may also lead to the potential adverse effect (regarding a steam explosion) if the cavity is partially filled with water.

The expected value for each case is as follows:

$$EV\ (\text{Do Nothing}) = R_5 \qquad (2.3)$$

$$EV\ (\text{Flood Cavity}) = P_1R_4+(1-P_1)[(1-P_2)R_1+P_2(1-P_3)R_2+P_2P_3R_3]$$

The evaluation of such a tree would proceed as follows. The risks associated with each endpoint would be determined using PRA methodology. This risk might be in terms of early or latent fatalities, population dose, conditional probability of early containment failure, etc. The chance node probabilities would be evaluated using both deterministic and probabilistic methods. For example, the question of feasibility would require the use of Human Reliability Analysis (HRA) and a knowledge of system behavior (e.g., pump capacities, flow rates, etc.). The question of effectiveness would require mechanistic calculations regarding heat transfer, materials behavior etc. The same is true for questions regarding adverse effects.

2.4 An Example

As an example of the use of Decision Trees and Influence Diagrams, we consider a decision regarding PWR cavity flooding as a means to prevent vessel failure. The measure of success can be a reduction in the risk of early or latent fatalities, of core-melt frequency or of early containment failure. For this simple example we consider as the measure of success the potential reduction in the Conditional Probability of Early Containment Failure, denoted P_{ecf}. Furthermore we wish to determine whether or not flooding the cavity to prevent vessel failure will reduce P_{ecf} given a potential adverse effect (in this simple example, an ex-vessel steam explosion). A detailed assessment of PWR cavity flooding is presented in Section 3.

The simplified Decision Tree shown in Figure 2.6 can be used, along with Equation (2.3), to evaluate this severe accident management strategy. Figure 7.3

in NUREG-1150 [3] gives a value of 0.025 for P_{ecf} , given a Station Blackout (SBO) sequence, in the Zion plant.

Early containment failure can be attributed to two phenomena: direct containment heating and ex-vessel steam explosions. In Section 3 of this report we derive the following values for the risks (R_i) and the probabilities (P_i) required in Equations (2.3), as follows:

$R_1 = 0$	If there is no vessel failure, the Conditional Probability of Early Containment Failure, $P_{ecf} = 0$.
$R_2 = 0$	If the vessel fails and the melt is quenched, $P_{ecf} = 0$
$R_3 = 0.01$	If the vessel fails and there is an ex-vessel steam explosion, but no direct containment heating, P_{ecf} is reduced.
$R_4 = 0.025$	If flooding is not successful; same as "do nothing".
$R_5 = 0.025$	Given in NUREG-1150; "do nothing".
$P_1 = 0.41$	The probability that the option is not feasible; that the arrival of water is not timely.
$P_2 = 0.098$	The probability that the option is not effective, given the water is there on time.
$P_3 = 0.5$	The probability of an adverse effect; i.e. of an ex-vessel steam explosion, given water in the cavity.

Before evaluating this strategy; we should note that if the flooding is not successful, there is the chance of an ex-vessel steam explosion when the cavity is partially full. This is treated in Section 3 along with other important phenomena.

Using Equations (2.3), the Expected Values can be evaluated as follows:

EV (Do Nothing) = 0.025 (2.4)

EV (Flood Cavity) = 0.011

An influence diagram for this example is shown in Figure 2.7a. The value of the consequence depends on the decision node (D) and the three chance nodes (C_1, C_2, and C_3) which are defined in Figure 2.6. The nodes C_2 and C_3 are not directly dependent on the decision because the probabilities of occurrence of a steam explosion and of vessel failure just depends on the success probability of cavity flooding, which in turn just depends on the decision node. Since the probability of a steam explosion is affected by the occurrence of vessel failure, the node C_2 depends only on the node C_1

The value ($\underline{V}$) is a vector given by:

$$\underline{V} = [\, f(R_1, R_2, R_3, R_4), R_5 \,] \qquad (2.5)$$

where the function (f) for cavity flooding has four elements (R_1, R_2, R_3, R_4) as noted in Figure 2.6. It is possible to remove C_3 by chance node removal, one of the operations for Influence Diagrams.

A given chance node can be removed if its only successor is the value node. This chance node is then removed by conditional expectation. The value becomes:

$$\underline{V} = [f(R_1, R_2\,(1 - P_3) + R_3\,P_3, R_4), R_5\,] \qquad (2.6)$$

where the function (f) for cavity flooding now has three elements.

Notice that the node C_2 in Figure 2.7b becomes a direct predecessor of the value node in this elimination process. Now this chance node, C_2 , can be eliminated by chance node removal and the value becomes:

$$\underline{V} = [\, f((1-P_2)\,R_1 + P_2\,(R_2\,(1 - P_3) + R_3\,P_3\,), R_4), R_5\,] \qquad (2.7)$$

In the same manner, the node C_1 in Figure 2.7c now becomes a direct predecessor of the value node, and can also be eliminated resulting in the value being given by:

$$\underline{V} = [P_1 R_4 + (1 - P_1) \{(1-P_2) R_1 + P_2 (R_2 (1 - P_3) + R_3 P_3)\}, R_5] \qquad (2.8)$$

which is the same as the value obtained from Equations 2.3. Figure 2.7d illustrates the final diagram, which has just two nodes. By comparing the value of each alternative, the optimal decision can now be made.

In this example, and on an expected value basis, one would choose to flood the cavity, in spite of the potential for adverse effects.

2.5 Decision Trees and Influence Diagrams

In this report, the use of Decision Trees and Influence Diagrams, first to structure the decision and second, to assess the strategy via either an Influence Diagram or a Decision Tree is presented. In searching the literature, we have found the following regarding each:

Advantages of Decision Trees

- Actual sequences are shown.
- Evaluation methodology and computer programs are well developed.

Advantages of Influence Diagrams

- A compact and unambiguous representation of probabilistic and deterministic dependency.
- May be easier to modify and evaluate alternative strategies.
- Rapid identification of important parameters.

Disadvantages of Decision Trees

- The large number of branches make them unwieldy.

Disadvantages of Influence Diagrams

- Individual sequences are not shown.

In this report we utilize the Influence Diagrams and Decision Trees to evaluate two strategies. Commercially available computer programs are available to quantify decision trees [4]. One needs only to supply the probabilities at the chance nodes and the risk values at the end of the tree. These codes calculate the expected values given for example, by Equations (2.3) and (2.8). The results of our studies are presented in Sections 3.0 and 4.0. In Section 5.0 the method for quantifying Influence Diagrams is presented. Section 6.0 presents conclusions and recommendations.

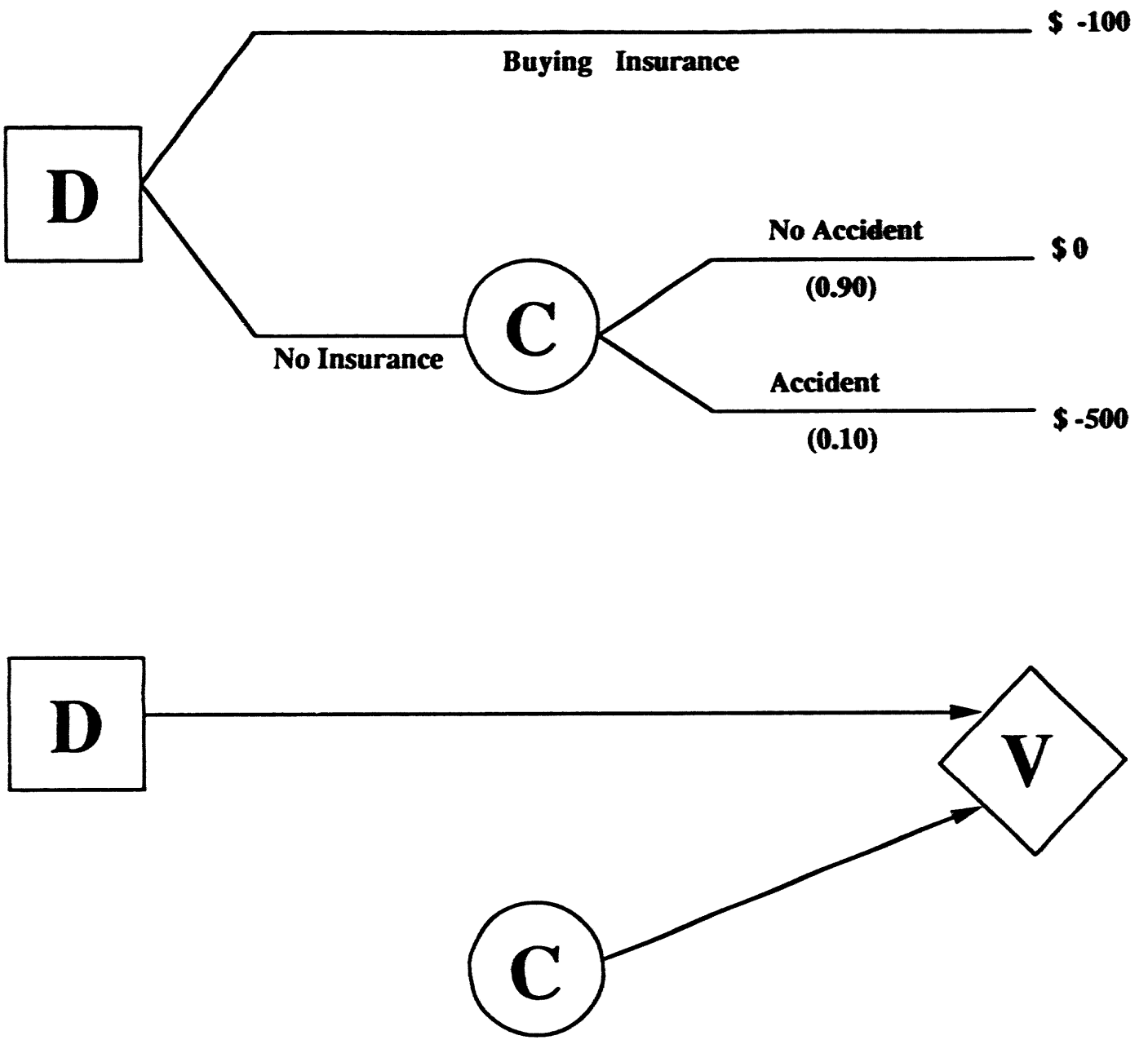

Figure 2.1. Decision tree and influence diagram for insurance example.

a)

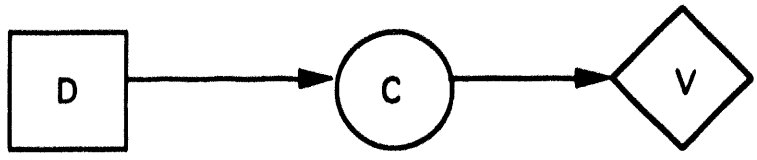

b)

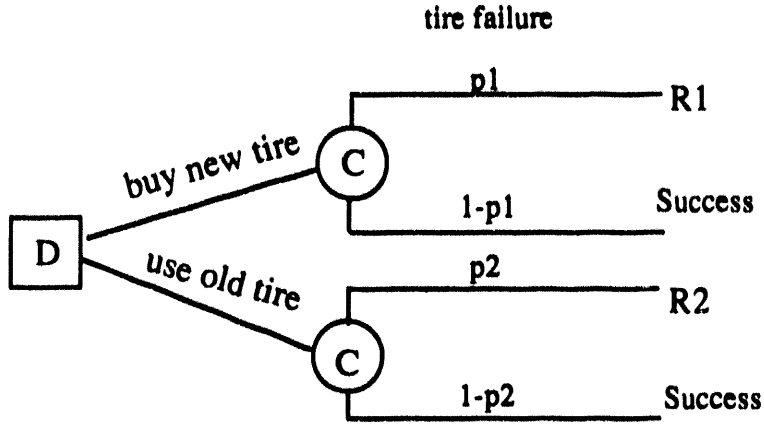

R1 = R2

D: buy new tire or not
p1: probability of tire failure (new tire)
p2: Probability of tire failure (old tire)
R1 = R2 = consequences of tire failure

Figure 2.2. Three cases with decision, chance, and value nodes.

c)

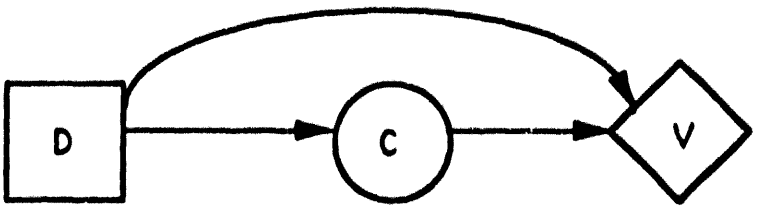

d)

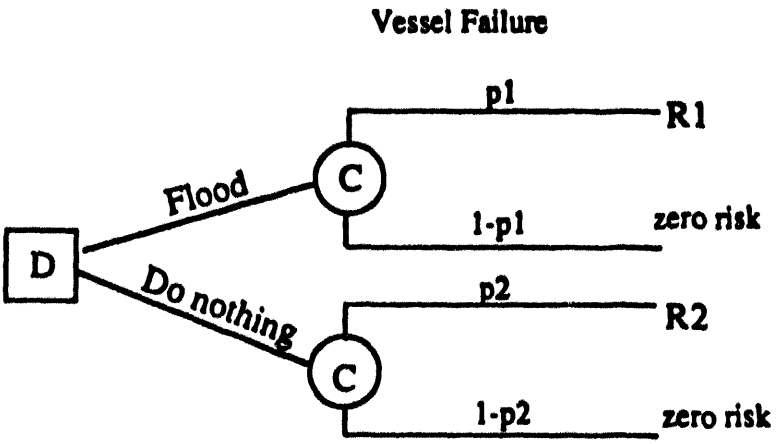

$R1 \neq R2$

D: flood the reactor cavity or not
p1: probability of vessel failure, cavity flooded
p2: probability of vessel failure, cavity dry
R1: risk of early fatality with cavity flooded
R2: risk of early fatality with dry cavity.

Figure 2.2 (continued). Three cases with decision, chance, and value nodes.

e)

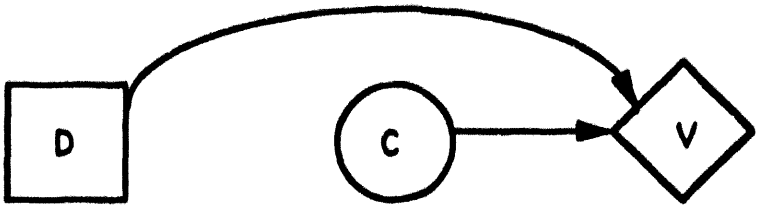

f)

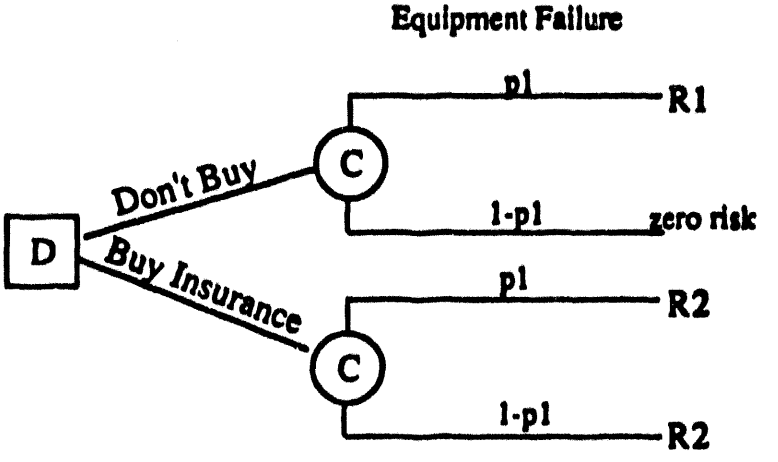

R1 ≠ R2

D: buy insurance
p1: probability of failure
R1: cost of repair
R2: cost of insurance.

Figure 2.2 (continued). Three cases with decision, chance, and value nodes.

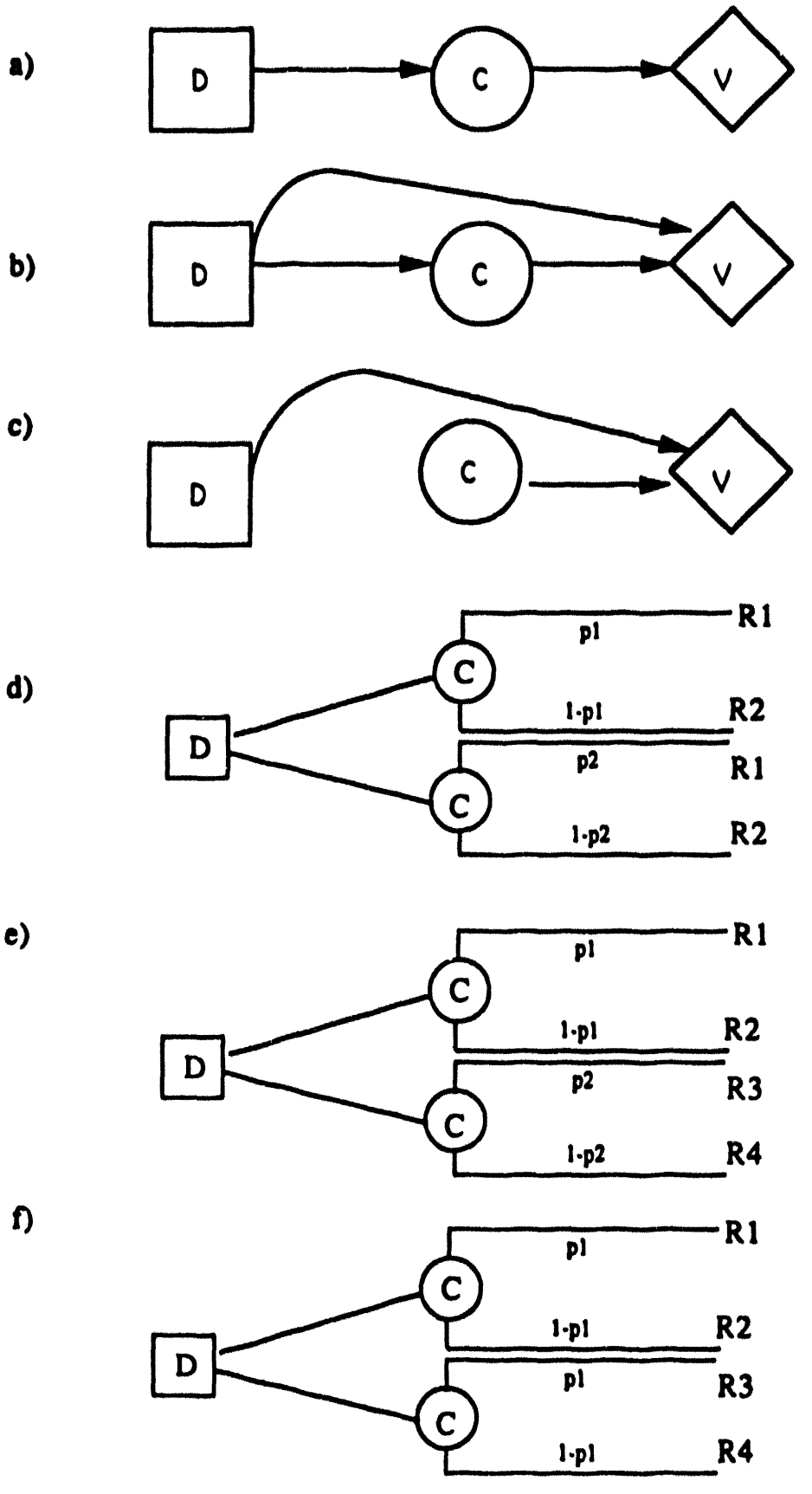

Figure 2.3. Three general cases with decision, chance, and value nodes.

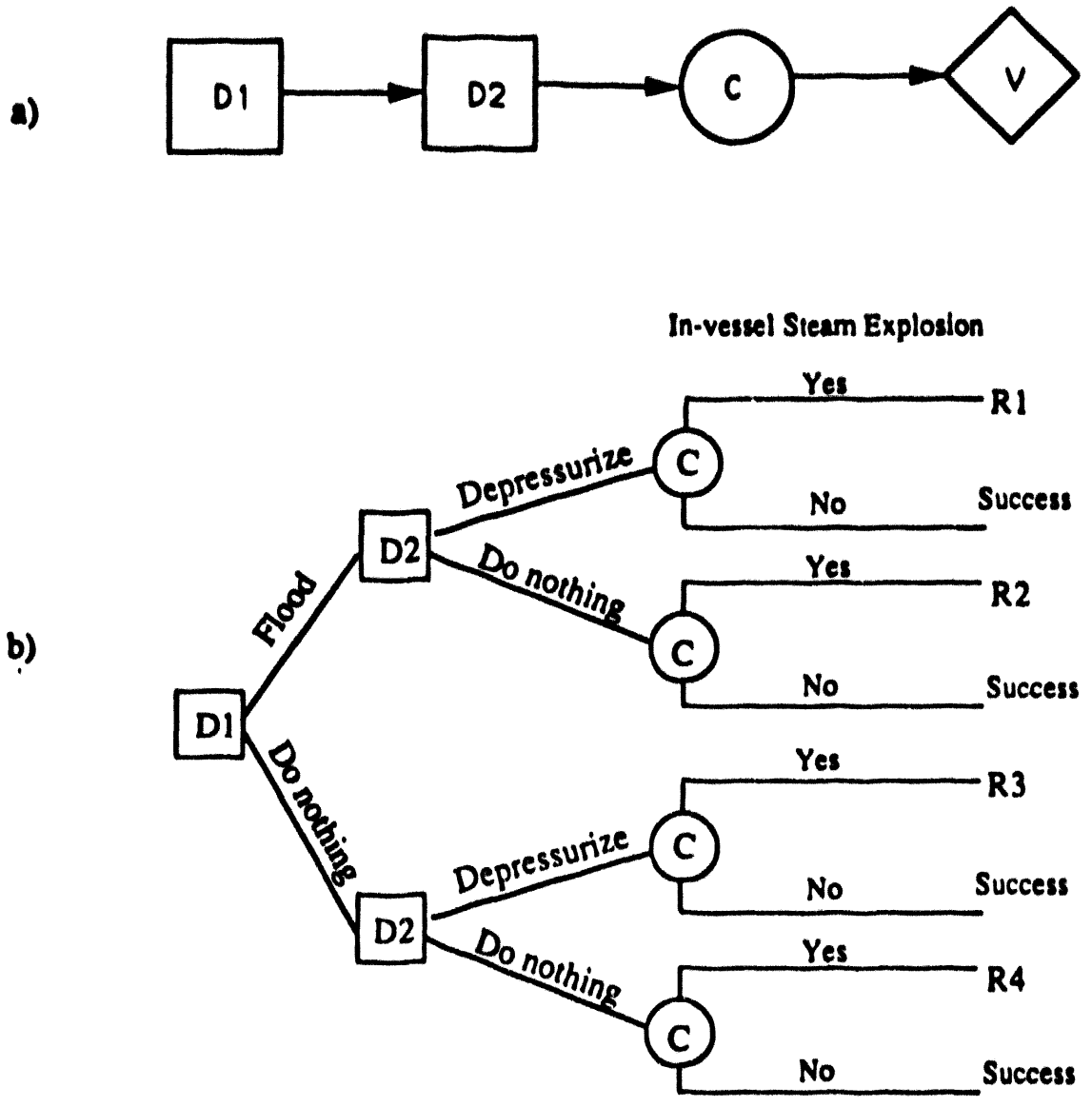

Figure 2.4. Influence diagrams and decision trees associated with multiple and sequential decisions.

c)

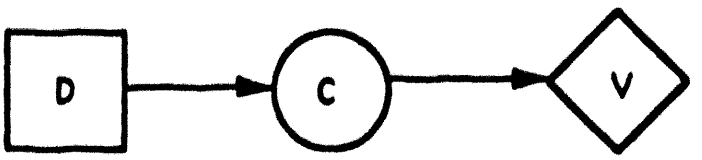

d)

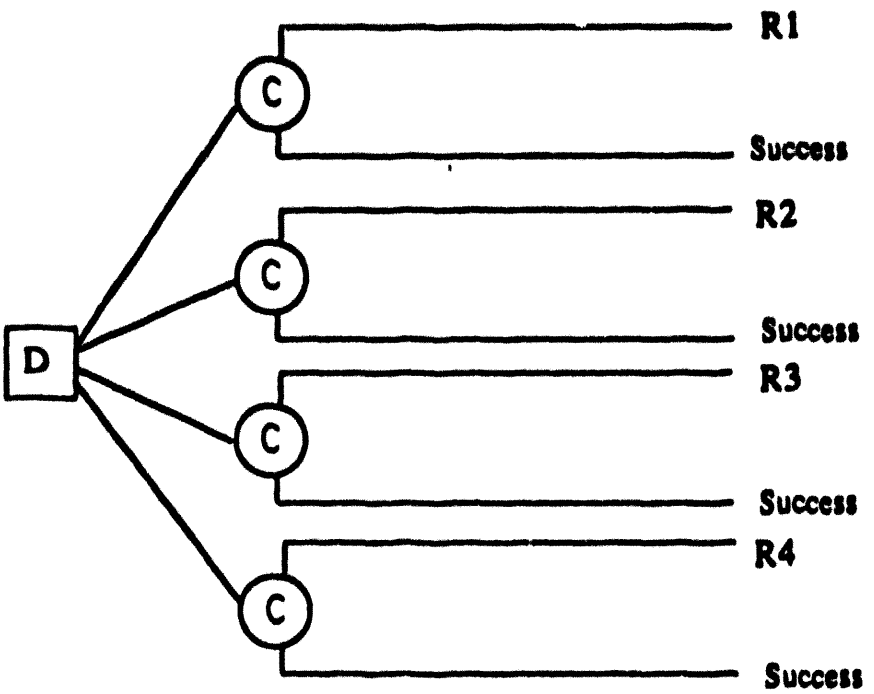

Figure 2.4 (continued). Influence diagrams and decision trees associated with multiple and sequential decisions.

e)

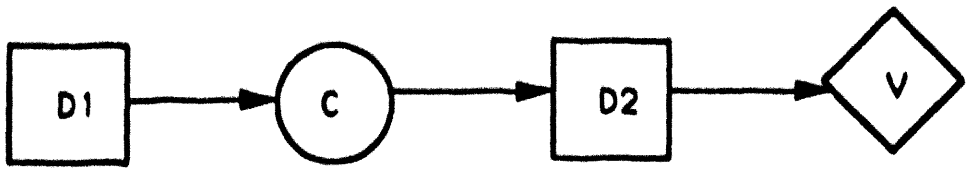

f)

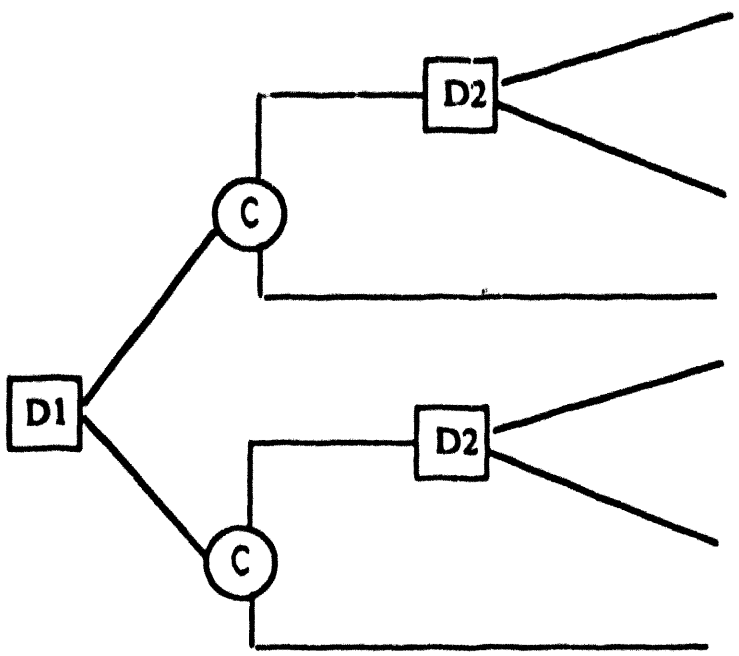

g)

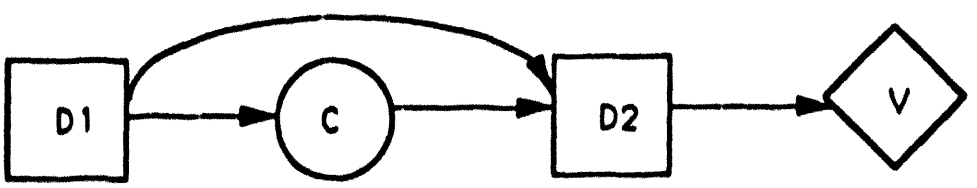

Figure 2.4 (continued). Influence diagrams and decision trees associated with multiple and sequential decisions.

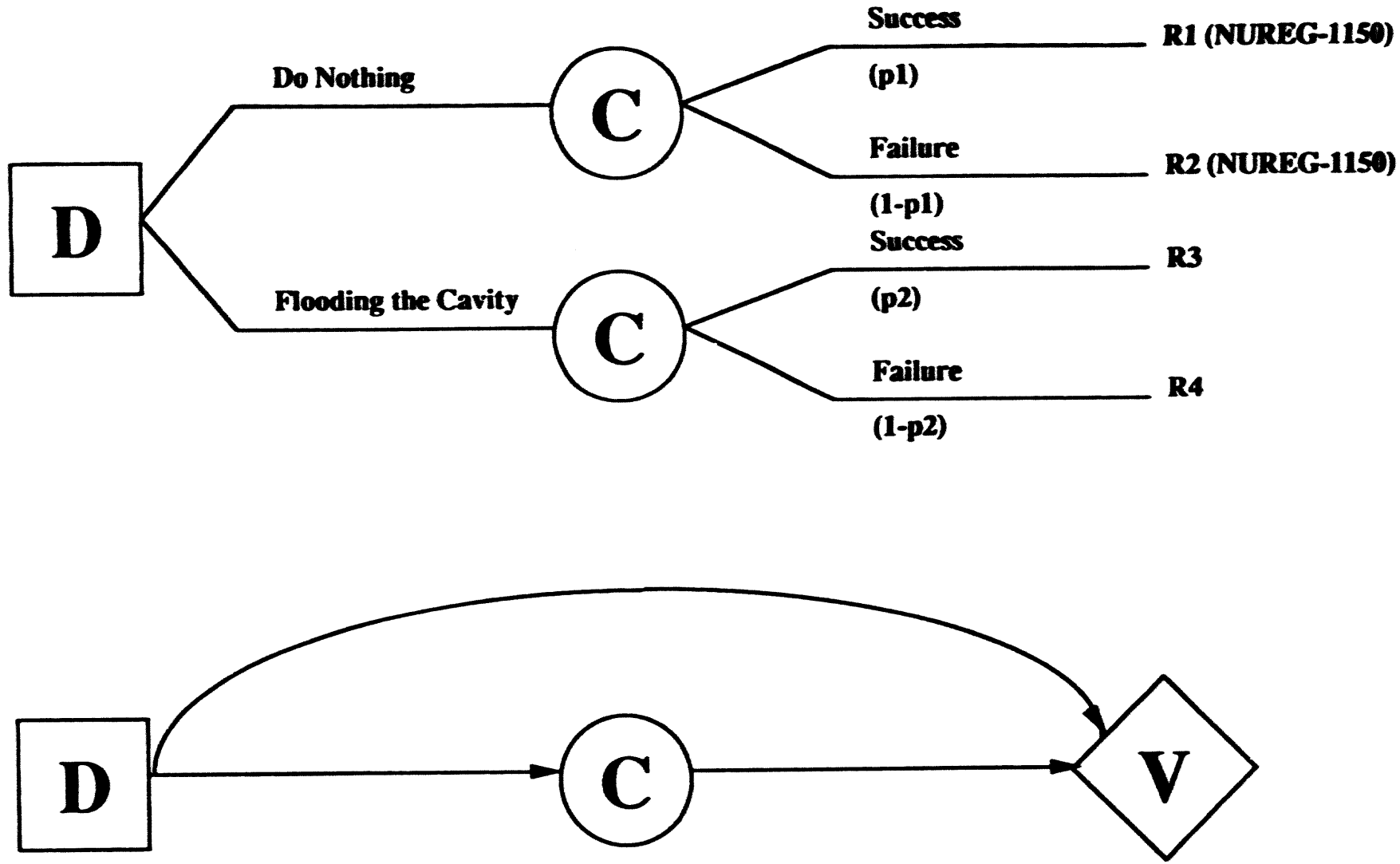

Figure 2.5. Decision tree and influence diagram for the flooding cavity example.

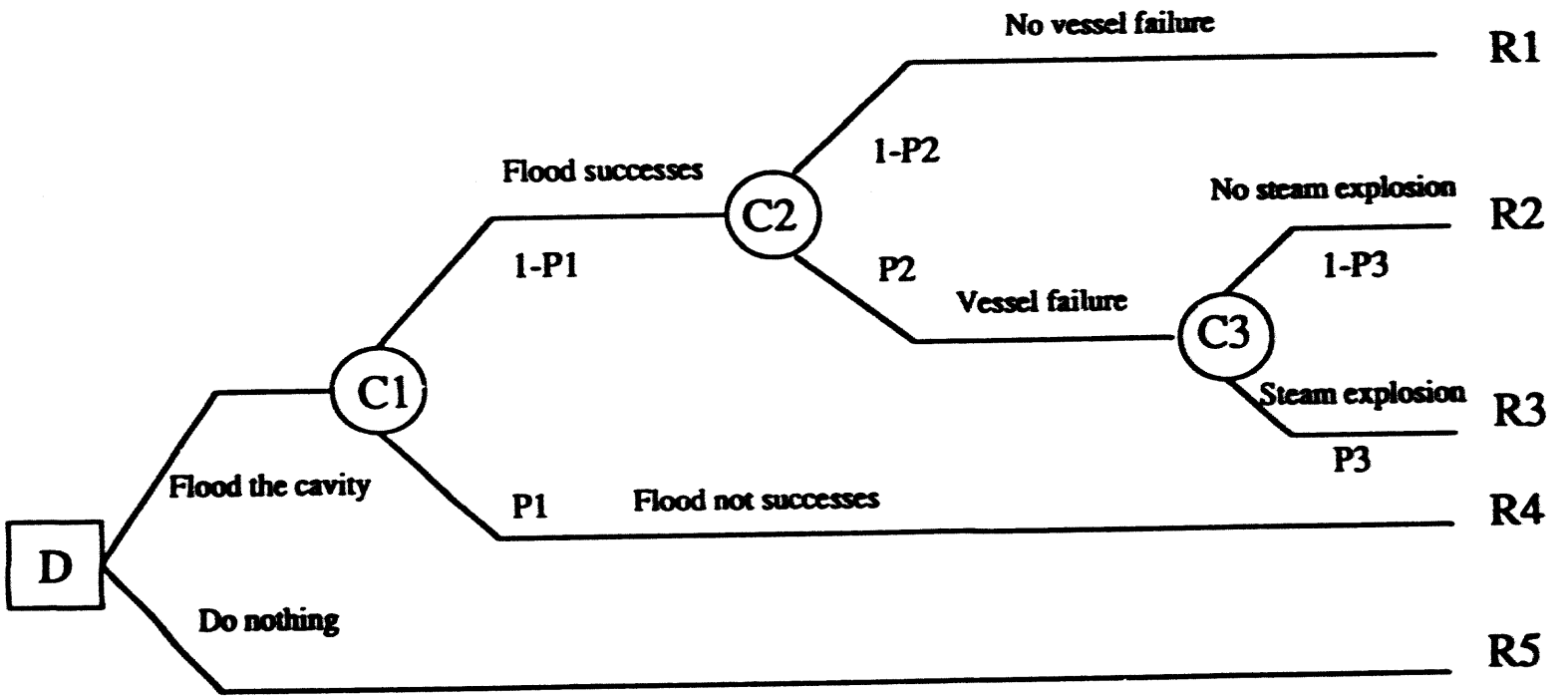

Figure 2.6. Decision Tree for PWR cavity flooding example.

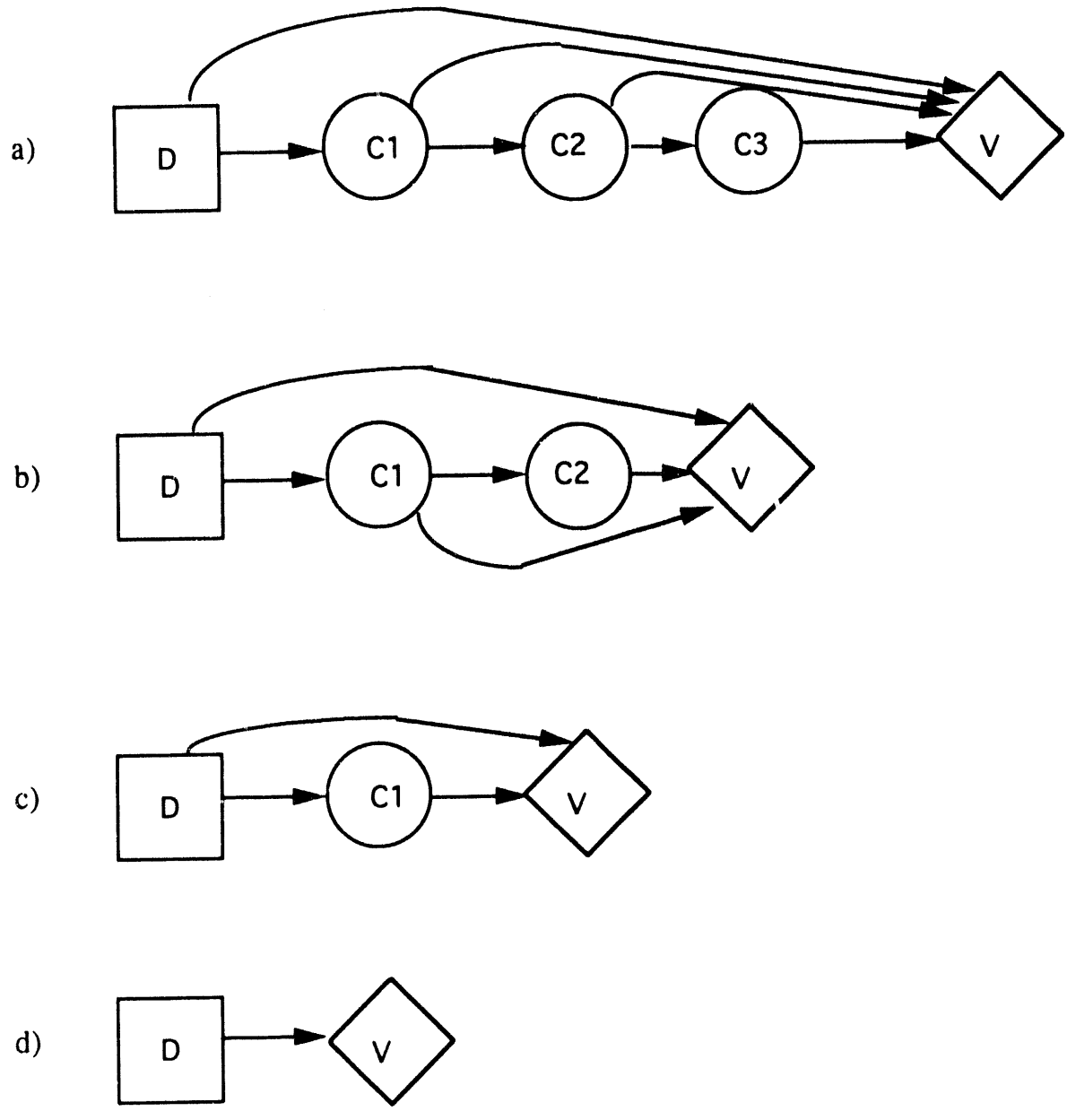

Figure 2.7. An influence diagram equivalent to Figure 2.6 and reduced diagrams.

3. PWR CAVITY FLOODING

3.1 Introduction

One of the candidate accident management strategies discussed during the PWR accident management workshop held at UCLA [1] is the idea of flooding the reactor cavity to the top of the vessel lower head, with the aim of cooling the vessel from the outside and possibly preventing vessel failure. This strategy could be especially useful for station blackout sequences, in which the emergency core cooling systems (ECCS) are unavailable. The operators could inject an alternative source of unborated water, such as fire water, into the cavity since they cannot inject it into the vessel due to recriticality concerns.

The evaluation of severe accident risks [3] has shown that the short term station blackout sequence is one of the most important contributors to risk. This sequence consists of the loss of off-site power as the initiating event followed by the failure of the emergency diesel generators to provide backup AC power. In addition, the auxiliary feedwater system fails to provide emergency feedwater to the steam generators. Since the heat removal capability of the steam generators is lost, the RCS will heat up and pressurize, leading to coolant loss through the power operated relief valves (PORVs). The loss of AC power results in the unavailability of all ECCS, and if power is not recovered, continued coolant loss will lead to core uncovery and damage.

The Surry plant was chosen for this evaluation because of the extensive information available on severe accidents, including the phenomena associated with their initiation and progression, and their consequent risks. The short term station blackout sequence was chosen because it is a significant contributor to risk and because many thermal-hydraulic analyses have been performed relating to it [5,6].

Since all emergency core cooling systems are rendered unavailable by the loss of AC power, and heat removal by the steam generators is also unavailable, the operators do not have any options available to them with respect to preventing or arresting core damage (unless AC power is recovered). However, if they can

cool the vessel from the outside they may be able to accomplish the second goal of accident management, prevention of vessel failure.

Flooding the cavity would also have the additional benefits (called secondary mitigative effects) of preventing high pressure melt ejection and associated direct containment heating. This occurs because vessel breach via a penetration failure would be eliminated with water present in the cavity, even if the vessel does fail. Similarly, the presence of water would possibly prevent a core-concrete interaction if the vessel fails anyway. However, there may be adverse effects associated with the strategy. One concern is that should the the strategy be successful in keeping the molten core inside the vessel, continued exposure of the steam generator tubes to hot gases circulating from the molten pool could result in their failure, if the hot leg or surge line does not fail first. Another concern is that should the vessel fail with the cavity full of water, an ex-vessel steam explosion could result in early containment failure.

In assessing this strategy the potential benefits must be measured against the potential for adverse effects, in an integrated fashion. The feasibility of this strategy, which is concerned with whether or not the operators will be able to fill the cavity up to the required level in time using the proposed equipment, must also be considered.

These considerations involve determining what information would be needed by the operators to diagnose the situation and implement the strategy on time. The instruments that would supply this information have to be identified and their performance under the accident conditions must be assessed. The sequence of operator actions necessary to successfully implement the strategy must be identified in order to formulate a suitable human reliability model in order to evaluate the likelihood of success. Also the reliability of the systems and equipment involved must be evaluated.

3.2 Construction of the Influence Diagram.

For this study, we begin with the construction of the influence diagram, as described below.

Decision Node D and Value Node V.

For this strategy, the influence diagram begins with a decision node and ends with a value node, represented by D and V respectively, in Figure 3.1a. The decision modeled by node D is whether or not to instruct the operators to initiate flooding of the reactor cavity using diesel driven fire pumps at the time of core uncovery.

In order to evaluate an accident management strategy, a suitable criterion is needed against which to compare the alternatives. This criterion is associated with the value node of the influence diagram, and for this strategy there are several possibilities: early fatalities, the conditional probability of early containment failure, economic loss, etc. The criterion should be chosen in such a way that all factors of the assessment are captured, including adverse effects and secondary mitigative effects.

If there were no adverse effects or secondary mitigative effects after vessel failure for the strategy considered in this section, the conditional probability of "no vessel failure" would be a good criterion since it is a direct measure of the feasibility and the effectiveness of the strategy. However, there are adverse effects and secondary mitigative effects associated with this strategy. Since the feasibility, effectiveness, adverse effects, and secondary mitigative effects all influence the offsite consequences, risk is used as a criterion in this study. Actually two measures of risk are used: early fatalities and late fatalities.

The values of the off-site consequences used for the two measures of risk in this study are obtained from NUREG-1150 [3], and are shown in Table 3.1 as a function of containment failure mode (ECF stands for early containment failure, LCF for late containment failure, and SGTR for steam generator tube rupture). Hence the value node has three direct predecessor nodes as shown in Figure 3.1b, and the expected risk, conditional on D, is a deterministic function of these nodes, i.e.

$$\langle V/(D_i)\rangle = V(ECF)P(ECF/D_i) + V(SGTR)P(SGTR/D_i,ECF,) + V(LCF)P(LCF/D_i,ECF,SGTR,). \quad (3.1)$$

where the bar denotes that the event does not occur, and the subscript i denotes either flood or no flooding. In order to quantify the probabilities in Equation (3.1), the influence diagram must be expanded until all nodes can be assessed. The first step is also shown in Figure 3.1b, which shows that the containment failure modes are influenced by the mode of vessel breach (VB).

Node VB.

Since the primary aim of flooding the cavity is to prevent vessel breach (VB) by cooling the vessel from the outside, it is modeled as a chance node in the influence diagram. The mode of vessel failure is also included in this node. In NUREG-1150 three modes of vessel failure are considered for the Surry Accident Progression Event Tree (APET): penetration failure, gravity pour and gross bottom head failure. In this study, it is only necessary to distinguish penetration failure from the other modes, and only for the case where the RCS pressure is high because this is the only case that affects early containment failure due to direct containment heating. The mode of vessel failure is irrelevant if the RCS pressure is low. Then there are three possibilities for the VB node: no vessel failure (no VB), penetration failure at high pressure (HPME) and either gross bottom head failure or gravity pour (BH).

The probability of vessel failure, and the mode by which it fails, depends on whether or not the cavity is flooded to the top of the bottom head before the core slumps (WC), the RCS pressure (RP), and whether or not core damage was arrested, due to recovery of AC power (R) and ECCS (CDA). The influence diagram is expanded to include these additional nodes, as shown in Figure 3.2. The conditional probabilities for the node VB are shown in Table 3.2, and are discussed as follows.

In case 1 core damage is assumed to be arrested via AC power recovery and hence ECCS recovery. The probability of no vessel failure is then 1.0.

In case 2 the RCS is at high pressure and the cavity is assumed to be flooded up to the top of the vessel lower head before core slump. Calculations performed by Park and Dhir, (see Appendix I and in Reference [7]) have shown that some

melting of the vessel inner wall is very likely in this situation. In addition, extremely large temperature variations in the vessel wall will result in thermal stresses well in excess of the yield stress for pressure vessel steel over much of the vessel thickness, but it is not known whether or not this will lead to failure of the vessel due to excessive stress or thermal creep, although it is judged to be likely. These calculations are discussed in more detail in Chapter 7, where a sensitivity and uncertainty analysis is performed, and in Appendix I. A base case value for the probability of vessel failure for this case is chosen to be 0.9. Given that the vessel fails, it was assumed that the vessel will fail by either penetration failure leading to high pressure melt ejection (HPME) or bottom head failure (BH), with equal probability for each.

In case 3, the RCS is at high pressure and there is no water in the cavity. Hence vessel failure is assured. The split fractions regarding the mode of vessel failure were obtained from reference [8] for this case.

Case 4 is similar to case 2 except that the RCS is at low pressure. The probability of no vessel failure for this case is conservatively chosen to be 0.1. This is also discussed in Chapter 7. Temperature and stress calculations are presented in Appendix I. Since the RCS pressure is low when the vessel fails, the probability of HPME is 0.0.

Case 5 is like case 3, but again, since the RCS pressure is low, the probability of HPME is 0.0.

Node CDA.

Even if AC power is recovered and the vessel is flooded, there is still a chance that the molten debris will not be in a coolable configuration and the vessel will fail anyway. There is also a chance that a fuel-coolant interaction could lead to vessel failure. The probability of core damage arrest, given AC power is recovered in time, is taken to be 0.9. This value was given in reference [8]. Obviously, if AC power is not recovered, the probability of core damage arrest is 0.0 (Table 3.3).

Node WC.

This node represents the question of whether or not the reactor cavity is flooded to the top of the vessel lower head, given that the operators were instructed to do so. The probability that this strategy is successfully implemented is composed of two parts: the probability that the operators successfully initiate the strategy in time and the probability that the fire pump system functions correctly.

Based on the facts that the station would be blacked out and the core exit thermocouples (CETCs) located in the core that may help in detecting core uncovery, which is powered by the station batteries, would be available, the failure of the plant operators to correctly initiate the strategy would be governed by two uncertain variables: the diagnosis and decision time, T_d, which is the time available for the operators to diagnose the situation, and the action time, T_a, which is the time required for the operators to initiate flooding of the reactor cavity. The auxiliary operators outside the control room are assumed to be available to operate the fire pump system.

Flooding the reactor cavity might involve the following steps:

(1) The control room operators detect core uncovery and dispatch an auxiliary operator to the emergency fire pumps.
(2) The auxiliary operator goes to the emergency fire pumps.
(3) The auxiliary operator starts the fire pumps .

The major uncertainty is associated with the critical time determined by the phenomena occurring during the melt progression. In order for the cavity flooding strategy to have a chance at being successful in preventing vessel failure, the water must reach the top of the vessel lower head before the core slumps into the lower head. Thus the critical time, $T_c = T_{cs} - T_{cu}$, is the time from core uncovery (T_{cu}) to core slump (T_{cs}). The time to core slump is needed because if the water reaches the vessel lower head after a significant amount of debris has relocated there, a film boiling situation will exist and the heat transfer will not be sufficient to cool the vessel enough to prevent melting and failure, as shown in Appendix I and in Reference [7]. Because the phenomena associated with melt

progression and relocation are very complicated, the time to core slump is highly uncertain. Table 3.4 shows estimates of T_{cs} obtained by three different computer simulations.

Another relevant parameter is the time required to fill the reactor cavity to the required level, T_f. This parameter is known [9] and is a function of the Surry reactor cavity volume (92,452 gal) and the fire pump capacity (2000 gpm) [10], and is calculated to be 46.2 minutes.

The human error probability (HEP), is the probability that $t = T_a + T_d + T_f$ exceeds $T_c = T_{cs} - T_{cu}$, i.e.,

$$HEP = P(t > T_{cs} - T_{cu})$$

$$= \int_0^\infty [1 - F_t(t)] f_{Tc}(t) dt, \qquad (3.2)$$

where

$f_{Tc}(t)$ = probability density function (pdf) of the critical time, $T_{cs} - T_{cu}$, and

$F_t(t)$ = cumulative distribution function (cdf) of the time required by the operators to complete the strategy.

Since the distributions in equation (3.2) are not available, the probability that the operators successfully initiate the strategy on time can be obtained from the "Human Error Handbook" [11] using times shown in Table 3.4. Since natural circulation in the reactor coolant system was not considered in the MARCH calculation in Table 3.4, these times calculated by MARCH are considered to be too conservative. The time calculated by SCDAP/RELAP in Table 3.4 is used for this report, and based on this time a value of 0.62 for the success probability was obtained from Figure 12-4 and Tables 20-8 and 20-13 of Reference [11]. The value of 0.95 is assumed for the availability of the fire system. Therefore, the probability that there is water in the cavity to the top of the vessel lower head before the core slumps, P(WC), is the product of successful operator actions,(1-HEP), and the availability of the fire system, Q (see Table 3.5).

Node RP.

This node represents the RCS pressure at vessel breach. Two possibilities are considered: low pressure (<200 psi) and high pressure (> 200 psi). This node depends on whether or not there is a temperature-induced failure of the hot leg, the surge line or a steam generator tube, as well as whether or not AC power is recovered, since the operators are instructed to depressurize the RCS if AC power is available. Temperature-induced hot leg or surge line failure is modeled by node (HSF), the possibility of a steam generator tube rupture before vessel breach is represented by a new node (ESGTR), and the recovery of AC power is modeled by the node (R), as shown in Figure 3.2. The conditional probabilities for node RP are shown in Table 3.6.

Node R.

This node represents the probability of AC power recovery (and subsequent recovery of ECCS) before vessel failure. The probability of AC power recovery before vessel failure is

$$\begin{aligned} P(R) &= P(T_{cu} < T_r < T_{vb} / T_r > T_{cu}) \\ &= P(T_{cu} < T_r < T_{vb}) / P(T_r > T_{cu}) \\ &= [F_{RAC}(T_{vb}) - F_{RAC}(T_{cu})] / [1 - F_{RAC}(T_{cu})] \end{aligned} \qquad (3.3)$$

where T_{cu} is the time to core uncovery, T_{vb} is the time to vessel failure and T_r is the time to recovery of AC power. FRAC(t) is the cdf for time to recovery of AC power at Surry, provided in Reference [12]. The times to vessel breach and core uncovery are the values given in Table 3.4 for the SCDAP/RELAP calculations. The probability of AC power recovery is then 0.26.

Node HSF.

In the TMLB' sequence the core begins to melt while the RCS is at or near the PORV setpoint pressure. Natural circulation of hot gases exiting the core region could result in the failure of the hot leg or (more likely) the pressurizer surge line. The probability of a hot leg or surge line failure (HSF) depends on

whether or not a steam generator tube rupture has occurred (ESGTR) [8]. If there is no SGTR, the probability of HSF is 0.72, otherwise the probability is 0.034, due to the reduced pressure.

Node ESGTR and Node SGTR.

There are two situations that could result in a steam generator tube rupture (SGTR). The first, which occurs before core slump, is the situation in which the core is melting at the PORV setpoint pressure. The steam generator tubes could be exposed to very hot gases circulating from the core region. If the hot leg or surge line does not fail first, one or more steam generator tubes could rupture. This possibility is represented by node ESGTR in Figure 3.2. The value of 0.02 for the probability of the occurrence of an early steam generator tube rupture is given in Reference [8]. This node affects nodes (RP) and (SGTR).

The second situation arises when external cooling keeps the molten core in the vessel, and the RCS remains at high pressure. In this situation, long term exposure of the steam generator tubes to hot gases exiting the core region could result in the rupture of one or more, given that no other failure of the RCS occurs first. This possibility is represented by node LSGTR, which is shown in Figure 3.3, and which influences node (SGTR).

Node LSGTR.

This node represents the probability of a late SGTR, as described above. This node depends on node VB, node R and node RP as shown in Figure 3.3. The conditional probabilities for this node are shown in Table 3.7. The only case in which a late SGTR is possible is the case where there is no vessel breach and the RCS pressure is high. It is assumed that if AC power is recovered, feed-and-bleed cooling of the core will be initiated, which would preclude an SGTR. For completeness, it is conservatively chosen to be 0.1.

Nodes ECF, DCH, VHS and CFE.

Node ECF represents the probability of early containment failure, either due to direct containment heating (DCH) or an ex-vessel steam explosion (EVSE). Since early containment failure due to an ex-vessel steam explosion is a possible adverse effect of flooding the reactor cavity, it is treated in this report even though it has been discredited elsewhere (see Reference [8] and Appendix H). The probability of early containment failure due to an ex-vessel steam explosion is conservatively chosen to be 0.01. A sensitivity study regarding EVSE and ECF is presented in Section 3.4 below.

At Surry, early containment failure due to DCH depends on the occurrence of a high pressure melt ejection, the amount of water present in the reactor cavity, the amount of the core ejected from the vessel and the size of the hole in the vessel after ablation (see Reference [13]). Reference [13] provides cumulative distribution functions for the containment pressure rise at vessel breach for nineteen different cases. These cases consist of combinations of RCS pressure at vessel breach, presence of water in the cavity, vessel hole size after ablation (large or small) and the fraction of core ejected (>40%, 20%-40%,or <20%). Of these nineteen cases, only those that have high RCS pressure apply here, of which there are twelve. For each of these twelve cases, the probability of early containment failure can be found by applying the Surry containment mean failure pressure (126 psig) to the cumulative distribution functions for the pressure rise at vessel breach. It is assumed in this study that if the cavity is filled with water up to the top of the vessel lower head the probability of early containment failure due to DCH is negligible because the core debris will be quenched when it enters the cavity.

The base case value of the probability of early containment failure due to an ex-vessel steam explosion was conservatively chosen to be 0.01. However, an ex-vessel steam explosion is possible only if there is water in the cavity.

The influence diagram is now expanded to include nodes EVSE (ex- vessel steam explosion), DCH (direct containment heating), VHS (vessel hole size) and CFE (core fraction ejected) as shown in Figure 3.4. The conditional probabilities for node ECF are shown in Table 3.8, as obtained from Reference [13]. The

probabilities for node VHS are shown in Table 3.9 and were obtained from Reference [8]. The probabilities for node CFE were obtained by applying the fractions given above to the cumulative distribution function provided in Reference [13], and are shown in Table 3.10. Node DCH is for representational purposes only, and for the evaluation it is included as part of node ECF.

Node EVSE.

This node represents the probability of the occurrence of a significant ex-vessel steam explosion, and depends on whether or not there is water present in the cavity, which occurs if the cavity is intentionally flooded by the operators (WC) or if AC power is recovered and the containment sprays actuated (R), and whether or not the vessel fails (VB), as shown in Figure 3.4. NUREG-1150 uses a value of 0.5 for the occurrence of a significant ex-vessel steam explosion at Surry, and that value is used here, even though a probability of 0.86 is given for PWRs in Appendix II (Section A.2) of this report (it is questionable if the experiments described there apply). The conditional probabilities for this node are shown in Table 3.11 and are given in Reference [8].

Node LCF and Node S.

Node LCF represents the possibility of a late containment failure. Only the basemat melt-through mode of late containment failure is considered here. Late containment failure due to slow overpressurization is possible only if the containment heat removal systems are lost for a period of several days, which is highly unlikely except for some external initiators (see Reference [8]).

The probability of late containment failure due to basemat melt-through depends on the occurrence of core-concrete interaction (CCI), represented by node CCI, the amount of the core participating in CCI, represented by node ACCI, and whether or not the sprays are operating during the period of CCI, represented by node S. These are shown in Figure 3.5. If there is no CCI the basemat will not melt. Also, continued deposition of water on top of the core debris in the cavity by the containment sprays will remove some of the decay heat from the debris and will reduce the amount of CCI. The conditional probabilities of node LCF are shown in Table 3.12 and are obtained from Reference [8]. The

conditional probability that the sprays are operating during the period of CCI is 1.0 if either AC power was recovered before vessel failure (node R), or if it is recovered during the period of CCI, represented by node LR (See Table 3.13 and Figure 3.5).

Node LR.

This node represents the late recovery (LR) of AC power, i.e., during the period of CCI. The time period of interest here is the time from vessel failure to the somewhat arbitrary time of 9 hours (as in Reference [8]). As was done for node R, the probability of recovering AC power during the period of CCI is

$$P(LR) = P(T_{vb} < T_r < T_a / T_r > T_{vb})$$
$$= [F_{RAC}(T_a) - F_{RAC}(T_{vb})]/[1 - F_{RAC}(T_{vb})]. \quad (3.4)$$

where T_{vb} and F_{RAC} are as described for node R and T_a is 9 hours. Then the probability of recovery of AC power during CCI is 0.94 if it was not recovered before vessel failure, and it is 0.0 if AC power was recovered before vessel failure. These are shown in Table 3.14.

Node CCI.

This node represents the occurrence of CCI and depends on if there is water in the cavity at the time of vessel failure, either due to flooding by the operators or spray actuation via recovery of AC power before VB, whether or not the core was ejected from the vessel at high pressure and whether or not there was an ex-vessel steam explosion, as shown in Figure 3.5. The conditional probabilities are shown in Table 3.15, and are given in Reference [8].

If there is no water in the cavity at the time of vessel failure the probability of CCI is 1.0. If there is water in the cavity, the ex-vessel debris might not be in a coolable configuration, so there is still a possibility of CCI.

Node ACCI.

This node represents the amount of the core that is available to participate in CCI and depends on whether or not the core debris was ejected at high pressure, whether or not there was a steam explosion, and the fraction of the core ejected at vessel failure (CFE), as shown in Figure 3.5. The conditional probabilities for this node are shown in Table 3.16, and are given in Reference [8].

3.3. CONSTRUCTION OF THE DECISION TREE.

Since the influence diagram shown in Figure 3.5 contains the probabilistic relationships and decisions as developed by the analyst, a consistent decision tree can be constructed directly from this diagram and necessary conditional probabilities can be assessed. Bases on the chain rule, which will be described in Chapter 5, an ordered list is constructed. The ordering of the top events of the decision tree will be the same as that for the ordered list. Each chance node of the influence diagram corresponds to a chance node of the decision tree. The branching probabilities of the tree are the same as the conditional probabilities of the influence diagram, and are conditional on the path through the tree. However, the decision tree corresponding to the influence diagram in Figure 3.5 would be very large; hence it is desirable to simplify the influence diagram as much as possible. This can be easily done by removing all nodes that have only one successor node, unless the direct successor node is the value node (chance node removal). Doing this removes the conditionality of the direct successor node on the node being removed, and makes the direct successor node conditional on the direct predecessor nodes of the node being removed, i.e.,

$$P(S=S_i/P_1,\ldots,P_n) = \sum_k P(S=S_i/N=N_k)P(N=N_k/P_1,\ldots,P_n), \quad (3.5)$$

where N is the node being removed, S is the direct successor node and $P_1,\ldots,P_n$ are the direct predecessor nodes. The details on the operation of chance node removal will be shown in Chapter 5. The resulting simplified influence diagram is shown in Figure 3.6, and the resulting conditional probabilities for nodes RP, VB, SGTR, ECF and LCF are given in Tables 3.17 - 3.21. The conditional

probabilities of the other nodes are unchanged. The decision tree corresponding to this influence diagram is shown in Figures 3.7 - 3.12.

In the decision tree, branches which have a probability of 0.0 are not shown. For example, consider the topmost path of Figure 3.7. The high pressure branch of node RP will occur with probability of 0.0, and the low pressure branch will occur with a probability of 1.0. Thus the high pressure branch is not represented.

Also, branches which are irrelevant are not shown. For example, consider the whole branch in which the cavity is completely filled with water. In this case the mode of vessel failure is irrelevant since there is no possibility of containment failure due to DCH. Thus the branch that distinguishes HPME from the other modes of vessel failure is not shown.

3.4 Quantification and Discussion.

As a first step, the influence diagram shown in Figure 3.6 and its equivalent decision tree, shown in Figures 3.7 - 3.12, were quantified using the "base case" values described in Section 3.2. The base case results are shown in Table 3.22 and Figure 3.13. The conditional probabilities of vessel failure, early containment failure, late containment failure, the occurrence of an ex-vessel steam explosion and the occurrence of a steam generator tube rupture are shown Table 3.23 and Figure 3.14, for both branches of the decision node (flood/not flood). Also shown is the expected risk (in terms of both early fatalities and latent cancer fatalities) for both branches of the decision node. It can be seen that the expected risk reduction, i.e.,

$$\langle \Delta R \rangle = \langle V(\text{not flood}) \rangle - \langle V(\text{flood}) \rangle, \qquad (3.6)$$

is positive for both measures of risk, so therefore instructing the operators to flood the cavity is beneficial using the base case values for each chance node.

In addition to the base case assessment, a sensitivity study was performed in order to determine which chance nodes are the most important in terms of affecting the decision of whether or not to flood the reactor cavity. The

influence diagram was evaluated with the following probabilities varied between 0.0 and 1.0:

P(WC/Flood) = the probability that the cavity is flooded to the top of the lower head before the core slumps, given that the operators are instructed to do so,

P(R) = the probability that AC power is recovered before vessel failure,

P(LSGTR/WC, no VB, high) = the probability of the occurrence of a late steam generator tube rupture given that cavity flooding has prevented vessel failure and the RCS is at high pressure.

P(VB/WC,No CDA) = the probability of vessel failure given that the cavity is flooded on time and core damage is not arrested,

P(EVSE/VB,WC or R) = the probability of the occurrence of an ex-vessel steam explosion given vessel failure and the presence of water in the cavity or the restoration of AC power, and

P(ECF/EVSE) = the probability of early containment failure given the occurrence of an ex-vessel steam explosion.

These probabilities were chosen because the risk calculation is most sensitive to them.

The results of these calculations are shown in Figures 3.10 - 3.15. The risk reduction is positive for all values of the probabilities listed above, except for P(LSGTR/WC, no VB, high), P(EVSE/VB, WC or R) and P(ECF/EVSE) which are related to the adverse effects of the occurrence of a late steam generator tube rupture or an ex-vessel steam explosion. For these three variables there is a range over which the risk reduction is negative. This implies that the decision to instruct the operators to flood the cavity is the preferred alternative, regardless of the values of the probabilities listed above, except for those associated with late steam generator tube ruptures and ex-vessel steam explosions. If the probability of a late steam generator tube rupture is greater than about 0.6,

flooding is detrimental. Furthermore, flooding is detrimental if the probability of the occurrence of an ex-vessel steam explosion is greater than about 0.85, or if the probability of early containment failure due to an ex-vessel steam explosion is greater than about 0.012.

In order to investigate how these important parameters affect the decision of whether or not to instruct the operators to flood the cavity, a systematic sensitivity analysis was performed. This analysis systematically varies parameters in order to determine in which cases one alternative is preferred over another, and can be classified as one-way, two-way, or three-way, depending on how many parameters are simultaneously varied. Figure 3.16 illustrates a two-way policy region analysis for the parameters P(EVSE/VB,WC or R) and P(ECF/EVSE) and Figure 3.17 for the two parameters P(EVSE/VB,WC or R) and P(No VB/Flood, High RP). In the shaded region of Figures 3.16 - 3.17, the decision to instruct the operators to flood the cavity is the preferred alternative, while in the un-shaded region the opposite is true. It can be seen from Figure 3.16 that if the occurrence of an ex-vessel steam explosion is assured, the alternative to not instruct the operators to flood would be preferred for all values of the probability of early containment failure due to a steam explosion. Figure 3.17 shows that the alternative to instruct the operators to flood would be preferred for all values of the probability of no vessel breach associated with flooding and high RCS pressure when the probability of an ex-vessel steam explosion is below approximately 0.81.

Table 3.1
Consequences of early and latent cancer fatalities (99.5% evacuation)

	Early Fatalities (EF)	Latent Cancer Fatalities (LF)
Early containment failure (ECF)	2.0	2275
Late containment failure (LCF)	0	122
Steam generator tube rupture (SGTR)	0.067	1444

Table 3.2
Conditional probability for node VB

CDA	RP	WC	P(no VB)	P(HPME)	P(BH)
yes	any	any	1.0	0.0	0.0
no	high	yes	0.1	0.45	0.45
no	high	no	0.0	0.79	0.21
no	low	yes	0.1	0.0	0.9
no	low	no	0.0	0.0	1.0

Table 3.3
Conditional probability for node CDA

R	P(CDA)
yes	0.9
no	0.0

Table 3.4
The accident progress timing (min) for the Surry TMLB' sequence determined by three codes

	MARCH	SCDAP/RELAP5	MELPROG
Core Uncovery	97	129	117
Core Slumping	143	> 180	248
Vessel Breach	155	> 180	265
Time Interval between core uncovery and core slumping	46	> 50	130

Table 3.5
Conditional probability for node WC

	Success	Failure
Flooding (D1)	0.59	0.41
Doing nothing (D2)	0.0	1.0

Table 3.6
Conditional Probability for node RP

R	HSF	P(High)	P(Low)
yes	-	0.0	1.0
no	yes	0.0	1.0
no	no	1.0	0.0

Table 3.7
Conditional Probability for node LSGTR

R	VB	RP	ESGTR	P(LSGTR)
no	no	high	no	0.1
else	-	-	-	0.0

Table 3.8
Conditional Probability for node ECF

WC	R	VB	CFE	VHS	EVSE	P(ECF)
-	-	no	-	-	-	0.0
yes	-	hpme	-	-	yes	0.01
yes	-	hpme	-	-	no	0.0
yes	-	bh	-	-	yes	0.01
yes	-	bh	-	-	no	0.0
no	yes	hpme	L	L	-	0.11
no	yes	"	M	L	"	0.04
"	"	"	S	L	"	0.0
"	"	"	L	S	"	0.04
"	"	"	M	S	"	0.0
"	"	"	S	S	"	0.0
"	no	"	L	L	"	0.19
"	"	"	M	L	"	0.10
"	"	"	S	L	"	0.0
"	"	"	L	S	"	0.05
"	"	"	M	S	"	0.02
"	"	"	S	S	"	0.0
"	yes	bh	-	-	yes	0.01
"	yes	bh	"	"	no	0.0
"	no	"	"	"	yes	0.01
"	"	"	"	"	no	0.0

Table 3.9
Conditional probability for node VHS

Size	P(VHS)
large	0.1
small	0.9

Table 3.10
Conditional Probability for node CFE

Fraction	P(CFE)
large (L)	0.2
medium (M)	0.55
small (S)	0.25

Table 3.11
Conditional Probability for node EVSE

VB	R	WC	P(EVSE)
bh	yes	-	0.5
"	no	yes	0.5
"	no	no	0.0
else	-	-	0.0

Table 3.12
Conditional Probability for node LCF

S	CCI	ACCI	P(LCF)
yes	yes	L	0.25
no	"	"	0.40
yes	"	M	0.05
no	"	M	0.20

Table 3.13
Conditional probability for node S

R	LR	P(S)
yes	any	1.0
no	yes	1.0
no	no	0.0

Table 3.14
Conditional probability for node LR

R	P(LR)
yes	0.0
no	0.94

Table 3.15
Conditional Probability for node CCI

VB	WC	R	RP	EVSE	P(CCI)
no	any	any	any	any	0.0
yes	yes	any	high	any	0.2
"	any	yes	"	yes	0.2
"	"	"	low	yes	0.2
"	yes	any	"	yes	0.2
"	"	"	"	no	0.65
"	any	yes	"	"	0.65
"	no	no	any	any	1.0

Table 3.16
Conditional probability for node ACCI

RP	EVSE	CFE	L	M	S
high	any	L or M	0.0	1.0	0.0
high	any	S	1.0	0.0	0.0
low	yes	any	0.5	0.5	0.0
low	no	any	1.0	0.0	0.0

Table 3.17
Conditional probability for node RP for simplified influence diagram

ESGTR	R	P(High)	P(Low)
yes	yes	0.0	1.0
yes	no	0.65	0.35
no	yes	0.0	1.0
no	no	0.28	0.72

Table 3.18
Conditional probability for node VB for simplified influence diagram

R	RP	WC	P(no VB)	P(HPME)	P(BH)
yes	low	yes	0.91	0.0	0.09
no	low	yes	0.1	0.0	0.9
no	high	yes	0.1	0.45	0.45
yes	low	no	0.9	0.0	0.1
no	low	no	0.0	0.0	1.0
no	high	no	0.0	0.79	0.21

Table 3.19
Conditional Probability for node SGTR for
simplified influence diagram

ESGTR	R	RP	VB	P(SGTR)
yes	any	any	any	1.0
no	yes	any	any	0.0
"	no	high	yes	0.0
"	"	"	no	0.1
"	"	low	any	0.0

Table 3.20
Conditional Probability for node ECF for
simplified influence diagram

VB	R	EVSE	CFE	P(ECF)
no	any	any	any	0.0
hpme	no	any	L	0.064
"	"	any	M	0.028
"	"	"	S	0.00
"	yes	"	L	0.047
"	"	"	M	0.004
"	"	"	S	0.00
bh	any	yes	any	0.01
"	"	no	"	0.00

Table 3.21
Conditional probability for node LCF

WC	VB	RP	CFE	EVSE	R	P(LCF)
any	no	any	any	any	any	0.00
yes	yes	high	L	"	yes	0.011
"	"	"	"	"	no	0.012
"	"	"	M	"	yes	0.011
"	"	"	"	"	no	0.012
"	"	"	S	"	yes	0.050
"	"	"	"	"	no	0.052
"	"	low	any	yes	yes	0.030
"	"	"	"	"	no	0.032
"	"	"	"	no	yes	0.16
"	"	"	"	"	no	0.17
no	"	high	L	any	yes	0.011
"	"	"	L	"	no	0.06
"	"	"	M	"	yes	0.011
"	"	"	"	"	no	0.06
"	"	"	S	"	yes	0.25
"	"	"	"	"	no	0.26
"	"	low	any	yes	yes	0.03
"	"	"	"	no	no	0.26
"	"	"	"	"	yes	0.16
"	"	"	"	yes	no	-

Table 3.22
Risk results of base case calculations

Criterion	Do Nothing	Flood	Δ R(%)
Early Fatalities	1.09 E-2	9.17 E-3	15.9
Late Fatalities	5.63 E +1	4.86 E+1	13.7

Table 3.23
Conditional probability results of base case calculations

Event	Do Nothing	Flood	Δ P(%)
Vessel Failure	7.66 E-1	7.21 E-1	5.9
Ex-vessel Steam Explosion	1.30 E-1	1.81 E-1	-28.2
Early Containment Failure	4.86 E-3	3.94 E-3	18.9
Late Containment Failure	1.63 E-1	9.75 E-2	40.2
Steam Generator Tube Rupture	1.80 E-2	1.92 E-2	-6.7

(a)

Risk (Early,Late Fatalities)

(b)

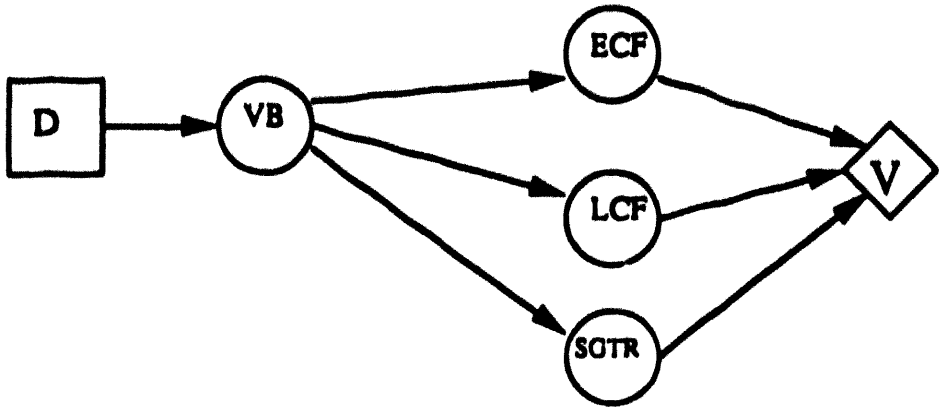

Figure 3.1. Initial influence diagram and influence diagram expanded to include ECF, LCF, SGTR, and VB.

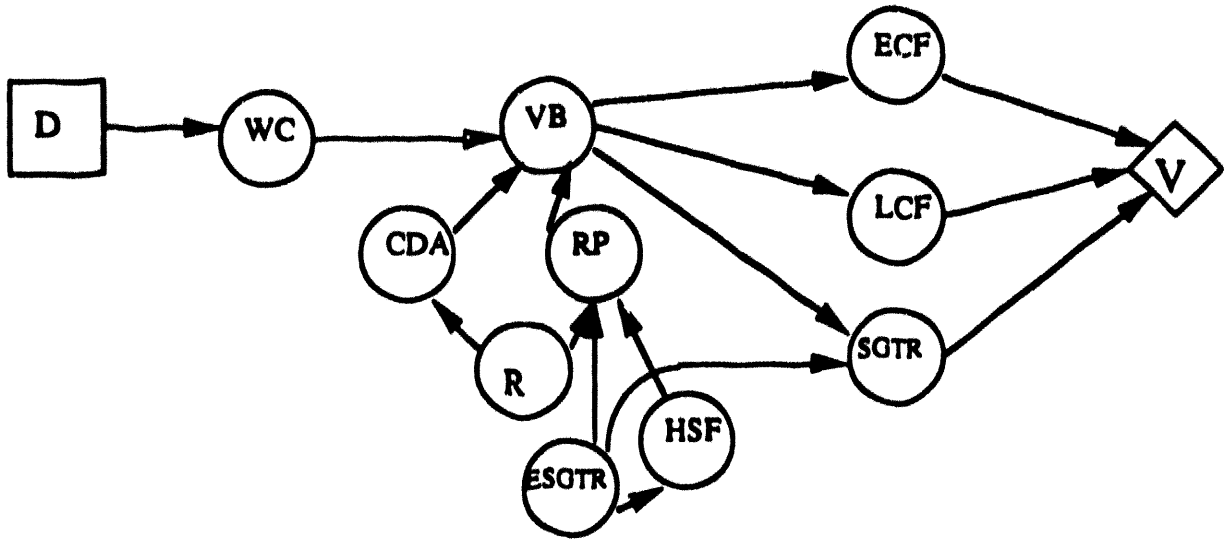

Figure 3.2. Influence diagram expanded to include node VB, and the nodes that influences VB, and SGTR.

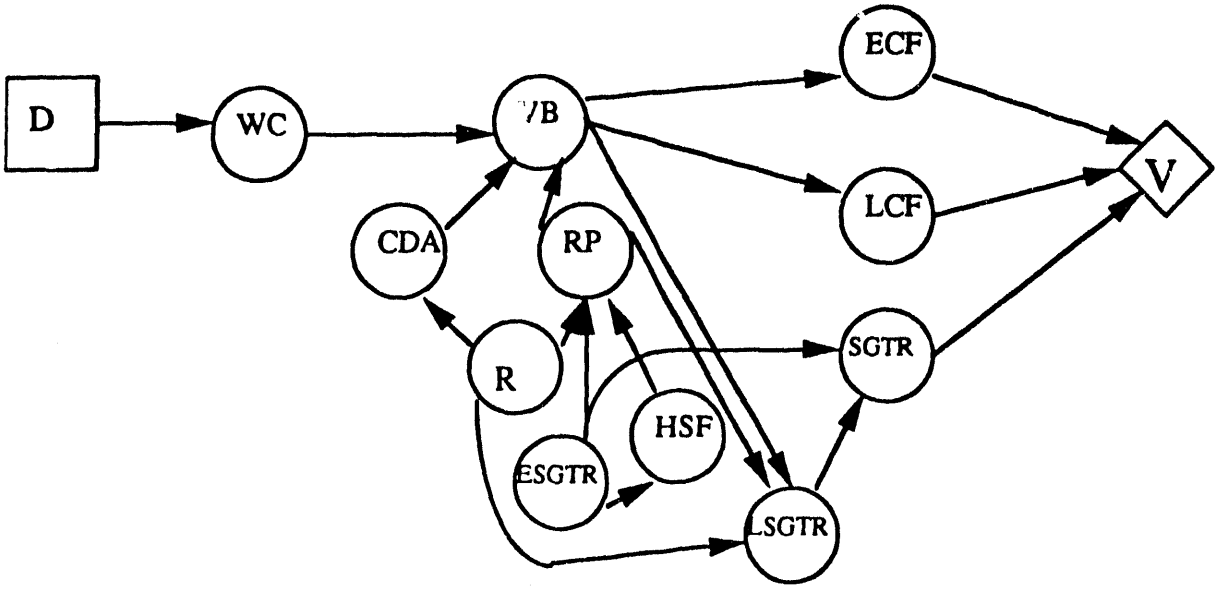

Figure 3.3. Influence diagram expanded to include node LSGTR.

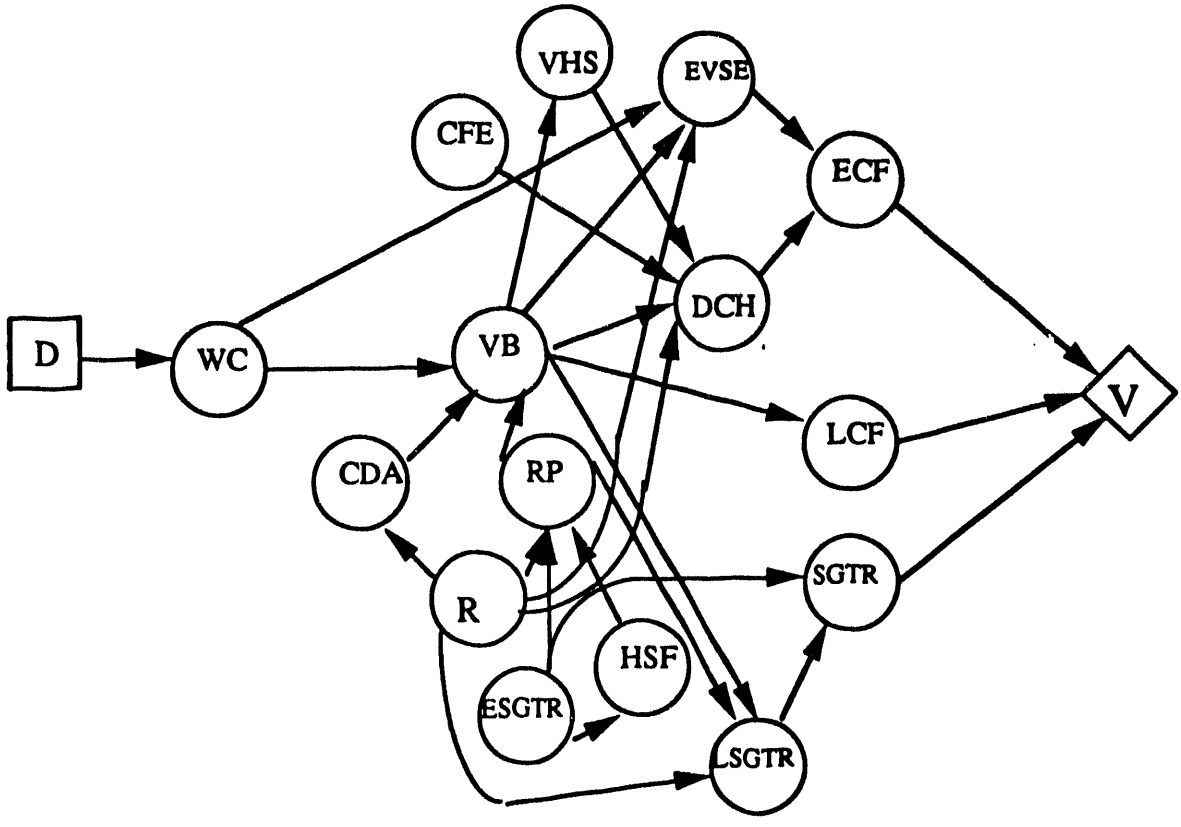

Figure 3.4. Influence diagram expanded to include nodes EVSE, ECF, and the nodes that influence them.

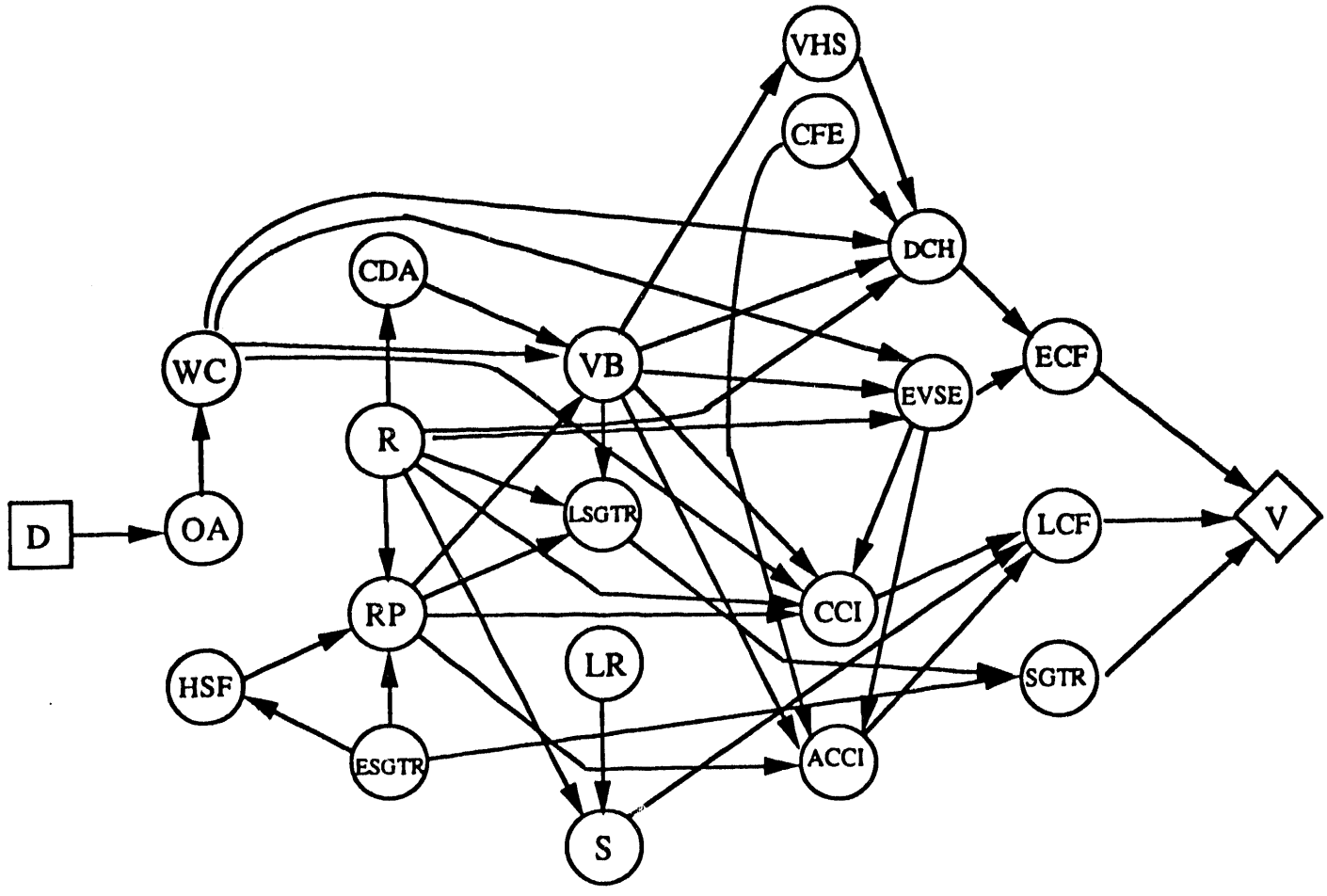

OA: operator action
WC: water in cavity
HSF: hot leg or surge line failure
CDA: core damage arrested
R: AC power recovered before VB
RP: RCS pressure at VB

ESGTR: early SGTR
VB: Vessel breach
LR: AC power recovered during CCI
CFE: core fraction ejected
VHS: vessel hole size
EVSE: ex-vessel steam explosion

CCI: core-concrete interaction
ACCI: amount of CCI
S: Sprays during CCI
ECF: early containment failure
LCF: late containment failure
SGTR: steam generator tube rupture

Figure 3.5. Final influence diagram.

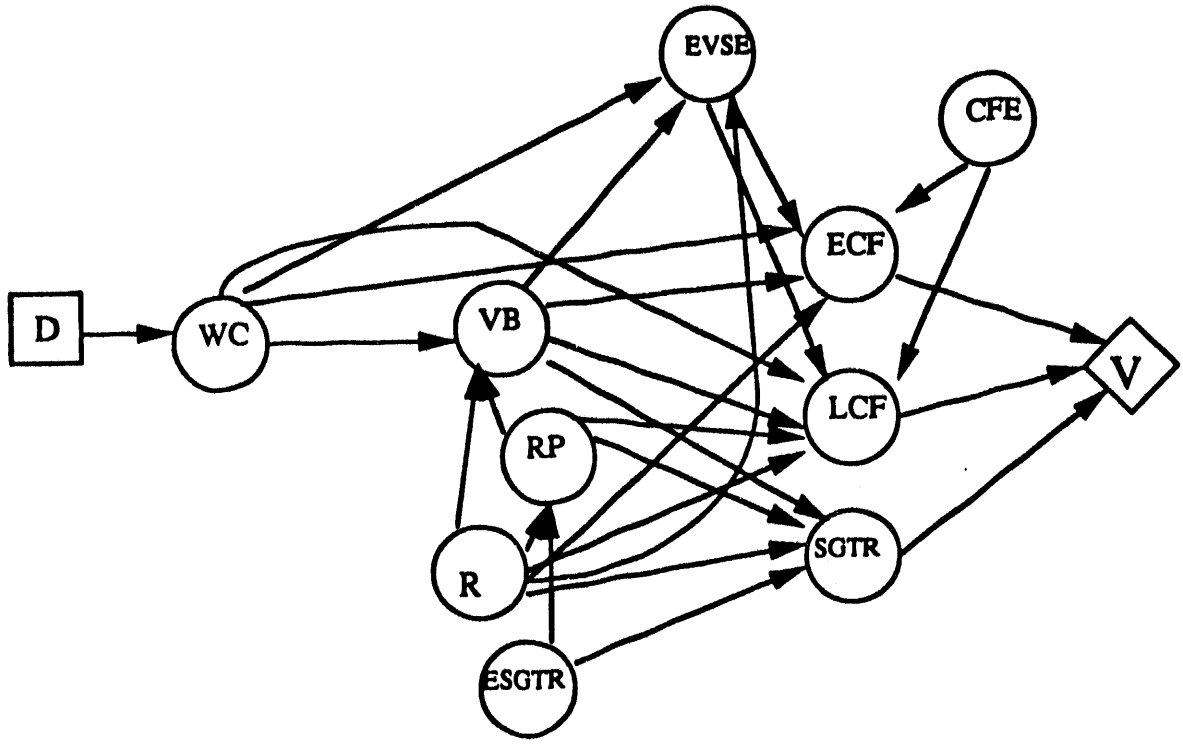

Figure 3.6. Simplified influence diagram.

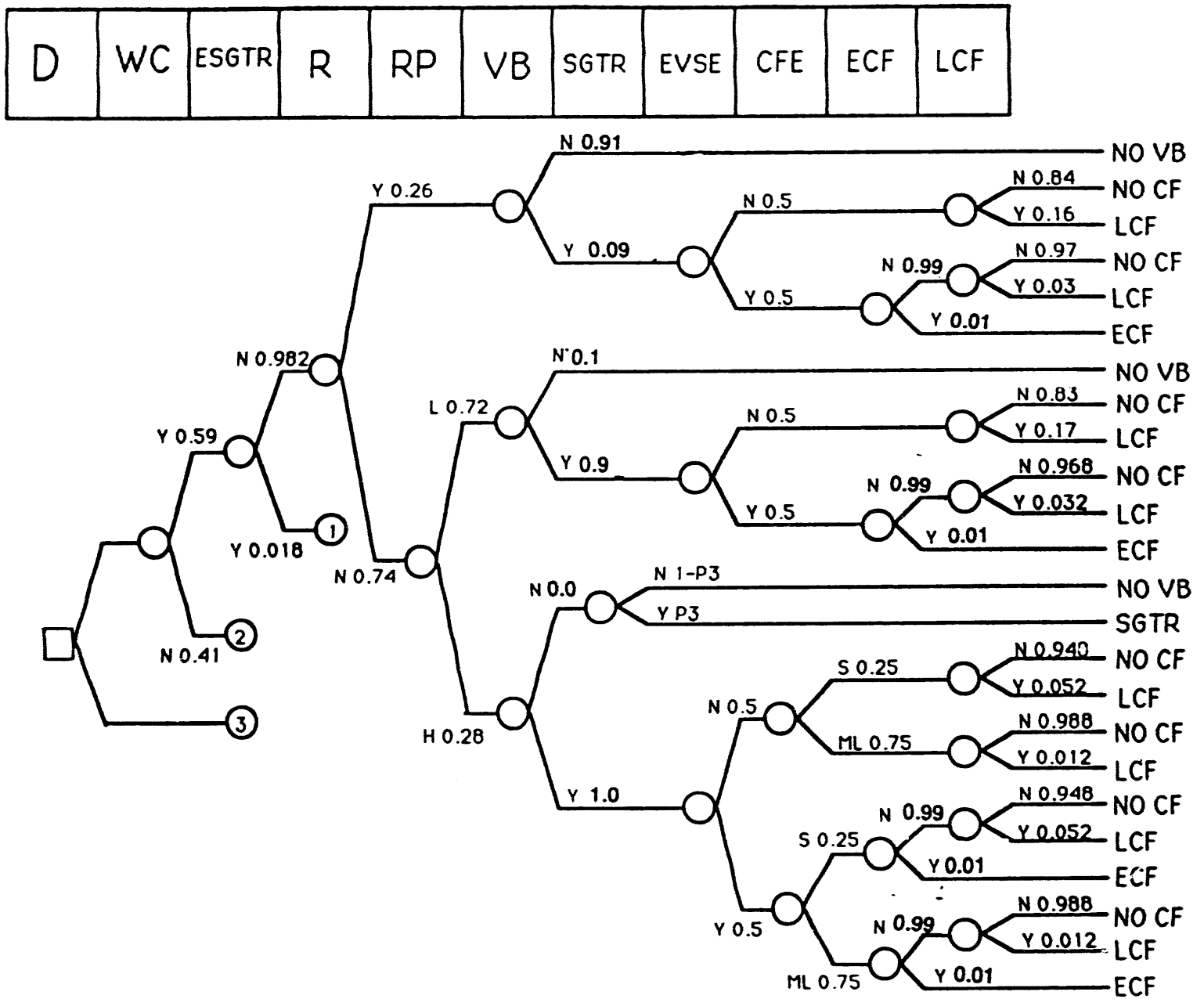

Figure 3.7. PWR decision tree.

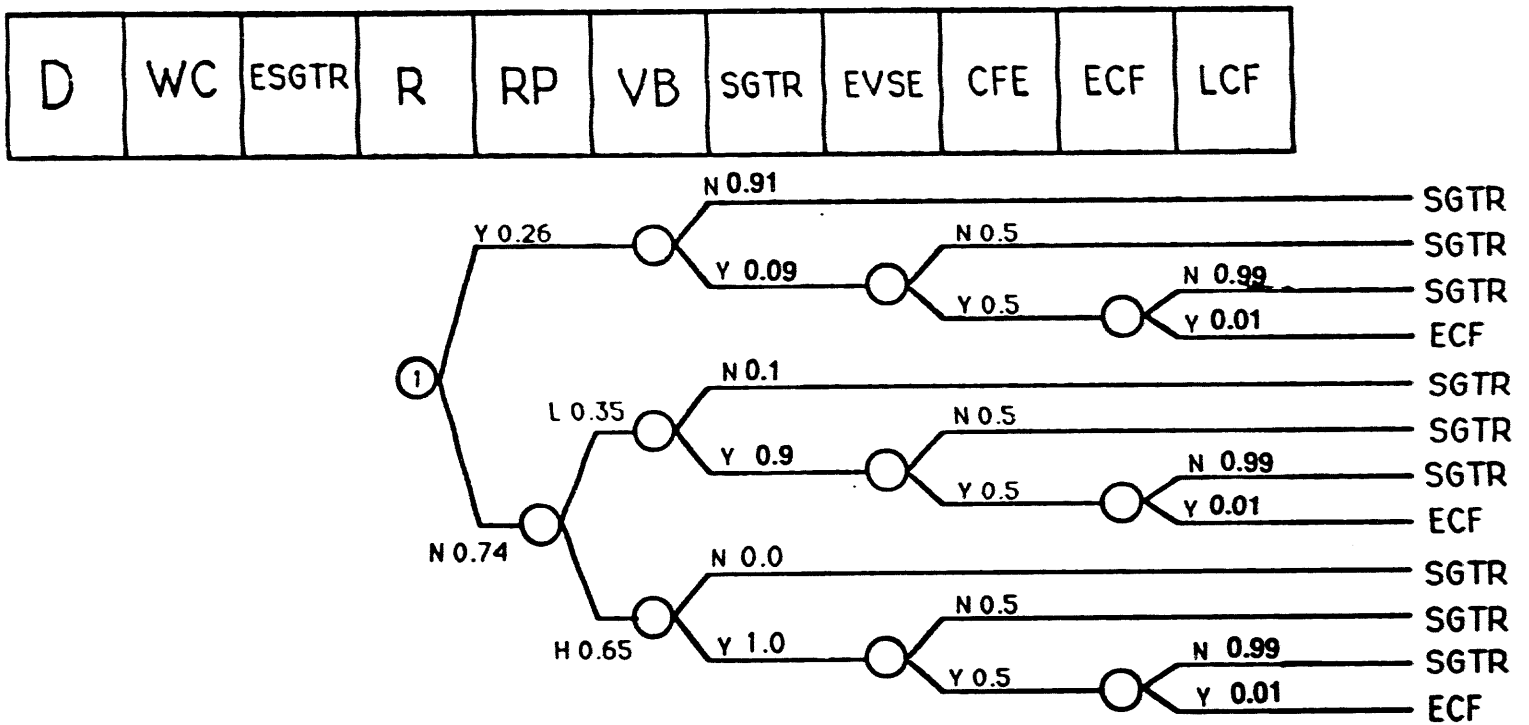

Figure 3.7 (continued). PWR decision tree.

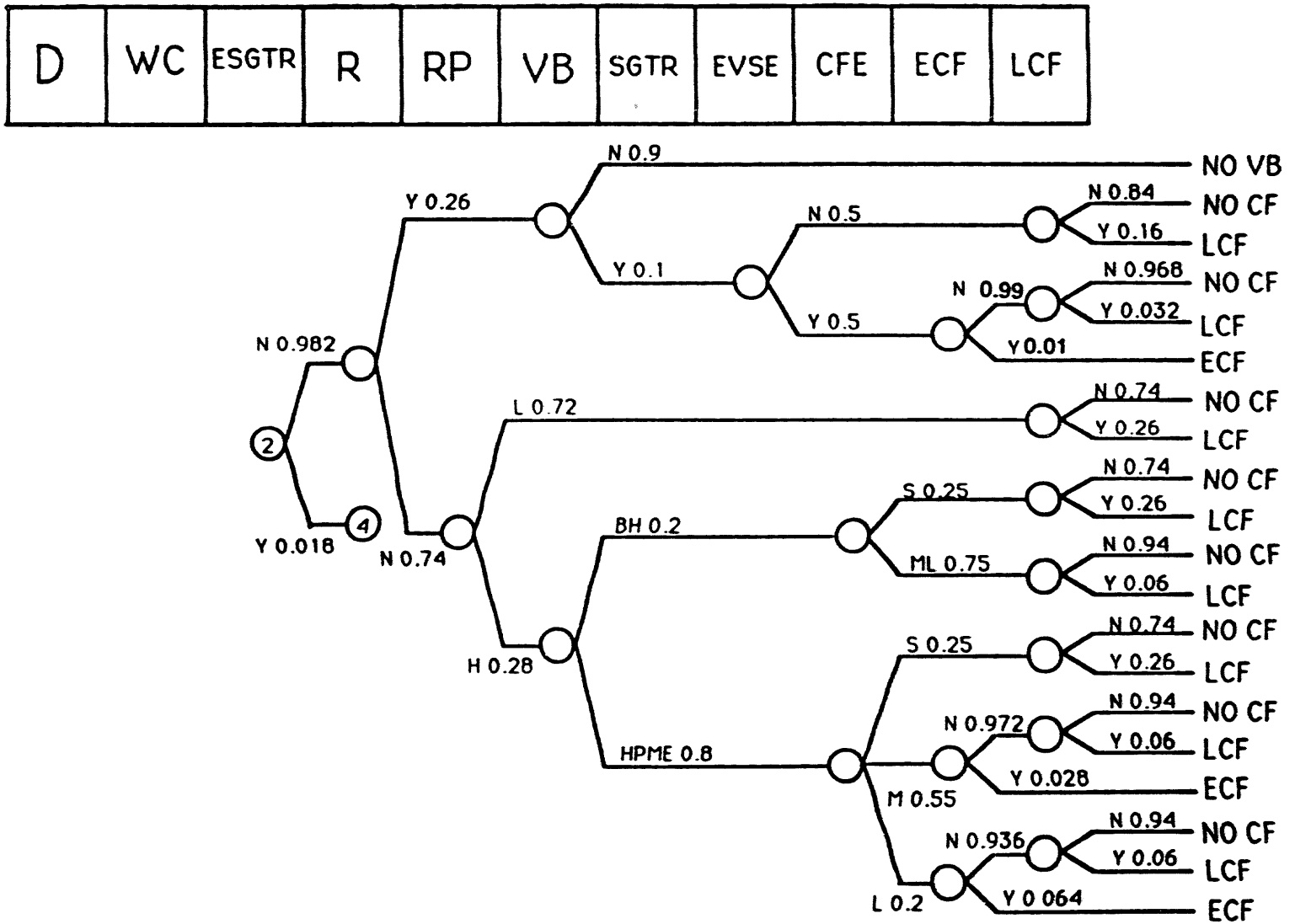

Figure 3.7 (continued). PWR decision tree.

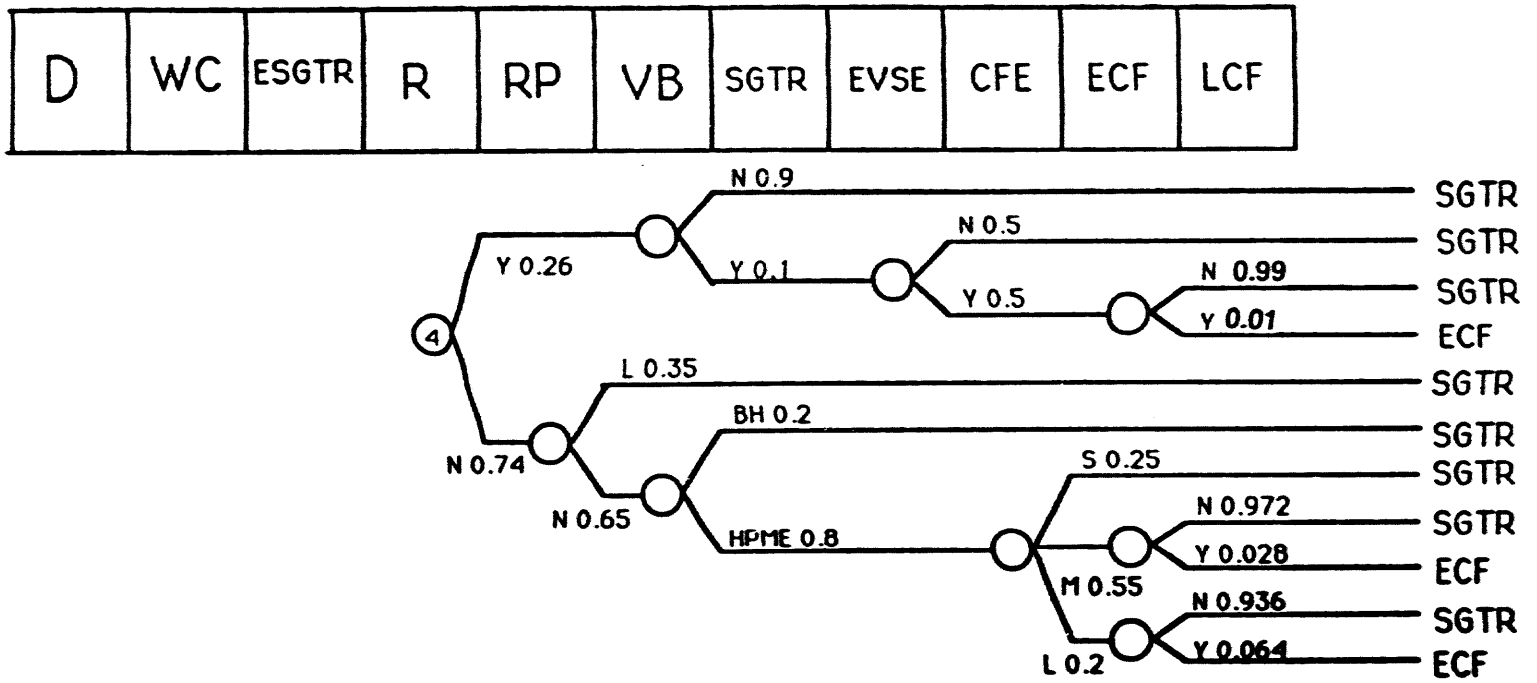

Figure 3.7 (continued). PWR decision tree.

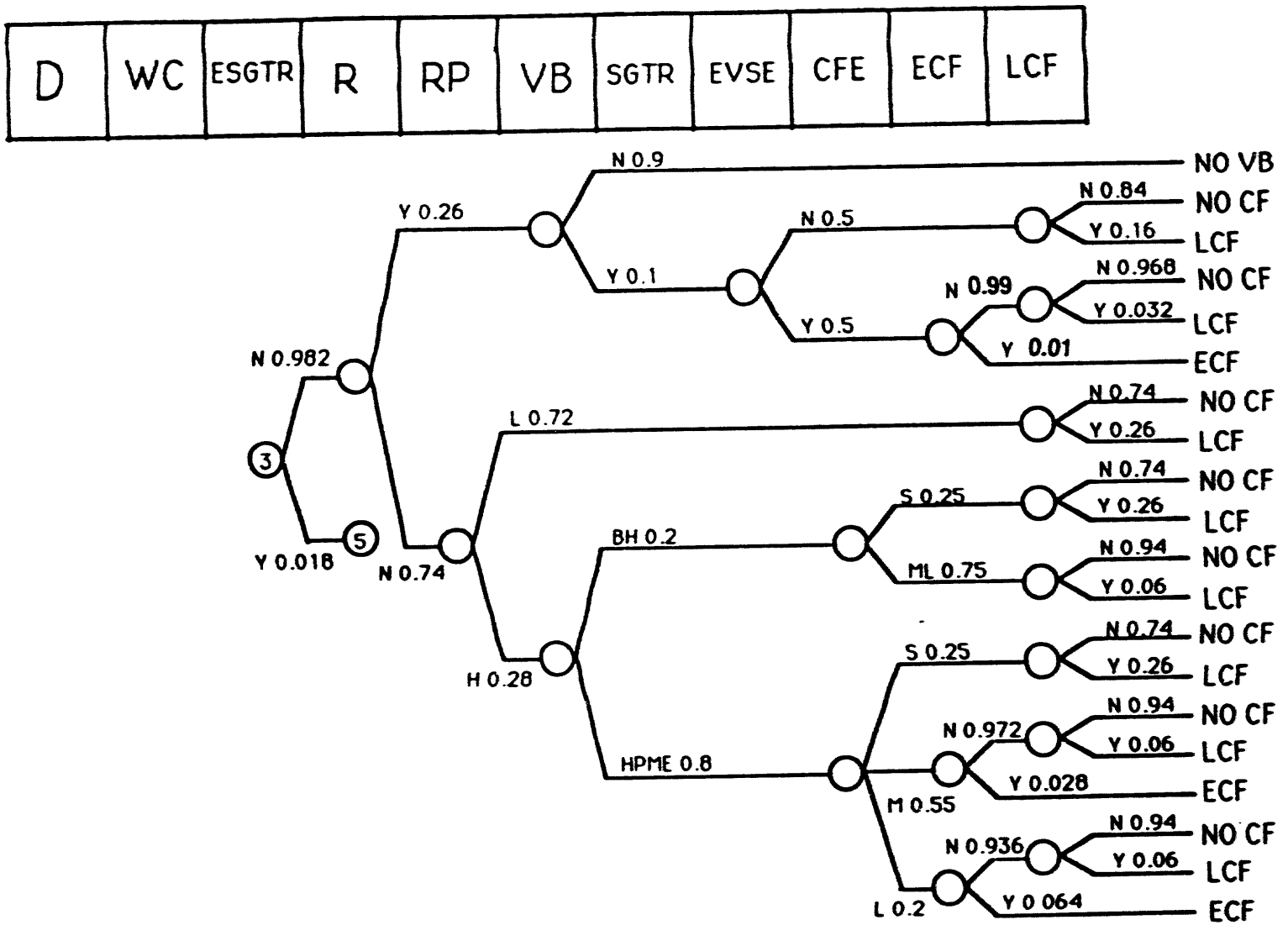

Figure 3.7 (continued). PWR decision tree.

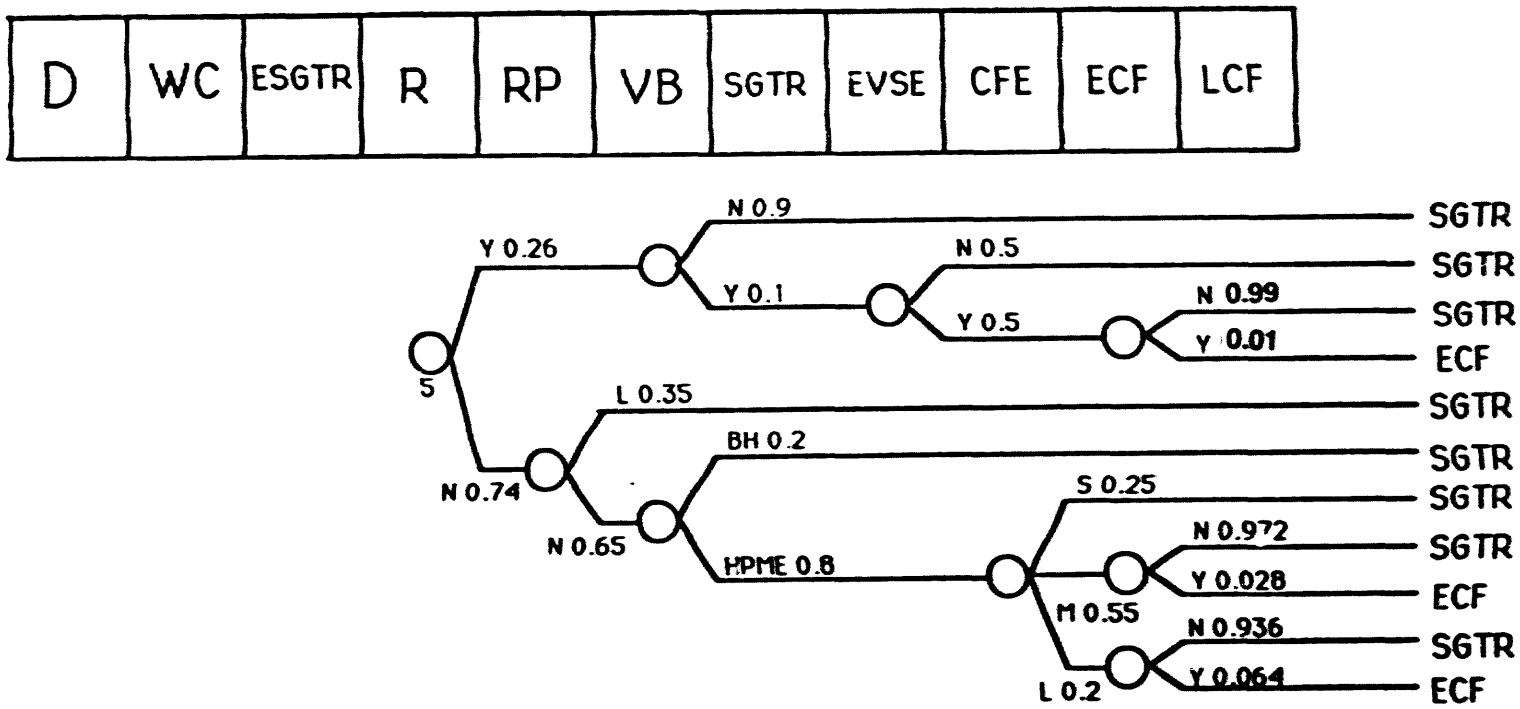

Figure 3.7 (continued). PWR decision tree.

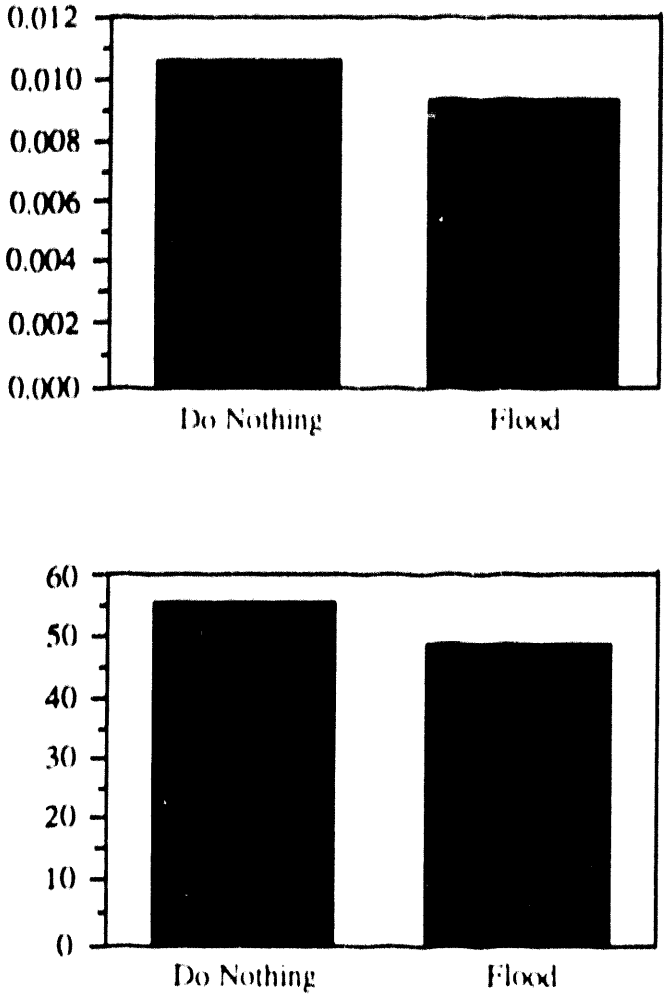

Figure 3.8. Risk results of base case calculations.

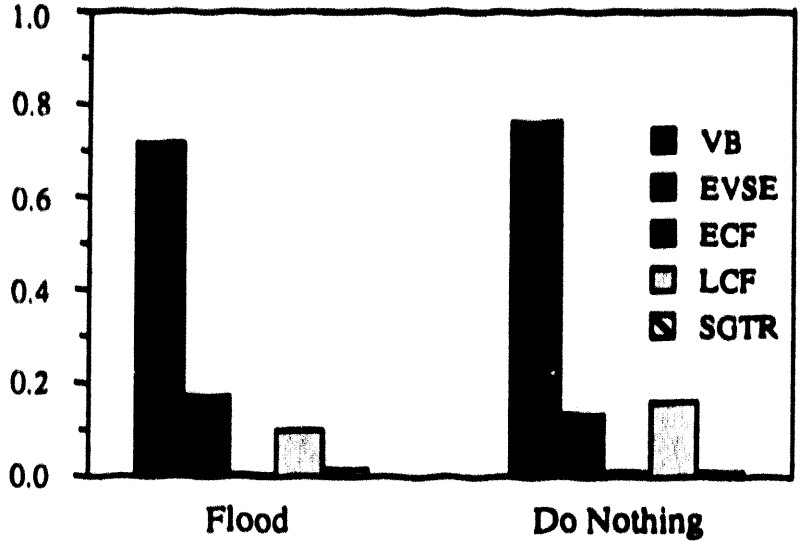

Figure 3.9. Conditional probability results for base case calculation.

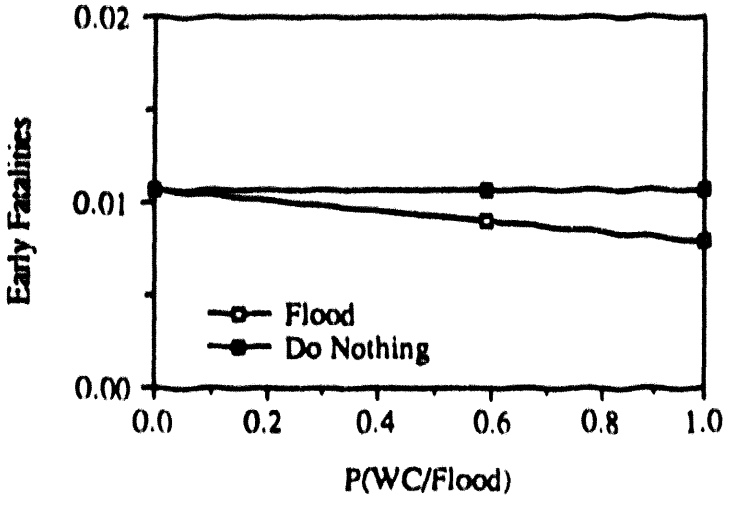

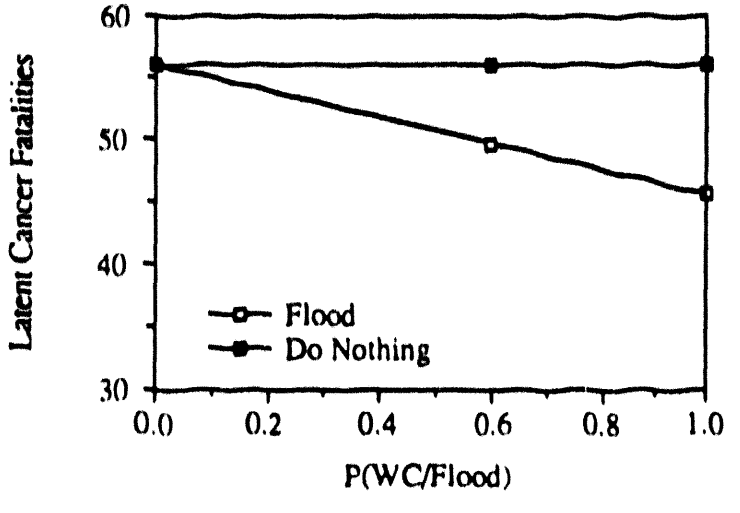

Figure 3.10. Risk sensitivity to the probability that the reactor cavity is flooded before core slump.

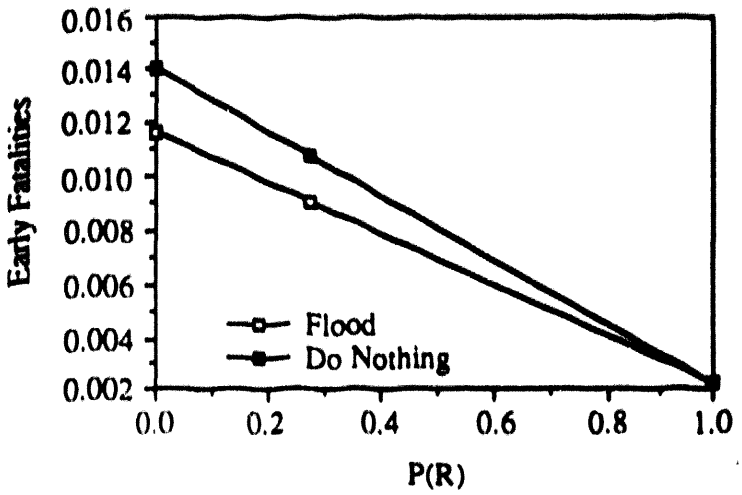

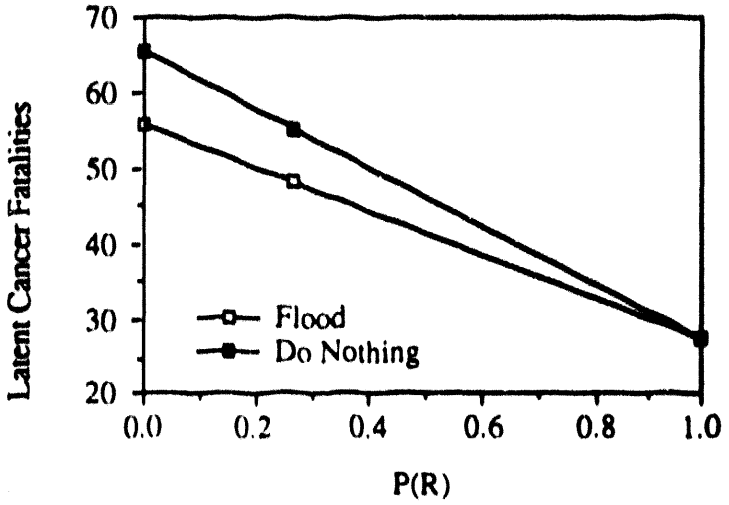

Figure 3.11. Risk sensitivity to the probability that AC power is recovered before vessel failure.

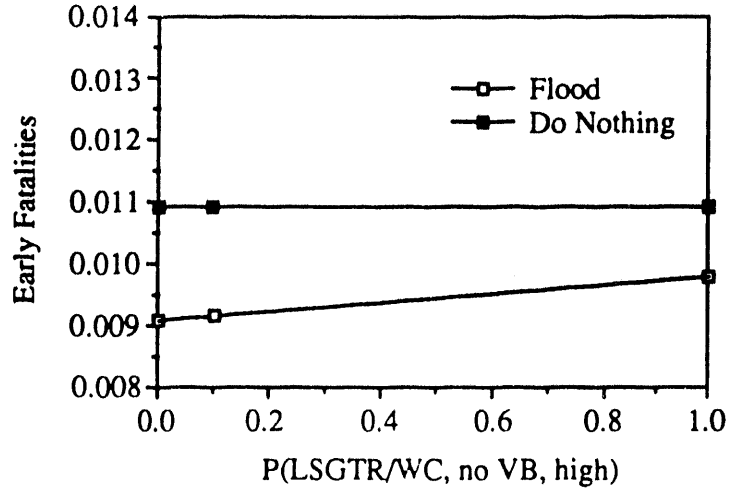

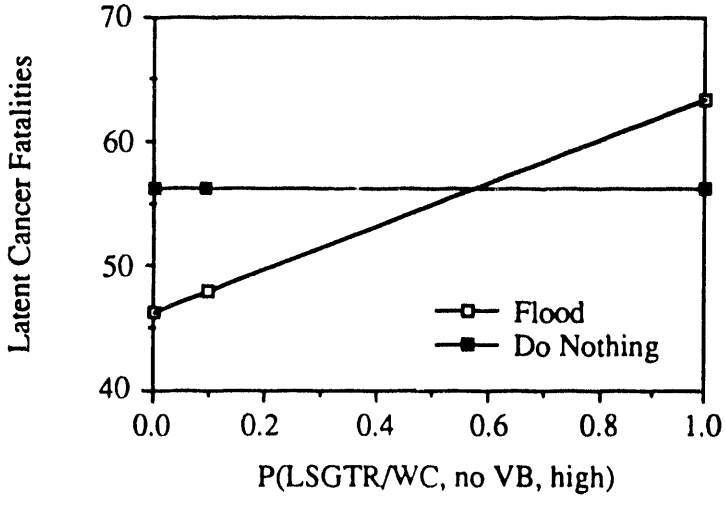

Figure 3.12. Risk sensitivity to the probability of a late steam generator tube rupture given water in cavity, no vessel failure and high RCS pressure.

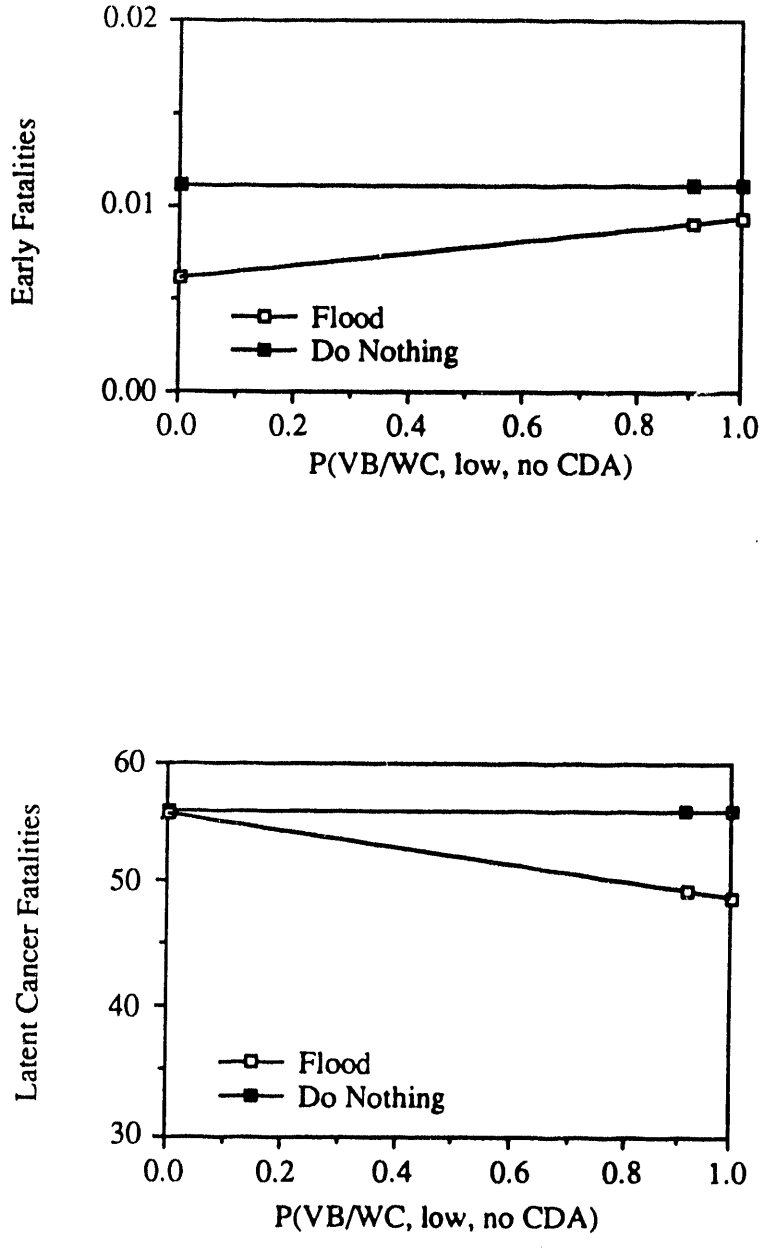

Figure 3.13. Risk sensitivity to the probability of vessel failure given water in cavity and no core damage arrest.

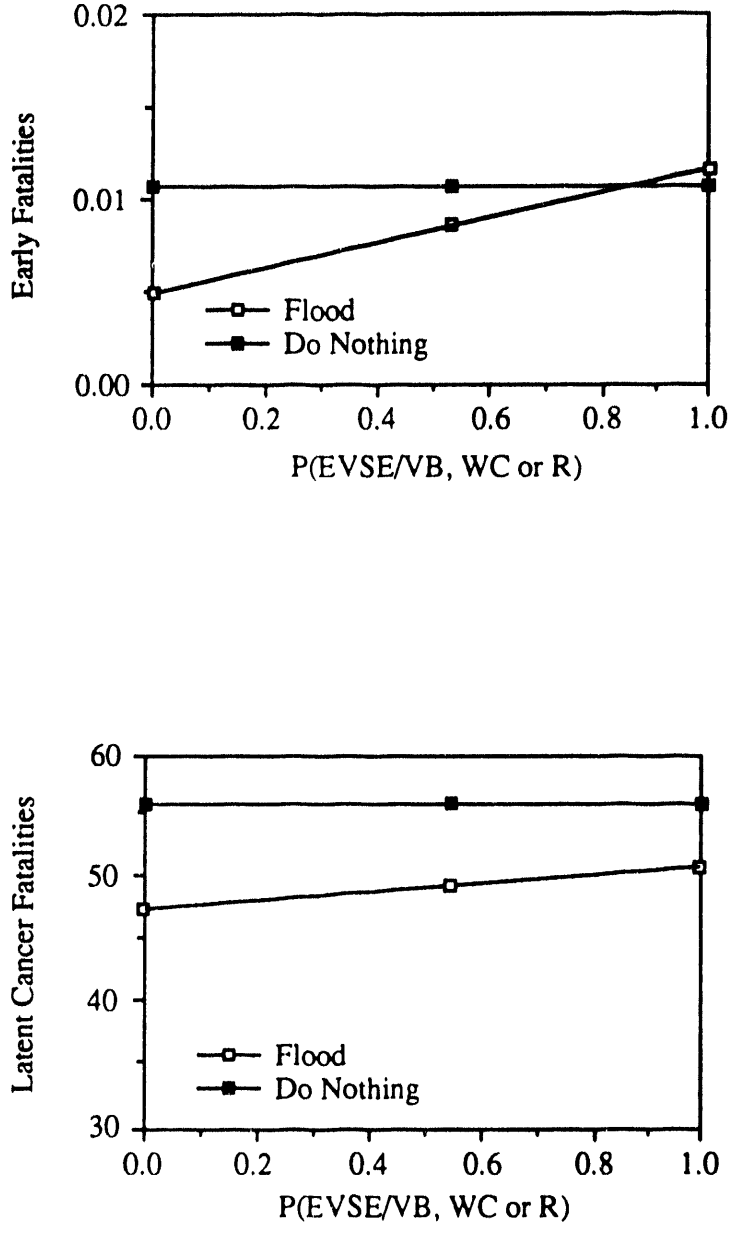

Figure 3.14. Risk sensitivity to the probability of an ex-vessel steam explosion given water present in the cavity.

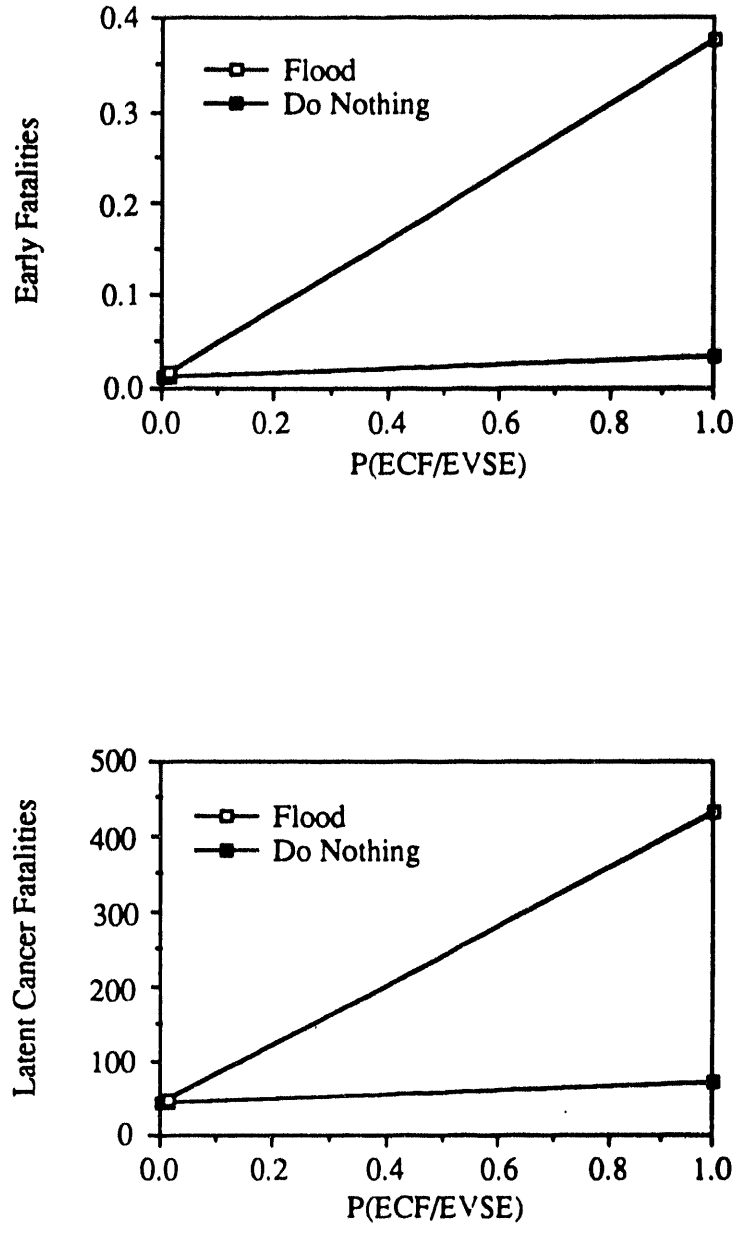

Figure 3.15. Risk sensitivity to the probability of early containment due to an ex-vessel steam explosion.

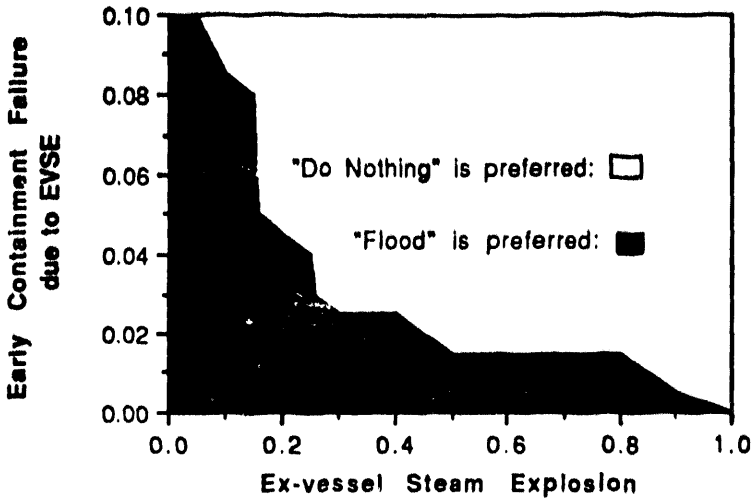

Figure 3.16 A two-way sensitivity analysis with a criterion of early fatality for two crucial parameters [P(EVSE/VB,WC, or R) and P(ECF/EVSE)].

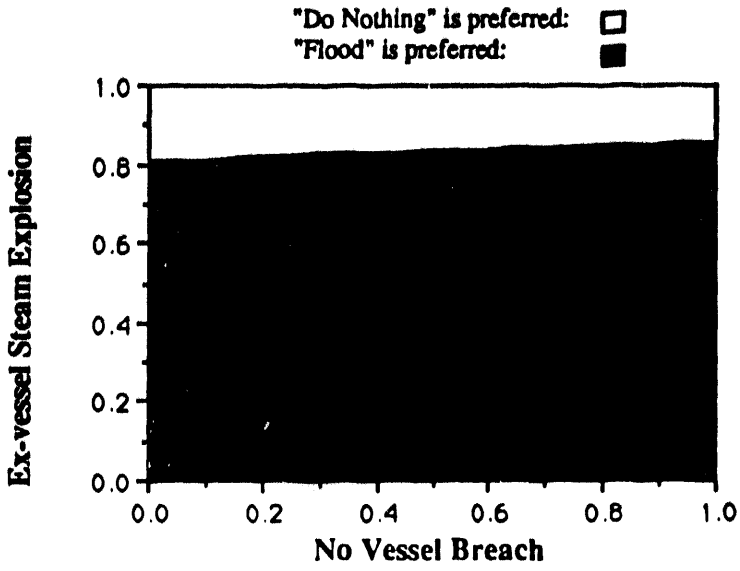

Figure 3.17 A two-way sensitivity analysis with a criterion of early fatality for two crucial parameters [P(No VB/Flood, High RCS Pressure) and P(EVSE/VB,WC, or R)].

4. BWR DRYWELL FLOODING

4.1 Introduction

Many candidate strategies to manage severe accidents have been identified and discussed during the two workshops held at UCLA. One of the candidate accident management strategies for BWRs is flooding the drywell up to the top of the vessel lower head. In this analysis, a BWR Mark I nuclear power plant (such as Peach Bottom) is used to illustrate the framework presented in Chapter 2. The strategy to be assessed is whether to flood the containment in a long term station blackout sequence or do nothing different than is analyzed in NUREG-1150 [3]. Primary containment flooding is already included in the BWR Owners' Group Emergency Procedure Guidelines [14], but the concept is intended for LOCA situations where the water within the drywell could enter the reactor vessel through the break. For severe accident sequences not involving a LOCA, flooding of the primary containment and the presence of water surrounding the reactor vessel might provide sufficient cooling of the reactor vessel bottom head to maintain the core and structural debris within the vessel [15]. Furthermore, given the proposals [16] for preventing failure of the Mark I drywell shell liner by flooding the drywell floor with water, primary containment flooding is a strategy worthy of consideration. Existing studies [17] indicate that a long time is required to raise the water level within the wetwell and drywell to surround the reactor vessel lower head, if existing systems are used. The long term station blackout sequence is chosen to examine the drywell flooding strategy because it is a dominant accident sequence and it has a relatively long time to core slump.

There are two concerns related to the feasibility of the strategy. The first concern is drywell venting in order to assure effective flooding. If the drywell is not vented during the flooding operation, the resulting high back-pressure would decrease the rate of low pressure injection from a system such as the fire pumps. The small drywell and wetwell volumes will result in pressures that may fail the drywell if there is insufficient venting. In the Mark I containment, the wetwell volume would not completely fill because of a trapped airspace in the top of the torus above the wetwell-to-drywell vacuum breaker. The volume taken up by the trapped air is significant in reducing the total free volume that must be filled when

attempting to flood the drywell, so care should be taken to ensure that inadvertent venting of the wetwell airspace does not occur during flooding. A method for opening the vent path without AC power should also be considered. The second concern is the capacity of the injection system used for flooding. Approximately 1.5 million gallons of water are needed to fill the containment up to the top of the vessel lower head. Early initiation of flooding using a fire pump is analyzed herein.

The effectiveness of this strategy relates directly to the probability of vessel failure given that the water level in the containment covers the lower vessel head. Whether the vessel would remain intact with water outside is currently a controversial issue. Reference [18] suggests that since there is a trapped air region inside the skirt and below some portion of the lower vessel head, natural circulation of air is not sufficient to cool the lower vessel head; thus the temperature of the lower vessel head would exceed the creep rupture temperature. An assessment based on steam cooling of the vessel lower head in the air pocket region (with a higher heat transfer coefficient than air) has been made in Appendix I, and the results are used in the assessment presented below.

In assessing the drywell flooding strategy, the potential benefits must be measured against the possibility of adverse effects by including other possible phenomena such as an ex-vessel steam explosion. Whether or not the operators will be able to flood the drywell up to the required level in the required time, using an available injection system (the feasibility of the strategy) should also be considered. Containment isolation failure is expected after core damage since the vent valves are open. Unfiltered venting is only considered in this analysis. Flooding the drywell could also help to reduce the chance of liner failure, if the vessel fails, a so-called secondary mitigation effect.

Influence diagrams and decision trees are used for the analysis presented below.

4.2 Construction of the Influence Diagram

An influence diagram can be used to represent the probabilistic and deterministic dependencies in a decision analysis. These kinds of dependencies cannot be represented by decision trees.

In a single decision problem, the initial influence diagram consists of two nodes, a decision node and a value node. This influence diagram is called a "minimal influence diagram" (See Fig.4.1. (a)). In this example, the decision node represents whether or not the operators decide to flood the drywell using a diesel-driven fire pump after the loss of off-site power. In order to evaluate the drywell flooding strategy using a systematic decision framework, two measures of risk are used: early and late cancer fatalities. The value node is decomposed into four direct predecessor nodes: early containment failure (ECF), liner melt-through (LM), containment isolation failure (IF), and late overpressurization containment failure (LCF) after vessel breach (VB) (See Fig.4.1. (b)). In this case, the following value function is used:

$$\begin{aligned} \langle V|D_j \rangle &= \sum_{i=1}^{4} C_i P_i \\ &= C(ECF)P(ECF|D_j) + C(LM)P(LM|\overline{ECF}, D_j) \\ &+ C(IF)P(IF|\overline{ECF},\overline{LM}, D_j) + C(LCF)P(LCF|\overline{ECF},\overline{LM},\overline{IF}, D_j) \end{aligned} \qquad (4.1)$$

where i = ECF, LM, IF and LCF,

C_i = Consequence for each mode of containment failure, and

P = Conditional probability, per unit time.

In general, when nodes are constructed in a time-sequence manner on an influence diagram, every direct predecessor will influence the next node. However, we can usually take advantage of domain-specific knowledge which indicates that some nodes are independent of some or all of their direct predecessors. Since adding arrows increases the complexity of a domain, we should use such knowledge as much as possible to reduce the number of arrows added.

Unlike the PWR case, the dependency between the four containment failure modes are strong in a BWR (Fig. 4.1. (c)). A detailed explanation will be given in Section 4.4. To be directly assessable an influence diagram should be expanded further until phenomenological and sequential relationships can be represented. Each containment failure mode is dependent upon several possible phenomena during a severe accident. For example, early containment failure (node ECF) is

caused by direct containment heating due to high pressure melt ejection (node HPME) and/or ex-vessel steam explosion (node EVSE). These nodes should be expanded between vessel failure (node VB) and early containment failure (node ECF). Also, containment vent (node CV) is expanded for drywell flooding (node WC).

Fig. 4.2 shows the final influence diagram used to evaluate the drywell flooding strategy. The directed arcs between nodes represent influences, i.e., the predecessor node affects the successor node through the conditional probabilities. All nodes are treated as probabilistic nodes. Table 4.1 shows the notation used in the influence diagram and decision tree.

4.3 The Decision Tree

A decision tree for the drywell flooding strategy in the long term station blackout sequence is shown in Fig. 4.3 (a) through Fig. 4.3 (d). This decision tree is consistent with the influence diagram in Fig. 4.2. The top events of the decision tree correspond to nodes on the influence diagram. The decision tree events are arranged in a timely manner, i.e., the earlier event is located on the left side. Note that if either the chance node probabilities are zero, or the consequence values are equal, branches can be collapsed, and the tree becomes asymmetric. Base case probabilities for each branch are shown above each branch. In some branches, the base case value is zero. These branches are kept for the sensitivity analysis presented in Section 4.6. APB1 through APB10 are accident progression bins used in the NUREG-1150 backup documents as consequence measures for each endpoint. They will be discussed in detail in Section 4.5.

4.4 Node Probabilities

Node D

The analysis starts with the plant damage states associated with the long-term station blackout sequence (PDS5) for the Peach Bottom Unit 2 reactor. The long-term station blackout sequence is composed of two scenarios [3]. High pressure injection is initially working, AC power is not recovered, and either: 1) the

batteries deplete, resulting in injection failure, re-closure of the ADS valves, and re-pressurization of the RPV (in those cases where an SRV is not stuck open), followed by boil-off of the primary coolant and core damage at high or low RPV pressure depending on whether an SRV is stuck open or not; or 2) HPIC and RCIC fail on high suppression pool temperature or high containment pressure, respectively, followed by boil-off and core damage at low RPV pressure (since if DC has not failed, ADS would still be possible, or an SRV is stuck open). The containment is at high pressure but less than or equal to the saturation pressure corresponding to the temperature at which HPCI will fail (i.e., about 40 psig at the start of core damage). Since all emergency core cooling systems are unavailable after battery depletion, the operators have no options available to them with respect to preventing core damage unless AC power is recovered. However, if the vessel can be cooled from the outside, i.e., flooding the vessel up to the top of the lower head using an independent injection system such as the fire pump, vessel failure might be prevented. If not, water in the drywell might prevent or delay containment failure.

The decision that has to be made in this situation is whether or not to initiate drywell flooding using a diesel driven fire pump.

Node CV

The node CV represents whether or not drywell venting can be achieved before the initiation of flooding. Drywell venting is needed for successful flooding. Possible drywell venting lines for Peach Bottom are the following [19]:

1) 2-in pipe from the drywell to the Standby Gas Treatment System (SGTS),
2) 6-in Integrated Leak Rate Test (ILRT) pipe from drywell,
3) 18-in drywell vent via duct-work to the SGTS,
4) 18-in drywell supply path, and
5) two 3-in drywell sump drain pipes.

In accident conditions, the 2-in lines will not be sufficient to prevent containment pressure from increasing so the 6-in ILRT line or other lines must be used. Also, if core damage has not occurred and the 6-in line is used, steam will be released directly to the environment and no adverse environments will be created in

the reactor building. To open the 6-inch ILRT path, a flange must be removed from the line. Also, two motor-operated valves and two air-operated valves must be opened locally. With a loss of power, motor-operated valves fail in an "as is" position. These valves can still be opened with a handwheel or wrench on the stub protruding at the top of the motor operator. With a loss of instrument air, all air-operated valves fail closed. Backup air bottles are installed to facilitate opening air-operated valves locally. Due to drywell water elevation considerations, the 18-in lines to the SGTS might be opened instead of the 6-in ILRT line.

NUREG 1150 analysis assigned a probability of successful wetwell venting for SBO sequences as 0.1 because opening the valves of the venting system needs AC power and is difficult to do in the harsh environment in the reactor building (i.e., radiation from fission products). Reference [19] gives a fault tree for containment venting. Four failure mechanisms were considered: local equipment failure, operator fails to vent, failure of instrument air system to provide air pressure, and loss of power to vent valves. In case of loss of all AC power, local and manual venting is necessary. In this case, only two factors are important for calculating venting failure probability, i.e, local equipment failure and operator fails to vent. Fig. 4.4. represents the fault tree in this case. In the figure, local equipment failure probability (PCV-SYS-HW-SYSTM) is 1.0×10^{-4} (1/demand)[19], and operator fails to vent probability (PCV-XHE-FO-PCV) is 0.5 [22]. Using the above data, the containment venting failure probability is 0.50.

It is evident that operator error probability dominates the venting failure probability. As discussed previously, the operator error probability (0.5) as given in [19] is too large for the case of drywell flooding. The operator has at least 2 hours to perform venting (this will be discussed in node WC) if the operator starts to prepare for venting right after loss of all AC power. With AC power available, it takes approximately 0.5 hours for the operator to defeat the interlock and open the vent path [20]. Without AC power, defeating the interlock is unnecessary, but the operator has to find the vent path and open the valve locally. In this case, 1 hour is a conservative upper bound and the time available is much larger than the time needed. There is still human error when the time available is greater than the critical time of about 80 minutes (non-response probability). The simulator exercises provide non-response probabilities that are moderately high; in

particular, it has been indicated that they are larger than 2×10^{-2} [21]. In this analysis, operator failure probability is chosen as 2×10^{-2}, and the containment venting failure probability is then 0.02. This value is chosen as a realistic base case probability (Table 4.2).

Node R

In building the influence diagram/decision tree for the BWR strategy study, some minor differences in approach were made, compared to the PWR study discussed in Chapter 3. In the PWR study, node R represents the probability of AC power recovery between the time the core uncovers and the time of vessel breach. For the BWR study, node R represents the probability of AC power recovery between the time the core uncovers and the time the core slumps. The BWR analysts assumed that after core slumping, recovery of AC power would not affect whether or not vessel breach occurred.

For modeling the recovery of AC, only off-site power is modeled. It is assumed that diesel generators can not be recovered easily after their failure. Reference [12] gives a Weibull distribution for non-recovery time of off-site AC power as follows:

$$f(t) = \lambda\beta\cdot\beta\cdot t^{\beta-1}\exp[-(\lambda t)^{\beta}] \qquad (4.2)$$

where $\lambda=1.1576$, $\beta=0.6396$; and hence

$$P[T \geq t] = \exp\left[-(\lambda t)^{\beta}\right]. \qquad (4.3)$$

Hodge [22] has addressed the timing for a BWR 4 Mark II reactor shown in Table 4.3 [22]. Since the Peach Bottom reactor is a BWR4, this result is assumed to be valid for this analysis. According to the table, t_{cu} = 10.6 hr is the core uncovery time and t_{cs} = 12.3 hr is the core slump time.

In this case,the AC non-recovery ($\bar{R}$) probability is calculated by

$$P(\bar{R}) = P[T\geq t_{cs} | T \geq t_{cu}] = \frac{P[T\geq t_{cs} \cap T\geq t_{cu}]}{P[\ T\geq t_{cu}\ ]}$$

$$\frac{P\,[T \geq t_{cs}]}{P\,[T \geq t_{cu}]} = 0.62 \qquad (4.4)$$

Uncertainties related to the quantification of the probability of recovery of AC power before core slumping include the probability density function (pdf) for recovery of off-site power and phenomenological uncertainty associated with core melt and relocation progression which affect the timing of core slumping.

Node RP

Node RP represents vessel pressure at failure which is an important ex-vessel phenomenological consideration. Unlike the PWR case, BWRs do not have a primary system loop. The pressure in a PWR can change due to a leak in the primary system such as a steam generator tube rupture or a surge line failure. However, it is unlikely that the pressure in a BWR vessel might change, except after operation of the ADS. Since we are starting with a long-term station blackout, it is assumed that vessel pressure remains "as is" after opening the ADS valves. In other words, the vessel is only at a low pressure state if the ADS valves are stuck open after DC power is lost. Otherwise, it is a high pressure state. The probability of the state of the vessel pressure is calculated below.

The long term station blackout consists of three sequences [23]: T1-P1BNU11, T1-BNU11, and T1-BU11NU21 (Table 4.4). These sequences involve a station blackout with or without one stuck open ADS valve and initially, successful operation of HPCI or RCIC. Battery depletion may or may not occur before core damage. If the battery is not depleted, the loss of room cooling can cause loss of the HPCI or RCIC. The vessel remains at low pressure if an ADS valve is stuck open, otherwise, it re-pressurizes on loss of DC. AC systems are available on recovery of AC power. Venting is not performed due to loss of AC. The typical time for core damage is between 10 to 13 hours.

Only if a valve is stuck open, can the vessel remain depressurized. According to Table 4.4, accident Sequence T1-P1BNU11 consists of a stuck open ADS valve; hence the probability of low reactor pressure is

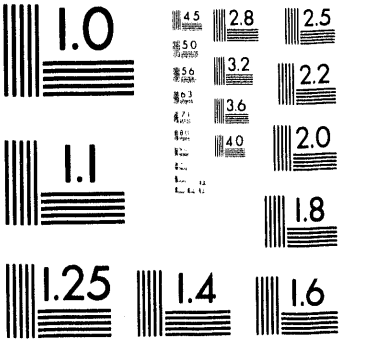
1.0
1.1
1.25
1.4
1.6
1.8
2.0
2.2
2.5
2.8
3.2
3.6
4.0
4.5
5.0
5.6
6.3

2 of 5

$$P(\overline{RP} \mid \overline{R}) = \frac{P(T1\text{-}P1BNU11)}{P(PDS5)} = 0.07 \qquad (4.5)$$

When AC power is recovered before core slumping, the vessel pressure is definitely low because of ADS operation (Table 4.5).

Node WC

The probability of the presence of water surrounding the bottom head of the vessel before core slumping is dependent upon whether or not the drywell can be vented, and the capacity of the fire pumps. This analysis assumes that the injection system is a diesel driven fire pump which is already aligned and fitted to the containment spray system. It is also assumed that water has to reach the top of the lower head before relocation of core debris begins (core slump), i.e., 737 minutes after loss of AC power.

The fire water system at Peach Bottom consists of two 2,500 gpm capacity, vertical turbine pumps (one electric-motor-driven and the other diesel-engine-driven) [24]. There is a crosstie between the High Pressure Service Water system and the RHR containment spray mode if AC power is available. In case there is no AC power and the diesel engine fire pump is to be used, the operator should align the fire protection system to the RHR containment spray mode. While information concerning fire pump alignment is unavailable, Reference [25] analyzed a representative plant from the BWR Mark I group of 24 nuclear units. The layout and physical arrangement of this plant was used to evaluate typical requirements for potential improvements. Among these improvements, the installation of a piping cross-tie between the fire protection system(FPS) and RHR system was discussed. Logic changes and electrical wiring are considered for proper valve alignments and flow path isolation. To modify the typical plant, the length of the pipe cross-tie between the FPS and RHR system was assumed to be 100 feet. Four additional valves are needed as part of this modification. One of the two 8-inch manually operated gate valves is considered for RHR heat exchanger isolation. The base case total cost of piping and logic modification is given as $613,600 in 1988 dollars.

It is estimated [15] that 208.000 ft^3 (1,550,000 gals.) of water would have to be added to containment so that the water within the drywell can reach a level (about 35 ft above the drywell floor) sufficient to cover the reactor vessel bottom head. If only the fire pump is used, the timing for achieving this level is 620 min. Comparing this with the timing in Table 4.3., the latest time that operator could start flooding using the fire pump is 737 - 620 =117 min (1.95 hr.) after loss of off-site power, if water has to surround the lower vessel before core slump. At this time DC power has not been depleted and HPCI/RCIC is still available. The operator would be reluctant to start flooding. The only possible situation in which fire pump flooding is likely to be employed is that it is hopeless to recover off-site power in 10 hours (e.g. large power grid damage due to severe weather) and it is also hopeless to run the on-site diesel generators within 10 hours (e.g. due to unrecoverable severe damage).

In this study, WC is defined as "water reaches 35 ft before core slump" and $\overline{WC}$ is defined as "water in the drywell is very shallow" or "no water in the drywell". Hence, the use of the the binary case ($P(WC) + P(\overline{WC}) = 1$) omits consideration of the possibility of an intermediate case.

It is assumed that the availability of water in the drywell is primarily based on the successful operation of the fire water system. Fig. 4.5 is a simplified version of the fire protection system fault tree of reference [26] in that valve and pipe failure are not considered since the detail configuration and failure data of Peach Bottom fire water system is unavailable. It is assumed that the proper fire system modifications in Peach Bottom have already been performed and a fire pump for flooding is included in the procedures. The operator only has to align the fire system to the RHR containment spray mode by opening and closing valves, and to start the diesel fire pump. The Grand Gulf plant has two nominally identical diesel fire pumps, each has a flow rate of 2000 gpm while Peach Bottom has only one 2500 gpm diesel fire pump. An assumption is made that the Peach Bottom diesel fire pump has the same reliability as any one of the Grand Gulf diesel fire pumps. In Fig. 4.5, unavailability due to maintenance (FWS-DDP-MA-DDPA) is 0.01 (1/demand), diesel pump failure to start probability (FWS-DDP-FS-DDPA) is 0.03 (1/demand), diesel pump failure rate (FWS-DDP-FR-DDPA) is 8.0×10^{-4} (1/hour), which gives a fire pump failure-to-run probability of 8.0×10^{-3} for 10 hours. The operator has 2 hours to perform the flooding operation, thus the operator error

rate (OER) is 0.02 as discussed in the drywell venting section. The fault tree with this data results in a probability of 0.07 for the flooding failure (Table 4.6).

It should be noted that uncertainty in the timing of core slump also influences the success of containment flooding. In reality, the operator might not flood until the core is uncovered. From Table 4.3, this leaves only 98.9 minutes to flood the containment; large capacity (at least 15,670 gpm) low pressure pumps are needed, and the pumps should have an independent power source.

Node VB

The vessel bottom head failure mechanism (Node VB) is dependent upon factors such as the temperature and composition of the corium, and the timing of its release from the degraded core region [27]. For example, a sudden release of hot molten corium directly into the plug area such as a guide tube or a control rod drive mechanism tube will most likely result in a penetration failure. On the other hand, if low-temperature (i.e. containing metallic constituents) corium is gradually released into the lower plenum, a slow heat-up of the entire vessel lower head can be anticipated, eventually leading to its gross failure.

When there is no water outside the vessel lower head, the most common failure mechanisms postulated for the vessel bottom head are those of gross melt-through and localized penetration tube failure. The chance of different potential modes of failure is affected by the presence of water outside the reactor vessel head. This matter is discussed in some detail in Appendix I.

When the water level reaches 35 feet above the drywell floor, part of the reactor vessel lower head can come into contact with the flooded water. However, there is trapped air in the vessel support skirt region during drywell flooding as shown in Fig 4.6 [18]. Hodge et al [18] have investigated the effect of external flooding of the drywell for the short term station blackout accident. They used a conduction model to study the behavior of the debris in the vessel lower head. They also considered heat transfer to the air in the vessel support skirt region. According to their analysis, the average vessel shell temperature in the vessel support skirt region exceeds the temperature at which the creep rupture can occur.

Studies in Appendix I indicate that with flooded water in the drywell (Fig. 4.7 and 4.8), the vessel inner wall temperatures were below the melting temperature of the vessel. These results were obtained by assuming that decay heat produced by the core material relocated in the vessel lower head produces convective motion in the melt, and that the air pocket is filled with steam generated by nucleate boiling on the outer wall of the vessel bottom head. Thus the outer wall temperature with the steam-filled air pocket region was lower than that obtained from Reference [18]. It is seen that the baffle plate temperature is predicted to be above the melting temperature of steel (1700 K). As a result, the baffle plate will fail and any water left in the downcomer region surrounded by the cylindrical vessel shell, the baffle plate and the lower core shroud will spill over the core debris.

The following two factors are considered: AC recovery before core slumping (Node R) and the presence of water in the drywell up to the bottom head of the vessel before core slumping (Node WC). This analysis assumes that if AC power could be recovered before core slumping, the vessel would not fail, whether or not containment flooding is successful. However, this assumption does not necessarily mean that node VB is a deterministic node. When there is water outside the lower head, the probability of vessel failure is expected to be lower than without water. For the base case calculation, the vessel failure probability given the presence of water is chosen as 0.4 (for all failure modes). This value is deduced from the temperature and stress analysis results given in Appendix I. If AC power is not recovered and water does not reach the lower head, the vessel failure probability is 1.0. A sensitivity study concerning the effect of this parameter is performed in Section 4.6. The conditional probabilities in Table 4.7 are used for the base case calculation.

Node HPME

Node HPME represents the probability of the effect of the high pressure melt ejection . Reference [29] gives a probability of 0.8 for this.

HPME might occur, both in case there is, or there is not water in the drywell. However, we expect that an ex-vessel steam explosion is dominant rather than DCH induced by HPME for the case of flooding in the drywell. Hence, the conditional

probability of HPME given a successful drywell flooding is assumed to be zero (Table 4.8).

Node EVSE

An ex-vessel steam explosion (Node EVSE) is dependent upon the vessel failure mode and the presence of water in the drywell. The contact mode of ex-vessel fuel-coolant interactions is one of the important factors for determining the magnitude of an ex-vessel steam explosion.

Due to the extreme uncertainty in the phenomena of an ex-vessel steam explosion, it is hard to quantify the corresponding probabilities of an ex-vessel steam explosion when there is water in the cavity. Table 4.9 shows the conditional probabilities based on the Peach Bottom APET results. This is also discussed in Appendix II.

Node ECF

The early containment failure (Node ECF) modeled in this analysis is either caused by DCH induced by HPME, or various failure mechanisms such as dynamic pressure (shock wave) and/or static pressure (overpressurization) induced by an ex-vessel steam explosion.

For high pressure melt ejection case, the probability of early containment failure due to DCH is extremely uncertain. This analysis uses expert opinions about pressure distribution given by independent 4 experts in the NUREG-1150 backup document for determining the probability of containment failure after vessel failure at high pressure and dry cavity [23](See Table 4.10). In order to combine these opinions, the method described in Appendix 4.A is used.

For this presence, we have three symmetric percentiles (0.1th, 50th, and 99.9th) from each of the four experts and use the values of $Z_{99.9} = 3.08$ and $w_i = 0.25$ since we have no information regarding the experts. Then, $\theta_m = 0.599$ and $\omega_m = 0.523$ are obtained for the most probable log-normal posterior distribution. Then, the containment failure probability due to HPME can be obtained by applying the Peach

Bottom containment failure pressure (9.1 bar or 132 psig) to this log-normal distribution as follows:

$$P\,[P_c \geq P_F] = P\,[Z \geq \frac{\ln P_F - \theta_m}{\omega_m}] = 1 - \Phi\,[\frac{\ln P_F - \theta_m}{\omega_m}] \qquad (4.6)$$

where P_c = random variable for containment pressure
P_F = containment failure pressure
Z = standard normal variable
Φ = standard normal distribution

The early containment failure probability due to HPME was obtained as 0.001.

The same method can be applied to calculate the probability of early containment failure due to an ex-vessel steam explosion using expert opinion. Tables 4.11 and 4.12 show expert opinion data for the pressure increase due to an ex-vessel steam explosion for high and low vessel pressure. In this case, we have θ_m = 0.3795 and ω_m = 0.966 for high vessel pressure and θ_m = - 0.0113 and ω_m = 1.096 for low vessel pressure. Using a containment failure pressure of 9.1 bar (132 psia), the probabilities were obtained as 0.03 for high vessel pressure and 0.02 for low vessel pressure. It is assumed that the distribution of pressure increase due to an ex-vessel steam explosion by the experts applies to the the case of 2 feet of water in the pedestal area. However, flooding of the drywell can lead to a 30 feet height of water in the pedestal area and reduce the free volume of the containment considerably. Considering this factor, the probability of early containment failure due to ex-vessel steam explosion for flooding drywell was estimated using a different approach. This is described in Appendix II. The results are shown in Table 4.13.

Node LM

An early failure mechanism in the NUREG-1150 study is liner melt-through (node LM), i.e., penetration of a BWR Mark I containment resulting from thermal attack of the steel containment shell by molten core debris [3].

The scenario for this mode of containment failure assumes that as core debris exits the reactor pressure vessel and is deposited on the floor within the reactor pedestal, it flows out of the pedestal region through an open doorway in the pedestal wall and onto the annular drywell floor. For the debris to contact the drywell shell, it must flow across the drywell floor until it contacts the containment shell along the line where the shell is embedded in the drywell floor. If hot debris contacts the drywell shell, two failure modes may occur; the combined effects of elevated containment pressure and local heating of the steel shell may result in creep rupture, or, the debris may melt through the carbon steel shell if it is hot enough.

In a study on the liner failure issue [16], liner failure given a flooded drywell was considered "physically unreasonable", and liner failure without water on drywell floor was considered a "virtual certainty". Hodge [31] further commented that "the current Mark I shell protection proposals are based upon a water level within the drywell reaching only to the lower lip of the vent pipes (about two feet above the drywell floor), with the overflow entering the pressure suppression pool. If drywell flooding to the level of the lower head (35 feet) could be achieved quickly enough, then the water in the drywell might in effect provide two lines of defense against containment failure: first, by serving to keep the debris within the reactor vessel and second, by protecting the drywell shell."

In this analysis, liner failure is conditional on vessel failure and the presence of water in drywell, as well as whether ECF occurs. The dependency on ECF is modelled such that when early containment failure due to an ex-vessel steam explosion and/or HPME occurs, liner melt-through is not considered, i.e., LM has a zero probability. If ECF does not occur, LM has a non-zero probability. This kind of dependency is chosen for the following two reasons. First, different events are arranged in a time sequence, and in general the later occurring event is dependent on whether or not the earlier event occurs. Second, we do not have a consequence measure for the case where both ECF and LM occur. In this case, we choose the consequence measure for ECF. Table 4.14 is based on the results of NUREG-1150.

Node IF

As stated earlier, venting of the drywell should be performed before flooding. Hence, early vent of the drywell causes containment isolation failure (Node IF).

This is due the fact that the vent valves are open when vessel breach occurs (we assume that the operator has already opened the vent valve for flooding and local reclosure is unlikely due to the high radiation after the vessel fails.) Since the capacity of the venting valves is not expected to be large enough to prevent the rapid pressure increase due to EVSE or HPME, ECF is assumed to be possible in this analysis. Also, LM is possible since it is not dependent upon venting. For simplicity, IF is treated only if there is no early containment failure (due to EVSE and/or HPME) or liner melt-through, that is it is given a zero probability if ECF occurs. This is chosen since the consequences of ECF and LM are more severe than that of IF. When ECF and IF both occur, for example, the consequence can be approximated by that of ECF. This is equivalent to the case when ECF occurs, but IF does not occur.

Node CCI

This is conditional on water being present in the drywell (node WC), the vessel failure (node VB), and the vessel pressure (node RP). When water is not present, the probability of a core-concrete interaction (CCI) is 1.0. When water is present, the probability depends on the vessel failure mode. The chance of corium participating in CCI in the high vessel pressure case is smaller than that of the low vessel pressure case when there is water in the cavity, since the high ejection rate makes the corium mix up with the water more rapidly and thus vaporize it to produce a pressure increase in the containment instead of participating in CCI. The probabilities in Table 4.16. are based on the Peach Bottom APET result [29].

Node LCF

Late containment failure (Node LCF) is conditional on the occurrence of CCI , early containment failure due to steam explosion and/or HPME, liner melt-through and isolation failure due to drywell venting. The previous assumption still holds. In other words, LCF occurs only if ECF, LM and IF do not occur. For the case when there is CCI, late overpressurization containment failure is expected due to the small free volume of the drywell, without drywell venting (Table 4.17).

4.5 Consequence Measures

The accident progression bins (APBs) in the NUREG-1150 backup document[23] utilize thirteen characteristics and each sequence in the accident progression analysis can be assigned to an APB. After calculating the frequency of all the bins, the XSOR code is used to perform source term calculations, the results are put into the PARTITION code, and then the MACCS code is used to perform a consequence analysis. The results of MACCS, combined with frequency, are used in the PRAMIS code to calculate the risk.

The purpose of this report is to develop a decision framework. A simplified consequence is therefore desirable. For presentation purposes in NUREG-1150, a set of "reduced" bins was adopted. There are 10 reduced bins for Peach Bottom. For each bin, there are essentially five characteristics: core damage, vessel breach, containment failure time, containment failure location, and reactor vessel pressure at the time of vessel breach. For example, in Table 4.18, the reduced bin "APB1" has the following characteristics: core damage occurs, vessel breach occurs, containment failure time is early, containment failure location is wetwell, and reactor pressure at the time of vessel breach is greater than 200 psia. Reference [23] calculated the frequency of each "reduced" bin contributing to all internal initiators (Fig. 2.5 - 6 in Reference [23]). This information is used in Table 4.18 to calculate the frequency of each accident progression bin. Table 5.1-1 in Reference [23] gives the total risk due to internal initiators. The mean value is reproduced in Table 4.19. Table 5.2-3 in Reference[23] gives the fractional contribution to mean risk (FCMR) for each "reduced" bin to total risk due to internal initiators and is reproduced in Table 4.20. Combining information from Table 4.19 and Table 4.20, one can obtain the risk induced by each accident progression bin.

Utilizing the concept that the risk of each bin is the product of frequency and consequence of each bin, and combining the frequency information in Table 4.18 and the risk information obtained above, the absolute consequence can be calculated for each "reduced" bin. The results are shown in Table 4.21. we assume the consequence measures in Table 4.21 are applicable for both the do nothing and the flooding cases. Using Table 4.21 as the endpoint value in the decision tree can bypass the process of source term and consequence calculations. However, the derivation of consequence in this manner averages the influence by different internal initiators and is only an approximation. For instance, when there is no

vessel breach, APB9 in Table 4.21 gives a non-zero consequence; this is largely due to a LOCA initiator. In this report, APB9 is set equal to zero.

4.6 Quantification

Influence Diagram

A formal algorithm for evaluating influence diagrams was developed by Shachter[32]. The detailed algorithm is shown in Chapter 5. According to the algorithm, the operation of the reversal of arcs is needed for handling the evidence nodes which represent the observed or experimental evidence, and do not have successor nodes. However, in the influence diagram developed in this analysis, the operation of arc reversal is not required since there are no such evidence nodes, where each node has its own successors or a value node. Only operations of joint probability are needed for calculation of the total probability and the dependence between nodes determines the unique conditioning variable in each term of the product. For example, consider the influence diagram with no decision node in Fig.4.9., where the variables $x_1,..x_7$ are marked 1,...,7 for short. We can now write the product distribution by inspection, going from parents to children:

$$P(x_1,..,x_7) = P(x_1)\, P(x_2)\, P(x_3 | x_1,x_2)\, P(x_4 | x_3)\, P(x_5 | x_4)\, P(x_6 | x_4)\, P(x_7 | x_4) \qquad (4.7)$$

Computing the marginal probability $P(x_i)$ would require summing $P(x_1,..x_n)$ over all 2^{n-1} combinations of the remaining n -1 variables which have binary values. The following is the example of how to evaluate the influence diagram in Fig.4.2.

Vessel Breach

The vessel failure probability is dependent upon two factors: R and WC (See Fig.4.2). The joint probability P(VB,WC,R) is calculated by

$$P(VB,WC,R) = P(VB|R,WC)\, P(R)\, P(WC) \qquad (4.8)$$

Since node WC is dependent upon node CV, the marginal probability P(VB) can be obtained by:

$$P(VB) = \sum_{R} \sum_{WC} \sum_{CV} P(VB|R,WC)\, P(WC|CV)\, P(R)\, P(CV) \qquad (4.9)$$

On the other hand, using the operation of intermediate chance node removal, one can build a collapsed influence diagram. This can be obtained by the removing the node which has only one successor unless the successor is a value node. The collapsed influence diagram applying the operation is shown in Fig. 4.10. The following two examples show how to do this operation.

Early Containment Failure due to Steam Explosion or HPME

The conditional probability of early containment failure (ECF), given vessel breach (VB), reactor pressure (RP) and water in the cavity (WC), can be obtained by removing the two intermediate nodes HPME and EVSE as follows (See Fig.4.10):

$$P(ECF|VB,RP,WC) = \sum_{EVSE} \sum_{HPME} P(ECF|HPME,EVSE,RP)\, P(HPME|VB,RP,WC)\, P(EVSE|VB,WC) \qquad (4.10)$$

The probability of ECF conditional on VB,RP, and WC is shown in Table 4.22.

Late Overpressurization Containment Failure

The conditional probability of late overpressurization containment failure (LCF), given vessel failure (VB), vessel pressure (RP), water in the cavity (WC), no early containment failure ($\overline{ECF}$), no liner melt-through ($\overline{LM}$), and no isolation failure ($\overline{IF}$), can be calculated by eliminating CCI node (See Fig.4.10) as follows:

$$P(LCF|\overline{ECF},\overline{LM},\overline{IF},VB,RP,WC) = \sum_{CCI} P(LCF|CCI,\overline{ECF},\overline{LM},\overline{IF})\, P(CCI|VB,RP,WC) \qquad (4.11)$$

The probability of LCF conditional on ECF,LM,IF,VB,RP, and WC is shown in Table 4.23.

Base Case Results

Table 4.24 summarizes the base case results and Table 4.25 shows the conditional probabilities of each containment failure mode given vessel breach. Also, to evaluate the strategy with respect to beneficial and adverse effects, some consequence measures could be assigned to each of the accident progression bins in Table 4.24 and the expected consequence for both early and late fatalities could be calculated. Table 4.26 shows these results.

From Table 4.24, the drywell flooding strategy seems to be beneficial for saving the reactor vessel, and the containment for both liner melt-through and late overpressurization failure in terms of marginal probability. However, this strategy has an adverse effect on early containment failure due to steam explosions. Also, it has an adverse effect on isolation containment failure due to drywell venting.

According to Table 4.25, the most dominant containment failure mechanism (except liner melt-through at high reactor pressure) given vessel breach, is isolation failure in the flooding case. More importantly, the contribution due to liner melt-through could be reduced by half for the flooded case compared to the case of no flooding. The reduction in probability of late overpressurization containment failure is due to the dry well vent, which results in isolation failure before late containment failure. While flooding is expected to increase the probability of an ex-vessel steam explosion, early containment failure due to an ex-vessel steam explosion or HPME is not a significant contributor compared to liner melt-through.

Whether one flood or does not flood the drywell does not change the total conditional probability of containment failure, given vessel failure. However, the most important result is that the risk reduction comes from the change of source terms. This is due to the fact that the influence diagram is modelled in a time sequential manner. In other word, when ECF does not occur, then either of LM, IF, or LCF is expected to occur. Also, if ECF, LM, and IF do not occur, LCF definitely occurs. In this sense, drywell flooding reduce the expected risk by shifting the source term from liner melt-through to isolation failure because isolation failure has a less severe source term than that of liner melt-through.

Decision Tree

Comparison with NUREG-1150

A computer code SUPERTRE [4] is used to evaluate the decision tree in Figure 4.3. The probabilities and consequences are as described above. The base case results for "do nothing" and for "flooding" are in Table 4.26. It shows that the base case risk reduction by flooding is 75% from doing nothing per a long term station blackout accident.

A comparison between the do nothing result of the decision tree and the NUREG-1150 result is desirable. Table 4.27 is based on information from Reference [23]. Table 4.28 compares the do nothing result with the NUREG-1150 SBO-LT calculation. As mentioned earlier, do nothing means do nothing different than analyzed in NUREG-1150. In Table 4.28, the absolute risk of the do nothing subtree is obtained by the product of frequency of the starting plant damage state (1.9×10^{-6} for PDS5) and the expected consequence in Table 4.26. Table 4.28 indicates that the decision tree predicts a smaller but similar risk compared to NUREG-1150. The difference is not surprising, since NUREG-1150 used 145 questions to model the accident progression while this analysis employs only 12 chance nodes to model the important phenomena relevant to the containment flooding strategy. Some of containment failure modes are not considered for the purpose of assessing the flooding strategy, e.g., wet well failure. As long as the do nothing subtree and flooding subtree are treated unbiased, (i.e., same degree of conservatism), relative risk reduction can still be used as a criterion.

Probability Distribution of Accident Progression Bins

Fig. 4.11 shows the probability distribution of each accident progression bin used in the decision tree. In the figure, APB8, 9 and 10 all have zero consequence, they are grouped together and denoted as "No failure" in fig. 4.11; they were put into one group. APB3 is the case of vessel breach at high pressure and early drywell failure, i.e., the most severe consequence. In Fig. 4.11 the flooding strategy gives a smaller probability for APB3 than do nothing while it has a larger probability for APB8, 9 and 10. A flooding decision is favored in this figure.

Simplified Decision Tree

Fig. 4.12 and Fig. 4.13 show the simplified decision tree for containment flooding with early fatalities and latent cancer fatalities as the criterion respectively. The simplified decision tree is used to demonstrate the influence of some important chance nodes. Only containment venting, water reaching the vessel lower head and vessel failure are considered as chance nodes. Once the vessel has failed, several containment failure modes are possible, depending on the physical situation. These failure modes are combined together into the endpoint value of the simplified decision tree. The results obtained from the simplified decision tree are listed in Section 4.8.

Bounding Calculation

The probabilities associated with chance nodes CV, WC and VB are important in determining the benefit of flooding. There are uncertainties in assessing these probabilities, as discussed in Section 4.4. The bounding calculation listed eight different probability combinations for the three nodes, each taking its extreme value (0 or 1) as one case. Table 4.29 shows the results of the bounding calculation. The best estimate result lies in the range of the bounding calculations.

Sensitivity Analysis

Sensitivity analyses are performed for those uncertain nodes, using the decision tree in Fig. 4.3 and the SUPERTRE software. The sources of uncertainty have been addressed above. This section summarizes the results of sensitivity analysis.

Fig. 4.14 and Fig. 4.15 show sensitivity analyses for the probability that water reaches the vessel lower head before core slump, given the drywell is vented. The ordinate is consequence conditional on the plant damage state. It can been seen that if water cannot reach the lower head, do nothing is slightly better than flooding, otherwise flooding is preferred.

Fig. 4.16 and Fig. 4.17 show sensitivity analyses for the probability of vessel failure, given AC power is not recovered and water reaches the lower head. It can be seen that even if the vessel is definitely failed, flooding is better than do nothing,

although the difference is small. The reason is, from the consequence point of view, that liner failure is worse than containment isolation failure.

Fig. 4.18 and Fig. 4.19 show sensitivity analysis for the probability of early containment failure due to HPME. It can be seen that in all cases flooding is better than do nothing, and if the probability is high, the result is more favorable to flooding. In both subtrees, HPME is only one of several competing mechanisms to fail the containment. If HPME does not fail the containment, the other containment failure modes occur. Furthermore, in the do nothing subtree, HPME is more likely because there is no water in the drywell.

Fig. 4.20 and Fig. 4.21 show a sensitivity analysis for the probability of early containment failure due to an ex-vessel steam explosion. Again, flooding is favored regardless of the probability. The consequence of do nothing is not changed because of no water in the drywell.

Fig. 4.22 and Fig. 4.23 show sensitivity analyses for the probability of late containment overpressurization failure. This probability only affects the do nothing subtree, and flooding is better than do nothing, based on the same argument as above.

4.7 Discussion

The influence diagram and the decision tree are equivalent methods. Relative risk reduction is a reasonable criterion despite the presence of uncertainty. However, relative risk reduction is only a good measure if the existing plant systems can be readily used with minor modifications, e.g., a fire pump for flooding. If additional equipment is needed, absolute risk reduction should be considered and value impact analysis may be necessary.

The decision analysis reveals that the difference in vessel failure probability, given the presence or absence of water around the vessel lower head, is the most important factor influencing the effectiveness of drywell flooding. While the effectiveness of water is still controversial, analysis performed at UCLA (see Appendix I) indicates water could keep the lower vessel head temperature below the melting temperature.

Should the vessel fail when there is water in the drywell, the large amount of water (35 feet above the drywell floor) would help to reduce the liner failure probability. But containment isolation failure due to venting can also set a direct pathway to the reactor building or outside. However, flooding might be still better from the view point of minimizing the consequences.

As indicated in the sensitivity analyses (Section 4.6), steam explosion is not a key factor influencing the flooding strategy, if one has a high chance of saving the vessel lower head. If the vessel should fail, isolation failure and liner failure are of concern even without a steam explosion. The steam explosion is only one of the several competing mechanisms to fail the containment.

Related to the feasibility of flooding, a fire pump(s) or a new high capacity, independently powered, low pressure pump(s) [15,17] could be considered. If the fire pump is used, flooding should be started no later than 2 hours after the loss of AC power. The precondition is that the operator should foresee that AC power will not be recovered within 12 hours (a possible scenario might be loss of power grid due to severe weather so that repair can not be performed within 12 hours; also the on site DG has unrecoverable mechanical damage). Modification of the existing fire protection system needs to be prepared at the plant. In reality, the operator might be reluctant to flood early, because DC is still available and HPCI is also available. Another reason for operator reluctance is that flooding will induce loss of wetwell function. Procedural changes have to be made if early flooding using fire pumps should be employed.

New low pressure, high capacity and independently powered pumps represent a plant modification. A value impact analysis should be performed if the new pumps were to be introduced, because of the potentially high cost associated with the new systems. The operator has to be able to monitor the status of the reactor core if late flooding (e.g., starting from core uncovery) is desirable.

4.8 Conclusion

The drywell flooding strategy is evaluated in this analysis to cope with the long term station blackout sequence in a BWR Mark I nuclear power plant, such as the

Peach Bottom Power Plant. A decision-oriented framework, namely, the influence diagram and decision tree method is employed for the analysis. The expected consequence per a long term station blackout accident is used as a decision criterion. The base case results show that there is 75% reduction in the expected consequence by flooding over doing nothing different as analyzed in NUREG-1150. Therefore, this analysis concludes that flooding is better than doing nothing in case of long term station blackout accident.

In addition, the following insights are also obtained through the analysis:

a) if containment is not vented, then flooding is equivalent to do nothing, since it is assumed no flooding is performed without venting,

b) if venting is performed but water does not reach the lower vessel head, flooding is slightly worse than do nothing because containment isolation failure is an early containment failure mode and is worse than late overpressurization failure when do nothing is chosen,

c) if water is not effective, i.e., the vessel still fails when water reaches the lower head, flooding is slightly better than do nothing; the main reason is in a flooded drywell, while isolation failure is inevitable, the liner failure probability decreases, resulting in a lesser consequence, and

d) if water is effective in preventing vessel failure, flooding is clearly better than do nothing.

Table 4.1 Influence Diagram and Decision Tree Notation

Notation	Descriptions
D	Decision at the starting plant damage state (i.e., long term station blackout) $\bar{D}$: Do nothing different as analyzed in NUREG-1150 D: Flood the containment
CV	Containment venting $\overline{CV}$: Venting fails, CV: Drywell is vented
R	AC recovery before core slump from core uncovery $\bar{R}$: AC not recovered, R: AC recovered
RP	Vessel pressure at vessel failure $\overline{RP}$: Vessel pressure is low, RP: Vessel pressure is high
WC	Water reaches lower vessel head, i.e., 35 feet above drywell floor $\overline{WC}$: No water in the drywell WC: Water reaches lower vessel head
VB	Vessel failure $\overline{VB}$: no vessel failure, VB: there is a vessel failure
HPME	High pressure melt ejection which can cause a direct containment heating (DCH) $\overline{HPME}$: there is no HPME, HPME: there is HPME
EVSE	Large ex-vessel steam explosion $\overline{EVSE}$: no large ex-vessel steam explosion EVSE: there is a large ex-vessel steam explosion
ECF	Early containment failure $\overline{ECF}$: No early containment failure, ECF: there is an early containment failure, early failure means immediate or soon after vessel failure due to EVSE and/or HPME
LM	Liner melt-through $\overline{LM}$: there is no liner melt-through, LM: there is a liner melt-through
IF	Containment isolation failure $\overline{IF}$: there is no containment isolation failure, IF: there is containment isolation failure
CCI	Large core concrete interaction $\overline{CCI}$: there is no large CCI, CCI: there is a large CCI
LCF	Late Containment overpressurization $\overline{LCF}$: no late over-pressurization failure, LCF: there is a late over-pressurization, late failure means containment overpressurization failure due to slow pressurization caused by CCI

Table 4.2. The Conditional Probabilities for Drywell Venting

Decision (D)	P(CV|•)*
Yes : Flood	0.98
No : No Flood	0.0

Table 4.3. Calculated Sequence of Events for BWR (Mark II) Long-Term Station Blackout [22]

Event	time(min)
Loss of AC power initiated scram	0.0
BWRSAR calculation initiated	630.0
Swollen water level falls below top of core	637.8
Relocation of core debris begins	736.7
Initial failure of bottom head penetrations	985.6
Molten debris from reactor vessel escaped	985.8

Table 4.4. Plant Damage States of Long Term Station Blackout (PDS5) [23]

Accident Sequence	Frequency	PDS vector	Description
T1-BNU11	1.64×10^{-6}	4-21S-2-22-S-22222-122	Loss of AC power, no stuck open ADS
T1-P1BNU11	1.31×10^{-7}	4-21S-1-23-3-22222-122	Loss of AC power, stuck open ADS
T1-BU11NU21	1.25×10^{-7}	4-21S-2-22-S-22222-122	Loss of AC power, no stuck open ADS
PDS5	1.9×10^{-6}	4-21S-2-22-X-22222-122	

Note: * denotes conditional probability given the conditions in the previous columns

Table 4.5 The Conditional Probabilities for Reactor Pressure

AC recovery before Core Slumping (R)	P(RP|•)
Yes	0.0
No	0.93

Table 4.6 The Conditional Probabilities for Successful Flooding

Drywell Venting (CV)	P(WC|•)
Yes	0.93
No	0.0

Table 4.7 The Conditional Probabilities for Vessel Breach

AC recovery (R)	Water in Drywell (WC)	P(VB|•)
Yes	Yes	0.0
Yes	No	0.0
No	Yes	0.4
No	No	1.0

Table 4.8 The Conditional Probabilities for High Pressure Melt Ejection

Vessel Breach (VB)	Reactor Pressure (RP)	Water in Drywell (WC)	P(HPME|•)
No	Any	Yes or No	0.0
Yes	Low	Yes or No	0.0
Yes	High	Yes	0.0
Yes	High	No	0.8

Table 4.9 The Conditional Probabilities for Ex-Vessel Steam Explosion

Vessel Breach (VB)	Water in Drywell (WC)	P(EVSE|•)
Yes	Yes	0.86
Yes	No	0.0
No	Yes	0.0
No	No	0.0

Table 4.10 Expert Opinion Data for the Pressure Increase due to HPME

		Pressure Increase(bar)		
Expert	Weight	0.1 %	50 %	99.9 %
1	0.25	0.36	3.9	9.3
2	0.25	0.2	2.4	5.2
3	0.25	0.35	3.4	8.8
4	0.25	0.22	3.4	5.2

Table 4.11 Expert Opinion Data for the Pressure Increase due to Ex-Vessel Steam Explosion on High Vessel Pressure

		Pressure Increase (bar)		
Expert	Weight	0.1 %	50 %	99.9 %
1	0.25	0.13	4.3	18.0
2	0.25	0.041	3.3	17.0
3	0.25	0.099	4.3	19.0
4	0.25	0.0091	3.1	18.0

Table 4.12 Expert Opinion Data for the Pressure Increase due to Ex-Vessel Steam Explosion on Low Vessel Pressure

Expert	Weight	Pressure Increase (bar)		
		0.1 %	50 %	99.9 %
1	0.25	0.13	2.9	17.0
2	0.25	6.0×10^{-4}	2.4	20.0
3	0.25	4.9×10^{-2}	2.9	17.0
4	0.25	4.8×10^{-3}	2.4	17.0

Table 4.13 The conditional probabilities for ECF

Steam Explosion (EVSE)	HPME	Vessel Pressure (RP)	P(ECF|•)
No	Yes	Low	0.0
No	Yes	High	0.001
Yes	No	High	0.523
Yes	No	Low	0.523
No	No	Any	0.0

Table 4.14 The Conditional Probabilities for Liner Melt-through

Vessel Breach (VB)	Water in drywell (WC)	Vessel Pressure (RP)	Early Containment Failure (ECF)	P(LM|•)
No	Any	Any	Any	0.0
Yes	Any	Any	Yes	0.0
Yes	No	High	No	0.79
Yes	No	Low	No	0.50
Yes	Yes	High	No	0.38
Yes	Yes	Low	No	0.32

Table 4.15 The Conditional Probabilities for Containment Isolation Failure

Vessel Breach (VB)	Drywell Venting (CV)	Early Containment Failure (ECF)	Liner Melt-through (LM)	P(IF|•)
No	Any	Any	Any	0.0
Yes	No	Any	Any	0.0
Yes	Yes	Yes	No	0.0
Yes	No	No	Yes	0.0
Yes	Yes	No	No	1.0

Table 4.16 The Conditional Probabilities for the Occurrence of Core-Concrete Interaction

Vessel Breach (VB)	Vessel Pressure (RP)	Water in Drywell (WC)	P(CCI|•)
No	Any	Any	0.0
Yes	High	No	1.0
Yes	Low	No	1.0
Yes	High	Yes	0.28
Yes	Low	Yes	0.84

Table 4.17 The Conditional Probabilities for Late Overpressurization Containment Failure

CCI Occurrence (CCI)	Early Containment Failure (ECF)	Liner Melt-through (LM)	Isolation Containment Failure (IF)	P(LCF|•)
No	Any	Any	Any	0.0
Yes	Yes	Any	Any	0.0
Yes	No	Yes	Any	0.0
Yes	No	No	Yes	0.0
Yes	No	No	No	1.0

Table 4.18 Frequency of "reduced" Accident Progression Bins (APBs) [23]

Bin name	Description	Fraction of CDF due to Internal Initiators	Frequency (1/yr)
APB1	VB, early CF, WW failure, RPV>200 psia at VB	0.022	9.55×10^{-8}
APB2	VB, early CF, WW failure, RPV<200 psia at VB	0.011	4.77×10^{-8}
APB3	VB, early CF, DW failure, RPV>200 psia at VB	0.341	1.48×10^{-6}
APB4	VB, early CF, DW failure, RPV<200 psia at VB	0.183	7.94×10^{-7}
APB5	VB, late CF, WW failure	0.003	1.30×10^{-8}
APB6	VB, late CF, DW failure	0.047	2.04×10^{-7}
APB7	VB, Vent	0.110	4.77×10^{-7}
APB8	VB, no CF	0.184	7.99×10^{-7}
APB9	No VB	0.089	3.86×10^{-7}
APB10	No CD	0.010	4.34×10^{-8}

Table 4.19. Annual Risk At Peach Bottom [23]

Risk Measure	Core Damage (1/yr)	Early Fatality(#/yr)	Late Cancer Fatality (#/yr)
Mean Value	4.34×10^{-6}	2.6×10^{-8}	4.6×10^{-3}

Table 4.20. Fractional APB contributions (%) to Risk (FCMR) [23]

APBs	Early Fatality	Latent Cancer Fatality
APB1	0.24	0.96
APB2	0.12	0.45
APB3	64.2	67.1
APB4	28.2	23.6
APB5	0.0	0.1
APB6	1.8	1.5
APB7	5.3	5.9
APB8	0.0	0.0
APB9	0.22	0.37
APB10	0.0	0.0

Table 4.21 Consequence of APBs

Bin name	Description	Early Fatality	Late Cancer Fatality
APB1	VB, early CF, WW failure, RPV>200 psia at VB	6.54×10^{-4}	463.0
APB2	VB, early CF, WW failure, RPV<200 psia at VB	6.54×10^{-4}	433.6
APB3	VB, early CF, DW failure, RPV>200 psia at VB	1.13×10^{-2}	2086.0
APB4	VB, early CF, DW failure, RPV<200 psia at VB	9.23×10^{-3}	1367.0
APB5	VB, late CF, WW failure	0.0	353.0
APB6	VB, late CF, DW failure	2.29×10^{-3}	338.3
APB7	VB, Vent	2.89×10^{-3}	568.5
APB8	VB, no CF	0.0	0.0
APB9	No VB	1.48×10^{-4}	44.0
APB10	No CD	0.0	0.0

Table 4.22 Conditional Probabilities for ECF
conditional on VB,RP and WC

Vessel Breach (VB)	Vessel Pressure (RP)	Water in Drywell (WC)	P(ECF|•)
No	Any	Any	0.0
Yes	High	Yes	0.45
Yes	High	No	0.0008
Yes	Low	Yes	0.45
Yes	Low	No	0.0

Table 4.23 Conditional Probabilities for LCF
conditional on ECF,LM,IF,VB,RP and WC

Vessel Breach (VB)	Reactor Pressure (RP)	Water in Drywell (WC)	Early Contain-ment failure (ECF)	Liner Melt-through (LM)	Isolation Failure (IF)	P(LCF|•)
Yes	High	Yes	No	No	No	0.28
Yes	High	No	No	No	No	1.0
Yes	Low	Yes	No	No	No	0.84
Yes	Low	No	No	No	No	1.0

Table 4.24 Summary of marginal probabilities for both Flooding and Do Nothing cases

Description	Flooding	Do Nothing	% change
Vessel Failure	2.81×10^{-1}	6.20×10^{-1}	- 55*
Early Containment failure at high vessel pressure	9.46×10^{-2}	4.61×10^{-4}	2.5×10^{4}**
Early Containment failure at low vessel pressure	7.12×10^{-3}	0.00	N/A
Liner Melt-through at high vessel pressure	8.43×10^{-2}	4.56×10^{-1}	- 82*
Liner Melt-through at low vessel pressure	4.71×10^{-3}	2.17×10^{-2}	- 78*
Isolation Failure	8.74×10^{-2}	0.00	N/A
Late Overpressurization Containment Failure	2.85×10^{-3}	1.43×10^{-1}	- 98*

Note: * means a decrease due to flooding.
** means an increase due to flooding.

Table 4.25 Conditional Probabilities of Containment Failure given Vessel Failure

Description	Flooding	Do Nothing	% change
P(ECF,RP|VB)	3.37×10^{-1}	7.44×10^{-4}	4.5×10^{4}*
P(ECF,$\overline{RP}$|VB)	2.53×10^{-2}	0.0	N/A
P(LM,RP|VB)	3.00×10^{-1}	7.35×10^{-1}	-59**
P(LM,$\overline{RP}$|VB)	1.68×10^{-2}	3.50×10^{-2}	-52**
P(IF|VB)	3.11×10^{-1}	0.0	N/A
P(LCF|VB)	1.01×10^{-2}	2.30×10^{-1}	-96**
Total	1.00	1.00	

Note: * means an increase due to flooding
** means a decrease due to flooding

Table 4.26 Expected Consequence Measures for Flooding and Do Nothing cases

Decision	Expected Early Fatalities	Expected Late Fatalities
Flooding	2.390×10^{-3}	4.400×10^{2}
Do Nothing	5.676×10^{-3}	1.028×10^{3}
Reduction (%)	58	57

Table 4.27 NUREG-1150 Long Term Station Blackout Result [23]

	Core Damage Frequency	Early Fatality	Latent Cancer Fatality
Mean Risk Due to Internal Initiators(1)	4.3×10^{-6} (1/yr)	2.6×10^{-8} (fatality/yr)	4.6×10^{-3} (fatality/yr)
SBO-LT (PDS5) Contribution Percentage(2)	43.4	45.2	57.0
Risk Measure of PDS5(3)=(1)×(2)/ 100	1.9×10^{-6} (1/yr)	1.2×10^{-8} (fatality/yr)	2.6×10^{-3} (fatality/yr)

Table 4.28 Comparison of Do Nothing Risk Result with NUREG-1150 SBO-LT Risk (PDS5 = 1.9×10^{-6}/yr)

	Early Cancer Fatality (fatality/yr)	Latent Cancer Fatality (fatality/yr)
NUREG-1150	1.2×10^{-8}	2.6×10^{-3}
Do Nothing Subtree	1.1×10^{-8}	2.0×10^{-3}

Table 4.29 Results for BWR Bounding Calculation

Probability			Early Fatality		Late Fatality	
P(CV)	P(WC |CV)	P(VB|$\bar{R}$, WC)	Do Nothing	Flood	Do Nothing	Flood
1.0	1.0	0.0	5.68×10^{-3}	0	1028	0.0
1.0	1.0	1.0	5.68×10^{-3}	5.16×10^{-3}	1028	951
1.0	0.0	0.0	5.68×10^{-3}	5.76×10^{-3}	1028	1061
1.0	0.0	1.0	5.68×10^{-3}	5.76×10^{-3}	1028	1061
0.0	1.0	0.0	5.68×10^{-3}	5.68×10^{-3}	1028	1028
0.0	1.0	1.0	5.68×10^{-3}	5.68×10^{-3}	1028	1028
0.0	0.0	0.0	5.68×10^{-3}	5.68×10^{-3}	1028	1028
0.0	0.0	1.0	5.68×10^{-3}	5.68×10^{-3}	1028	1028

Note: P(CV): Probability of a successful drywell venting.

P(WC|CV): Probability of the presence of water in a drywell given a drywell venting.

P(VB|$\bar{R}$,WC): Probability of the vessel failure given non-recovery of AC power and the presence of water surrounding a lower vessel head.

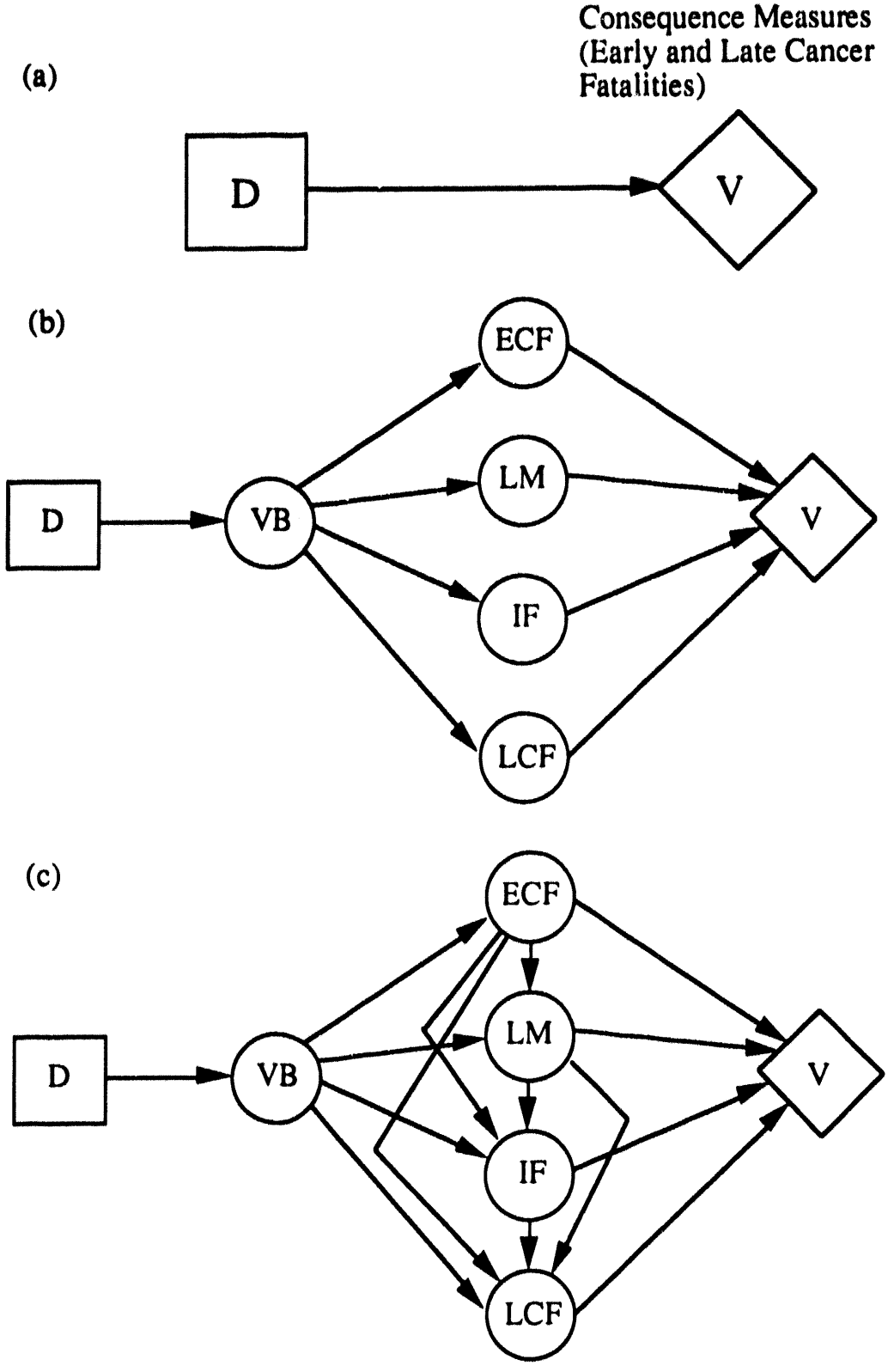

Fig.4.1 The construction and expansion of the influence diagram for BWR Drywell Flooding

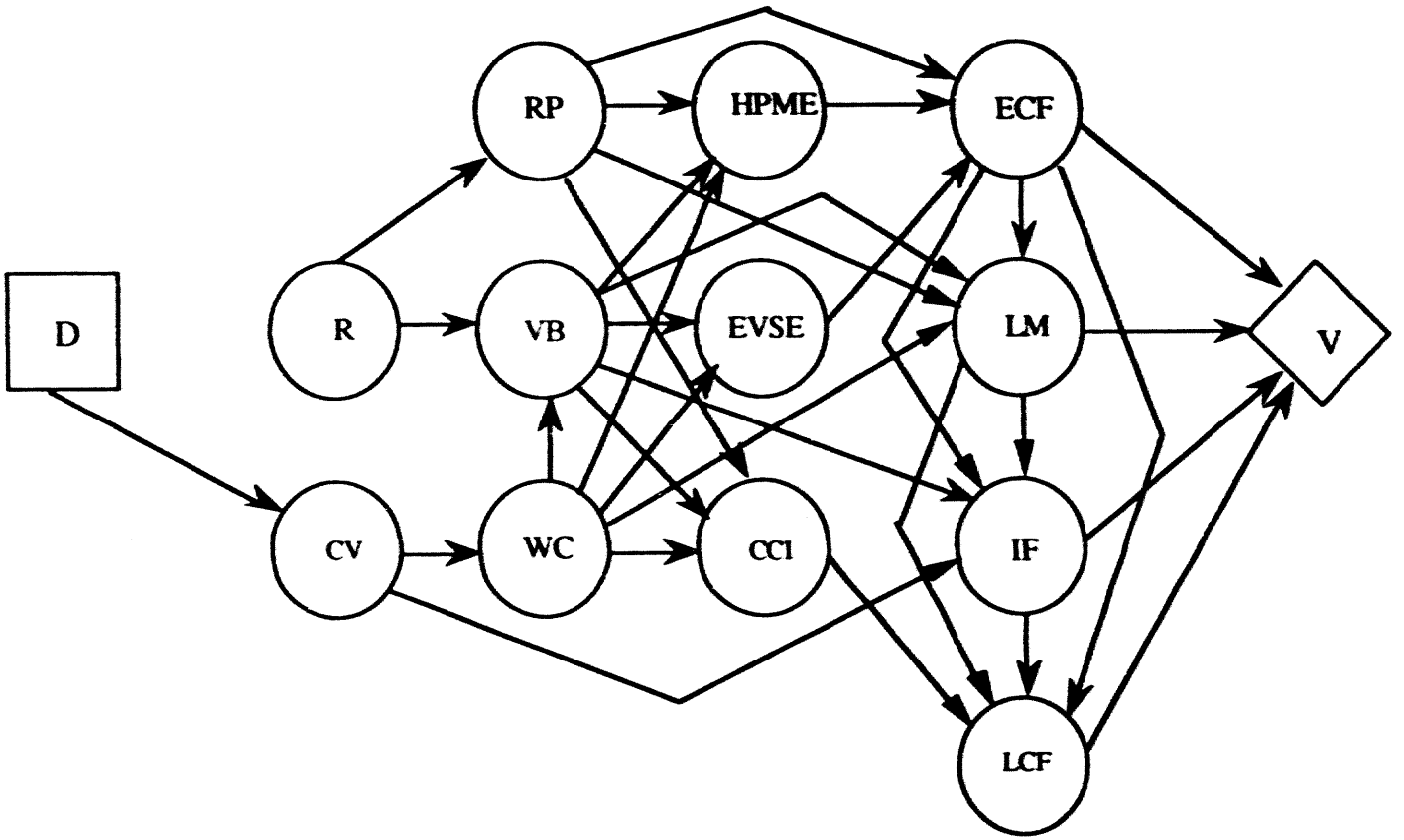

Fig. 4.2. Influence Diagram for Drywell Flooding Strategy applied to Peach Bottom SBO-LT Sequences

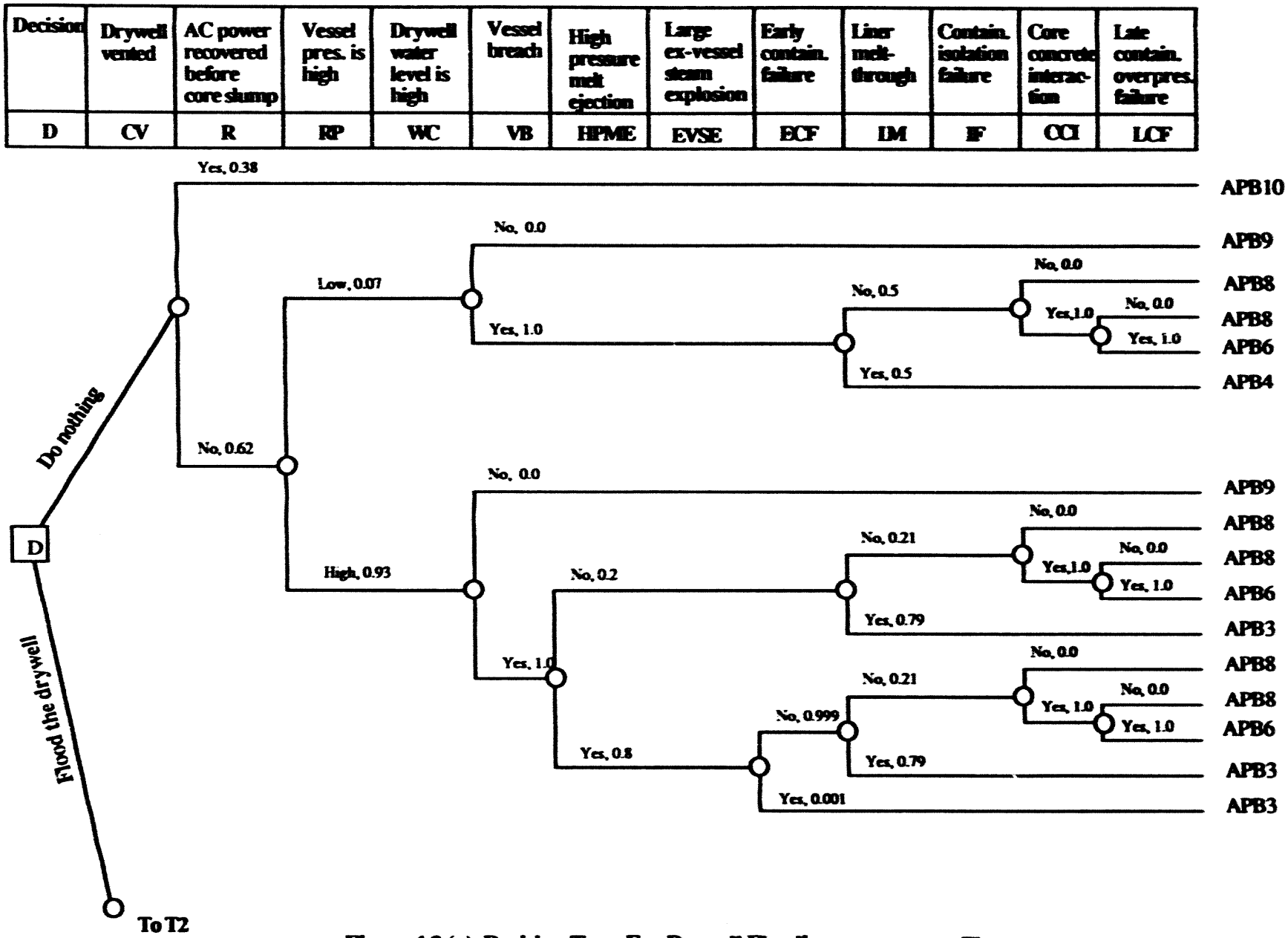

Figure 4.3 (a) Decision Tree For Drywell Flooding TI

Decision	Drywell vented	AC power recovered before core slump	Vessel pres. is high	Drywell water level is high	Vessel breach	High pressure melt ejection	Large ex-vessel steam explosion	Early contain. failure	Liner melt-through	Contain. isolation failure	Core concrete interac-tion	Late contain. overpres. failure
D	CV	R	RP	WC	VB	HPME	EVSE	ECF	LM	IF	CCI	LCF

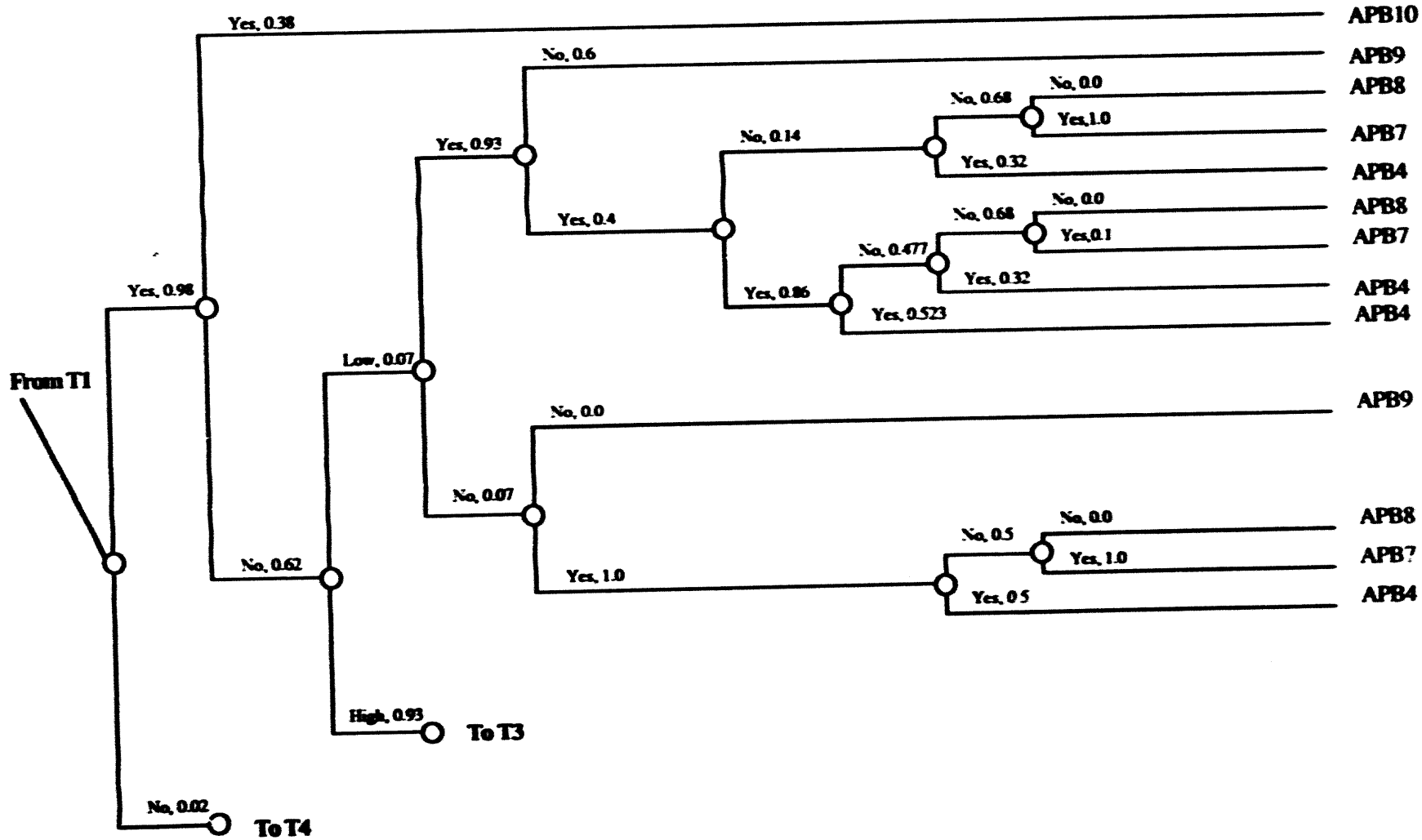

Figure 4.3 (b) Decision Tree For Drywell Flooding (Continued)

T2

Decision	Drywell vented	AC power recovered before core slump	Vessel pres. is high	Drywell water level is high	Vessel breach	High pressure melt ejection	Large ex-vessel steam explosion	Early contain. failure	Liner melt-through	Contain. isolation failure	Core concrete interac-tion	Late contain. overpres. failure
D	CV	R	RP	WC	VB	HPME	EVSE	ECF	LM	IF	CCI	LCF

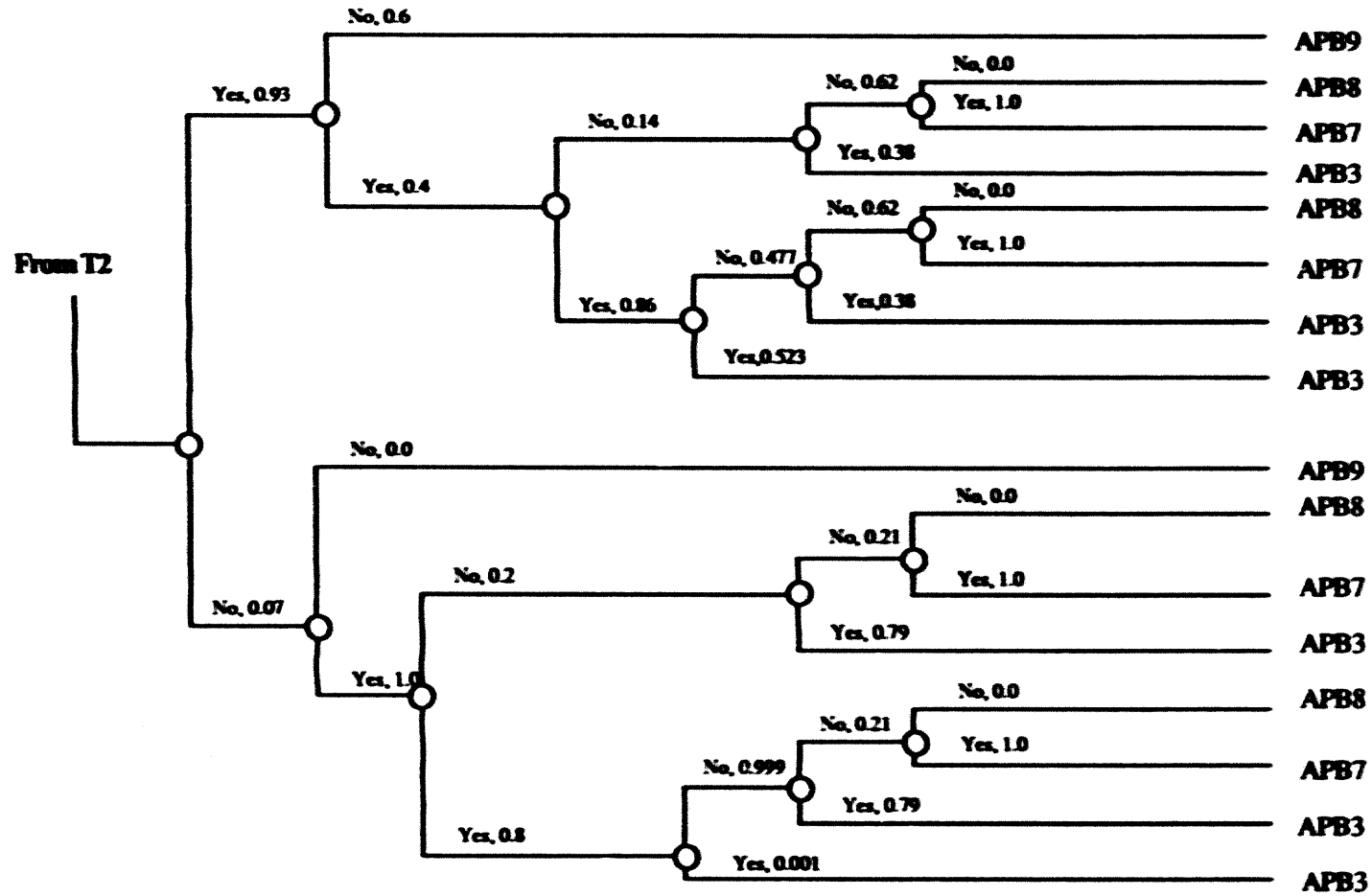

Figure 4.3 (c) Decision Tree For Drywell Flooding (Continued)

T3

Decision	Drywell vented	AC power recovered before core slump	Vessel pres. is high	Drywell water level is high	Vessel breach	High pressure melt ejection	Large ex-vessel steam explosion	Early contain. failure	Liner melt-through	Contain. isolation failure	Core concrete interac-tion	Late contain. overpres. failure
D	CV	R	RP	WC	VB	HPME	EVSE	ECF	LM	IF	CCI	LCF

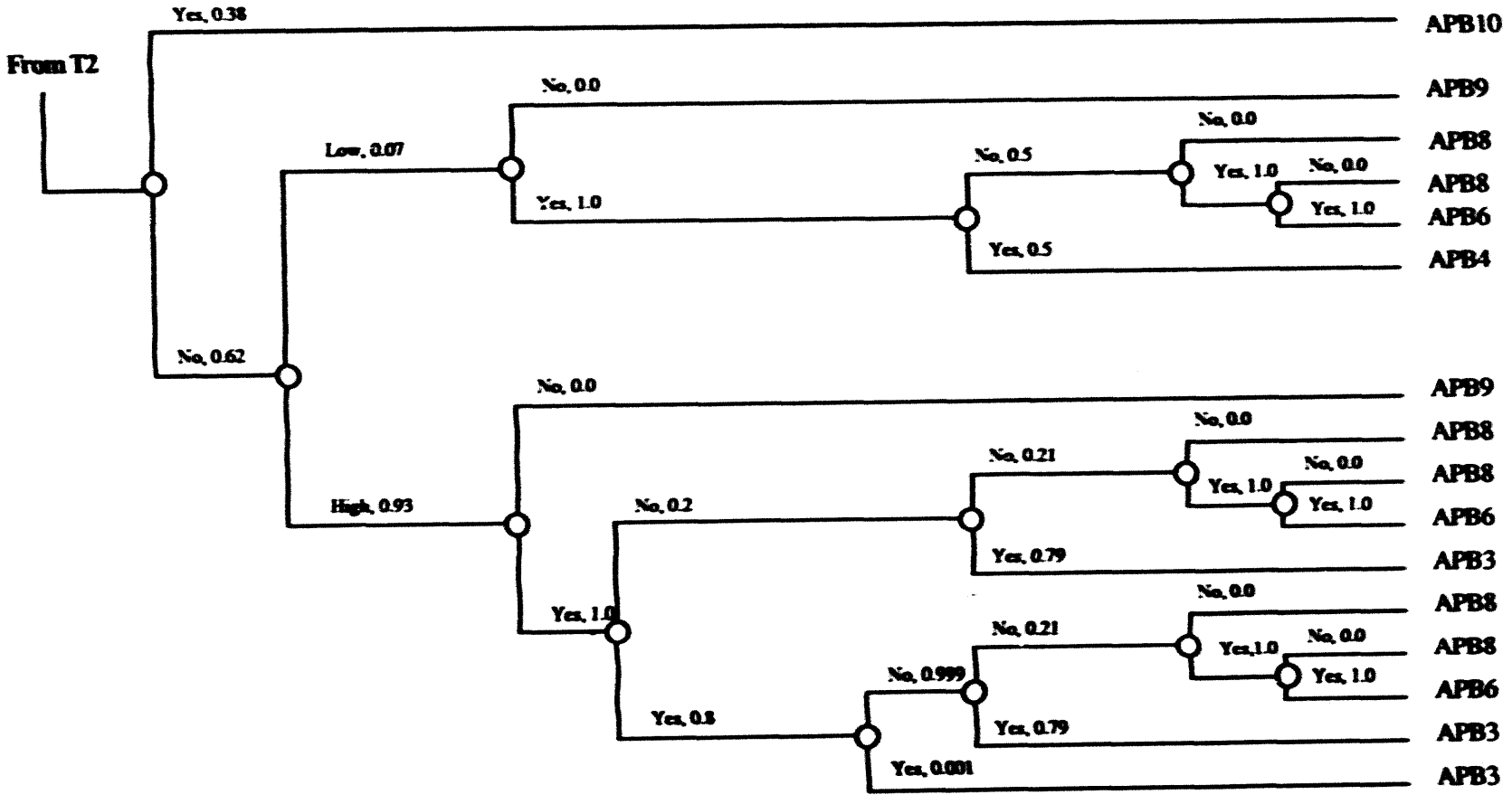

Figure 4.3 (d) Decision Tree For Drywell Flooding (Continued)

T4

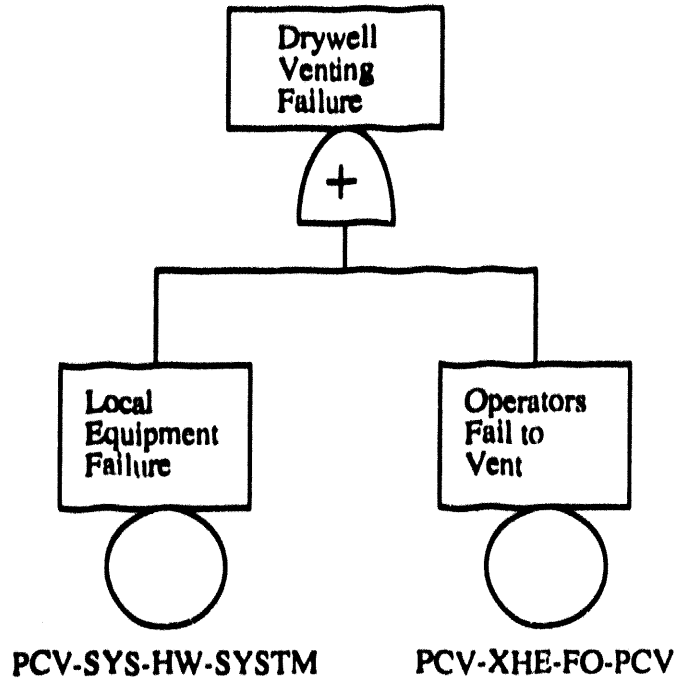

PCV-SYS-HW-SYSTM: 10^{-4} (1/demand)
PCV-XHE-FO-PCV: 0.02 (1/demand)

Fig. 4.4 Fault Tree For Drywell Venting

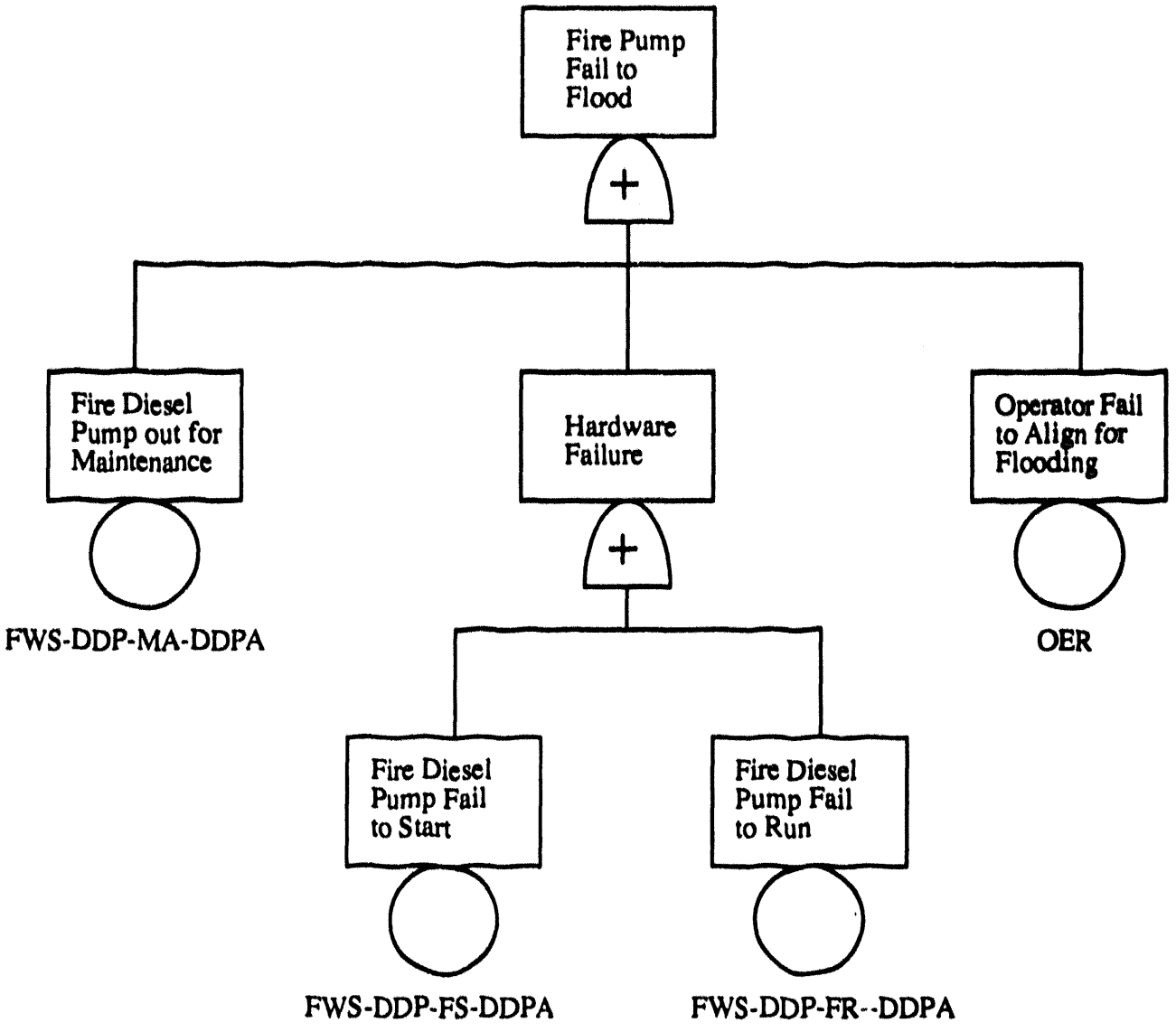

PWS-DDP-MA-DDPA: 0.01 (1/demand)
FWS-DDP-FS-DDPA: 0.03 (1/demand)
FWS-DDP-FR-DDPA: 0.0008 (1/hour)
OER: 0.02 (1/demand)

Fig. 4.5 Fault Tree For Drywell Flooding

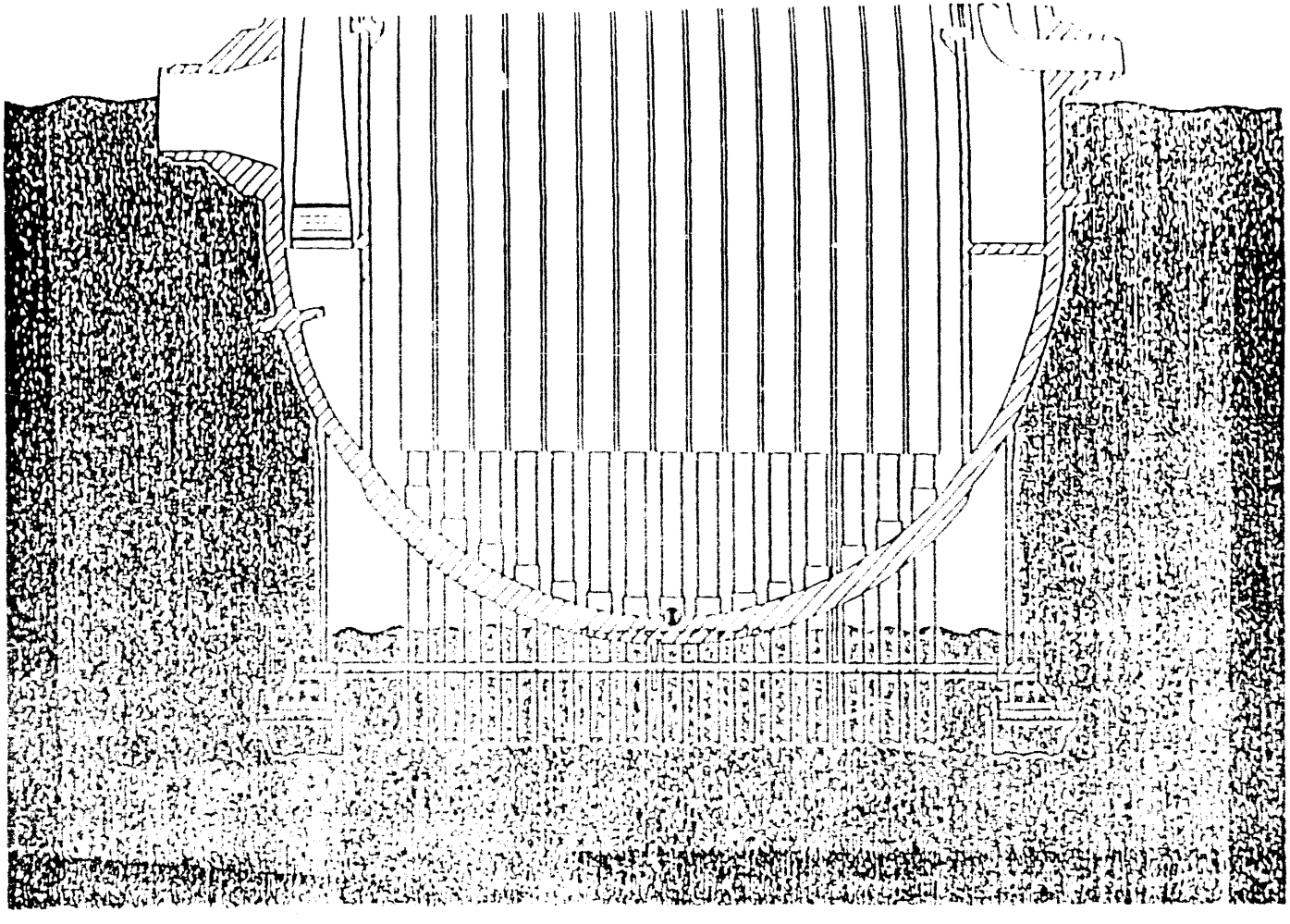

Figure 4.6 Atmosphere trapping within the reactor vessel support skirt would limit water contact with the vessel wall in that region [15]

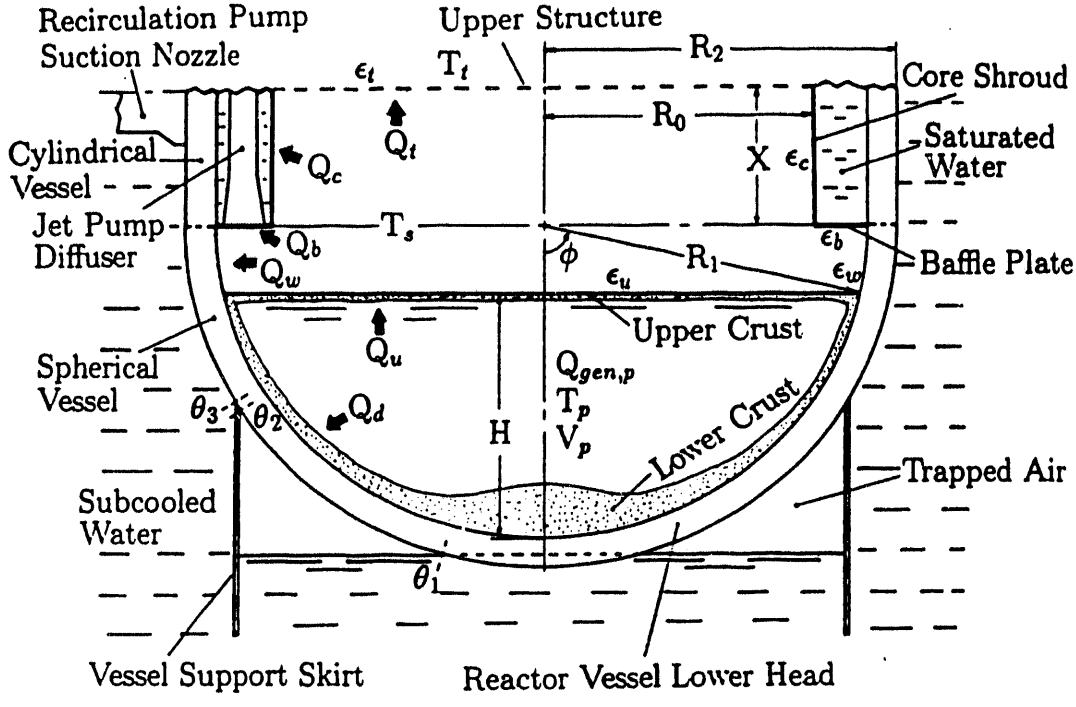

$Q_{gen,p}$ = Heat Generation in the Pool
Q_u = Heat Transfer to the Top of the Pool
Q_d = Heat Transfer to the Lower Part of the Pool
Q_w = Heat Transfer to the Dry Wall of the Vessel Lower Head
Q_b = Heat Transfer to the Baffle Plate
Q_c = Heat Transfer to the Core Shroud
Q_t = Heat Transfer to the Upper Structure

Figure 4.7. Schematic Diagram of the Core Material Relocated in the Vessel Lower Head[28].

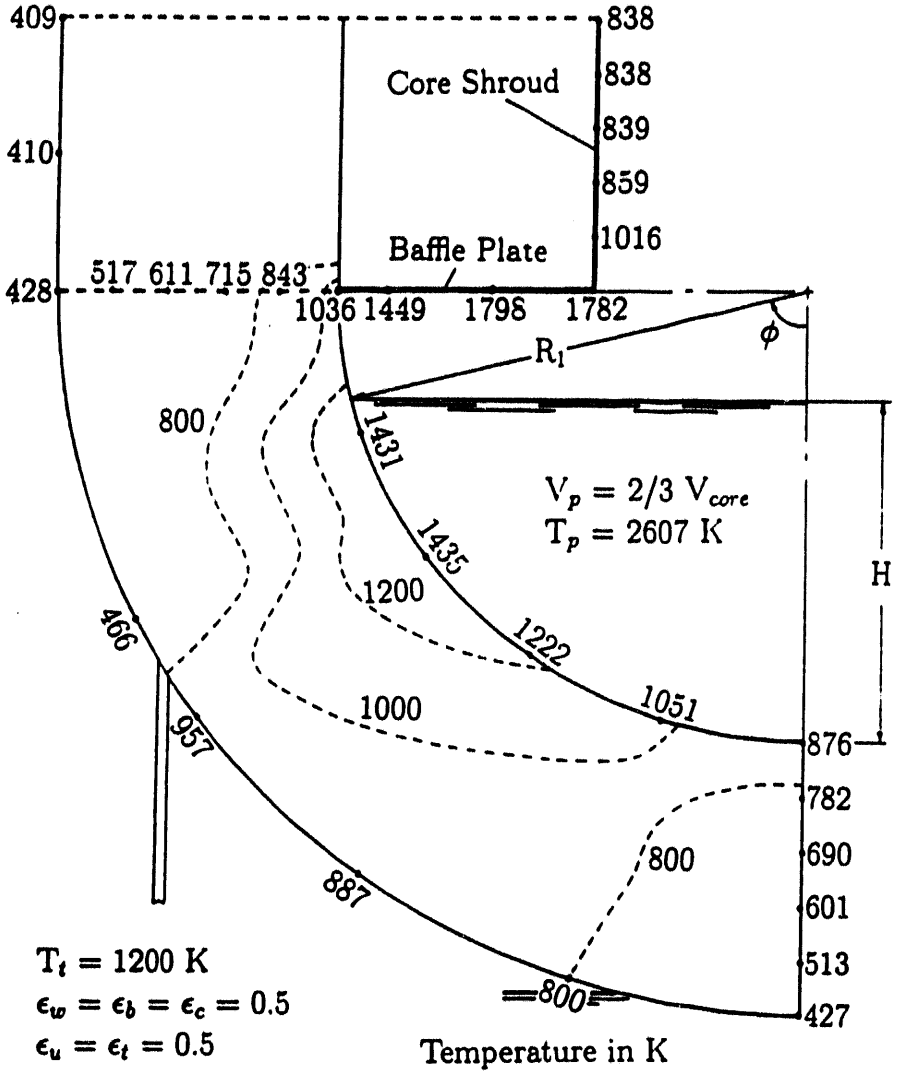

Figure 4.8. Temperature Distribution in the Vessel Shell Based on Mayinger et al's Correlation. [28]

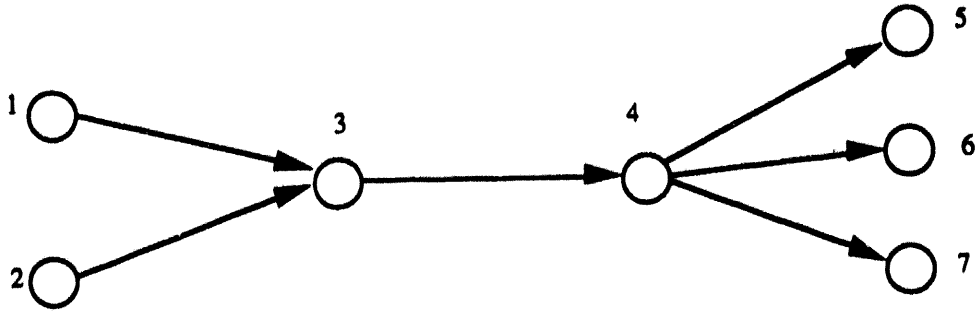

Fig.4.9. A Directed Network

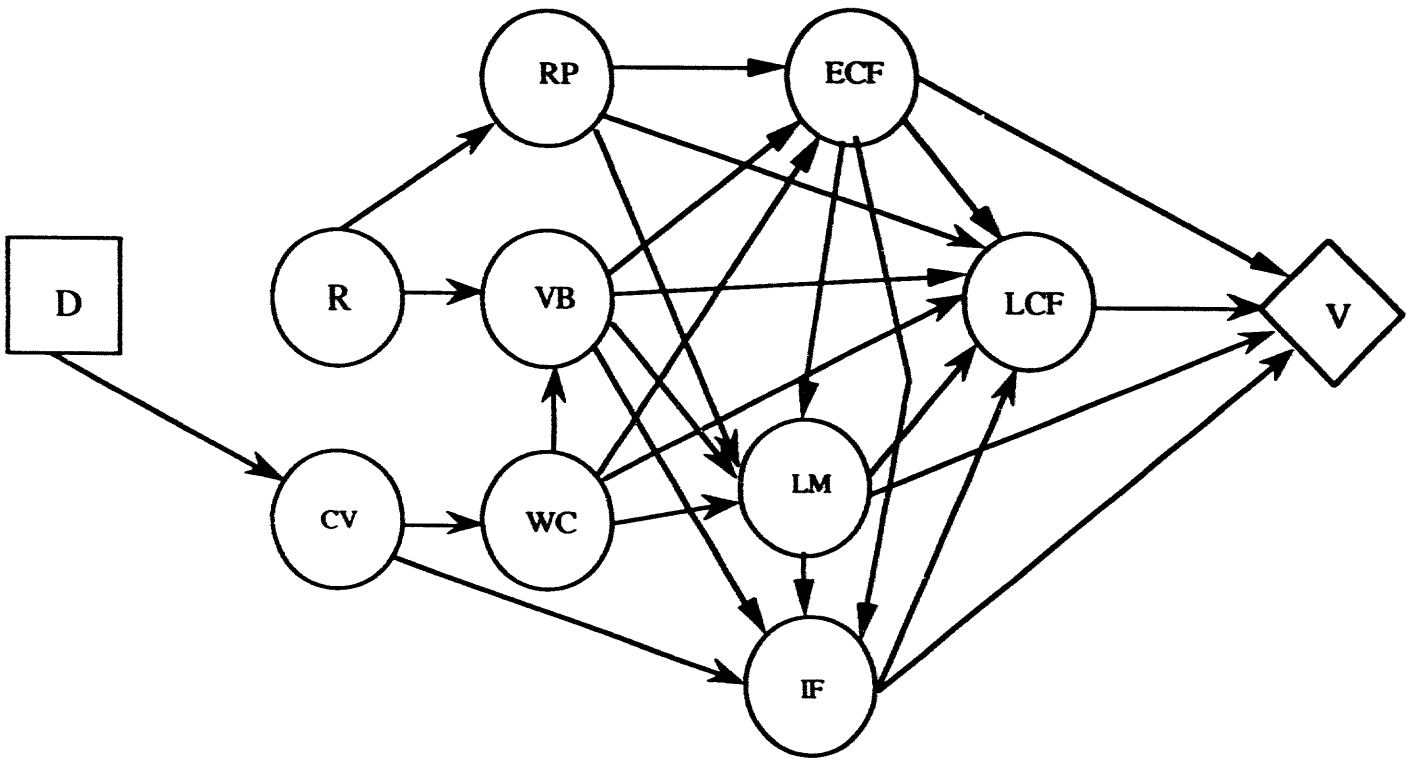

Fig. 4.10. A Collapsed Influence Diagram for Drywell Flooding Strategy on Peach Bottom LT-SBO Sequences

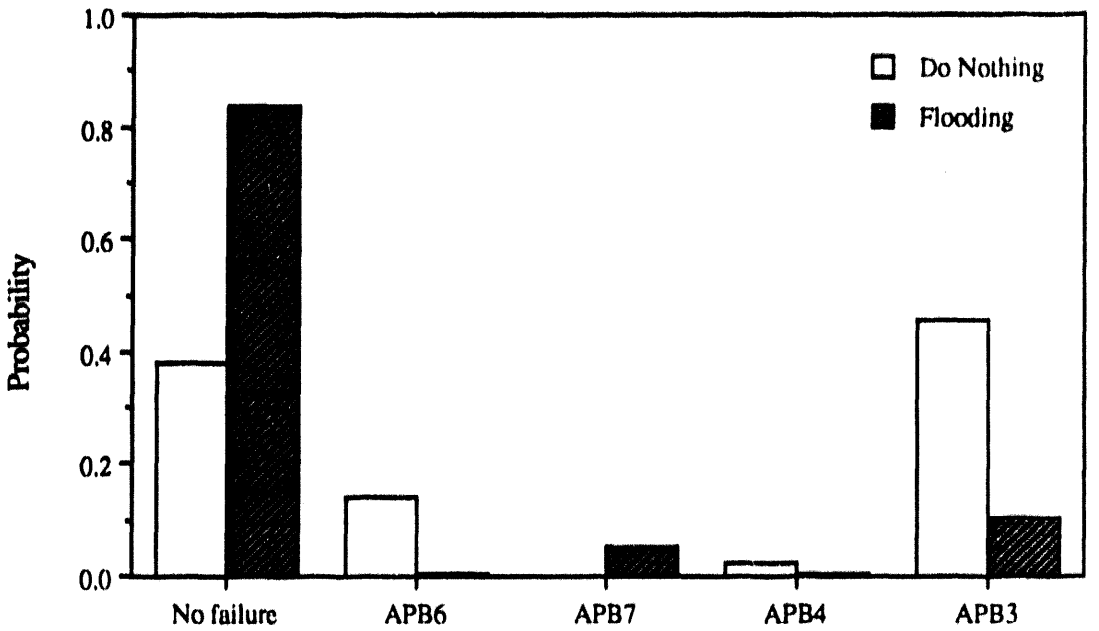

Figure 4.11 Probability Distribution of APBs for BWR Decision Tree

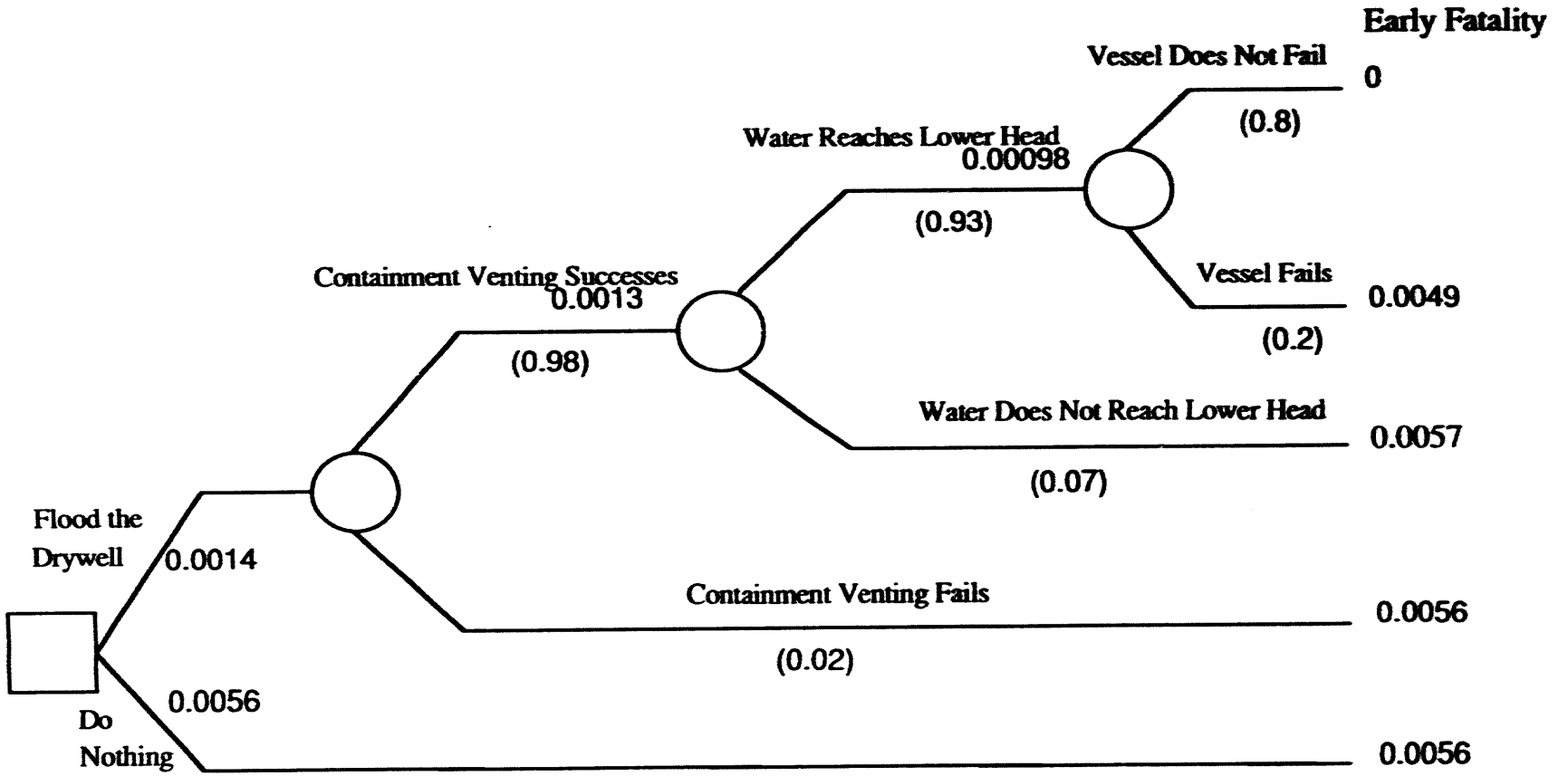

Fig. 4.12 Simplified Decision Tree for BWR (Early Fatality)

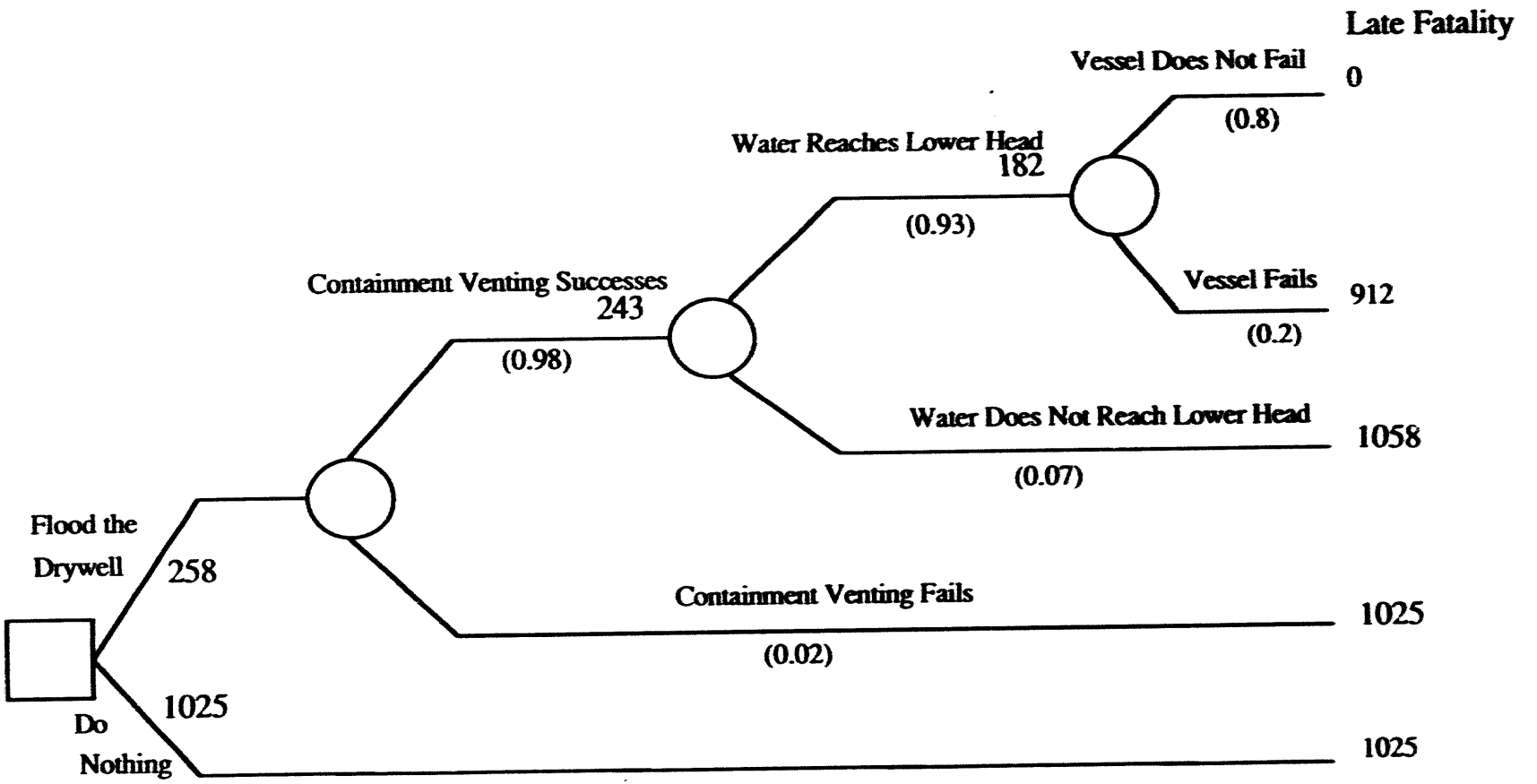

Fig. 4.13 Simplified Decision Tree for BWR (Latent Cancer Fatality)

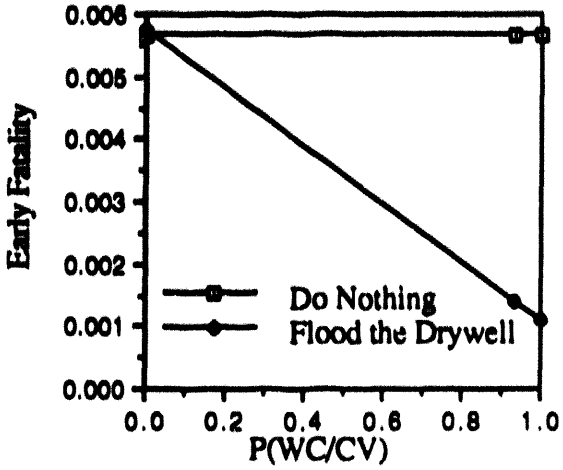

Fig.4.14 Sensitivity of Probability That Water Reaches Lower Head Given Drywell is vented (Early fatality)

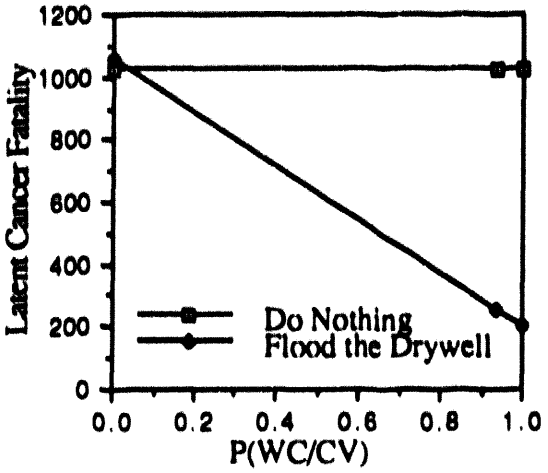

Fig.4.15 Sensitivity of Probability That Water Reaches Lower Head Given Drywell Is Vented(Latent Cancer Fatality)

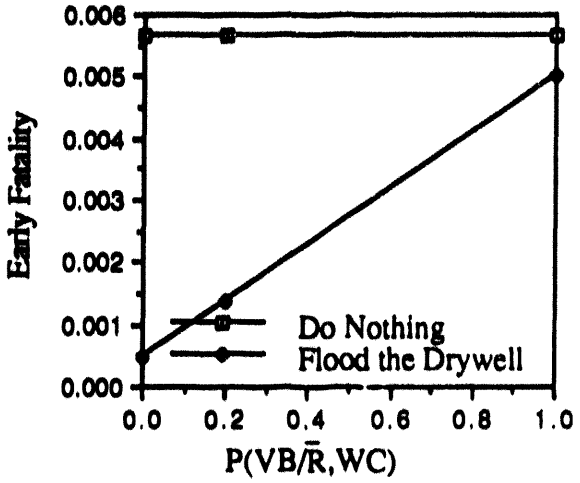

Fig.4.16. Sensitivity of Probability of Vessel Failure Given AC Non-recovery and Water Surrounds Lower Head (Early Fatality)

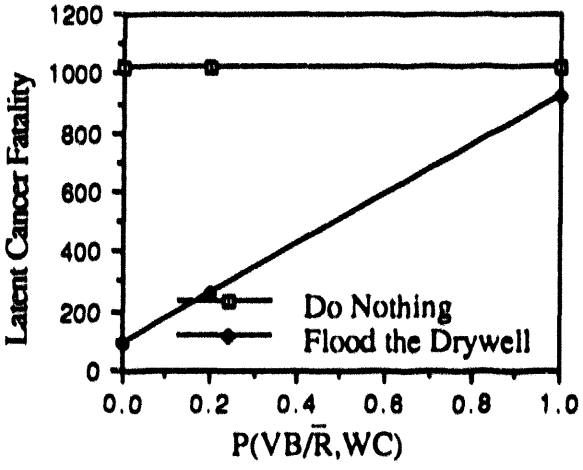

Fig.4.17 Sensitivity of Probability of Vessel Failure Given AC Non-recovery and Water Surrounds lower head (Late Fatality)

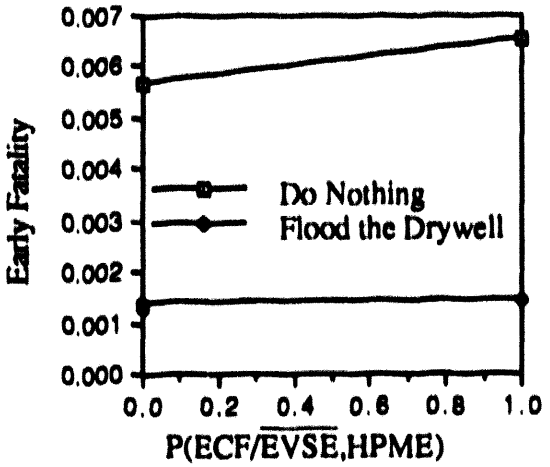

Fig.4.18 Sensitivity of Probability of Early Containment Failure Due to HPME (Early Fatality)

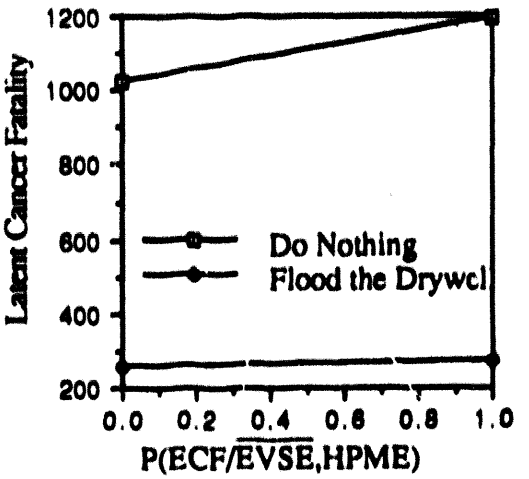

Fig.4.19 Sensitivity of Probability of Early Containment Failure Due to HPME (Latent Cancer Fatality)

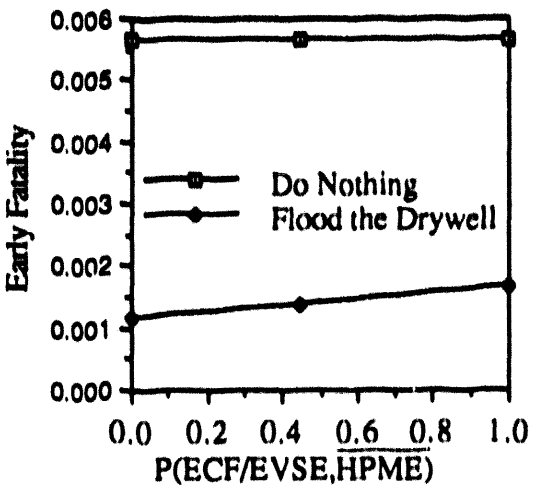

Fig.4.20 Sensitivity of Probability of Early Containment Failure Due to Ex-vessel Steam Explosion (Early Fatality)

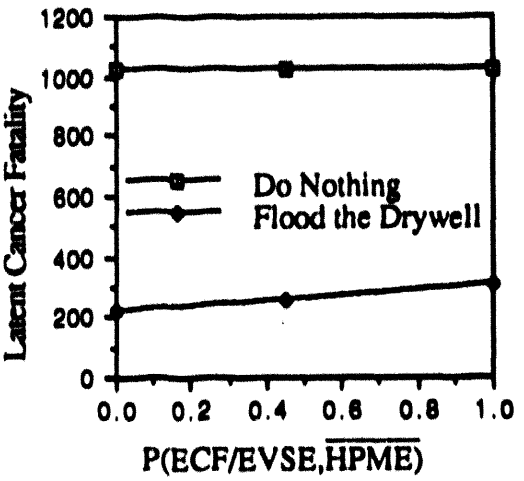

Fig.4.21 Sensitivity of Probability of Early Containment Failure Due to Ex-vessel Steam Explosion (Latent Cancer Fatality)

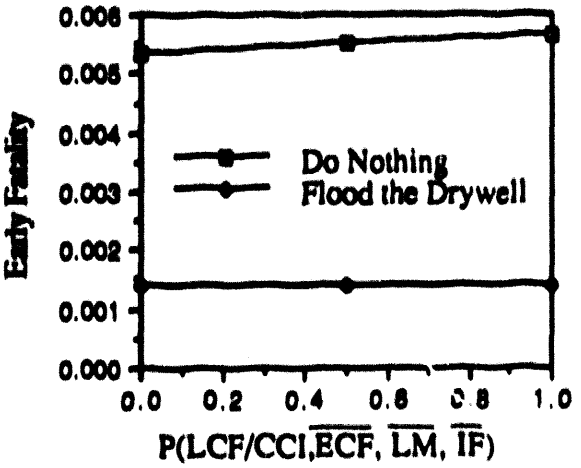

Fig.4.22 Sensitivity of Probability of Late Containment Overpressurization Failure Given CCI and No Other Failure Modes(Early Fatality)

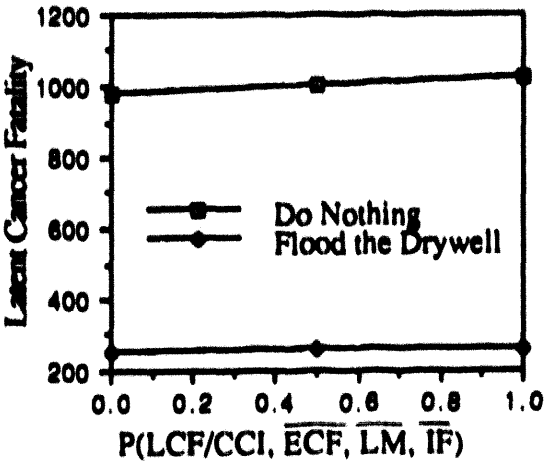

Fig.4.23 Sensitivity of Probability of Containment Overpressurization Failure Given CCI and No Other Failure Modes(Late Fatality)

5. EVALUATION OF INFLUENCE DIAGRAMS

5.1 Basic Rules

In general, once constructed, influence diagrams can be quantified and solved in order to evaluate decision strategies. Solving the influence diagram means to compute the expected values associated with the attributes of the value node, given the possible decisions. Computation of probabilities in the influence diagram is straightforward, although it is sometimes inefficient. Inefficiency of computation results from evidence variables which represents one of two kinds of chance variables (parameter variables being the other) [34,35]. A parameter variable in any model corresponds to a random variable denoted by a chance node, while an evidence variable (which may be represented by a shaded node for convenience) is relevant to observed or experimental evidence. This evidence introduces minor complications in the evaluation. The basic operations for evaluating influence diagrams containing these two kinds of chance variables have been developed [34,35,36] and are summarized as follows.

(1) *Arc reversal.* Given an influence diagram containing an arc from a chance node X to another node Y, but with no other directed path from X to Y, this arc can be reversed to point from Y to X. In the modified diagram, both X and Y inherit each other's conditional predecessors.

(2) *Sink node removal.* Any node in the influence diagram can be converted into a sink node by a suitable sequence of arc reversal operations. A chance node that has no successors can be eliminated.

(3) *Chance node removal.* Two nodes with a directed arc from X to Y can be replaced by a single node. The condition for this operation is that Y must be the only successor of X.

(4) *Decision node removal.* A decision node is removed by optimization, i.e., by

selecting the decision alternative that maximizes (minimizes) the expected value.

An example, the objective of which is to calculate P(Y/X), employing these operations, is illustrated in Figure 5.1. In this example, X and Y are conditionally independent given Z. The probabilities P(X/Z), P(Y/Z), and P(Z) are given. The diagram of Figure 5.1b follows from the reversal of the arc [Z,X] in Figure 5.1a, where there is only one directed path between X and Z. These two diagrams (Figures 5.1a and 5.1b) are equivalent. Then, the theorem of total probability for P(X) can be used, i.e.,

$$P(X) = \Sigma_Z P(X/Z)P(Z) \tag{5.1}$$

and from Bayes' theorem, P(Z/X) is obtained,

$$P(Z/X) = \frac{P(X/Z)P(Z)}{\Sigma_Z P(X/Z)P(Z)} \tag{5.2}$$

where Σ_Z is the sum over all possible values of Z.

Figure 5.1c is the final influence diagram. Thus, the conditional probability of Y given X is calculated using the operation of chance node removal, i.e.,

$$P(Y/X) = \Sigma_Z P(Y/Z)P(Z/X) \tag{5.3}$$

where the equality holds, because Z has only one successor,Y, as shown in Figure 5.1b.

The sink node removal operation is also demonstrated in the same example. The arc [Z,Y] of Fig. 5.1b is reversed (Fig. 5.1d). Here we need to add arc [X,Y] to perform this arc reversal, because both node Z and node Y should inherit each other's conditional predecessors. Applying Bayes' theorem once more we obtain the probability P(Z/X,Y) as follows:

$$P(Z|X,Y) = \frac{P(Y/Z)P(Z/X)}{\Sigma_z P(Y/Z)P(Z/X)} \qquad (5.4)$$

In order to show how these operations are applied, an example associated with a used car buyer is made as follows. The buyer can decide whether or not to buy a used car. There are two choices, D (Do not buy) and B (Buy). The car can be of either good quality, or bad quality. It is assumed the the buyer knows from experience that the chance of good quality is 0.7, and of poor quality 0.3.

There is an intimate friend of the decision maker, who is a mechanic. The mechanic checks the quality of the car for his friend without cost. If the car is of good quality, there is 0.7 probability that the mechanic will recognize it (or say "good"), there is 0.2 probability that he will say "so-so (medium)", and there is 0.1 probability that he will say "poor". If the car is of poor quality, the probabilities of the mechanic recognizing it as good, medium, and poor are 0.15, 0.25, and 0.6, respectively. We shall assume the buyer's objective is to maximize the expected satisfaction value.

The following satisfaction values are assumed as follows. The buyer gets satisfaction 100 if the car is of good quality and he buys it. He gets 0 if the car is of poor quality and he buys it. The rest are in-between values. He gets 70 if the car is of poor quality and he does not buy it, while he gets 20 if the car is of good quality and he does not buy it.

The equivalent influence diagram is shown in Figure 5.2a, where node TR and Q represent the mechanic's judgement and the condition of the car, respectively. The influence diagram operations described above are shown in Figure 5.2b - 5.2e. Since node Q has two successors, the operation of chance node removal cannot be applied. In order to reduce two successors to one successor, the operation of arc reversal is applied. Since the influence diagram contains an arc from the chance node Q to another node TR, but with no other directed path from Q to TR, the operation of arc reversal can be applied using Eqn. (5.2), as presented in Figure 5.2b. Then using Eqn. (5.3), node Q is

absorbed into the value node, as shown in Figure 5.2c. The decision node D is removed by maximizing the expected value of the satisfacton, as shown in Figure 5.2d. The process ends when all predecessors to the value node have been removed (Figure 5.2e). The detailed calculations are as follows;

Let Q_1 = event "the car is good"
Q_2 = event "the car is poor"
TR_1 = event "the mechanic judged the car is good"
TR_2 = event "the mechanic judged the car is medium"
TR_3 = event "the mechanic judged the car is poor".
D_1 = D = Decision not to buy the car
D_2 = B = Decision to buy the car.

Then

$P(Q_1) = 0.70$	$P(Q_2) = 0.30$
$P(TR_1 / Q_1) = 0.70$	$P(TR_1 / Q_2) = 0.15$
$P(TR_2 / Q_1) = 0.20$	$P(TR_2 / Q_2) = 0.25$
$P(TR_3 / Q_1) = 0.10$	$P(TR_3 / Q_2) = 0.6$

Probabilistic notation for the value is;

$V(D_1 / Q_1) = 20$	$V(D_2 / Q_1) = 100$
$V(D_1 / Q_2) = 70$	$V(D_2 / Q_2) = 0$

In order to find $P(TR_i)$ associated with Figure 5.2b, arc reversal operation is applied as follows;

From the definition of joint probablity

$$P(TR_i) = P(TR_i, Q_i) + P(TR_i, Q_i)$$

Using the Bayes' theorem

$$P(TR_1) = P(TR_1 / Q_1)\, P(Q_1) + P(TR_1 / Q_2)\, P(Q_2)$$
$$= 0.7 \times 0.7 + 0.15 \times 0.3 = 0.535$$

Similarly,

$$P(TR_2) = P(TR_2 / Q_1)\, P(Q_1) + P(TR_2 / Q_2)\, P(Q_2)$$
$$= 0.2 \times 0.7 + 0.25 \times 0.3 = 0.215$$

$$P(TR_3) = P(TR_3 / Q_1)\, P(Q_1) + P(TR_3 / Q_2)\, P(Q_2)$$
$$= 0.1 \times 0.7 + 0.60 \times 0.3 = 0.250$$

And to find $P(Q_j / TR_i)$, the Bayes' theorem is applied again.

$$P(Q_j / TR_i) = \frac{P(Q_j)\, P(TR_i / Q_j)}{P(TR_i)}$$

$$P(Q_1 / TR_1) = \frac{0.7 \times 0.7}{0.535} \cong 0.92$$

$$P(Q_1 / TR_2) = \frac{0.7 \times 0.2}{0.215} \cong 0.65$$

$$P(Q_1 / TR_3) = \frac{0.7 \times 0.1}{0.250} = 0.28$$

$$P(Q_2 / TR_1) = \frac{0.3 \times 0.15}{0.535} \cong 0.08$$

$$P(Q_2 / TR_2) = \frac{0.3 \times 0.25}{0.215} \cong 0.35$$

$$P(Q_2 / TR_3) = \frac{0.3 \times 0.6}{0.250} \cong 0.72$$

Figure 5.2c and 5.2d represent removal of the Q node and its absorption into the

value node. Then we need $V(D_1/TR_1)$, $V(D_1/TR_2)$, $V(D_1/TR_3)$, $V(D_2/TR_1)$, $V(D_2/TR_2)$, $V(D_2/TR_3)$.

Using Eq. (5.3)

$$V(D_1/TR_1) = \sum_{i=1}^{2} V(D_1/Q_i)\, P(Q_i/TR_1)$$
$$= 20 \times 0.92 + 70 \times 0.08 = 24$$

$$V(D_1/TR_2) = \sum_{i=1}^{2} V(D_1/Q_i)\, P(Q_i/TR_2)$$
$$= 20 \times 0.65 + 70 \times 0.35 \cong 38$$

$$V(D_1/TR_3) = \sum_{i=1}^{2} V(D_1/Q_i)\, P(Q_i/TR_3)$$
$$= 20 \times 0.28 + 70 \times 0.72 = 56$$

$$V(D_2/TR_1) = \sum_{i=1}^{2} V(D_2/Q_i)\, P(Q_i/TR_1)$$
$$= 100 \times 0.92 = 92$$

$$V(D_2/TR_2) = \sum_{i=1}^{2} V(D_2/Q_i)\, P(Q_i/TR_2)$$
$$= 100 \times 0.65 = 65$$

$$V(D_2/TR_3) = \sum_{i=1}^{2} V(D_2/Q_i)\, P(Q_i/TR_3)$$
$$= 100 \times 0.28 = 28$$

Hence,

if TR_1 occurs, it is D_2, "Buy"
if TR_2 occurs, it is D_2, "Buy"
if TR_3 occurs, it is D_1, "Do not buy".

This is where one can stop since a guidance for decision is given. Figure 5.2d represents degree of satisfaction associated with the decision optimization. Figure 5.2e shows total expected value; i.e., satisfaction.

The same result can be obtained from an evaluation of the equivalent decision tree, as shown in Figure 5.3, and can be interpreted as follows: If the friend says "good" or "so-so", then buy; if the friend says "poor", do not buy. As shown above, the decision tree is more clear in representing outcome states and policy results than the influence diagrams. The policy results of influence diagrams are revealed by examining the values for each choice contained in the underlined data structure as shown in Figure 5.2.

An alternate formulation of the solution is as follows [36]. First, a list is constructed of all the nodes with no conditional predecessors. Then, we add one node to the end of the list by choosing any node whose conditional predecessors, if any, are all already on the list. This process is continued and, since there are no cycles in the influence diagram, all of the nodes can be ordered this way. There is at least one ordered list, say, $[X_1,X_2,X_3,\ldots,X_n]$, of the nodes in the influence diagram. A fully specified influence diagram, which is not missing any data or conditional probability distributions for any of the variables, contains the joint distribution factored into conditional distributions (called the chain rule):

$$P(X_1,X_2,X_3,\ldots,X_n)= P(X_1)P(X_2/X_1)P(X_3/X_1,X_2)\ldots P(X_n/X_1,X_2,\ldots,X_{n-1}). \qquad (5.5)$$

Because directed cycles are not permitted in an influence diagram, the joint distribution is always uniquely determined.

As an example, consider a case with independent nodes (chance nodes B and C in Figure 5.4a are independent). The two possible ordered lists are [B,C,A]

and [C,B,A]. Now, suppose that we wish to compute P(A). Then, the calculation proceeds as follows:

$$\begin{aligned} P(A) &= \Sigma_{B,C} P(A,B,C) \\ &= \Sigma_{B,C} P(A/B,C)\ P(C/B)\ P(B) \\ &= \Sigma_{B,C} P(A/B,C)\ P(C)\ P(B) \end{aligned} \tag{5.6}$$

where $\Sigma_{B,C}$ is the sum over all possible values of B and C. Clearly, the same expression would have been obtained, if we had used the other ordered list of the nodes. It is important that the conditional probability P(A/B,C) be assessed in terms of its direct predecessor nodes.

For the case with dependence between nodes B and C (Figure 5.4b), the only ordered list is [B,C,A]. In the same manner as before we get

$$\begin{aligned} P(A) &= \Sigma_{B,C} P(A,B,C) \\ &= \Sigma_{B,C} P(A/B,C)\ P(C/B)\ P(B) \end{aligned} \tag{5.7}$$

where $\Sigma_{B,C}$ is the sum over all possible values of B and C.

5.2 Application to Vessel Breach

As a further example, we consider the effect of PWR cavity flooding on vessel breach. Looking at the final influence diagram (Figure 3.5), node VB is influenced by three nodes, namely, WC (water in the cavity), CDA (core damage arrest), and RP (RCS pressure at vessel breach). Since node VB is considered as the target event, it is changed into the value node, as shown in Figure 5.5a, where the decision node (to flood or not to flood) affects only node WC.

The conditional probabilities for node VB are shown in Table 5.1. In case 1, core damage is assumed arrested via AC power recovery and hence ECCS recovery. The probability of no vessel failure is then 1.0. In case 2, the RCS is

at high pressure and the cavity is assumed to be flooded. The probability of vessel failure for this case is conservatively chosen to be 1.0. Given that the vessel fails, it is assumed that the vessel will fail by either a penetration failure leading to high pressure melt ejection (HPME) or bottom head failure (BH), with equal probability for each. In case 3, the RCS is at high pressure, there is no water in the cavity and vessel failure is assured. The split fraction regarding the mode of vessel failure was taken from Reference 4. Case 4 is similar to case 2 except that the RCS is at low pressure. The probability of no vessel failure is assumed to be 0.1. Case 5 is also similar to case 3. Since the RCS pressure is low, the probability of HPME is 0.0.

Since each predecessor of the node VB have a successor into that node (node VB), the operation of arc reversal is not required. For a single decision problem, the operation of decision node removal is also not required.

In the first operation, chance node removal eliminates node CDA since the value node is its only successor. The changed conditional probabilities for node VB are calculated using Eqn (5.3) and are shown in Table 5.2 (VB is Y, CDA is Z, and R is X). In the same manner, it is possible to remove node HSF and then node ESGTR (Figure 5.5b). In the next operation in Figure 5.5b, since the R node has two successors, the RP node is removed first (Figure 5.5c). Then the conditional probabilities for the VB node are obtained in Table 5.3. The final operation removes the WC node and the R node. Then the final diagram has just two nodes (Figure 5.5d), and the final results are shown in Table 5.4.

The probability of no vessel breach as a result of the decision to flood the cavity at the time of core uncovery is 0.267, while that for the "do-nothing" decision is 0.234. Therefore, based on these results, flooding the reactor cavity is somewhat better than not flooding it.

We can also use the second method described in the preceding section to evaluate the diagram in Fig. 5.5a. A possible ordered list for the seven nodes is [WC, ESGTR, HSF, R, RP, CDA, VB]. According to the chain rule, the probability of vessel failure, given each decision, is as follows:

$$P(VB / D) = \Sigma_{WC,ESGTR,HSF,R,RP,CDA}\, P(VB / CDA,RP,R,HSF,ESGTR,WC,D)x$$
$$P(CDA / RP,R,HSF,ESGTR,WC,D)\, P(RP / R,HSF,ESGTR,WC,D)x$$
$$P(R / HSF,ESGTR,WC,D)\, P(HSF / ESGTR,WC,D)x$$
$$P(ESGTR / WC,D)\, P(WC / D)$$
$$= \Sigma_{WC,ESGTR,HSF,R,RP,CDA}\, P(VB / CDA,RP,WC)\, P(CDA / R)x$$
$$P(RP / R,HSF,ESGTR)\, P(R)\, P(HSF / ESGTR)x$$
$$P(ESGTR)\, P(WC / D). \qquad (5.8)$$

The probabilities required in Eqn. (5.8) are given in Tables 3.3 -3.6 and 5.1. The results are as before.

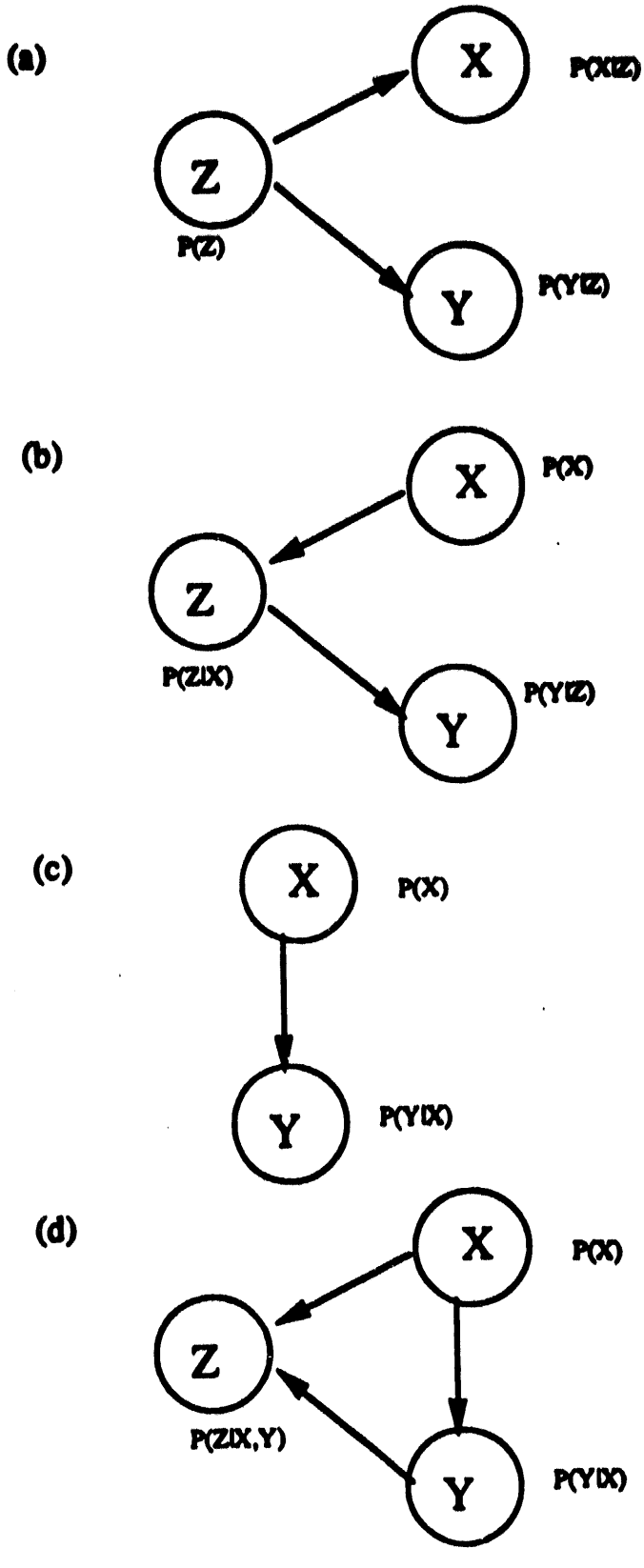

Figure 5.1. An example of arc reversal and node removal.

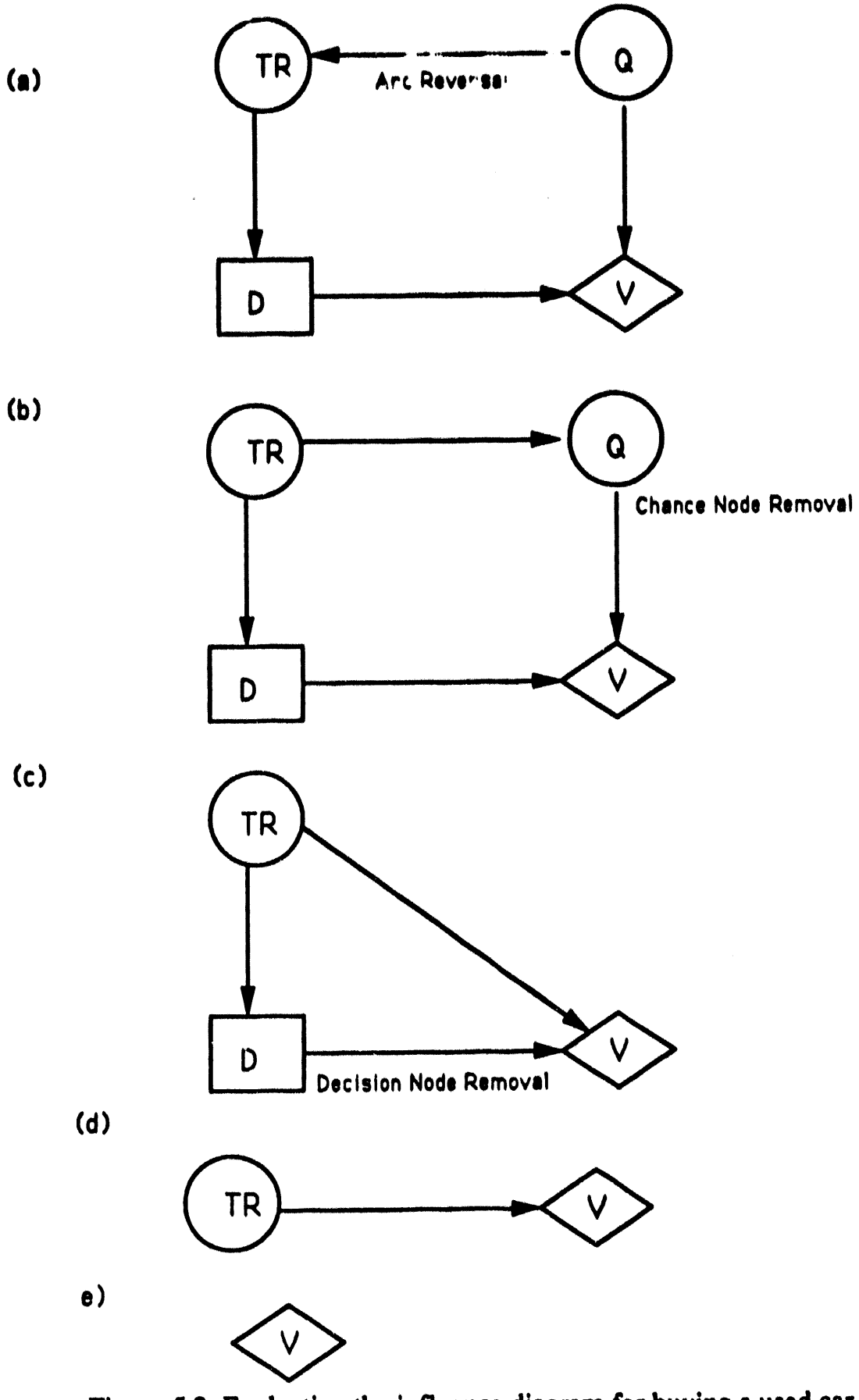

Figure 5.2. Evaluating the influence diagram for buying a used car.

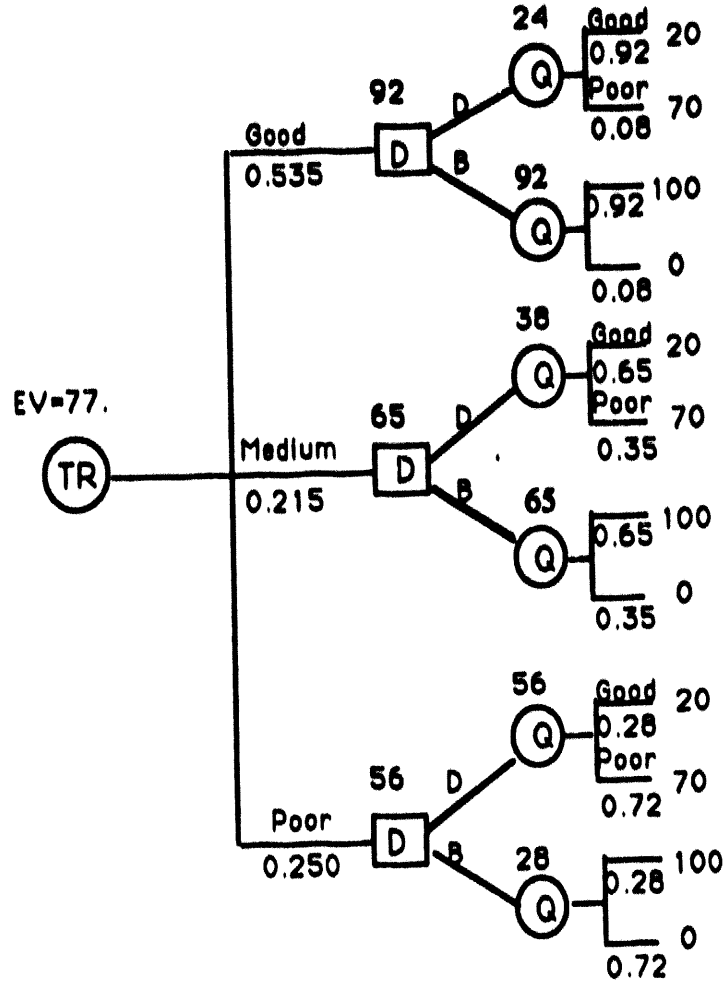

B = Buy D = Don't Buy
P(Q | TR) = {0.92, 0.65,0.28} by Bayes' Formula

Figure 5.3. Equivalent decision tree for Figure 5.2a.

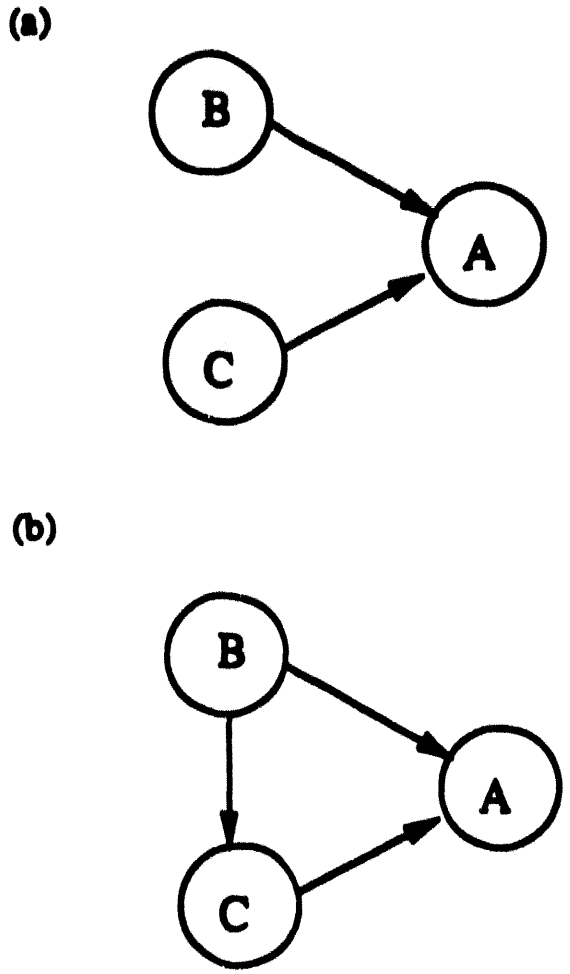

Figure 5.4 Basic influence diagrams (a) without and (b) with probabilistic dependence

a)

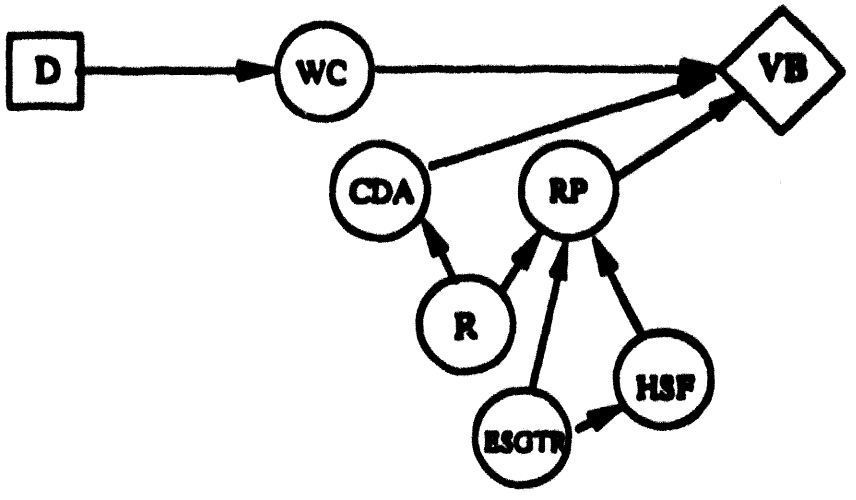

b)

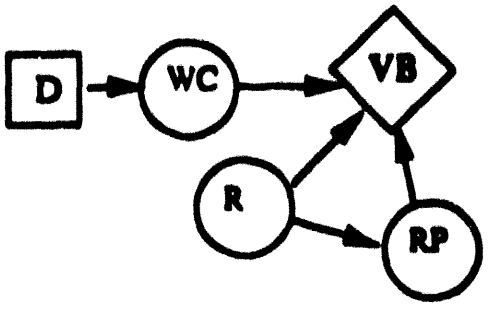

c)

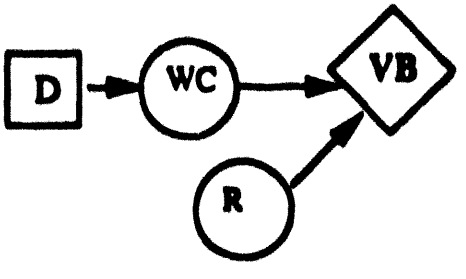

d)

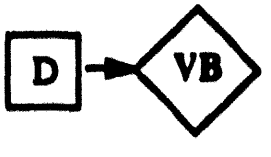

Figure 5.5. Evaluating the influence diagram up to node VB.

Table 5.1
Conditional probability for node VB

CASE	CDA	RP	WC	P(no VB)	P(HPME)	P(BH)
1	yes	-	-	1.0	0.0	0.0
2	no	high	yes	0.0	0.5	0.5
3	no	high	no	0.0	0.79	0.21
4	no	low	yes	0.1	0.0	0.9
5	no	low	no	0.0	0.0	1.0

Note: The underlined values are discussed in Chapter 3. The rest are taken from Ref. [8].

Table 5.2
Reduced conditional probability for node VB
with nodes WC, R, and RP

WC	R	RP	P(no VB)	P(HPME)	P(BH)
yes	yes	high	0.90	0.05	0.05
"	"	low	0.91	0.0	0.09
"	no	high	0.0	0.5	0.5
"	"	low	0.1	0.0	0.9
no	yes	high	0.9	0.08	0.02
"	"	low	0.9	0.0	0.1
"	no	high	0.0	0.79	0.21
"	"	low	0.0	0.0	1.0

6. MULTIPLE DECISION MODEL

6.1 Introduction

The decision analysis framework described in the preceding chapters is not limited to the assessment of accident management strategy based on a single decision. It can be employed to evaluate a sequence of strategies based on multiple decisions. In reality, accident management is not just a single action undertaken by plant personnel, rather it is an ongoing cyclic process of diagnosis, decision making, action and observation. In an accident situation the operators must diagnose the plant state using all of the available information, including instrumentation readings, direct observations and other aids, as well as their own knowledge base. They must then decide on an appropriate action among several possibilities, undertake that action and then see if that action has the desired effect on the state of the plant. This is an ongoing process, and will continue until the operators have either brought the plant to a safe, stable state or have to evacuate the control room.

Thus it is apparent that the assessment of a single strategy, in the absence of other actions that may be implemented before, after or even simultaneously with the one under consideration, may not be very meaningful. Sequential combinations of strategies may have a much different effect on the plant when considered together than would be apparent if they are evaluated separately. As mentioned in Chapter 3, for example, the strategy of flooding the reactor cavity in order to prevent vessel failure has the adverse effect of exposing the steam generator tubes to the risk of rupture if the RCS remains at high pressure. However, if the RCS is intentionally depressurized by the operators, or a surge line or hot leg failure occurs, the risk of a late steam generator tube rupture would be eliminated. Therefore, the benefit of cavity flooding might be much greater if it is performed in conjunction with primary system depressurization.

It is also evident from the analysis performed in Chapter 3 that a best estimate type of assessment may be misleading, especially when considerable uncertainty is involved. For the set of strategies and sequences assessed in this chapter and in the next, uncertainty is involved. This uncertainty is associated with both

operational issues and phenomenological issues. Therefore it is necessary to not only evaluate the base case (or best estimate) scenario and perform sensitivity calculations, but the uncertainty in the input variables must be propagated through the decision model. Hence an uncertainty analysis should be performed in order to assess the importance of the uncertain variables and issues.

In this chapter an influence diagram that models a sequence of three separate accident management strategies is described. As in Chapter 3, the strategies are assessed with respect to the short-term station blackout (TMLB') sequence at the Surry plant. Each of the nodes contained in the model presented in this chapter are described, including the input distributions used to represent the state-of-knowledge uncertainty associated with the probabilities and the issues modeled by those nodes. Many of the nodes described in this chapter are very similar to the corresponding nodes discussed in Chapter 3, with the primary difference being that they represent a state-of-knowledge distribution rather than a best estimate point value.

It should be pointed out that two types of uncertainty are modeled here; that due to stochastic variability in data, and that due to an insufficient state-of-knowledge. Many of the nodes represent the occurrence of events which are deterministic in nature, i.e., they will always occur or never occur, given the state of the predecessor nodes, but due to insufficient knowledge one cannot predict which. In these cases, a split fraction over the states of "always" or "never" is an adequate way to describe the state-of-knowledge about these issues. A value of 0.5 would indicate maximum uncertainty and a value of 0.0 or 1.0 would indicate absolute certainty. For the nodes in which a stochastic process is modeled, i.e., where there is a probability for the occurrence of an event or state, the state-of-knowledge is described by a continuous distribution over a range of possible probabilities, or, as in the case of the recovery of ac power, over the values of the parameters in the distribution that models the stochastic variability.

6.2 Influence Diagram Model

The influence diagram described in this section, and shown in Figure 6.1, models a combination of three separate accident management strategies:

* flooding the reactor cavity at the time of core uncovery in order to cool the reactor vessel lower head and prevent or delay vessel failure,
* depressurizing the primary system in order to mitigate direct containment heating of the containment, and
* initiating feed-and-bleed cooling of the core, if ac power is recovered in order to arrest core damage and prevent vessel failure.

The cavity flooding strategy and its associated benefits and adverse effects are described in Chapter 3.

For the depressurization strategy it is assumed that the operators have the ability to open the power operated relief valves (PORVs) during a station blackout. The feasibility of this strategy is discussed in more detail later in this section. The benefits of this strategy include the prevention of a high pressure melt ejection (HPME) and associated direct containment heating (DCH), as well as the fact that depressurization would make more systems available to the operators for vessel injection should ac power be recovered, and would minimize the likelihood of a steam generator tube rupture. However, this strategy has the adverse effects of increasing the likelihood of an in-vessel steam explosion. If this explosion is energetic enough, it could lead to vessel failure and possibly even a-mode failure of the containment, and additional hydrogen generation.

In order for the operators to be able to inject water into the vessel, ac power must be recovered first. If ac power is recovered and feed-and-bleed cooling of the core is initiated, core damage could be arrested and vessel failure prevented. This strategy also has the adverse effect of additional hydrogen generation which could pose a threat to the containment later in the accident. Also, there is some uncertainty as to whether or not the core would be in a coolable configuration, especially if water is injected late in the melt progression.

6.2.1 Decision Nodes

Since both the cavity flooding strategy and the depressurization strategy would be initiated at approximately the time of core uncovery, these two strategies are modeled as one decision node. This node (D1 in Figure 6.1) has four output alternatives: depressurize the primary system and initiate flooding of

the reactor cavity, depressurize only, flood only, and do nothing (recall that in Chapter 3, the decision nodes had two alternatives, to flood or do nothing).

Node D2 models the decision of whether or not to initiate feed-and-bleed cooling of the core if and when ac power is recovered. This node has two output alternatives: initiate feed-and-bleed cooling when ac power is recovered or do nothing. Informational arcs toward node D2 in Fig. 6.1 denotes that the decision maker knows the outcome of node R (recovery of ac power in time) when decision node D2 is made, and decision D1 when decision D2 is made ("no forgetting arc").

Since there are two decision nodes, one with four alternatives and one with two, there are overall eight decision alternatives in this model. The diagram can be evaluated for each of the eight alternatives, including uncertainty propagation and analysis. The optimum set of alternatives can be found and the uncertainty associated with each combination of strategies can be characterized.

6.2.2 Chance Nodes

Many of the chance nodes shown in Figure 6.1 are similar to those in the influence diagram described in Chapter 3. However, in the influence diagram described in this chapter, the chance node probabilities are modeled as distributions representing uncertainty rather than point values.

Nodes HQ1 and HQ2

These nodes model whether or not the strategies are successfully implemented. Node HQ1 is associated with both cavity flooding and depressurization, and depends on the output state of the decision node D1. Node HQ2 is associated with feed-and-bleed and depends on the decision node D2, as well as the chance node R, which models the timing of AC power recovery.

The assessment of the human error rates associated with the three strategies is limited in scope because the current Surry emergency operating procedures

(EOPs) do not contain specific instructions associated with the severe accident management strategies considered in this paper. This lack of specific procedures prevents a detailed human reliability analysis. In order to assess the likelihood that the strategies are successfully implemented, it is assumed that procedures exist in the Surry EOPs for these strategies, and assumptions are made regarding the actions required by the operators in order to successfully implement them.

The accident sequence evaluation program (ASEP) HRA procedure [37], a shortened version of THERP [11], was used to perform the HRA for the important operator tasks associated with these strategies. This method considers a task as two activities: diagnosis and action. Diagnosis refers to the detection and recognition of an abnormal event and includes interpretation and decision making. Action refers to performance of the activities indicated by written or memorized procedures. Both definitions are based on the THERP method.

For the depressurization strategy, Reference [38] provides human error probabilities (HEPs) quantified via the ASEP procedure, assuming available times for diagnosis of 5, 10 and 20 minutes. In this report, it is assumed that the procedures will instruct the operators to initiate depressurization when the core exit thermocouples (CETCs) read a temperature in excess of 922 K (the "late" depressurization strategy described in Reference [38]), and that cautions are provided sufficiently early in the procedures so that the operators would be prepared to initiate depressurization as soon as the CETCs read the high temperature setpoint. Thus, 20 minutes is used for the available time for diagnosis in this report.

For the cavity flooding strategy, it is assumed that multiple ex-control room actions would be required for successful initiation. Furthermore, since about 45 minutes are required to fill the cavity at a flow rate of 76 Kg/s (2000 gpm), it is assumed that the time available for diagnosis is 10 minutes to allow enough time to perform the required ex-control room actions, which results in a total of 55 minutes. For the feed-and-bleed strategy, the time available for diagnosis depends on when AC power is recovered. However, to keep things simple, a nominal time of 20 minutes is assumed for the available time for diagnosis.

As mentioned earlier, decision making is included in the diagnosis part of the ASEP procedure. The HEPs calculated by this procedure usually ignore the possibility that the operators would hesitate to initiate the action if there were some economic consequences associated with it, and recovery by some other means was still possible. During the Davis-Besse loss of feedwater accident [39] the shift supervisor hesitated to initiate primary system feed-and-bleed, even though instructed by the EOPs to do so. Since primary system feed-and-bleed is a messy operation that would cost several million dollars to clean up, and since recovery of feedwater was imminent, the supervisor decided to wait.

For the depressurization strategy, if the "early" depressurization strategy described in [38] was being considered, it is possible that the operators would decide not to initiate depressurization at the time of steam generator dryout, and wait for restoration of AC power or feedwater instead. However, for the "late" depressurization strategy, when the CETCs reach the high temperature setpoint, core damage is imminent and there is less time available for the RCS to depressurize, so it is much more likely that the operators would decide to initiate depressurization.

Also, the feed-and-bleed strategy considered in this report is applied to a much different situation than the one the operators faced in the Davis-Besse accident. Here, they would have to decide to initiate feed-and-bleed after core damage had already started. In this situation, since the plant has already suffered a great deal of damage, the additional damage caused by bleeding RCS water into the containment would be negligible, and thus it is unlikely that the operators would hesitate.

It should be pointed out that the distributions are conditional on whether or not the operators are instructed to implement the strategies. For Node HQ2 there is only one state-of-knowledge distribution since there are only two output states of node D2, and one state is the case in which the operators are instructed to "do nothing", i.e., they are not instructed to implement feed-and-bleed cooling of the primary system. However, for Node HQ1 there are three distributions, one for each of the combinations of the two strategies modeled by node D1, i.e. flood the cavity, depressurize the primary system, or both. In this analysis the equipment is assumed to always function properly. The parameters for the distributions

associated with those elementary strategies are produced from Figure 8-1 and Table 8-5 of Reference [37], and are shown in Tables 6.1 and 6.2.

Node R

As described in Chapter 3, Node R represents whether or not ac power is recovered before vessel failure. There is both stochastic variability and state-of-knowledge uncertainty associated with the timing of ac power recovery. The time to recover ac power can be modeled as a random variable with a probability density $f(t/\Theta)$, where Θ are parameters which are themselves unknown and whose uncertainty can be described by a state-of-knowledge distribution $\pi(\Theta)$. If actual loss off off-site power events are used as evidence, $\pi(\Theta)$ can be obtained via Bayesian updating, as shown in [12].

For simplicity, the time to recover ac power is modeled in this analysis as an exponential distribution, i.e.

$$f_{RAC}(t) = \lambda e^{-\lambda t} \tag{6.1}$$

where $1/\lambda$ is the mean time to recover off-site power. The distribution representing the uncertainty in λ, $\pi(\lambda)$, is obtained via Bayes' Theorem, i.e.

$$\pi(\lambda) = k\pi_0(\lambda)\lambda^n e^{-\lambda\Sigma i t i} \tag{6.2}$$

where $\pi_0(\lambda)$ is the prior distribution of λ, n is the number of loss of off-site power events, t_i is the time at which ac power is recovered for the ith event, and k is the normalization constant. Reference [12] provides the time to recovery of AC power of 63 recorded incidents of loss of off-site power at nuclear power plants. If the prior distribution of λ is taken to be non-informative, i.e. $\pi_0(\lambda) = 1$, then the posterior distribution of λ is

$$\pi(\lambda) = (1.43E33)\lambda^{63}e^{-76.22\lambda}\,. \tag{6.3}$$

Therefore, given λ and the time of core uncovery and vessel failure, the probability of AC power recovery before vessel failure, given that it was not recovered before core uncovery, is

$$P(R/\lambda) = (e^{-\lambda T_{cu}} - e^{-\lambda T_{vf}})/(e^{-\lambda T_{cu}}) \qquad (6.4)$$

where T_{cu} is the time of core uncovery and T_{vf} is the time of vessel failure. These times are themselves uncertain, but in keeping with previous PRAs and other analyses, a best estimate is used. These estimates are discused in Chapter 3.

Node CDA

As described in Chapter 3, Node CDA represents whether or not core damage is arrested given that feed-and-bleed cooling of the core is initiated before vessel failure. Even if ac power is recovered on time and primary system feed-and-bleed is successfully initiated, there is still a chance that the in-vessel debris will not be in a coolable configuration and the vessel will fail anyway. In [8], the state-of-knowledge uncertainty in the probability that the core is in a coolable configuration is somewhat arbitrarily modeled as a uniform distribution from 0.8 to 1.0. Due to a lack of information, these values are used in this analysis and the distribution is given in Table 6.3.

Node RP

Chance Node RP represents the RCS pressure when the vessel fails. This node has two output states: high pressure (> 200 psia) or low pressure (< 200 psia) and depends on whether or not the RCS is depressurized by the operators (node D1, nodes HQ1 and R), whether or not a hot leg or surge line failure has occurred (node HSF) and whether or not a steam generator tube rupture has occurred (node SGTR). If a hot leg or surge line failure occurs, or if the operators depressurize the RCS, the RCS pressure will be low when the vessel fails. However, there is some uncertainty as to the pressure at vessel failure if an SGTR occurs. Therefore, since this is purely a state-of-knowledge uncertainty, it is

expresed as a split fraction over the states of high and low pressure. These split fractions are given in Table 6.4.

Node HSF

As described in Chapter 3, Node HSF represents whether or not a temperature induced hot leg or surge line failure occurs during the initial stages of core degredation. It depends on whether or not the RCS is depressurized by the operators (node D1, nodes HQ1), and whether or not an SGTR occurs (node SGTR) before hot leg or surge line failure.

If the RCS is depressurized by the operators, the probability of a hot leg or surge line failure during the early stages of core degredation is 0.0, although it could fail during the later stages when the RCS pressure is low anyway. If a steam generator tube rupture only occurs, the probability of a hot leg or surge line failure subsequently occurring is uncertain. The state-of-knowledge distribution for the probability is shown in Table 6.5. This distribution can be found in [13] and was obtained via expert opinion. Note that there is a finite probability that this is a deterministic process, i.e., the probability of a surge line or hot leg failure may be 0.0 or 1.0. If there is no intentional depressurization of the RCS, and no occurrence of an SGTR, the probability of a hot leg or surge line failure occurring is again uncertain. The state-of-knowledge distribution for the probability in this case is shown in Table 6.5 and can also be found in [13].

Node SGTR

As in Chapter 3, this node represents the occurrence of a temperature induced steam generator tube rupture early in the progression of core damage. This node also depends on whether or not the RCS is intentionally depressurized by the operators (node D1, nodes HQ1 and R). If so, the probability of an SGTR is 0.0. Otherwise, this probability is uncertain and its state-of-knowlege distribution is shown in Table 6.6, and can be found in [13]. Note that this distribution, and the one for node HSF, were generated by expert opinion before recent studies on intentional and unintentional depressurization [38,40], and do not reflect that research.

Node VB

As in Chapter 3, this node represents the mode of vessel failure. There are three output states of this node: penetration failure (HPME), bottom head failure or gravity pour (BH), and no vessel failure. These modes are described in Chapter 3. This node depends on whether or not core damage is arrested (node CDA), whether or not flooding of the reactor cavity has occurred (node D1, nodes HQ1 and R), and the RCS pressure when the vessel fails (node RP).

The mode of vessel failure is uncertain for all of the cases. Since the uncertainty is purely state-of-knowledge, it is expressed as a split fraction (a discrete probability distribution between 0 and 1) over the possible modes of vessel failure for all cases. These split fractions can be found in Ref. [8], except for the cases where the reactor cavity has been flooded.

As discussed in Chapter 3, there are two ways in which the reactor cavity can be flooded, either by operation of the containment sprays if AC power is recovered early, or via intentional flooding using an alternative source of water by the operators. Since it is possible that vessel failure can be prevented if the water level in the cavity reaches the top of the lower head before significant relocation of core debris, the probability of no vessel failure in this case is the product of the probability that the cavity is flooded up to the level of the lower head before the core slumps, and the probability that vessel failure is prevented given the presence of water.

Since the containment sprays are actuated automatically if AC power is recovered, and since it takes about one hour for the cavity to completely fill due to the sprays, the probability that the cavity will be filled due to the operation of the containment sprays is

$$P1 = [F_{RAC}(T_{cs} - 1.0) - F_{RAC}(T_{cu})] / F_{RAC}(T_{cu}) \qquad (6.5)$$

where $F_{RAC}(t)$ is the cumulative distribution for the recovery of off-site power (given l) and T_{cs} is the time to core slump (in hours). This is discussed in more detail in Chapter 3. The probability that the cavity is filled with water due to the

implementation of the cavity flooding strategy by the operators is contained in the probability of Node HQ1.

As discussed in Chapter 3 and Appendix I, it is uncertain as to whether or not the presence of water around the vessel lower head will ultimately prevent vessel failure. Calculations described in Appendix I and in Reference [7] show that the vessel will most likely not melt through. However, it is likely that the lower head will still fail due to excessive thermal stress or thermal creep. The probability of no vessel failure, given the presence of water around the lower head, is assumed to be 0.1 for both the high and low RCS pressure cases. The effect of changes in the state-of-knowledge of this issue will be investigated in Chapter 7 of this report. Table 6.7 summaries the conditional probabilites associated with node VB. Note that vessel failure due to the possibility of an in-vessel steam explosion which will lead to a-mode failure of the containment (node AM) is also contained in Table 6.7.

Node AM

This node represents whether or not an in-vessel steam explosion leads to an a-mode failure of the containment. It depends on the RCS pressure (node RP) and whether or not core damage is arrested (node CDA). The split fractions for this node are shown in Table 6.8 and can be found in [8]. If core damage is arrested the probability of an a-mode failure of the containment is 0.0.

Node CFE

As in Chapter 3, this node represents the fraction of the core ejected from the vessel. The split fractions are the same as those given in Chapter 3 and are shown in Table 6.9. Node CFE has no predecessor nodes.

Node VHS

Again, as in Chapter 3, this node represents the size of the hole in the vessel when it fails. It depends on the mode of vessel failure (node VB), and has the same split fraction as those given in Chapter 3, which are shown in Table 6.10.

Node EVSE

This node represents whether or not an ex-vessel steam explosion occurs. It depends on whether or not there is water in the cavity when the vessel fails (node D1, nodes HQ1 and R), and if the vessel fails (node VB). Since this is a stochastic process, there is a probability for the occurrence of an ex-vessel steam explosion, which is highly uncertain. The state-of-knowledge distribution for this probability is taken to be a uniform distribution from the values of 0.1 to 0.9, as was done in [8]. This is somewhat arbitrary, but for lack of anything better the same is done here. The state of knowledge parameters regarding EVSE are shown in Table 6.11.

Node DCH

This is a deterministic node (a double circle) in that it strictly depends on the output of node VB. It represents the occurence of direct containment heating phenomena. If the vessel fails via a penetration at high pressure (a high pressure melt ejection), then node DCH is true, otherwise it is false.

Node ECF

This node represents the occurrence of an early containment failure (ECF). This node depends on whether or not there is direct containment heating (node DCH), whether or not an ex-vessel steam explosion occurs (node EVSE), whether or not there is an α-mode failure event (node AM), whether or not there is water in the cavity (nodes D1, HQ1, and R), the fraction of the core ejected from the vessel (node CFE) and the size of the hole in the vessel (node VHS). The split fractions for this node are the same as those used in Chapter 3, except for the addition of the case in which there is an α-mode failure of the containment (node

AM is true). In this case the probability of early containment failure is 1.0. The values for this node are presented in Table 6.12. Note that the nodes ECF, VHS and DCH have been absorbed into node ECF, as was done in Chapter 3, and so are not shown in the table.

6.2.3 Value Node.

In Chapter 3, public risk (early fatalities and latent cancer fatalities) was used as a criterion for the best estimate assessment of the cavity flooding strategy. However, there are drawbacks to this approach. If all the characteristics of accident progression that affect radioactive release, and thus risk, are considered in the assessment, the resulting influence diagram would be quite large and the value node would have many direct predecessors. It would be preferable if a criterion that only depends on a few nodes of the diagram is used.

In the assessment described in this and the following chapter, node ECF is used as the value node (it is a chance node in the influence diagram described in Chapter 3). The eight decision alternatives are evaluated with respect to the change in the conditional probability of early containment failure (ECF). This does not consider the adverse effect of a late steam generator tube rupture. In order to do that, a value model would have to be constructed that relates the impact of a steam generator tube rupture to that of early containment failure, which is outside the scope of this project. However, this will be investigated to some extent through sensitivity studies presented in Chapter 7.

THIS PAGE LEFT INTENTIONALLY BLANK

Table 6.1
Conditional probabilities for node HQ1 .

Case D1	Distribution Type	P(success)		
		mean	5%	95%
flood	lognormal	0.73	0.55	0.99
depressurize	lognormal	0.91	0.68	0.99
both	lognormal	0.67	0.0	0.98
do nothing	none	0.0	-	-

Table 6.2
Conditional probabilities for node HQ2 .

Case D2	R	Distribution Type	P(success)		
			mean	5%	95%
feed-and-bleed	yes	lognormal	0.91	0.67	0.99
feed-and-bleed	no	none	0.0	-	-
do nothing	-	none	0.0	-	-

Table 6.3
Conditional probabilities for node CDA

Case HQ1	Distribution Type	P(CDA)		
		mean	5%	95%
success	uniform	0.9	0.81	0.99
failure	none	0.0	-	-

Table 6.4
Conditional probabilities for node RP

Case					Distribution Type	RP	
D1	HQ1	HSF	R	SGTR		P(high)	P(low)
flood	-	yes	-	-	none	0.0	1.0
flood	-	no	yes	-	none	0.0	1.0
flood	-	no	no	yes	discrete	0.67	0.33
flood	-	no	no	no	none	1.0	0.0
dep.	yes	yes	-	-	none	0.0	1.0
dep.	yes	no	yes	-	none	0.0	1.0
dep.	yes	no	no	-	discrete	0.0	1.0
dep.	no	yes	-	-	none	0.0	1.0
dep.	no	no	yes	-	none	0.0	1.0
dep.	no	no	no	yes	discrete	0.67	0.33
dep.	no	no	no	no	none	1.0	0.0
both	yes	yes	-	-	none	0.0	1.0
both	yes	no	yes	-	none	0.0	1.0
both	yes	no	no	-	discrete	0.0	1.0
both	no	yes	-	-	none	0.0	1.0
both	no	no	yes	-	none	0.0	1.0
both	no	no	no	yes	discrete	0.67	0.33
both	no	no	no	no	none	1.0	0.0
do nothing	no	yes	-	-	none	0.0	1.0
do nothing	no	no	yes	-	none	0.0	1.0
do nothing	no	no	no	yes	discrete	0.67	0.33
do nothing	no	no	no	no	none	1.0	0.0

Table 6.5
Conditional probabilities for node HSF

Case			Distribution Type	P(HSF)		
D1	HQ1	SGTR		mean	5%	95%
flood	-	yes	expert opinion	0.022	0.0	0.10
flood	-	no	expert opinion	0.76	0.0	1.0
dep.	success	-	none	0.0	-	-
dep.	failure	yes	expert opinion	0.022	0.0	0.10
dep.	failure	no	expert opinion	0.76	0.0	1.0
both	success	-	none	0.0	-	-
both	failure	yes	expert opinion	0.022	0.0	0.10
both	failure	no	expert opinion	0.76	0.0	1.0
nothing	failure	yes	expert opinion	0.022	0.0	0.10
nothing	failure	no	expert opinion	0.76	0.0	1.0

Table 6.6
Conditional probabilities for node SGTR

Distribution Type	P(SGTR)		
	mean	5%	95%
expert opinion	0.014	0.0	0.093

Table 6.7
Conditional probabilities for node VB

Case						Distribution Type	VB		
D1	HQ1	AM	CDA	R	RP		HPME	BH	None
-	-	yes	-	-	-	none	0.0	0.0	1.0
-	-	no	yes	-	-	none	0.0	0.0	1.0
flood	succ.	no	no	no	high	discrete	0.45	0.45	0.1
flood	succ.	no	no	-	low	discrete	0.0	0.9	0.1
flood	fail	no	no	yes	low	discrete	0.0	0.5	0.5
flood	fail	no	no	no	high	discrete	0.8	0.2	0.0
flood	fail	no	no	no	low	none	0.0	1.0	0.0
dep.	-	no	no	yes	low	discrete	0.0	0.5	0.5
dep.	-	no	no	no	high	discrete	0.8	0.0	0.0
dep.	-	no	no	no	low	none	0.0	1.0	0.0
both	succ.	no	no	no	high	discrete	0.45	0.45	0.1
both	succ.	no	no	-	low	discrete	0.0	0.9	0.1
both	fail	no	no	yes	low	discrete	0.0	0.5	0.5
both	fail	no	no	no	high	discrete	0.8	0.2	0.0
both	fail	no	no	no	low	none	0.0	1.0	0.0
do noth	fail	no	no	yes	low	discrete	0.0	0.5	0.5
do noth	fail	no	no	no	high	discrete	0.8	0.2	0.0
do noth	fail	no	no	no	low	none	0.0	1.0	0.0

Table 6.8
Conditional probabilities for node AM

Case		Distribution Type	P(AM)
CDA	RP		
yes	-	degenerate	0.0
no	high	discrete	8.0E-4
no	low	discrete	8.0E-3

Table 6.9
Conditional probabilities for node CFE

Distribution Type	CFE		
	High	Medium	low
disctere	0.2	0.55	0.25

Table 6.10
Conditional probabilities for node VHS

Case	Distribution Type	VHS	
VB		large	small
none	irrelevant	-	-
PF	disctere	0.1	0.9
BH	none	1.0	0.0

Table 6.11
Conditional probabilities for node EVSE

Case				Distribution Type	P(EVSE)		
D1	HQ1	R	VB		mean	5%	95%
-	-	-	no	none	0.0	-	-
-	failure	yes	yes	uniform	0.5	0.14	0.86
-	failure	no	yes	none	0.0	-	-
flood	success	-	yes	uniform	0.5	0.14	0.86
dep.	success	yes	yes	uniform	0.5	0.14	0.86
dep.	success	no	yes	none	0.0	-	-
both	success	-	yes	uniform	0.5	0.14	0.86
do nothing	-	yes	yes	uniform	0.5	0.14	0.86
do nothing	-	no	yes	none	0.0	-	-

Table 6.12
Conditional probabilities for node ECF

Case						P(ECF)		
AM	D1	HQ1	R	VB	EVSE	mean	5%	95%
Yes	-	-	-	-	-	1		
No	Flood	Succeed	-	HPME	Yes	0.01	0	0
"	"	"	-	"	No	0	-	-
"	"	"	-	BH	Yes	0.01		
"	"	"	-	"	No	0		
"	"	Fail	Yes	HPME	-	-		
"	"	"	No	"	-	0.028	0	0
"	"	"	Yes	BH	Yes	0.01		
"	"	"	No	"	No	0		
"	Depressurize	Succeed	Yes	"	Yes	0.01		
"	"	"	"	"	No	0		
"	"	Fail	"	HPME	-	-		
"	"	"	No	"	-	0.028		
"	"	"	Yes	BH	Yes	0.01		
"	"	"	"	"	No	0		
"	Both	Succeed	-	HPME	Yes	0.01		
"	"	"	-	"	No	0		
"	"	"	-	BH	Yes	0.01		
"	"	"	-	"	No	0		
"	"	Fail	Yes	HPME	-	-		
"	"	"	No	"	-	0.028		
"	"	"	Yes	BH	Yes	0.01		
"	"	"	"	"	No	0		
"	Nothing	"	Yes	HPME	-	-		
"	"	"	No	"	-	0.028		
"	"	"	Yes	BH	Yes	0.01		
"	"	"	"	"	No	0		

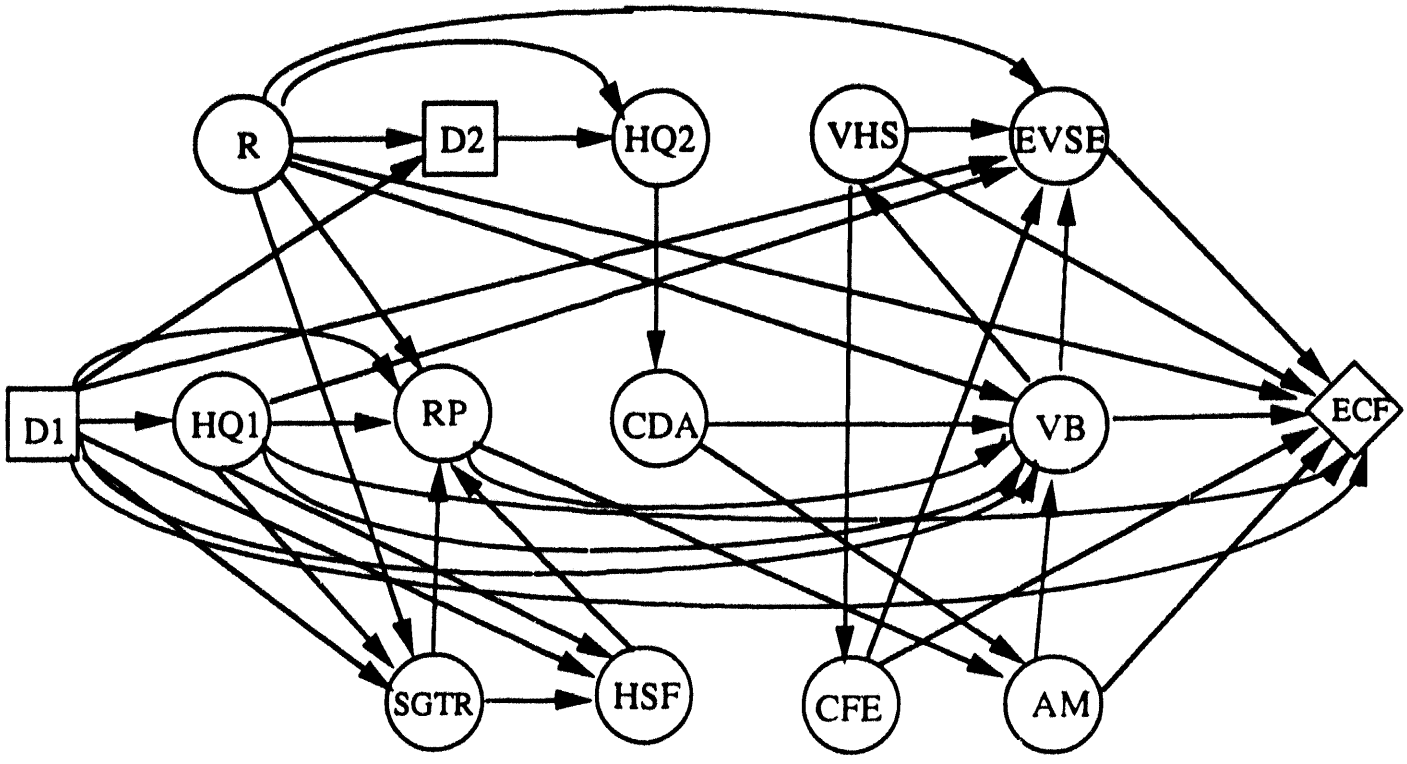

AM: Alpha mode failure
VB: Vessel breach
CDA: Core damage arrested
CFE: Core fraction ejected
DCH: Direct containment heating
D1: {Flood, Depressurize, Both, Do nothing}
D2: {Feed-and-bleed, Do nothing}
ECF: Early containment failure

EVSE: Ex-vessel steam explosion
HQ: Human reliability and hardware avaialbility
HSF: Hot leg or surge line failure
R: AC power recovered before VB
RP: RCS pressure at VB
SGTR: Steam generator tube rupture
VHS: Vessel hole size

Figure 6.1. Influence diagram for PWR severe accident management strategies with two sequential decision nodes.

7. UNCERTAINTY AND SENSITIVITY ANALYSIS FOR PWR STRATEGIES WITH MULTIPLE DECISIONS

7.1 Introduction

In the previous chapter, and in Chapter 3, a decision analysis framework is described for assessing severe accident management strategies. Given a set of possible accident management alternatives, a decision model is constructed that allows the analyst to rank the alternatives, and (hopefully) to find the preferred alternative based on a value criterion and assumptions regarding the inputs to the model. In the previous chapter a set of eight accident management alternatives are described with respect to a set of initial conditions (the TMLB' accident sequence or plant damage state). A value function is constructed that relates a numerical criterion to the eight decision alternatives through the chance nodes of the decision model, which are intended to represent the possible ways the accident sequence might progress, given the decision alternative and initial conditions. The occurrence of various events and the values of parameters modeled by the chance nodes may be highly uncertain. How this uncertainty is characterized and propagated through the decision model depends on the type of uncertainty being considered.

Results of the following calculations are also described in this Chapter:

1) A best-estimate assessment for the proposed strategies is performed. The decision alternatives (strategies) are ranked with respect to the conditional frequency of early containment failure (called the value).

2) Given the preferred best estimate decision alternative, a sensitivity analysis is performed. The input variables are then ranked with respect to the effect on the value.

3) The sensitivity of the ranking regarding the decision alternatives to changes in the input variables is presented.

4) The uncertainty distributions are propagated through the influence diagram and the decision alternatives ranked.

5) The sensitivity of the uncertainty in the value to the degree of the uncertainty in the input variables is investigated. Given the preferred decision alternative, the input variables are ranked with respect to the reduction in the variance in the output distribution of the Value.

7.2 Types of Uncertainty

As discussed in Chapter 6.1, two basic types of uncertainty are considered here: that due to stochastic variability and that due to inadequate knowledge or data (state-of-knowledge uncertainty). Some of the chance nodes in the influence diagrams describing severe accident management represent phenomenological events that are deterministic in nature, i.e., they will always occur or never occur given the states of the predecessor nodes; we just cannot predict which. The uncertainty associated with such nodes is purely state-of-knowledge, and the distribution that characterizes that uncertainty is a split fraction over the two possible states, namely the event will always occur (with a probability of 1.0) or never occur (with a probability of 0.0).

A few nodes, however, represent phenomenological events that are stochastic in nature, i.e. they will occur with a rate of occurrence λ, but, due to inadequate data, the value of λ is uncertain. In this case the distribution that describes the state-of-knowledge uncertainty is a continuous probability density function (pdf) over the possible values of the rate of occurrence of the event. A special case of this is the recovery of AC power, represented by node R. In this case the event in question is whether or not AC power is recovered by a certain specified time, and the stochastic variability associated with the occurrence of this event is described by a distribution over time, which becomes a rate when the time by which AC power is recovered is specified. Due to limited data, the shape of the distribution for the recovery of AC power is uncertain, and this state-of-knowledge uncertainty is characterized by a distribution over the values of parameters contained in the expression for the distribution that describes the stochastic variability.

Sometimes the distinction between a deterministic event and a stochastic event is not that clear cut, and we are uncertain whether a certain event is purely deterministic or if there is some stochastic variability associated with it. An example of this is the occurrence of a hot leg or surge line failure. In the NUREG-1150 expert opinion assessment of this event, some of the experts thought that it was deterministic, and others thought otherwise. The aggregate distribution that characterizes the uncertainty associated with this event reflects this, in that there is a finite probability that it would never occur or always occur.

7.3 Analysis

The evaluation of the strategies modeled by the influence diagram described in the previous chapter involves four different types of analysis, each of which provides different information. The first is a best estimate assessment, which involves evaluating the influence diagram with the best estimate values of the variables for inputs, as was done in Chapter 3. For distributed variables, the best estimate is their mean values. This analysis results in a ranking of the decision alternatives with respect to the expected value of the output of the decision model, and the preferred decision alternative according to this criterion can be identified.

The second type of analysis, sensitivity analysis, investigates the effect of changes in input variables on output predictions. Two types of sensitivity analysis are conducted. A partial derivative measure sensitivity analysis determines the effect the choice of the values of the input variables has on the value of the output, given a (preffered) decision alternative. This is accomplished by calculating the partial derivative of the output with respect to each of the input variables, about the base case. If the model, in this case the influence diagram, can be represented as a function, f, with n uncertain inputs $x_1,.. ,x_n$, i.e.

$$y = f(x_1,...,x_n), \tag{7.1}$$

and if $x^0 = (x_1^0,...,x_n^0)$ represents the base case, or best estimate case, then the partial derivative sensitivity measures are

$$|\partial y/\partial x_1|_{x0},\ldots,|\partial y/\partial x_n|_{x0}. \qquad (7.2)$$

These sensitivities represent the slopes of the tangents to the response surface at the best estimate values. This is a local approach in that it considers the behavior of the function only in the vicinity of the best estimate values.

The second type of sensitivity analysis, a nominal range sensitivity analysis, involves varying each input variable in turn, while the rest of the variables remain at the best estimate or expected values, in order to see how the variation in the input affects the variation in the output. Each variable is set at either extreme of its input distribution, e.g., at either the 95% and 5% values for stochastic variables and at the extremes of a reasonable range for the split fractions for the deterministic events. Since the split fractions represent our degree of belief about whether or not an event will occur, the concept of confidence intervals for these variables is meaningless. The influence diagram is evaluated for each of these cases, and the most important variables in terms of their impact on the output, in this case the conditional probability of early containment failure, can be found. In this manner, the variables for which the choice of values actually changes which decision alternative is preferred, can be identified. This is more than a local measure because it evaluates the model for extreme values of each input variable, but it is less than global because it holds all the others at their nominal values.

Given the two or three most important variables as determined by the sensitivity analysis, a policy region analysis can be performed. This shows for the range of values of the important variables which decision alternative is preferred over the rest. This involves simultaneously varying the most important variables over their entire range. The result for a two-way policy region analysis (two variables are considered) is a two dimensional space. For every point in that space the preferred alternative can be identified. This was done in Chapter 3 and is shown in Figures 3.24 and 3.25.

The third type of analysis involves the propagation of uncertainty. Here the distributions of the input variables are propagated through the decision model, and the result is a distribution over the values of the output. Since there are eight decision alternatives in the case studied here, this technique results in eight output

distributions, one for each alternative. There are several methods developed for the propagation of uncertainty; the method employed here is Monte Carlo Simulation. How each variable is sampled is determined by what kind of uncertainty is associated with it. Deterministic variables are sampled zero-one. This means that every sample observation contains either the value of 0.0 or the value of 1.0 for the occurrence probability of the event modeled by the node in question, and what fraction of the observations contain the value of 1.0 is determined by the split fraction that characterizes the state-of-knowledge uncertainty about the occurrence of the event in question. For nodes that model stochastic events, the continuous distribution of the occurrence frequency of the event in question is sampled. Every sample observation then results in a point value of the event occurrence frequency. The influence diagram is evaluated for every member of the sample, and results in a point value for the conditional frequency of early containment failure for each decision alternative, for each member. The sample set of these probabilities can be shown as a sample distribution (one for each decision alternative), and can be ranked with respect to the mean value of the output distribution (or the median) and the variance of the output distributions.

The fourth type of analysis, uncertainty importance analysis, determines the effect of changes in the input variable distributions on the output distribution. Here, the uncertainty in each of the uncertain variables is reduced to zero, one at a time , and the remaining distributions are propagated through the influence diagram. For each variable being studied, the expected value is used as the input distribution rather than the original state-of-knowledge distribution. For stochastic variables the expected value is the mean of the continuous pdf. For deterministic events, either a probability of 0.0 or 1.0 is used as the zero uncertainty input, whichever is more likely, according to the split fraction that expresses our state-of-knowledge uncertainty. Given a decision alternative, therefore, the uncertain variables can be ranked according to the reduction in the variance of the output distribution, when the uncertainty in those variables is removed.

7.4 Base Case Results and Sensitivity Analysis

The base case consists of the best estimate values for the rates of occurrence of the events modeled by the nodes of the influence diagram described in Section III. As mentioned earlier, the best estimate values are the expected values of the uncertainty distributions, and they are shown in Table 7.1. The distributions are discussed in Chapter 6. The influence diagram shown in Figure 6.1 was evaluated using these values, as described in Chapter 5, and the results are shown in Table 7.2, for each of the eight decision alternatives. It can be seen that the preferred decision alternative is A3, depressurize the primary system and initiate feed-and-bleed cooling of the core, if and when AC power is recovered. The next best alternative is A1, flood the reactor cavity and feed-and-bleed, and so on.

An important point to note is the fact that cavity flooding and primary system depressurization are equally effective in preventing early containment failure due to DCH, given that the strategies are successfully initiated. However, depressurization is preferred over cavity flooding in the base case because the depresurization strategy has a higher probability of being successfully initiated and cavity flooding has the drawback of possible early containment failure due to an ex-vessel steam explosion. They are both preferred over A5 (initiate both cavity flooding and depressurization, along with feed-and-bleed) because instructing the operators to do both at roughly the same time decreases the frequency that either will be successfully initiated, and there is no benefit gained in terms of preventing early containment failure.

The uncertain variables were ranked according to the partial derivative measure of sensitivity described above, for the two preferred decision alternatives: A1 (flood and feed-and-bleed) and A3 (depressurize and feed-and-bleed). The rankings are shown in Figures 7.1 and 7.2. The most important variables for decision alternative A3 are: X9 (the probability of an α-mode failure of the containment given low RCS pressure) and to a much lesser extent, X16 (the probability of early containment failure due to an ex-vessel steam explosion). The most important variables for decision alternative A1 are X9, X16 and X8 (the α-mode failure probability at high RCS pressure).

It can be seen from Figures 7.1 and 7.2 that X9 is by far the most important in terms of its effect on the expected value of the frequency of early containment failure. Furthermore, it appears that the variables related to the probability of early containment failure have the most impact on the value of the output (given a decision alternative).

For the second type of sensitivity analysis (nominal range sensitivity analysis), in order to identify which variables are important in terms of changing the preferred decision alternative, all nineteen of the uncertain variables were varied over their plausible ranges. The uncertain variables are the same as those shown in Table 7.1, and the results of the sensitivity analysis are shown in Figures 7.3 - 7.21. In these figures, the conditional frequency of early containment failure for each decision alternative is shown as a function of the value of the uncertain variable being studied. For most of the uncertain variables, the relative ranking of the decision alternatives does not change. The variables that are important in terms of the decision alternative rankings, according to Figures 7.3 - 7.21, are: X3 (the occurrence of a hot leg or surge line failure given no SGTR), X7 (the failure of vessel given water in the cavity, low RCS pressure and no core damage arrest), X16 (early containment failure due to ex-vessel steam explosion), X17 (early containment failure due to direct containment heating given a high pressure melt ejection), X18 (high pressure melt ejection given a dry cavity and high RCS pressure at vessel failure) and X19 (the RCS pressure is low at vessel failure given that RCS depressurization is initiated by the operators). All of these variables actually change the preferred decision alternative, depending on the value of the uncertain variable being considered.

In Figure 7.5 it can be seen that if the rate of occurrence of a hot leg or surge line failure (X3) is between 0.0 and about 0.2, the preferred decision alternative is A1 (flood and feed-and-bleed only), and if it is greater than 0.2, the preferred decision alternative is A3 (depressurize and feed-and-bleed only). All three of the preferred decision alternatives include feed-and bleed cooling of the core, i.e. it is always better to feed-and-bleed, regardless of what other strategies are initiated, and regardless of the value of X3.

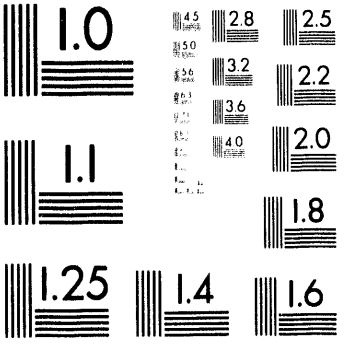
1.0
1.1
1.25
1.4
1.6
1.8
2.0
2.2
2.5
2.8
3.2
3.6
4.0
4.5
5.0
5.6
6.3

3 of 5

To understand the results of this sensitivity study, consider the following. The conditional frequency of early containment failure, given either A1 or A3 and failure of whichever strategy is initiated, is the same, regardless of the decision alternative or the value of X3. Also, if depressurization (A3) is initiated and is successful, the value of X3 is irrelevant. Therefore, the question of whether or not A1 is preferred over A3 is driven by how the value of X3 affects the conditional frequency of ECF, given decision alternative A1 and successful flooding of the reactor cavity. In this case, if the hot leg or surge line fails, the conditional frequency of ECF is 6.1E-3, which is higher than the conditional frequency of ECF given A3 and successful depressurization (4.9E-3). However, given A1 and successful flooding without the occurrence of a hot leg or surge line failure, the conditional frequency of ECF is 2.6E-3, which is lower than that for A1 and successful depressurization. Therefore, if the rate of HSF (X3) is high enough, A3 becomes preferred over A1. If there is a hot leg or surge line failure and AC power is recovered, A1 and A3 are equivalent. However, if AC power is not recovered, depressurization (which in this case is equivalent to doing nothing) is preferred, because of the adverse effect of a possible ex-vessel steam explosion if the cavity is flooded. If a hot leg or surge line failure does not occur, and AC power is not recovered, A1 becomes preferred because of the adverse effect of a possible α-mode failure of the containment for A3.

In Figure 7.9, it can be seen that the decision alternatives that include the depressurization of the primary system are affected by the values of X7 (vessel failure given water in the cavity, low RCS pressure and no core damage arrest). For values of X7 less than 0.9, A3 (depressurize the RCS) is the preferred decision alternative, while for values of X7 greater than 0.9 A1 (flood the reactor cavity) is the preferred decision alternative. This is because at high values of X7, the benefit of preventing vessel failure (and thus early containment failure) if the cavity is flooded outweighs the adverse effect of a possible ex-vessel steam explosion.

In Figure 7.18, it can be seen that the decision alternatives are affected by the values of X16 (early containment failure due to an ex-vessel steam explosion). For values of X16 greater than 0.002, A3 is the preferred decision alternative, and for values of X16 less than 0.002 A1 is preferred. This is because the adverse effect of possible early containment failure due to an ex-vessel steam

explosion outweighs the benefit of possibly preventing vessel failure if the cavity is flooded.

Figure 7.19 shows that for values of X17 (early containment failure due to DCH) of less than about 0.008, decision alternative A7 (feed-and-bleed only) is preferred, for values of X17 greater than 0.008, decision alternative A3 (depressurize and feed-and-bleed only) is preferred. At values of X17 below 0.008 depressurization in the absence of flooding becomes detrimental because the benefit gained by preventing DCH is outweighed by increasing the likelihood of an a-mode failure of the containment. The sensitivity results for X18 (high pressure melt ejection given that the cavity is not completely flooded and the RCS pressure is high) are similar, for similar reasons.

Figure 7.21 shows that for values of X19 (the probability that the RCS does not completely depressurize given that the operators initiate depressurization) of less than about 0.16, A3 is the preferred decision alternative. It is interesting to note that there is a small range of X19 (0.16 - 0.25) where A1 is preferred, but above 0.25 A5 (initiate all three strategies) is the preferred decision alternative. This is because, for high values of X19, depresssurization actually increases the chance that the RCS will be at high pressure when the vessel fails, since depressurization precludes an early failure of the hot leg or surge line. Since DCH is assumed to be impossible if the cavity is completely full of water, this is a beneficial effect from the viewpoint of preventing an a-mode failure of the containment.

Figure 7.22 shows the results of a policy region analysis where the variables X16 (early containment failure due to an ex-vessel steam explosion) and X9 (a-mode failure given low RCS pressure) were simultaneously varied. It can be seen from the figure that as the probability of an a-mode failure (given low RCS pressure) is increased, at some point decision alternative A1 becomes preferred over decision alternative A3, and the point at which that happens depends on the probability of early containment failure due to an ex-vessel steam explosion. In other words, Figure 23 shows how the competing adverse effects related to decision alternatives A1 and A3 affect which of the two alternatives are preferred.

7.5 Uncertainty Propagation

A sample size of 10000 observations was used to propagate the uncertainty in the key variables through the influence diagram. The result is eight output distributions, one for each decision alternative. The ranking of the decision alternatives with respect to the mean and the variance of the distributions is shown in Table 7.3. Decision alternative A3 (depressurize the RCS and initiate feed-and-bleed cooling) is preferred, with respect to the expected value of the conditional frequency of early containment failure. Furthermore, A3 has the smallest variance in the distribution of the conditional frequency of early containment failure. Based on these results, it must be concluded that A3 is the preferred strategy, even when uncertainty is considered.

7.6 Uncertainty Importance Analysis

Table 7.4 shows the results of the uncertainty importance analysis for the preferred decision alternative, A3. The uncertain variables are ranked according to the variance of the output distribution of the conditional frequency of early containment failure for decision alternative A3. It can be seen that variable X9 (the probability of an α-mode failure of the containment given low RCS pressure) is the most important in terms of contributing to the uncertainty in the conditional probability of early containment failure, given decision alternative A3. This can be taken to mean that reducing the uncertainty related to the credibility of the occurrence of an α-mode failure would have the most impact on reducing the uncertainty about the preference of decision alternative A3. Also, variable X16 (the probability of early containment failure given an ex-vessel steam explosion) is also important with respect to the uncertainty in the preference of A3. As mentioned above, resolution of these two issues is important to the identification of whether or not it is better to flood the reactor cavity or depressurize the RCS (in terms of preventing early containment failure).

7.7 Conclusions and Discussion

In this chapter an influence diagram is used as the basis for a framework for evaluating severe accident management strategies. This framework is very flexible in that it can be applied to any kind of accident management strategy for any sequence, including cases where multiple decisions are involved.

In a Chapter 3, public risk (early fatalities and latent cancer fatalities) was used as a criterion for the best estimate assessment of the cavity flooding strategy. However, there are drawbacks to this approach. If all the characteristics of accident progression that affect radioactive release, and thus risk, are considered in the assessment, the resulting influence diagram would be quite large and the value node would have many direct predecessors. It would be preferable if a criterion that only depends on a few nodes of the diagram is used. In this chapter the conditional frequency of early containment failure was used to assess the proposed strategies.

Three accident management strategies were evaluated with the decision model described in Chapter 6. A best-estimate analysis was conducted in order to rank the decision alternatives with respect to the expected conditional frequency of early containment failure. In addition, sensitivity studies were carried out in order to identify which variables are important in terms of changing the preferred decision alternative, and which variables have the most affect on the conditional frequency of early containment failure, given the preferred alternative. Furthermore, an uncertainty analysis was conducted in order to identify which variables are importantant in terms of their contribution to the uncertainty in the conditional frequency of early containment failure for the preferred decision alternative.

Based on the analyses described above, the following conclusions can be drawn for the PWR short term station blackout sequence.

1. It is always better to initiate feed-and-bleed cooling of the core, no matter what other strategies are initiated, and irrespective of the uncertainty in the key variables.

2. It is better to initiate depressurization of the primary system, over other strategies, based on minimizing the conditional frequency of early containment failure. This strategy is the preferred alternative with respect to both the expected value and the uncertainty about that value.

3. The ranking of the eight alternatives is sensitive to the values of several variables, most of which represent phenomenological issues about which there is considerable uncertainty. These issues include early containment failure due to direct containment heating or ex-vessel steam explosions, and hot leg or surge line failure due to natural circulation. The sensitivity studies show that further research leading to changes in the state-of-knowledge about these issues could change the ranking of the strategies.

4. The expected conditional frequency of early containment failure for the preferred strategy is very sensitive to the value of the probability of the occurrence of α-mode failure of the containment. Furthermore, the uncertainty about this issue is the dominant contibutor to the uncertainty about the conditional frequency of early containment failure for that strategy.

Table 7.1 Base case values for node probabilities.

Variable		Base Case Value
X1	P(HQ2)	0.91
X2	P(HSF/SGTR)	0.022
X3	P(HSF/no SGTR)	0.76
X4	P(SGTR)	0.014
X5	P(EVSE / BH)	0.5
X6	P(no VB / flood, high RP)	0.1
X7.	P(no VB / flood, low RP)	0.1
X8	P(AM / high RP)	0.0008
X9	P(AM / low RP)	0.008
X10	P(high RP / SGTR)	0.67
X11	P(HQ1 / flood)	0.73
X12	P(HQ1 / depressurize)	0.91
X13	P(HQ1 / both)	0.67
X14	P(CDA / HQ2)	0.9
X15	P(R)	0.51
X16	P(ECF / EVSE)	0.01
X17	P(ECF / DCH)	0.028
X18	P(HPME / no flood, high RP)	0.79
X19	P(high RP / depressurization)	0.0

Table 7.2. Best estimate probability of early containment failure for the base case.

Decision Alternative	Description	P(ECF)	Rank
A1	flood only/ feed-and-bleed	6.34E-3	2
A2	flood only / do nothing	1.15E-2	6
A3	depressurize only / feed-and-bleed	5.25E-3	1
A4	depressurize only / do nothing	1.04E-2	5
A5	flood and depressurize / feed-and-bleed	7.14E-3	4
A6	flood and depressurize / do nothing	1.23E-2	8
A7	do nothing / feed-and-bleed	6.89E-3	3
A8	do nothing / do nothing	1.20E-2	7

Table 7.3. Expected value and standard deviation of the probability of early containment failure

Decision Alternative	Expected Value of P(ECF)	Standard Deviation	Rank
A1	6.4E-3	0.056	2
A2	1.2E-2	0.095	6
A3	5.3E-3	0.053	1
A4	1.1E-2	0.093	5
A5	7.5E-3	0.065	4
A6	1.3E-2	0.100	8
A7	7.1E-3	0.058	3
A8	1.2E-2	0.092	7

Table 7.4. Uncertainty importance ranking of input variables.

Variable	Zero-Uncertainty Variance
X9	0.015
X16	0.046
X17	0.046
X15	0.048
X1	0.049
X12	0.050
X14	0.050
X3	0.051
X5	0.051
X8	0.051
X18	0.051
X2	0.052
X4	0.052
X10	0.052
X13	0.053
X11	0.053
X6	0.053
X7	0.053

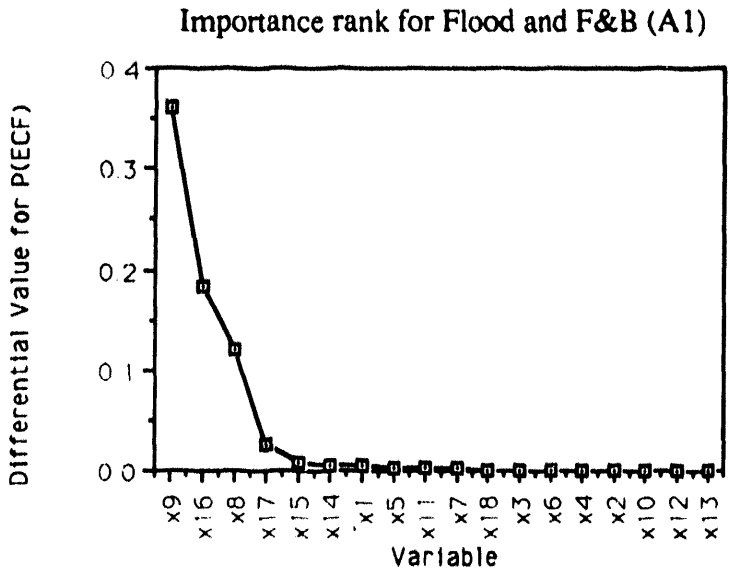

Figure 7.1. Results of importance analysis using partial derivatives for strategy A1.

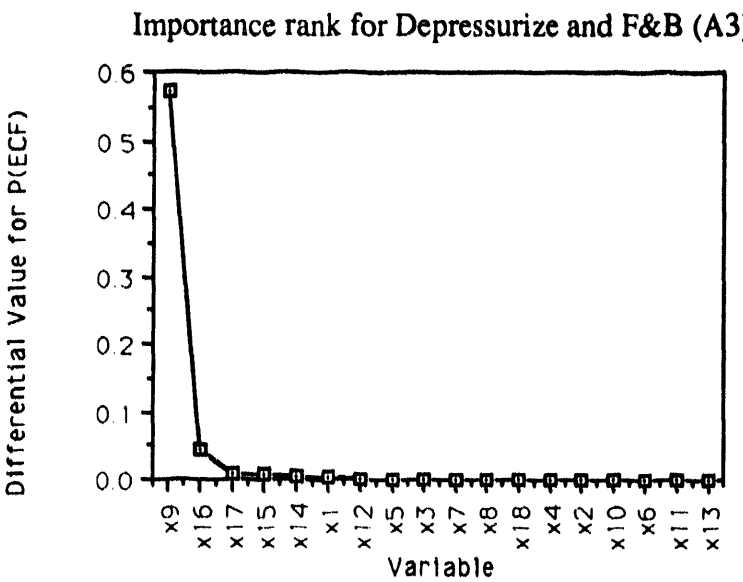

Figure 7.2. Results of importance analysis using partial derivatives for strategy A3.

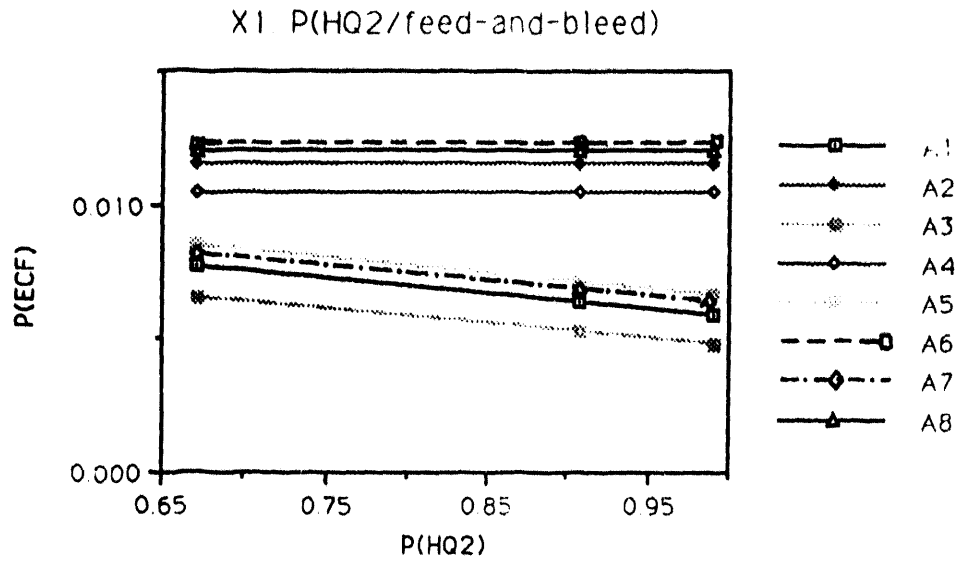

Figure 7.3. ECF sensitivity to the probability that feed-and-bleed is successfully implemented.

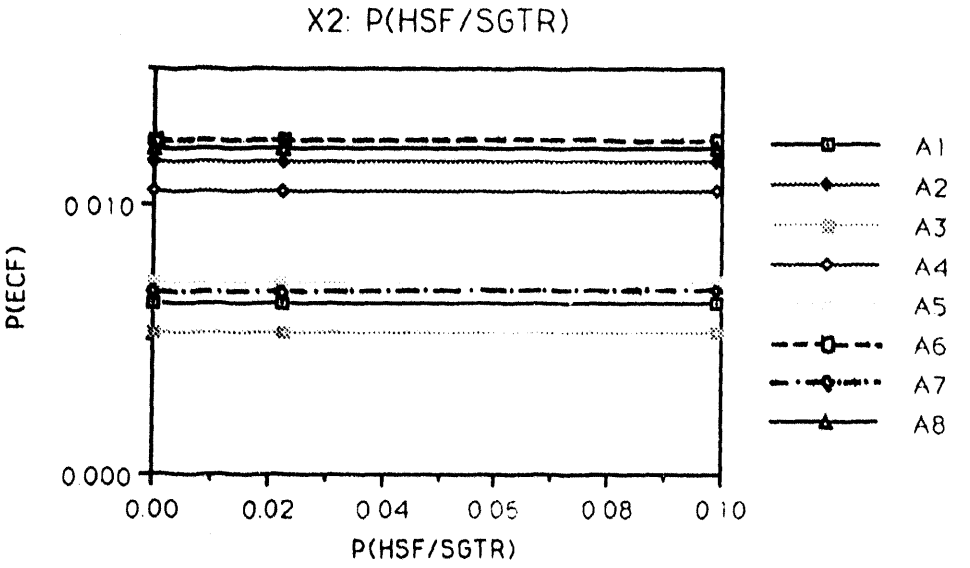

Figure 7.4. ECF sensitivity to the probability that the hot leg or surge line fails given SGTR.

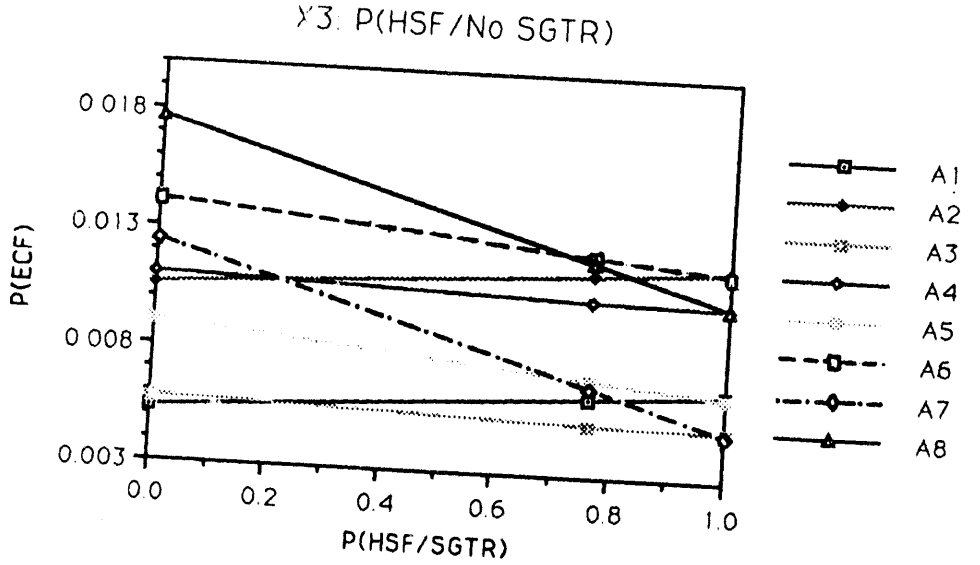

Figure 7.5. ECF sensitivity to the probability that the hot leg or surge line fails given no SGTR.

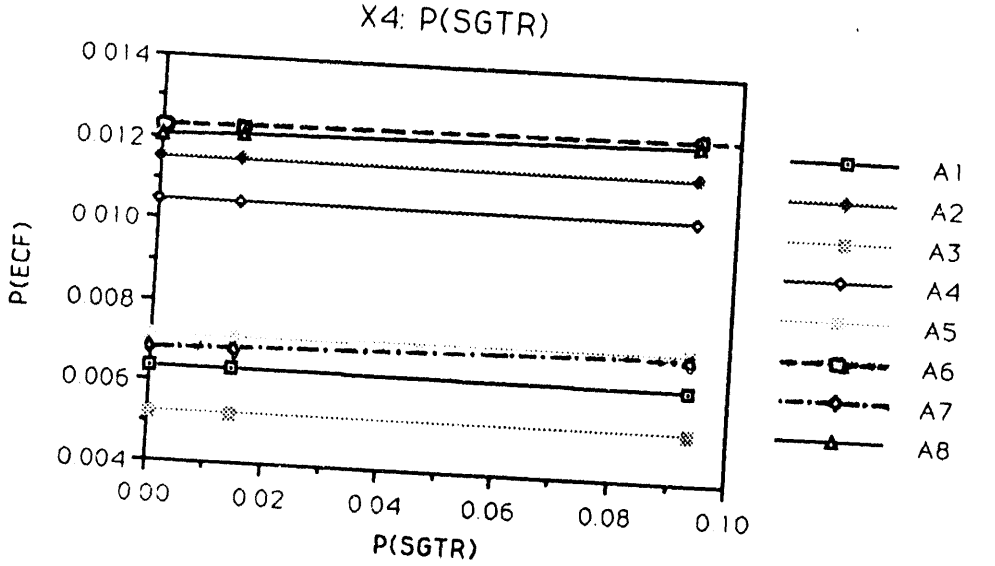

Figure 7.6. ECF sensitivity to the probability that steam generator tube ruptures occur.

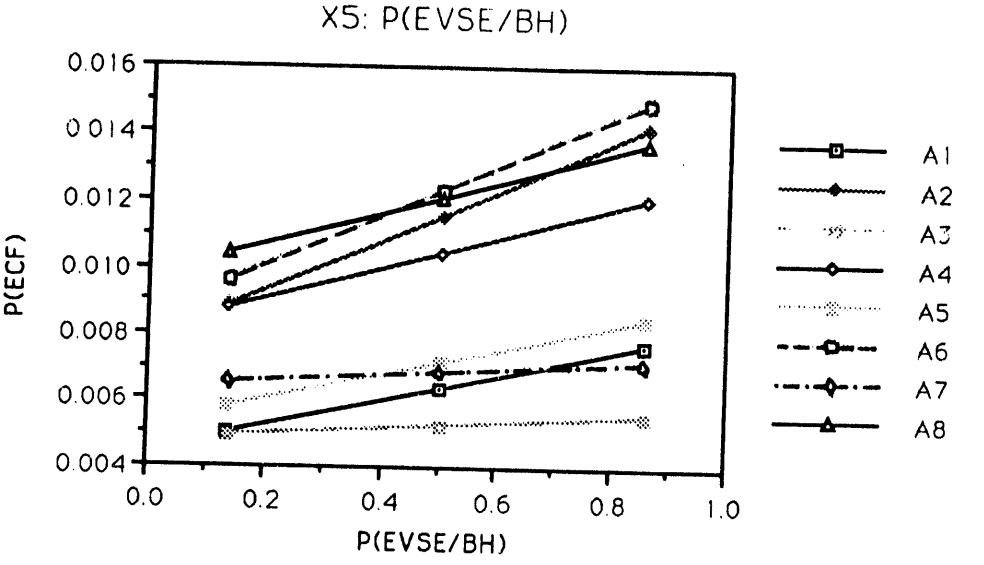

Figure 7.7. ECF sensitivity to the probability that ex-vessel steam explosion occurs given bottom head failure of vessel.

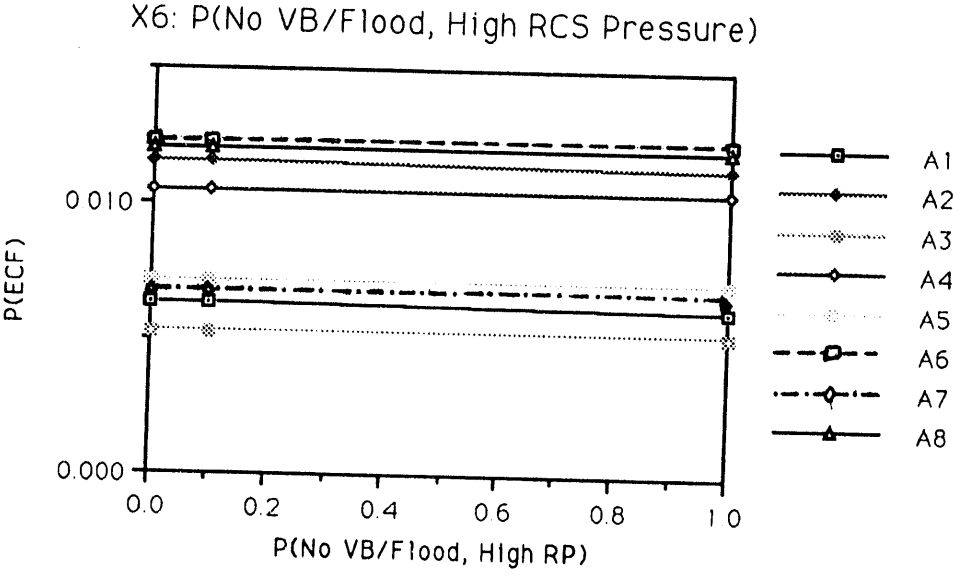

Figure7.8. ECF sensitivity to the probability that no vessel breach occurs given water in the cavity and high RCS pressure.

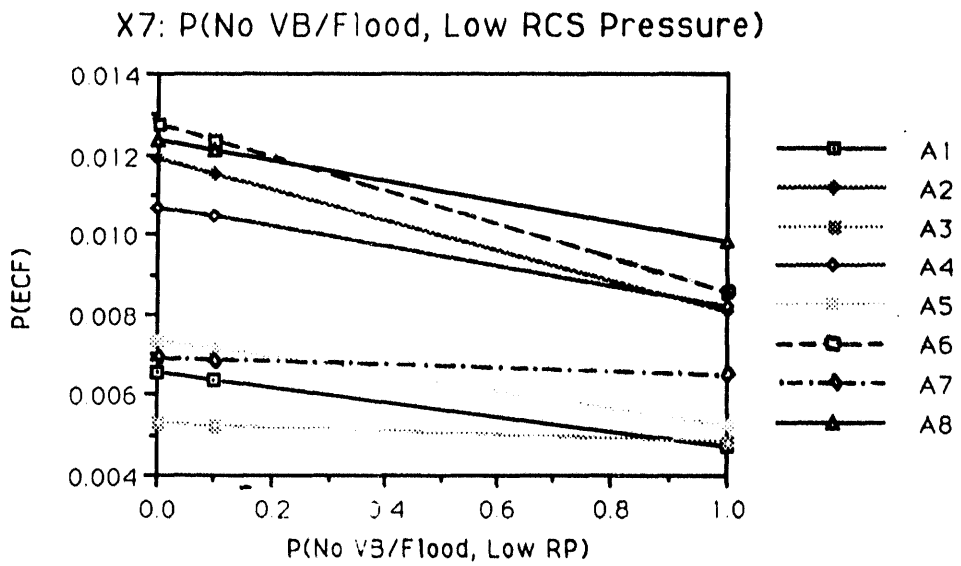

Figure 7.9. ECF sensitivity to the probability that vessel fails given water in the cavity, low RCS pressure and no core damage arrest.

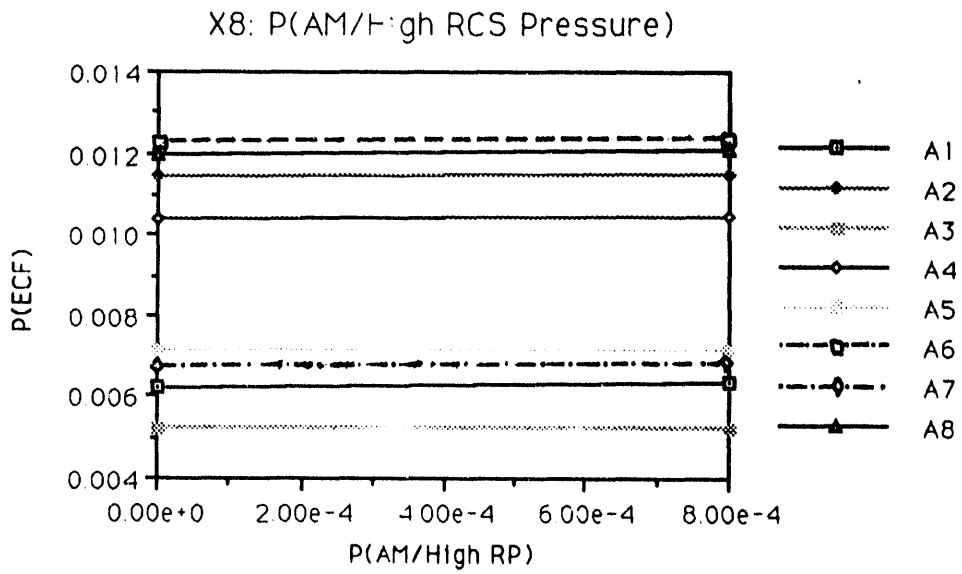

Figure 7.10. ECF sensitivity to the probability that alpha mode failure occurs given high RCS pressure.

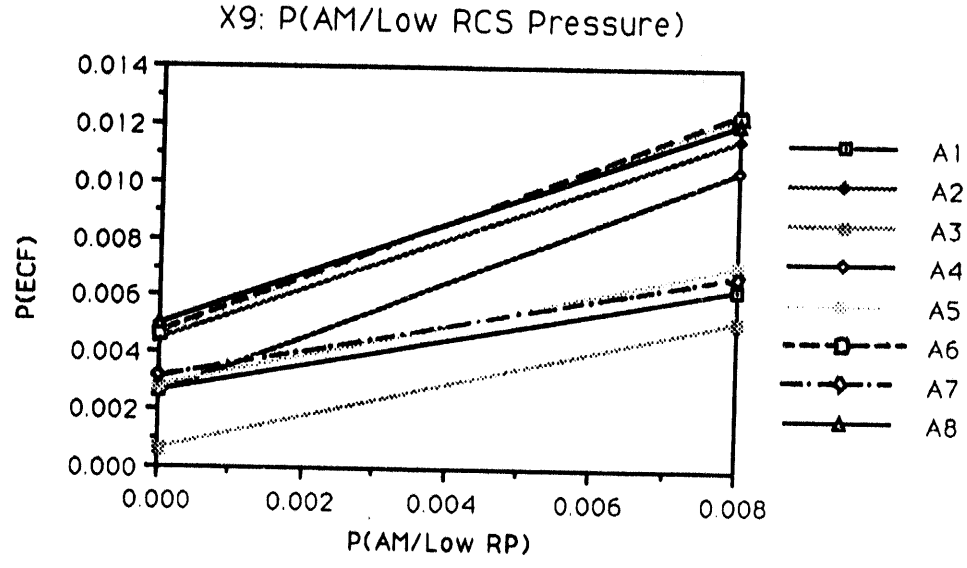

Figure 7.11. ECF sensitivity to the probability that alpha mode failure occurs given low RCS pressure.

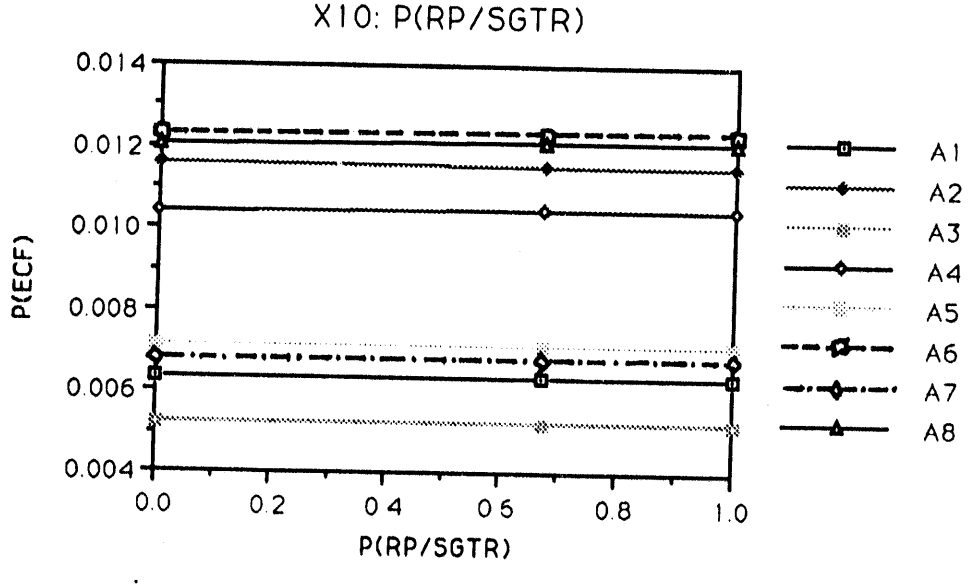

Figure 7.12. ECF sensitivity to the probability that RCS pressure is high given SGTR.

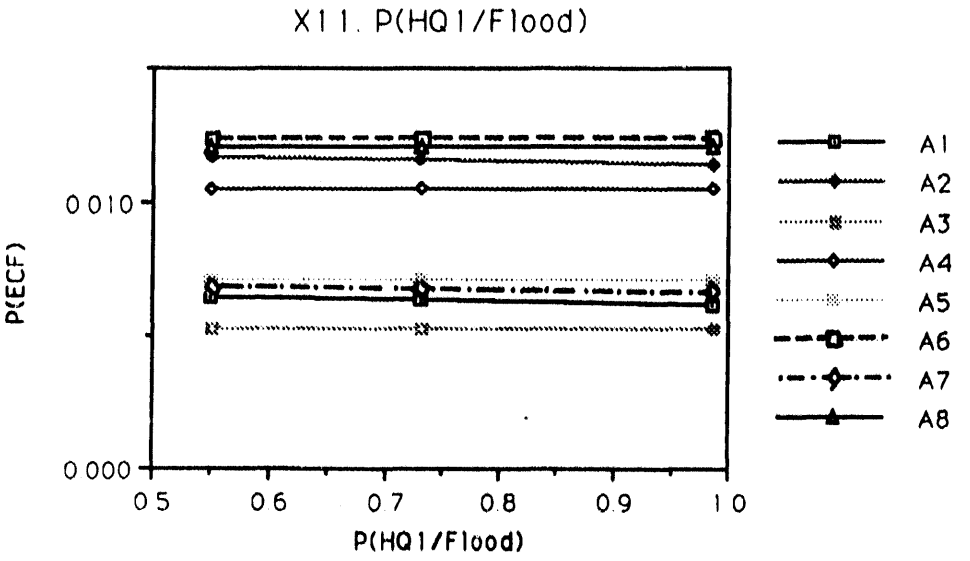

Figure 7.13. ECF sensitivity to the probability that the reactor cavity is flooded before core slumping.

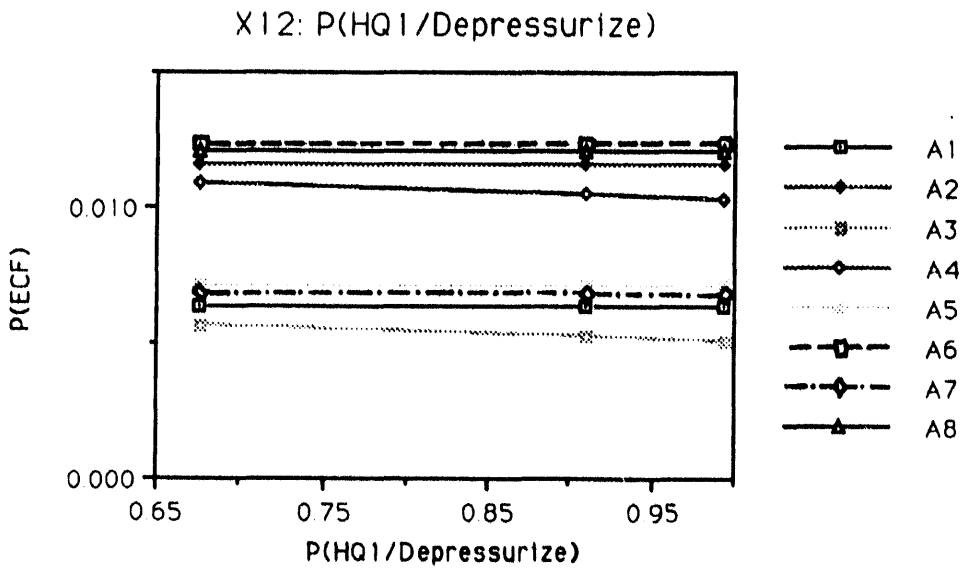

Figure 7.14. ECF sensitivity to the probability that depressurization is successfully implemented.

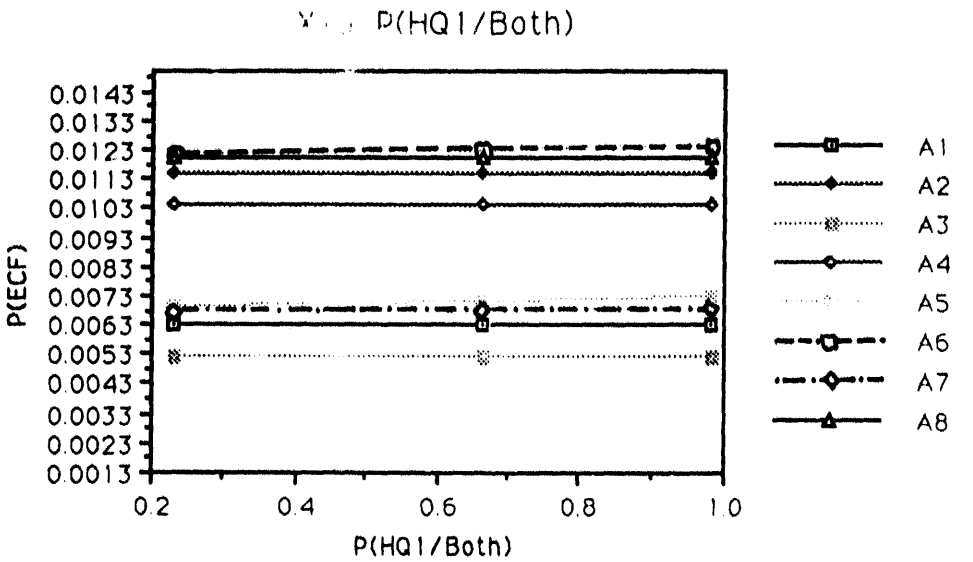

Figure 7.15. ECF sensitivity to the probability that depressurization and flooding are successfully implemented.

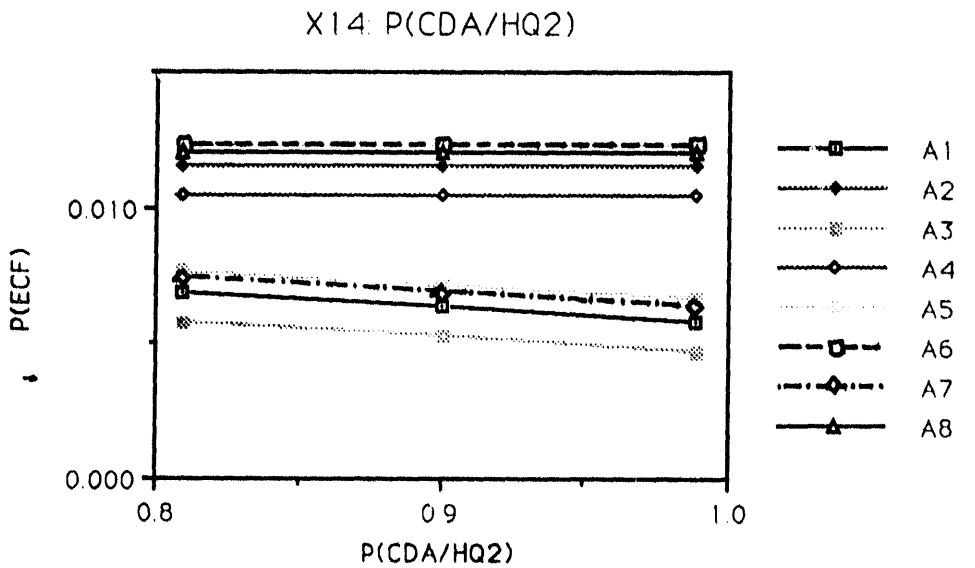

Figure 7.16. ECF sensitivity to the probability that core damage is arrested given AC power recovery.

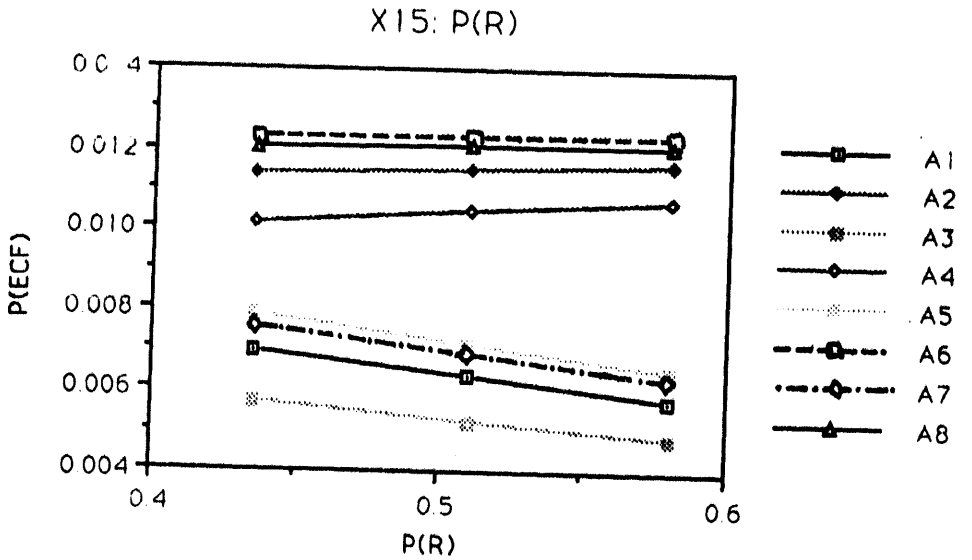

Figure 7.17. ECF sensitivity to the probability that AC power is recovered before vessel breach.

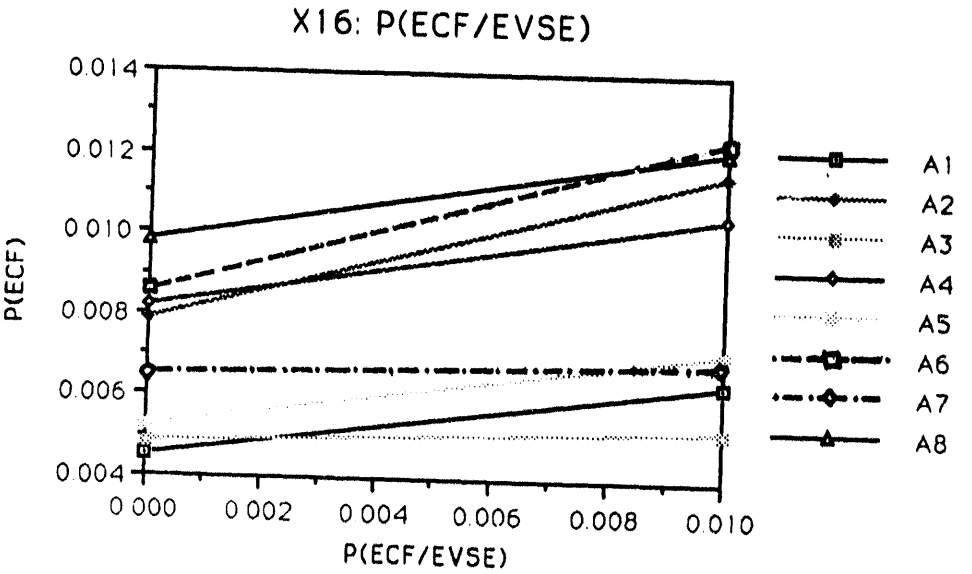

Figure 7.18. ECF sensitivity to the probability that early containment failure occurs given the occurrence of ex-vessel steam explosion.

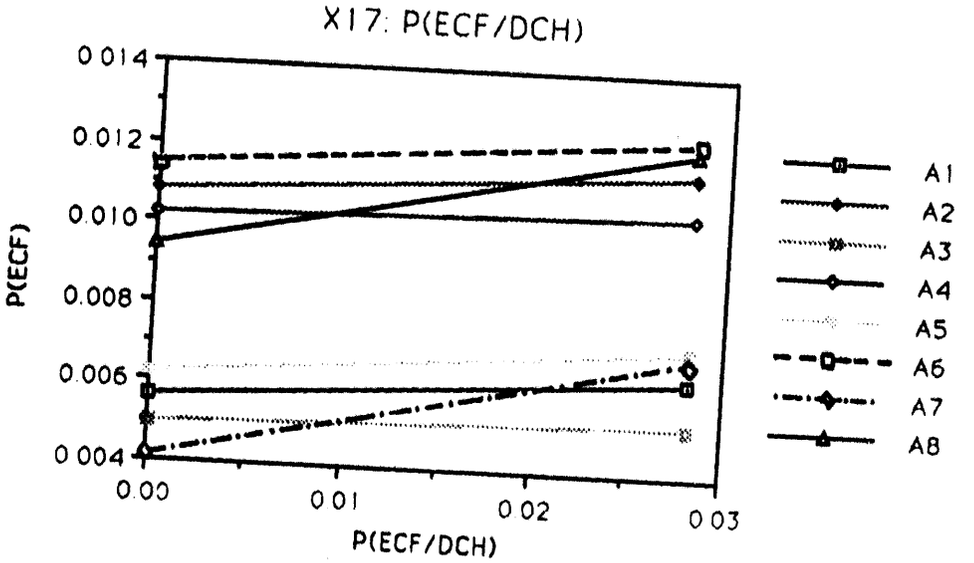

Figure 7.19. ECF sensitivity to the probability that ECF due to DCH occurs.

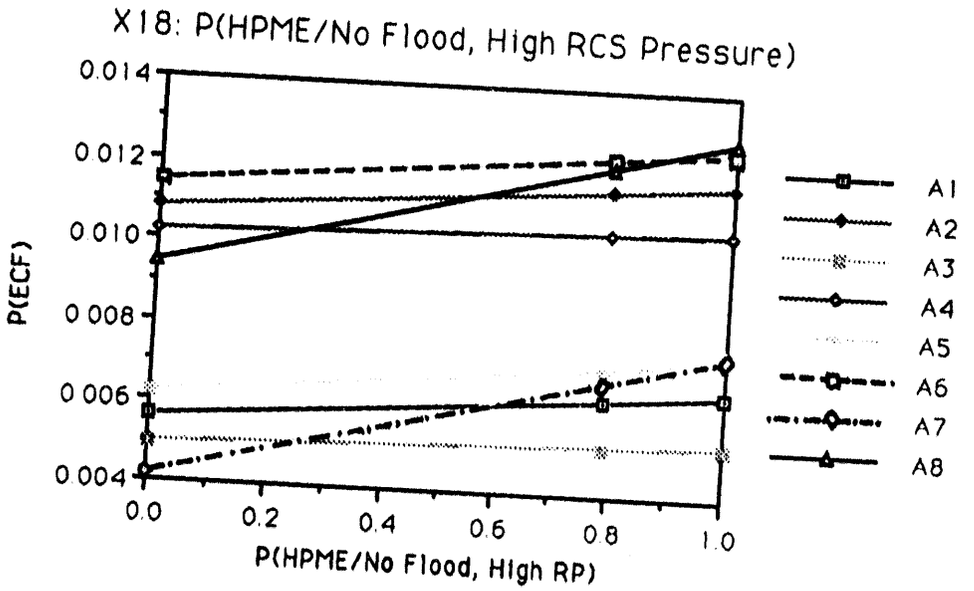

Figure 7.20. ECF sensitivity to the probability that high pressure melt ejection occurs given high RCS pressure.

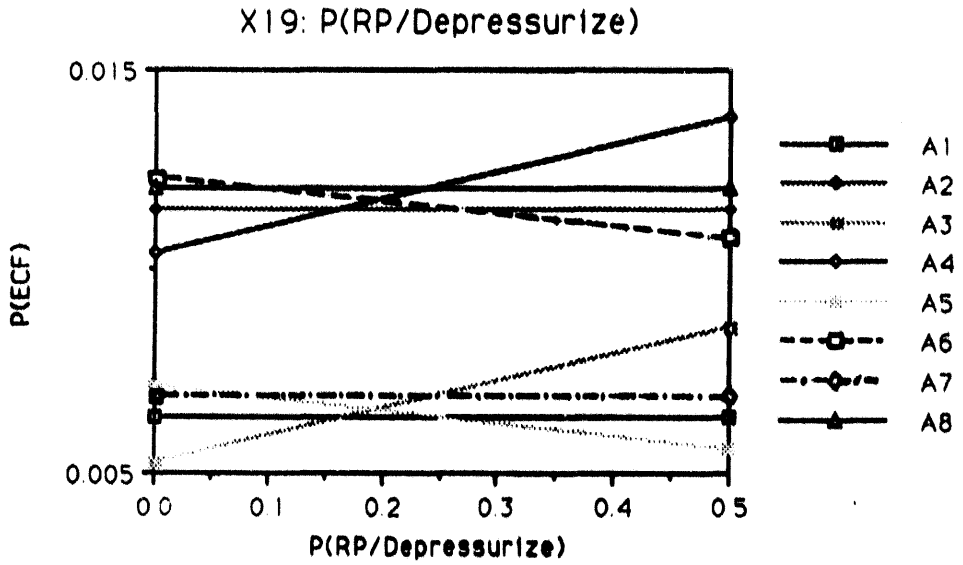

Figure 7.21. ECF sensitivity to the probability that RP is high given depressurization.

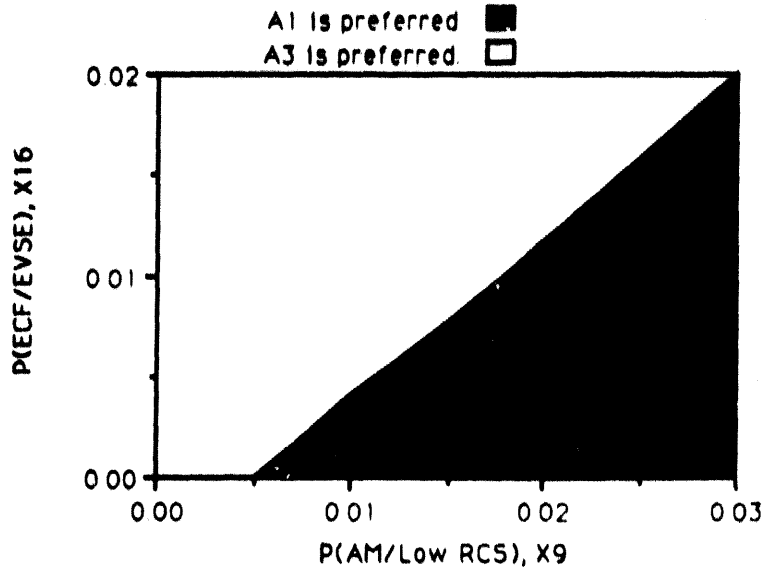

Figure 7.22. A two-way policy region analysis for the variables X9 and X16 and decision alternatives A1 and A3.

8. CONCLUSIONS AND RECOMENDATIONS

Some potential accident management strategies are inherently complex, involving both benefits and adverse aspects and subject to large uncertainties. Influence Diagrams represent a valuable tool for examining and illuminating the various interrelationships among the many factors involved. Decision Trees, equivalent to the Influence Diagram, both represent a second way of illustrating complex relationships and provide an automated tool for solving for the various outcomes of the potential strategy.

It appears to be practical to propagate uncertainties through the Influence Diagrams and Decision Trees, thereby providing much more information for the decision-making process on whether or not to adopt a strategy. Moreover, Decision Trees and Influence Diagrams can be used to evaluate strategies containing sequential decisions, and to evaluate alternative (or multiple) strategies.

The use of Influence Diagrams/Decision Trees has a second valuable benefit. It requires a systematic examination of the various potential factors which could affect the outcome of a particular strategy. The factors required include feasibility, effectiveness and adverse effects. As a result of this requirement, a more complete examination and evaluation of candidate accident management strategies may result, and factors sometimes overlooked, such as spurious information and errors of commission, may be identified and factored into the assessment.

In this study, Influence Diagrams and Decision Trees have been used first to examine two severe accident management strategies, PWR cavity flooding to prevent vessel failure, and BWR drywell flooding to prevent vessel failure and/or containment failure. A commercially available computer code called SUPERTRE was used to quantify the Decision Tree, and a method for direct quantification of the Influence Diagrams was developed in this study. Data and models relied heavily on NUREG-1150, and on independent analyses by UCLA and other NRC contractors.

For the PWR cavity flooding case, the major uncertainties include the effectiveness of the water in removing heat and preventing vessel failure/penetration, the potential for steam generator tube rupture versus surge line failure, and the potential for an ex-vessel steam explosion. On balance, water in the cavity appears to reduce risks regardless of uncertainty, except for the extreme cases of a steam explosion or steam-generator tube rupture. Water in the cavity has the secondary mitigating effect of reducing the potential for early containment failure due to direct containment heating and late containment failure.

For the BWR drywell flooding case, the major uncertainty is the effectiveness of the water in preventing vessel failure. Steam explosions are not a key factor influencing the flooding strategy, if one has a high chance of saving the vessel lower head. If the vessel should fail, isolation failure and liner failure are of concern even without a steam explosion. The steam explosion is only one of the several competing mechanisms to fail the containment. The analysis shows that flooding is favorable regardless of the conditional probability of early containment failure given a steam explosion.

In addition to evaluating the single PWR cavity flooding strategy, a combination of three strategies was assessed: Flooding the reactor cavity at the time of core uncovery in order to cool the reactor vessel lower head and prevent or delay vessel failure; depressurizing the primary system in order to mitigate direct containment heating; and initiating feed-and-bleed cooling of the core if AC power is recovered before vessel failure in order to arrest core damage and prevent vessel failure. As a result of this study, the following can be concluded. It is always better to initiate feed-and-bleed cooling of the core, no matter what other strategies are initiated, and irrespective of the uncertainty in the key variables. In ranking the three strategies, taken singly or in combination, the major uncertainties include the potential for direct containment heating, ex-vessel steam explosions and hot leg or surge line failure due to natural circulation.

The highest ranked strategy, with respect to minimizing the probability of early containment failure, is depressurization and feed-and-bleed cooling if AC power is recovered. This is followed by cavity flooding and feed-and-bleed cooling, and third ranked is feed-and-bleed cooling alone.

Related to the feasibility of flooding, a fire pump or a new high capacity, independently powered low pressure pump could be considered. If the fire pump is used, flooding should be started no later than 2 hours after the loss of AC power. The precondition is that the operator should foresee that AC power will not be recovered within 12 hours (A possible scenario might be loss of power grid due to severe weather so that repair can not be performed within 12 hours; also the on site DG has unrecoverable mechanical damage). Modification of the existing fire protection system needs to be prepared at the plant. In reality, the operator might be reluctant to flood early, because DC is still available and HPCI is also available. Another reason is flooding will induce loss of wetwell function. Procedural changes have to be made if early flooding using fire pumps should be employed.

If new low pressure, high capacity and independently powered pumps are to be introduced, a value impact analysis should be performed because of the potentially high cost associated with the new systems. The operator has to be able to monitor the status of the reactor core, if late flooding (e.g., starting from core uncovery) is desirable.

Influence Diagrams and Decision Trees have proven valuable tools in the understanding of these two strategies. It is recommended that a method be developed for propagating uncertainty through the trees and/or diagrams in order to assess the magnitude of the uncertainty associated with the adverse effects.

9. REFERENCES

[1]. W. E. Kastenberg, editor, "Summary of a Workshop on Severe Accident Management For PWRs," NUREG/CR-5781, UCLA (November 1991).

[2]. W. E. Kastenberg, editor, "Summary of a Workshop on Severe Accident Management For BWRs," NUREG/CR-5780, UCLA (November 1991).

[3]. USNRC, "Severe Accident Risks: An Assessment for Five Nuclear Power Plants," NUREG-1150, vols. 1 and 2, (June 1989).

[4]. SUPERTREE Decision Analysis Software, Version 5, Copyright 1987 SDG Decision Systems.

[5]. J. E. Kelly, R. J. Henninger and J. F. Dearing, "MELPROG/MOD1 Analysis of a TMLB' Accident Sequence," NUREG/CR-4742, (Sept. 1986).

[6]. P. D. Bayless, "Analysis of Natural Circulation During a Surry Station Blackout Using SCDAP/RELAP5," NUREG/CR-5214, (1988).

[7]. H. Park and V. Dhir, "Steady-State Thermal Analysis of External Cooling of a PWR Vessel Lower Head," AIChE Symposium Series, No. 283, Vol. 97, P.1, 1991.

[8]. R. J. Breeding, J. C. Helton, W. B. Murfin, et al., "Evaluation of Severe Accident Risks: Surry Unit 1 Appendices," NUREG/CR-4551, Vol. 3, Part 2, (Oct. 1990).

[9]. R. J. Breeding, J. C. Helton , W. C. Murfin, et al., "Evaluation of Severe Accident Risks: Surry Unit 1 Main Report," NUREG/CR-4551, Vol. 3, Part 1, (Oct. 1990).

[10]."Zion Final Safety Analysis Report," Vol. 4 (9.9) , Commonwealth Edison Company, Chigago, (1982).

[11]. A. D. Swain and H. E. Guttman, "Handbook of Human Reliability Analysis with Emphasis on Nuclear Power Applications," NUREG/CR-1278, (1987).

[12]. R. L. Iman, et al., "Modeling Time to Recovery and Initiating Event Frequency for Loss of Off-site Power Incidents at Nuclear Power Plants," NUREG/CR-5032, (Jan 1988).

[13]. F.T. Harper, T.D. Brown, R.J. Breeding, et. al., "Evaluation of Severe Accident Risks: Quantification of Major Input Parameters," NUREG/CR-4551, Vol. 2, Parts 1 and 2, (Dec. 1990).

[14]. "BWR Owners Group Emergency Procedure Guidelines". Revision 4, General Electric Topical Report NEDO-31331, (March 1987).

[15]. S.A. Hodge, "Recommendations for Further Assessment of Certain BWR (IN-VESSEL) Late Accident Mitigation Strategies," Letter Report, Sept. 25, 1990, ORNL/NRC/LTR-90/19.

[16]. T.G. Theofanous, et. al., "The Probability of Linear Failure in a Mark I Containment," NUREG/CR-5423, (September, 1991).

[17]. W.A. Condon, S.R. Greene, R.M. Harrington and S.A. Hodge, "SBLOCA Outside Containment at Browns Ferry Unit One-Accident Sequence Analysis," NUREG/CR-2672, Vol. 1, ORNL/TM-8119/V1, (Nov. 1982).

[18]. S.A. Hodge, et. al., "External Flooding of a BWR Reactor Vessel As a Late Accident Mitigation Strategy; Detailed Assessment of Boiling Water Reactor In-Vessel Strategies Program," Letter Report, ORNL/NRC/LTR-91/9, (August 27, 1991).

[19]. A.M. Kolaczkowski, et. al., "Analysis of Core Damage Frequency: Peach Bottom, Unit 2, Internal Events," NUREG/CR-4550, Vol. 4, Part 1, (August 1989).

[20] K.C. Wagner, et. al., "An Overview of BWR Mark I Containment Venting Risk Implications," NUREG/CR-5225, EGG-2548 Addendum 1, (June 1989).

[21]. G.E. Apostolakis, "A Critique of Recent Models for Human Error Rate Assessment," Reliability Engineering and System Safety, **22**, pp. 201-217, (1988).

[22]. S.A. Hodge, et. al., "Identification and Assessment of BWR (In-Vessel) Severe Accident Mitigation Strategies (draft)," NUREG/CR-5869, (May 1992).

[23]. A.C. Payne, et. al., "Evaluation of Severe Accident Risks: Peach Bottom, Unit 2, Main Report," NUREG/CR-4551, SAND86-1309, Vol. 4, Part 1, (Dec. 1990).

[24]. "Updated Final Safety Analysis Report, Peach Bottom Atomic Power Station Unit 2&3," Vol. 5, PHILADELPHIA ELECTRIC COMPANY, (March, 1988).

[25]. E. Claiborne, et. al., "Cost Analysis for Potential BWR Mark I Containment Improvements," NUREG/CR-5278, SEA 87-253-07-A:1, (Jan. 1989).

[26]. M.T. Drouin, et. al., "Analysis of Core Damage Frequency: Grand Gulf, Unit 1, Internal Events," NUREG/CR-4550, SAND86-2084, Vol. 6, Part 1, (Sept. 1989).

[27]. W.I. Rij, "A Survey of Current Models of BWR Lower Head Failure Used in the Severe Accident Codes APRIL, MELCOR, MELPROG and SCDAP/RELAP," ORNL/NRC/LTR-90/26, Oak Ridge National Laboratory, (Sept. 1990).

[28]. H. Park and V.K. Dhir, "Effect of External Flooding on Retention of Core Material in A BWR Lower Head," Proceedings of the 7th Conference on Nuclear Thermal Hydraulics, pp. 315-322, ANS Winter Meeting, (1991).

[29]. A.C. Payne, et. al., "Evaluation of Severe Accident Risks: Peach Bottom, Unit 2, Appendices," NUREG/CR-4551, SAND86-1309, Vol. 4, Part 2, (Dec. 1990).

[30]. Ali Mosleh and G. Apostolakis, "The Assessment of Probability Distributions from Expert Opinions with an Application to Seismic Fragility Curves," Risk Analysis, Vol. 6, pp. 447-461, (1986).

[31]. S.A. Hodge, "BWR (In-Vessel) Late Accident Mitigation Strategies," ORNL/NRC/LTR-90/18, Letter Report, Sept. 15, 1990.

[32]. Ross D. Shachter, "Probabilistic Influence and Influence Diagrams," Operations Research, **36** (4), (1988).

[33]. J. Pearl, Probabilistic Reasoning in Intelligent Systems: Networks of Plausible Inference., Morgan Kaufmann Publishers, Inc. San Mateo, CA, (1988).

[34]. R.D. Shachter, D.M., Eddy and V. Hasselblad, "An Influence Diagram Approach to the Confidence Profile Method for Health Technology Assessment," presented at the Conference on Influence Diagrams for Decision Analysis, Inference and Prediction, Berkeley, CA, (May 1988).

[35] R M. Oliver and J.Q. Smith, Influence Diagrams, Belief Nets and Decision Analysis, John Wiley and Sons, (1990).

[36]. R.D. Shachter, "Evaluating Influence Diagrams," Operations Research, **34**, No. 6, (1986).

[37]. A.D. Swain, "Accident Sequence Evaluation Program Human Reliability Procedure," NUREG/CR-4772, (1987).

[38]. D.J. Hanson, D.W. Golden, R. Chambers, et. al., "Depressurization as an Accident Management Strategy to Minimize the Consequences of Direct Containment Heating," NUREG/CR-5447, EGG-2574 (1990).

[39]. G.A. Murphy, "Summary of NUREG-1154: Loss of Main and Auxiliary Feedwater at the Davis-Besse Plant on June 9, 1985," *Nuclear Safety*, **27**, 233 (1986).

[40]. C.A. Dobbe and D.L. Knudson, "Assessment of the Potential for High Pressure Melt Ejection Resulting from a Surry Station Blackout Transient," Idaho National Engineering Laboratory, EGG-2689, May 1993.

APPENDIX I

THERMAL CONSIDERATIONS

EXECUTIVE SUMMARY

Flooding of the cavity of a Pressurized Water Reactor (PWR) and the drywell of a Boiling Water Reactor (BWR) is one of many accident management strategies being proposed to manage severe accidents in light water reactors. In this work the effect of external cooling on the thermal behavior of the vessel lower head containing molten core material was numerically investigated using a two dimensional implicit finite difference scheme. Results were obtained for the vessel shell temperature, pool temperature and the crust thickness for both unsteady state (PWR) and steady state (PWR and BWR) conditions. For both cases, the thermal behavior of the vessel lower head was investigated by parametrically changing the emissivity of the pool free surface, the vessel wall, the baffle plate (BWR), the core shroud (BWR) and the upper structure; and the temperature of the upper structure. Steady state results were obtained by using two different heat transfer coefficients for the natural convection in the molten pool. This was done to understand as to how uncertainties in the modeling of a physical process can influence the evaluation of accident management strategies. For a certain set of parameters, nucleate boiling on the outer surface of the vessel wall was found to be effective in lowering the temperature of the inner wall of the vessel below the melting temperature of the steel. It was found that some melting of the PWR vessel inner wall is predicted to occur and that for most of the cases, melting of the BWR baffle plate would occur.

The axisymmetric distributions of effective stresses and displacements in the vessel shell are obtained by using the numerically calculated temperature distributions in the hemispherical and cylindrical (BWR) vessel shells when the cavity (or the drywell) is flooded with water. A finite element scheme implemented through the computer code, NASTRAN is used. The stresses in the vessel shell in accordance with Von-Mises criterion are obtained for the clamped and the roller conditions at the upper region of the vessel shells. From the elastic analysis the stresses across the PWR vessel shell are predicted to exceed the yield stress of steel vessel, introducing the possibility of a large plastic deformation, in which case the survival of the vessel shell is in question. The present calcula-

tions suggest a high probability of the PWR vessel failure. However, the stresses in the BWR vessel shell are predicted to be lower than the yield stress of steel. For a given system pressure, the creep rupture times after slumping of the core material into the lower vessel head are determined by using the relationship between the Larson-Miller parameter and the equivalent stress. Because of large temperature gradients across the vessel wall, the creep rupture times for the reactor vessel are dependent upon the temperature of the radial location chosen for the calculations.

NOMENCLATURE

A	area (m^2)
F	radiation shape factor
g	gravitational acceleration (m/s^2)
H	pool depth (m)
h_{fs}	latent heat of fusion (J/kg)
h	heat transfer coefficient (W/m^2 K)
k	thermal conductivity (W/m K)
M	total number of nodes in r-direction
N	total number of nodes in θ-direction
P	pressure (Pa)
Q	rate of heat transfer (W)
Q_{gen}	heat generation rate (W)
q	heat flux (W/m^2)
q_{gen}	volumetric heat generation (W/m^3)
R_a	Rayleigh number
R_0	inner radius of core shroud (m)
R_1	inner radius of vessel lower head (m)
R_2	outer radius of vessel lower head (m)
r	radial distance (m)
S	equivalent stress (Pa)
T	temperature (K)
T_m	melting temperature of the pool (K)
t	time (sec)
u	displacement (m)
V	volume (m^3)
X	height of water in the downcomer region (m)
x	vertical distance from the top of the hemisphere (m)
y	vertical distance from the upper surface of the pool (m)
z	vertical distance from the vessel inner wall (m)

Greek Letters

ϵ	emissivity
θ	angle along the vessel wall (deg)
θ_0	pool angle (deg)
δ	crust thickness (m)
ρ	density (kg/m^3)
α	thermal diffusivity (m^2/s)
β	coefficient of thermal expansion (1/K)
ν	kinematic viscosity (m^2/s)
σ	Stefan-Boltzmann constant (W/m^2 K^4)
σ_Y	yield stress (Pa)
σ_{ij}	stress tensor (Pa)

Subscripts

a	steam in the air pocket
av	average
c	core shroud
cd	lower crust
cu	upper crust
d	lower
e	water in the downcomer region
L	subcooled water
max	maximum
p	pool
r	rupture
s	upper structure (PWR)
t	upper structure (BWR)
u	upper
v	cylindrical vessel shell
w	spherical vessel shell

I.1. INTRODUCTION

Severe accidents in light water reactors initiate with core uncovery and continued undercooling the reactor core. During prolonged undercooling, the core starts to degrade and lose its geometry. If the operators are successful in injecting water into the vessel during the degradation period, the accident can be terminated as was demonstrated in the Three Mile Island (TMI) accident. In the absence of water injection, the core material will go through several quasi-stable melting-freezing scenarios before relocating into the lower plenum of the vessel. Existence of water in the lower plenum at the time of relocation will lead to fuel-coolant interactions. At high system pressures these interactions are expected to be benign. However, at low system pressures concerns with respect to consequences of energetics of the interactions still exist. If the fuel-coolant interactions in the lower plenum are not energetic or not of sufficient strength to fail the reactor vessel in time and quenching of the core material is not sustained, the core material can melt through the vessel.

One of the management strategies currently being considered for severe accidents is to flood the cavity of a Pressurized Water Reactor (PWR) and the drywell of a Boiling Water Reactor (BWR) and thereby contain the core material in the vessel indefinitely. The idea here is that cooling of the reactor vessel wall will prevent the molten core material contained in the vessel lower head from melting through the vessel. The BWR Owner's Group Emergency Procedure Guidelines (EPG's) [1] (contingency #6) currently provide for primary containment flooding where all other means of reactor vessel injection have failed, but the concept is intended for LOCA situations in which water within the drywell could enter the reactor vessel through the break. For severe accident sequences not involving LOCA, however, flooding of the drywell and the presence of water surrounding the lower portion of the reactor vessel might provide sufficient cooling of the reactor vessel lower head to maintain the molten core within the vessel.

I.1.1 Overview

The earliest study on the effectiveness of cooling the outer wall of the vessel in containing the relocated core in the vessel is that of Condon et al [2]. In their analysis, the pool containing molten core material was assumed to be in the form of stratified layers of UO_2 and steel. One dimensional steady state analysis was conducted with a specified temperature for the vessel outer wall. It was shown that for realistic decay heat generation rates, the flooding of the reactor drywell will prevent the vessel melt through. They did not consider the creep rupture of the vessel shell because they performed the steady state analysis. It was also concluded that for Browns Ferry plant, RHRSW pumping capacity will have to be upgraded to flood the drywell in 30 minutes (the time elapsed between beginning of melting and major core slumping calculated with MARCH code). Also, an issue was raised with respect to overpressurization of the drywell which could prevent flooding unless the containment was vented.

O'Brien and Hawkes [3] have performed the thermal analysis on the viability of external water flooding of the cavity of the PWR in case of a severe accident with partial core melting and core relocation to the reactor vessel lower head. For the molten pool in the reactor vessel lower head, the turbulent natural convection heat flux distribution predicted from the FIDAP simulation was used to determine the vessel wall temperature. Vessel wall temperature and heat fluxes were obtained over a range of decay heating values using a one-dimensional heat conduction model. It was concluded that if the numerically predicted turbulent natural convection heat transfer coefficients are correct and the higher water level can be maintained, some localized wall thinning may occur, but vessel thermal failure is unlikely.

Hodge et al [4] have investigated the external flooding of a Boiling Water Reactor (BWR) vessel as a late accident mitigation strategy. Calculations were made based upon the short-term Station Blackout severe accident sequence for Browns Ferry or Peach Bottom plant. The HEATING code was employed in their study for detailed analyses of the reactor vessel wall temperature including heat conduction through the wall. The

thermal behavior of the debris in the vessel lower head and the effect of this debris bed upon the recator vessel wall temperature were considered in their study by applying the BWRSAR code developed at ORNL. Their lower plenum debris bed models represent decay heating, heat conduction and radiative heat transport within the debris as well as the effects of material melting, relocation and freezing. While their model has no representation of the liquid circulation, the associated increase in heat transport was crudely represented by increasing the mass-averaged and phase-averaged local thermal conductivity by a factor of 10 whenever the liquid mass within a control volume exceeded two-thirds of the total control volume mass. Due to the poor heat loss to the atmosphere trapped in the vessel support skirt, the highest average wall temperature beneath the skirt attachment weld reached levels at which creep rupture would be anticipated. For the case with complete venting of the vessel support skirt (so that the pocket of trapped gas is entirely eliminated), creep rupture of the wall was not predicted. It was concluded that the most important contribution of drywell flooding will be to shift the expected failure mode from penetration failure to creep rupture of the vessel bottom head beneath the support skirt attachment.

Thinnes [5] performed the TMI-2 lower head creep rupture analysis by using ABAQUS, a structural element code with geometric and material nonlinear capabilities. Material creep behavior and ultimate strength properties were derived from data resulting from material tests preformed up to 922K. The results of the creep analysis showed that the stress gradient throughout accident was dominated by the temperature effects even though the maximum integration point temperature was only about 1000 K. The conclusions drawn from his calculations were that rupture of the lower head resulting from large temperature differences across the vessel wall is not probable and that even though the wall inner surface temperature is important, average wall temperatures are more critical to the structural capacity of the vessel.

Stress calculations by Thinnes to assess creep failure of the reactor vessel lower head during the TMI-2 accident showed the need for creep properties at very high temperatures. To extend the structural property

database and to aid further structural calculations, creep tests at temperatures up to 1473 K have been performed at INEL [6]. Because of high oxidation rates on the test coupons, the creep tests were performed in an inert atmosphere, which requires an environmental chamber filled with argon gas. The guard heater outside the chamber was installed in order to achieve high material temperature. The temperatures of the test coupons were found to be uniform. Due to the high ductility of the material at high temperatures, extensometers were installed inside the environmental chamber to measure the entire time-dependent creep response. The test coupons for the creep tests were fabricated from samples oriented with longitudinally (meridional orientation with respect to the vessel) and transversely (radial or through-wall orientation) in the vessel plate material.

I.1.2 Objectives of the Present Work

The purpose of the this work is to investigate in detail the effectiveness of flooding the cavity of a PWR and the drywell of a BWR in containing the core in the vessel in case melting and relocation of the core to the vessel lower head occurs. Two dimensional transient and steady state analyses [7,8] for the flooding of a PWR cavity were carried out including the heat loss by radiation to the upper regions of the reactor vessel and the unwetted portion of the vessel lower head. Two dimensional steady state analysis for the flooding of a BWR drywell was also carried out [9] including the heat loss by radiation to the unwetted portion of the vessel lower head, the baffle plate, the core shroud and the upper structure. The heat loss to the steam-containing air pocket of the BWR vessel support skirt was also considered. Effect of internal circulation in the molten core material on heat transfer at the bounding walls is determined by extrapolating to the desired range the correlations available in the literature. In carrying out the analysis, various constituents of the core material are assumed to be mixed homogenously.

Known temperature distributions in the vessel shell are used to calculate the thermal stresses and to assess the possibility of failure of the reactor vessel due to creep rupture at temperatures that are lower than the melting temperature of steel. In this work a two-dimensional finite element scheme with two types of boundary conditions in the top region of the hemispherical (PWR) and cylindrical (BWR) vessel shells is used to calculate the stress field in the vessel wall. The Von-Mises yield criterion is then applied to each element in the vessel shell. Also, in the present work the creep rupture times after slumping of the core material into the vessel lower head are determined. A master creep curve is obtained using the data reported in reference [6].

I.1.3 Problem Analysis

In carrying out the analysis, it is assumed that the cavity of a PWR and the drywell of a BWR are flooded prior to slumping of the core. Insulation on the lower head is generally installed in sections and is not required to be water-tight as such water can flow through the joints in the insulation and directly contact the vessel surface. Any net steam produced during boiling is also assumed to escape freely. The temperature of the flooded water is taken to be 323 K. The lower head of a PWR is cladded with 18Cr-8Ni stainless steel with a thickness of 0.32 to 0.95 cm. And the BWR bottom head is cladded with Inconel with a thickness of 0.32 cm. Since the thickness of the clad is much smaller than the vessel shell thickness (17.15 cm for a PWR and 24 cm for a BWR), the clad on the vessel inner wall is not included in the modeling of the vessel lower head. The slumping of the core material into the vessel lower head occurs instantaneously and at the time of core slumping the core material temperature is the melting temperature (2500 K) of corium. Upon core slumping, it is assumed that no fuel-coolant interactions occur.

Since the contact temperature between the relocated core material and the vessel inner wall is below the freezing temperature (2500 K) of corium, a crust will begin to form on the inner wall of the vessel immediately after core slumping. Because of radiative heat loss, corium will freeze at the free surface of the pool as well. During this initial period, the rate of heat transfer from molten corium to the vessel inner wall will be higher than the heat loss to water at the outer surface of the vessel. As a result, the reactor vessel will heat up. Corium will stay at its melting temperature until all of the solids present in the slumped material are completely melted. If after complete melting of the solids, the decay heat exceeds the heat loss rate at the pool boundary, the pool temperature will begin to rise. Since the fraction of the solids initially present in the slumped core material is not known, in this study, the pool temperature was arbitrarily assumed to remain at the melting temperature of corium until the heat transfer rate to the vessel wall of the reactor vessel was equal to the heat loss rate at the outer wall. The transient analysis provided the crust growth, remelting and heatup of the pool as a result

of mismatch between heat generation rate and heat loss rate. In the steady state analysis, equilibrium pool temperature was determined by equating the heat generation rate in the pool with the heat loss rate.

The decay heat in the corium was taken to be about 0.9 % of full power (PWR) and to be the value at 10 hours (BWR) after reactor shutdown. These values were obtained from references [10,11]. The internal heat generation resulting from the radioactive decay of fission products assures that most of the pool remains molten and also induces natural convection in the pool. The heat transfer coefficients due to free convection in the molten pool can be used to estimate the heat transfer into upper and lower parts of the hemispherical molten pool. Relatively few experimental and theoretical studies of natural convection in internally heated fluids contained in hemispherical vessels have been performed. These studies have been mostly limited to Rayleigh numbers ranging from 10^4 to 10^{12} which are much smaller than the Rayleigh numbers of interest here ($Ra=1.57\times10^{17}$ for a PWR and $Ra=1.24\times10^{17}$ for a BWR). Mayinger et al [12] solved the partial differential equations governing natural convection with volumetric energy source in a hemispherical cavity. They used the finite-difference form of these equations with a semi-empirical model of the eddy diffusivities for heat and momentum. Gabor et al [13] performed experiments in a hemispherical pool container made of spun copper to study of heat transfer with internal heat generation in the pool. The pool container served both as a heat transfer surface and as an electrode. $ZnSO_4$-H_2O electrolyte was used as the heat generating liquid. Frantz and Dhir [14] performed experiments to investigate natural convection heat transfer in internally heated spherical pools with external cooling. In their experiments, Freon-113 was used as the test liquid in a Pyrex bell jar, which was cooled externally with subcooled water. The pool was heated using a 750 Watt magnetron taken from a conventional microwave. Experimental data of Frantz and Dhir appear to lie closer to the numerical predictions of Mayinger et al. Whereas, the results of Gabor et al for average Nusselt number were found to be much smaller than the numerical predictions of Mayinger et al. As recognized by the authors themselves, one of the identified reasons for this is the non-uniformity of heat generation rate in the pool since the electrical

current density decreases radially from the center electrode to the wall. To be complete, correlations suggested by Mayinger et al and Gabor et al have been applied in this work. The results based on these correlations are also compared. However, emphasis should be placed on the results obtained by using the correlation of Mayinger et al.

The thermophysical properties of corium at elevated temperatures have considerable uncertainty. The extreme conditions under which core meltdown occurs make the measurements and calculations of properties extremely difficult. For this reason, an estimate of these properties can only be made when the composition of the molten core materials is known. The results presented in this work are based on the mean values of thermophysical properties of corium. Earlier studies [15,16,17] in this area were reviewed. Knowing the possible range of temperatures of interest, mean values were determined. The mean values of these properties are listed in Table I.1. Figures I.1 and I.2 show schematic diagrams of the core material relocated in the PWR and BWR vessel lower heads respectively.

In this study a finite element code (NASTRAN) in conjunction with the linear elasticity theory is employed to calculate the displacement and stress fields in the spherical (PWR and BWR) and cylindrical (BWR) vessel shells. Large deformation theory or plasticity analysis may be appropriate to obtain more reliable results. The creep rupture times after core slumping are determined by using the properly chosen wall temperature and the master creep curve obtained from the data reported in reference [6]. Various assumptions made in carrying out the analysis are:

1. The cavity of a PWR is flooded prior to slumping of the core material.
2. The temperature of the flooded water is taken to be 323 K.
3. No fuel-coolant interactions (FCIs) occur upon core slumping.
4. The pool temperature remains constant until the heatup of the pool.

Table I.1: Properties used in the calculations

Corium	$\rho_p = 8200$ kg/m^3 $c_{p,p} = 470$ J/kg K $k_p = 3.6$ W/m K $\alpha_p = 9.3 \times 10^{-7}$ m^2/s $\nu_p = 4 \times 10^{-7}$ m^2/s $\beta_p = 1.4 \times 10^{-4}$ 1/K $Q_{gen,p} = 29.5$ MW (V_{core}, PWR) $Q_{gen,p} = 16.757$ MW (2/3 V_{core}, BWR)
Vessel Shell	$\rho_w = 8000$ kg/m^3 $c_{p,w} = 600$ J/kg K $k_w = 50$ W/m K $\alpha_w = 1.04 \times 10^{-5}$ m^2/s
Crust	$\rho = 8100$ kg/m^3 $c_p = 520$ J/kg K $k = 8$ W/m K $\alpha_p = 1.9 \times 10^{-6}$ m^2/s $h_{fs} = 2.7 \times 10^5$ J/kg q_{gen} (PWR) $= 8.0 \times 10^5$ W/m^3 q_{gen} (BWR) $= 3.0 \times 10^5$ W/m^3

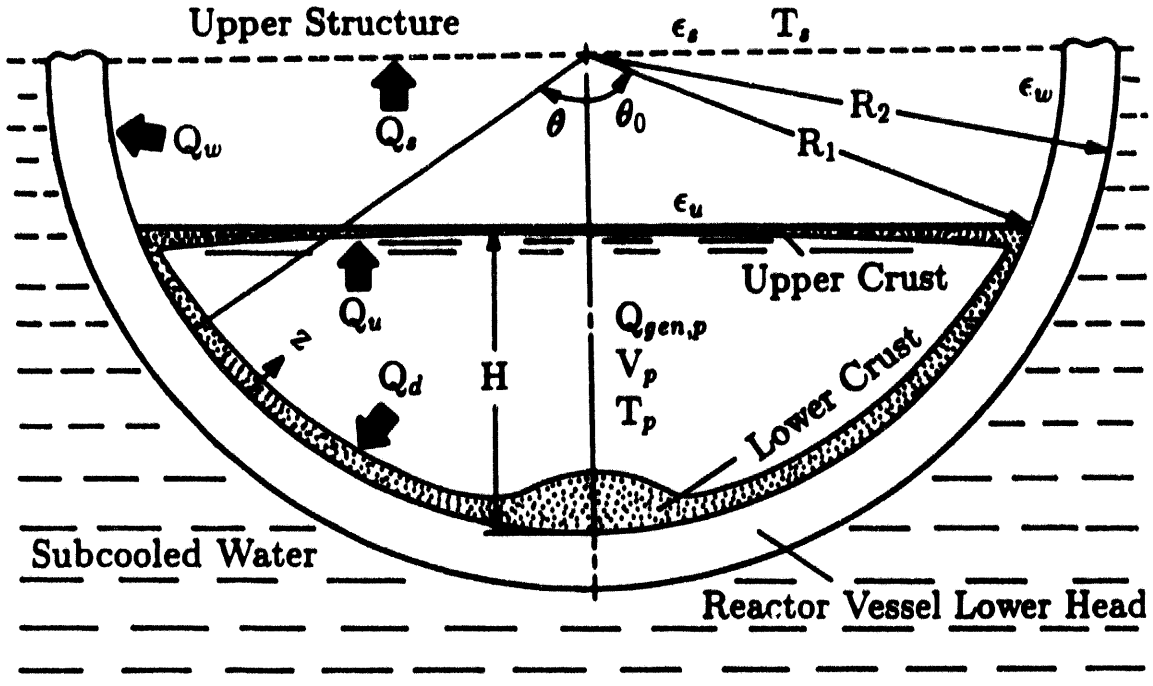

R_1 : Inner Radius of Vessel Lower Head
R_2 : Outer Radius of Vessel Lower Head
H : Pool Depth
θ_0 : Pool Angle
V_p : Pool Volume
T_p : Pool Temperature
$Q_{gen,p}$: Heat Generation in the Pool
Q_u : Heat Transfer to the Top of the Pool
Q_d : Heat Transfer to the Lower Part of the Pool
Q_s : Heat Transfer to the Upper Structure
Q_w : Heat Transfer to the Dry Wall of the Vessel Lower Head

Figure I.1: Schematic of the core material relocated in the PWR vessel lower head

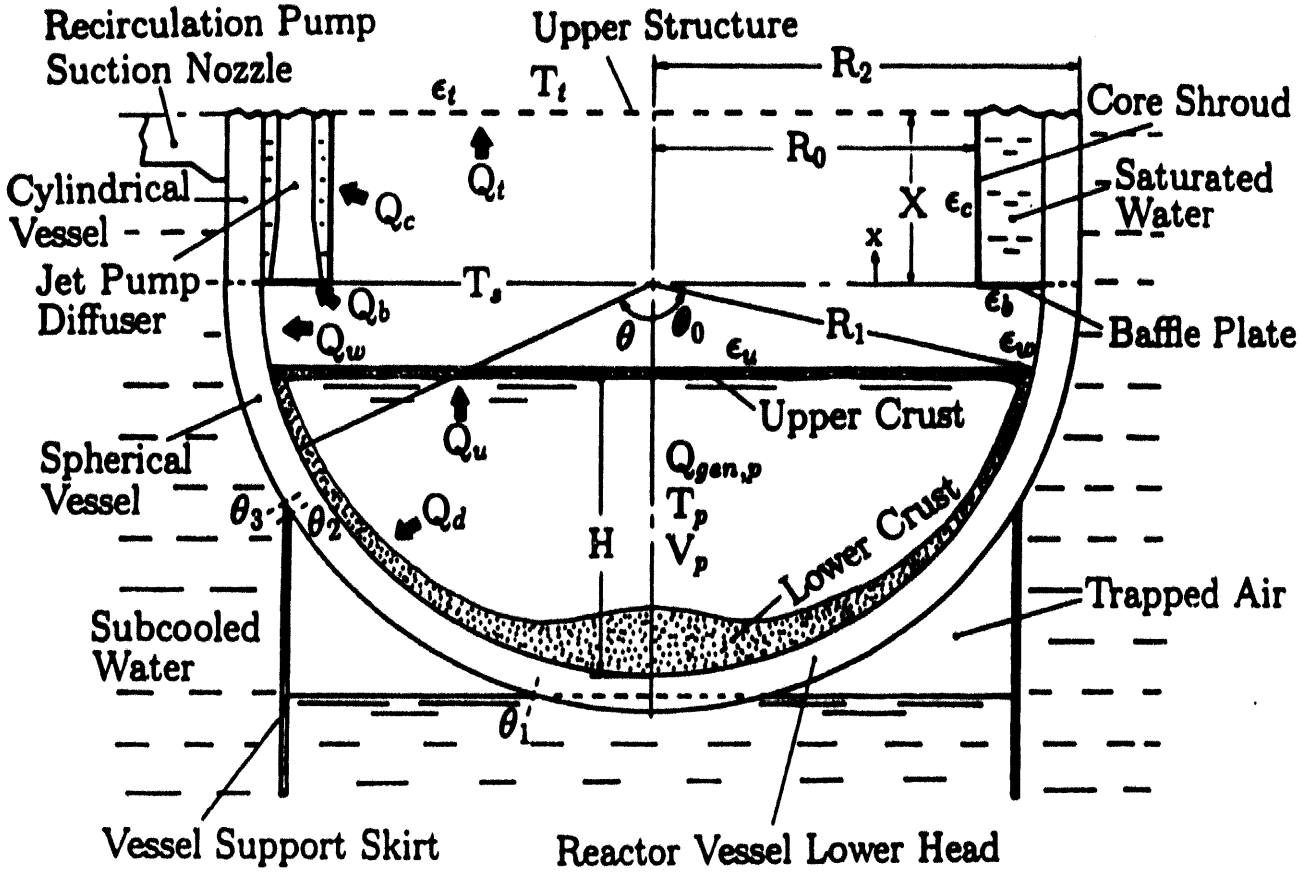

$Q_{gen,p}$ = Heat Generation in the Pool
Q_u = Heat Transfer to the Top of the Pool
Q_d = Heat Transfer to the Lower Part of the Pool
Q_w = Heat Transfer to the Dry Wall of the Vessel Lower Head
Q_b = Heat Transfer to the Baffle Plate
Q_c = Heat Transfer to the Core Shroud
Q_t = Heat Transfer to the Upper Structure

Figure I.2: Schematic of the core material relocated in the BWR vessel lower head

5. The heatup time of the pool to reach steady state temperature is about the same as the time needed for natural convection process to attain steady state.

6. Mean values of the thermophysical properties of corium can be used.

7. The temperature of the upper surface of the pool is uniform.

8. The radiative transport of heat is independent of wavelength and direction.

9. The radiation shape factors can be calculated by assuming that structural elements between the pool free surface and the core plate do not participate.

10. Steam is totally transparent to radiative transfer of energy.

11. The linear elasticity thoery can be used to calculate the displacement and stress fields in the vessel shell.

I.2 THERMAL BEHAVIOR OF THE PWR VESSEL SHELL

I.2.1 TRANSIENT ANALYSIS

Governing Differential Equation of the Vessel Shell

The differential equation for the two-dimensional transient temperature in the spherical shell of the vessel is given by

$$\frac{1}{r^2}\frac{\partial}{\partial r}\left(r^2\frac{\partial T_w}{\partial r}\right)+\frac{1}{r^2 sin\theta}\frac{\partial}{\partial \theta}\left(sin\theta\frac{\partial T_w}{\partial \theta}\right)=\frac{1}{\alpha_w}\frac{\partial T_w}{\partial t} \qquad (I.1)$$

where the finite difference form of Equation (I.1) is shown in Appendix I.A.

The initial temperature of the vessel shell is arbitrarily assumed to be 420 K at t=0. Outer vessel wall temperature during nucleate boiling will be close to this value. Prior to core material relocation, the vessel inner wall will be in contact with steam. If the system pressure is known, the vessel inner wall temperature can be easily prescribed. Here, it should be pointed out that the calculated transient and steady state vessel temperatures are not sensitive to the assumed value of the initial temperature of the shell.

The corresponding boundary conditions at t > 0 are

$$-k_w\frac{\partial T_w}{\partial r}=k_{cd}\frac{\partial T_{cd}}{\partial z}, \quad 0\le\theta\le\theta_0, \quad r=R_1, z=0$$

$$-k_w\frac{\partial T_w}{\partial r}=q_{w,rad}, \quad \theta_0<\theta\le\pi/2, \quad r=R_1$$

$$-k_w\frac{\partial T_w}{\partial r}=h_L(T_w-T_L), \quad r=R_2$$

$$\frac{\partial T_w}{\partial \theta}=0, \quad \theta=0,\pi/2$$

For single phase natural convection on the outside of the vessel, the correlation proposed by Churchill and Churchill [18] is used. Since in the

lower portion of the hemisphere heat transfer coefficient is a weak function of position, an average heat transfer coefficient is used. In case subcooled boiling occurs on the vessel outer wall, approximate correlations reported in references [19,20] are used. The radiative heat fluxes from the upper surface of the pool to the unwetted vessel wall and the upper structure are calculated by using the enclosure theory of the radiation heat transfer [21]. After the pool temperature increases above the melting temperature of corium, heat transfer from the pool to the crust/pool interface is assumed to take place by natural convection. For free convection with internal heat sources, the correlations developed by Mayinger et al [12], Gabor et al [13], Kulacki and Emara [22] and Jahn and Reineke [23] are employed.

Variation of the Crust Thickness

After relocation of the core material into the vessel lower plenum, the corium in the vessel lower head can have both the liquid and the solid phases. It is assumed here that the partially molten pool remains at a uniform temperature, T_m, until the pool heats up to a temperature above its melting temperature.

At any location along the wetted vessel wall, one-dimensional transient heat conduction equation with a distributed heat source in the lower crust is given as

$$\frac{\partial T_{cd}}{\partial t} = \alpha_{cd}\frac{\partial^2 T_{cd}}{\partial z^2} + \frac{q_{gen,cd}}{\rho_{cd}c_{p,cd}} \tag{I.2}$$

The corresponding initial and boundary conditions are

$$\begin{aligned} T_{cd} &= T_m, \quad t = 0 \\ T_{cd} &= T_m, \quad z = \delta_{cd}, t > 0 \\ T_{cd} &= T_w, \quad z = 0, r = R_1, 0 \le \theta \le \theta_0, t > 0 \end{aligned}$$

The equation governing the time dependent thickness of the lower crust is

$$\rho_{cd}h_{fs}\frac{d\delta_{cd}}{dt} = k_{cd}\frac{\partial T_{cd}}{\partial z}\Big|_{z=\delta_{cd}} - h_d(T_p - T_m) \tag{I.3}$$

where h_d is zero prior to the heatup of the pool.

Assuming that the crust thickness is uniform along the upper surface of the pool, the one-dimensional transient heat conduction equation in the upper crust is written as

$$\frac{\partial T_{cu}}{\partial t} = \alpha_{cu} \frac{\partial^2 T_{cu}}{\partial y^2} \tag{I.4}$$

where

$$\begin{aligned} T_{cu} &= T_m, && t = 0 \\ k_{cu} \frac{\partial T_{cu}}{\partial y} &= q_{u,rad}(t), && y = 0, t > 0 \\ T_{cu} &= T_m, && y = \delta_{cu}, t > 0 \end{aligned}$$

The time dependent thickness of the upper crust is given by

$$\rho_{cu} h_{fs} \frac{d\delta_{cu}}{dt} = k_{cu} \frac{\partial T_{cu}}{\partial y} \Big|_{y=\delta_{cu}} - h_u (T_p - T_m) \tag{I.5}$$

where h_u is set to be equal to zero before the heatup of the pool.

If the heat generation in the upper crust is included, the term $(q_{gen,cu}/2k_{cu})$ δ_{cu}^2 should be considered at any time. This term is negligible when the thickness of the crust is small. As an example, the difference between the upper surface temperatures with and without the generation are found to be within 1 %. Therefore, in writing Equation (I.4) heat generation in the upper crust is not included because the thickness of this crust is expected to be small.

The boundary conditions can be determined by considering the radiation heat transfer from the upper surface of the pool and the time-dependent pool temperature and by using the heat transfer coefficient for natural convection from the pool.

Radiation Heat Transfer

Assuming that the surfaces are diffuse and gray and that the steam above the pool surface is totally transparent to radiative transfer of energy, the relationships for radiative heat exchange using the enclosure

theory can be written as

$$Q_i - \sum_{j=1}^{n} F_{ij}(1-\epsilon_j)\left(\frac{\epsilon_i A_i}{\epsilon_j A_j}\right)Q_j = \epsilon_i A_i \sigma \left(T_i^4 - \sum_{j=1}^{n} F_{ij} T_j^4\right) \qquad (I.6)$$

for t > 0 and i, j = u, w, s.

Simple calculations are performed in Appendix I.B to estimate the effect of the steam on the vessel wall temperature. It is found that about 13 % of the radiative heat flux from the pool surface is predicted to be absorbed by steam, which does not affect the vessel inner wall temperature significantly. However, the superheated steam (above 2000 K) may interact with the structure remaining in the vessel, resulting in a subsequent melting of the vessel internal. Also, the circulating steam in the reactor coolant system (RCS) raises the possibitity of the failure of the hot leg or the stream generator tubes.

Using T_w as the average temperatures along the unwetted vessel wall, the desired radiation heat transfer rates and the shape factors are obtained as

$$Q_u = \frac{(f_5 + f_6)f_3 + (f_1 - f_2)f_7}{f_{11}} \qquad (I.7)$$

$$Q_w = \frac{(f_6 - f_4)f_3 - (f_2 + 1)f_7}{f_{11}} \qquad (I.8)$$

and

$$F_{u-w} = 1 - \frac{1}{2}\left(Z - \sqrt{Z^2 - 4Y^2}\right) \qquad (I.9)$$

where the expressions for f's, Y and Z are listed in the Appendix I.C.

The value of Q_w can be used as the boundary condition along the dry wall and Q_u can be used to determine the pool temperature for a certain set of parameters of ϵ_u, ϵ_w, ϵ_s and T_s.

Convective Heat Transfer Coefficient in the Pool

The average heat transfer coefficients due to free convection in the molten pool were used to estimate the heat transfer into upper and lower parts of the molten pool. The local heat transfer coefficient along the hemispherical surface was introduced to reflect the convective motion of the molten corium in the vessel lower head.

The average heat transfer coefficients for the hemispherical wall were obtained from the work of Mayinger et al [12] and Gabor et al [13] and for the upper surface of the pool from the result of Kulacki and Emara [22]. Assuming that these correlations can be extended to large Rayleigh numbers as encountered in this problem, the average heat transfer coefficient based on the correlation of Mayinger et al can be written for the lower curved surface as

$$h_{d,av} = 0.55\left(\frac{g\beta_p q_{gen,p} R_1^5}{\alpha_p \nu_p k_p}\right)^{0.2} \frac{k_p}{R_1} \tag{I.10}$$

The correlation of Gabor et al on the other hand yields

$$h_{d,av} = 0.55\left(\frac{g\beta_p q_{gen,p} R_1^5}{\alpha_p \nu_p k_p}\right)^{0.15} \frac{k_p}{R_1}\left(\frac{H}{R_1}\right)^{1.1} \tag{I.11}$$

Based on the data of Frantz and Dhir [14], weak effect of H/R_1 on Nusselt number is found and their experimantal data appear to lie closer to the numerical predictions of Mayinger et al. Therefore, the heat transfer coefficients predicted from Mayinger et al's work is more reliable.

For the flat top of the hemispherical pool, the correlation of Kulacki and Emara gives

$$h_{u,av} = 0.345\left(\frac{g\beta_p q_{gen,p} H^5}{\alpha_p \nu_p k_p}\right)^{0.226} \frac{k_p}{H} \tag{I.12}$$

Streamlines shown in reference [3] indicate the presence of a single convection cell for turbulent natural convection, with upflow near the centerline and downflow along the hemispherical boundary. An experimental investigation performed by Frantz and Dhir [14] shows that local heat transfer coefficients increase monotonically from the bottom of the reactor vessel to a peak value in the region near the pool free surface. Their results are consistent with those for a semicircular obtained in reference [23].

Based on the theoretical results of the local distribution of heat transfer coefficients in a semicircular cavity [23], the local heat transfer coefficient along the hemispherical wall is assumed to vary sinusoidally and is

expressed as

$$h_d(\theta) = h_{d,av}\left(b_1 sin^2\theta + b_2\right) \tag{I.13}$$

The constants, b_1 and b_2, can be determined by integrating the above equation over the pool angle, θ_0, equating it to the average heat transfer coefficients given by Equations (I.10) or (I.11) and choosing the appropriate value of $h_d(0)/h_{d,av}$ from [23]. This approach yields b_1 and b_2 as

$$b_1 = \frac{9.12(1 - cos\theta_0)}{8 - 9cos\theta_0 + cos3\theta_0}, \quad \theta_0 \neq 0$$

and

$$b_2 = 0.24$$

The above expressions for the local and average heat transfer coefficients can be used to calculate the crust thickness and heat flux into the vessel wall at any time.

Time-Dependent Pool Temperature

After the start of the heatup of the molten pool, the pool temperature increases with time. The equation governing the temperature of the pool bounded by the upper and lower crusts is given by

$$\rho_p c_{p,p} V_p \frac{dT_p}{dt} = Q_{gen,p} - \left(A_d h_{d,av} + A_u h_{u,av}\right)\left(T_p - T_m\right) \tag{I.14}$$

with $T_p = T_m$ at $t = t_1$, where t_1 is the time when the pool begins to superheat above its melting temperature.

The solution of the above equation is

$$T_p = T_m + G_a(1 - exp[-G_b(t - t_1)]) \tag{I.15}$$

where

$$G_a = \frac{Q_{gen,p}}{A_d h_{d,av} + A_u h_{u,av}}$$

$$G_b = \frac{A_d h_{d,av} + A_u h_{u,av}}{\rho_p c_{p,p} V_p}$$

Since the upper crust is thinner than the lower crust, during heatup of the pool the upper crust would disappear at some time $t = t_2$. Thereafter

the pool temperature without the upper crust (by assuming a uniform temperature of the upper surface of the pool) is determined as

$$\rho_p c_{p,p} V_p \frac{dT_p}{dt} = Q_{gen,p} - A_d h_{d,av}(T_p - T_m) - A_u h_{u,av}(T_p - T_u) \qquad (I.16)$$

for $t > t_2$.

From Equation (I.7), the pool temperature can be related to the temperature of the upper surface of the pool, $T_u(t)$, as

$$Q_u = A_u h_{u,av}(T_p - T_u) = \frac{(f_5 + f_6)f_3 + (f_1 - f_2)f_7}{f_{11}} \qquad (I.17)$$

Heat Transfer to Subcooled Water

The outside vessel wall temperature, $T_{wo}(\theta)$, varies along the hemispherical surface of the vessel lower head. Heat transfer coefficients for natural convection, nucleate, transition and film boiling at different outer wall temperatures are needed to calculate the heat loss into the subcooled water. In this study it is assumed that water is at one atmosphere pressure and has a subcooling of 50 K.

The average natural convection heat transfer coefficient for a submerged hemisphere is obtained from the general correlation suggested by Churchill and Churchill [18]. The proposed overall correlating equation for all geometries is of the form

$$Nu^{1/2} = Nu_0{}^{1/2} + \left[\frac{Ra/300}{(1 + (\frac{0.5}{Pr})^{9/16})^{16/9}}\right]^{1/6} \qquad (I.18)$$

where Nu_0 is equal to 2 for spheres, 0.36 for horizontal cylinders and 0.68 for vertical plates.

It can be seen that in the above correlation, the effect of Nu_0 is relatively small compared to the second term which is only dependent upon the characteristic length and the Prandtl number. Hence, the relation for a sphere can be used to approximate the heat transfer coefficient of natural convection around a hemisphere.

For a liquid subcooling of 50 K, the heat transfer coefficient is determined from Equation (I.18) as

$$h_L = 0.135(1.414 + 21.76(T_{wo} - T_L)^{1/6})^2, \quad 323 \leq T_{wo} \leq 409K \qquad \text{(I.19)}$$

For fully developed nucleate boiling on a sphere, the effect of the gravity is negligible. Thus the heat transfer coefficient on the lower and upper portions of the sphere are approximately same. It is reasonable to assume that the heat transfer coefficient for fully developed nucleate boiling on a hemisphere can be approximated by that for a sphere.

The heat transfer coefficients in the nucleate and transition boiling are obtained by extrapolating the experimental results of Dhir [19,20]. For liquid subcooling of 50 K, the heat transfer correlations in nucleate and transition boiling are found to be

$$h_L = 0.55\frac{(T_{wo} - T_{sat})^3}{(T_{wo} - T_L)}, \quad 409 \leq T_{wo} \leq 633K \qquad \text{(I.20)}$$

and

$$h_L = 532.5\left(\frac{553}{T_{wo} - T_{sat}}\right)^{5.393}, \quad 633 \leq T_{wo} \leq 926K \qquad \text{(I.21)}$$

Since even with the radiative contribution included the total amount of heat transfer in the film boiling region is much less (by a factor of 10) than that in the nucleate boiling region as shown in Appendix I.D, the outer wall temperature in the film boiling region was found to exceed the melting temperature of the steel vessel. Therefore, when vessel outside wall temperature exceeds the minimum film boiling temperatures, complete failure of the vessel wall is expected to occur.

Concerns have been raised about the applicability of the nucleate boiling at the very bottom of the hemisphere. Due to the downward-facing orientation of the hemispherical lower head, vapor film may form on the wall, leading to film boiling at a reduced heat flux compared to nucleate boiling heat fluxes. Simple calculations are performed in Appendix I.E to assess the possibility of the formation of vapor film on the vessel bottom surface. As an illustration, insulated boundary condition is used on the

bottom wall for the angular position (θ) from 0 to 4.5°. It is found that the predicted temperature of vessel bottom at $\theta = 0°$ is lower than the minimum film boiling temperature (about 926 K). Therefore, it can be assumed that the formation of vapor film on the bottom wall is rare due to the high degree of liquid subcooling.

During the cooling process of the reactor vessel lower head, the water surrounding vessel wall will be heated, resulting in a reduced heat loss from the outer wall, as a result the vessel shell temperature will increase. An extreme case is considered in Appendix I.E to assess the increase of the vessel shell temperature when saturated water instead of subcooled water is present around the vessel lower head. It is found that the vessel outer wall temperatures will exceed the melting temperature of steel vessel (1700 K) over a wide region and the complete failure of vessel shell is expected.

I.2.2 STEADY-STATE ANALYSIS

For various pool volumes, several equilibrium states are characterized by the steady state pool temperature and the thickness of the crust separating the molten pool from the vessel.

Governing Differential Equation of the Vessel Shell

The differential equation for the two-dimensional steady-state temperature in the spherical shell of the vessel is given by

$$\frac{1}{r^2}\frac{\partial}{\partial r}\left(r^2\frac{\partial T_w}{\partial r}\right)+\frac{1}{r^2 sin\theta}\frac{\partial}{\partial \theta}\left(sin\theta\frac{\partial T_w}{\partial \theta}\right)=0 \qquad \text{(I.22)}$$

The corresponding boundary conditions are

$$-k_w\frac{\partial T_w}{\partial r}=k_{cd}\frac{dT_{cd}}{dz}, \quad 0\leq\theta\leq\theta_0, \quad r=R_1, z=0$$

$$-k_w\frac{\partial T_w}{\partial r}=q_{w,rad}, \quad \theta_0<\theta\leq\pi/2, \quad r=R_1$$

$$-k_w\frac{\partial T_w}{\partial r}=h_L(T_w-T_L), \quad r=R_2$$

$$\frac{\partial T_w}{\partial \theta}=0, \quad \theta=0,\pi/2$$

The boundary conditions along the vessel wall are determined as follows :

Equations (I.10), (I.11), (I.12) and (I.13) for the average and local heat transfer coefficients can be used to calculate the equilibrium crust thickness and the rate of heat transfer into the vessel wall. The expressions for the radiation heat transfer given by Equations (I.7) and (I.8) and the shape factor given by Equation (I.9) can be used for the boundary condition along the unwetted vessel wall and in turn can be employed to determine the pool temperature for a certain set of values of ϵ_u, ϵ_w, ϵ_s and T_s.

For a uniform temperature of the upper surface of the pool, the tem-

perature of the pool without the upper crust is obtained as follows :

$$Q_{gen,p} = A_d h_{d,av}(T_p - T_m) + A_u h_{u,av}(T_p - T_u) \tag{I.23}$$

or

$$T_p = \frac{Q_{gen,p} + A_d h_{d,av} T_m + A_u h_{u,av} T_u}{A_d h_{d,av} + A_u h_{u,av}} \tag{I.24}$$

where

$$A_u h_{u,av}(T_p - T_u) = \frac{1}{f_{11}}\left(f_3(f_4 - f_6 f_9) + f_7(f_1 + f_2 f_9) + f_{10}(f_1 f_6 + f_2 f_4)\right) \tag{I.25}$$

For a particular temperature of the vessel outer wall, the heat transfer coefficients in natural convection or nucleate and transition boiling can be used to calculate the heat loss to the subcooled water.

Equilibrium Crust Thicknesses

At any location along the wetted vessel wall, one-dimensional steady state heat conduction equation with a distributed heat source in the lower crust is given as

$$\frac{d^2 T_{cd}}{dz^2} + \frac{q_{gen,cd}}{k_{cd}} = 0 \tag{I.26}$$

The corresponding boundary conditions are

$$T_{cd} = T_w, \quad z = 0, r = R_1$$
$$T_{cd} = T_m, \quad z = \delta_{cd}$$

The equation governing the equilibrium crust thickness is

$$k_{cd}\frac{dT_{cd}}{dz}\Big|_{z=\delta_{cd}} = h_d(T_p - T_m) \tag{I.27}$$

The resulting expression for the equilibrium crust thickness at any location along the vessel wall is obtained as

$$\delta_{cd} = \frac{-h_d(T_p - T_m) + \sqrt{[h_d(T_p - T_m)]^2 + 2k_{cd}q_{gen,cd}(T_m - T_{wi})}}{q_{gen,cd}} \tag{I.28}$$

where $T_{wi} = T_w(r=R_1)$.

The heat flux into the wetted vessel wall is obtained as

$$q_{wi} = k_{cd}\frac{dT_{cd}}{dz}\,|_{z=0} = \frac{q_{gen,cd}}{2}\delta_{cd} + (T_m - T_{wi})\frac{k_{cd}}{\delta_{cd}} \tag{I.29}$$

In the above equations T_{wi} varies along the vessel inner wall.

Assuming that the crust thickness is uniform along the upper surface of the pool, the one-dimensional heat conduction equation in the upper crust is written as

$$\frac{d^2T_{cu}}{dy^2} = 0 \tag{I.30}$$

where

$$T_{cu} = T_u, \quad y = 0$$
$$T_{cu} = T_m, \quad y = \delta_{cu}$$

The equation governing the upper crust thickness is

$$k_{cu}\frac{dT_{cu}}{dy}\,|_{y=\delta_{cu}} = h_{u,av}(T_p - T_m) \tag{I.31}$$

The resulting expression for the upper crust thickness is obtained as

$$\delta_{cu} = \frac{k_{cu}(T_m - T_u)}{h_{u,av}(T_p - T_m)} \tag{I.32}$$

where T_u is determined by considering the radiative heat transfer from the upper surface of the pool.

In writing equation (I.30) heat generation in the upper crust is not included because the thickness of this crust is expected to be small.

I.3 THERMAL BEHAVIOR OF THE BWR VESSEL SHELL

Governing Differential Equation of the Vessel Shell

The differential quations for the two-dimensional steady-state temperature in the spherical and cylindrical shells of the vessel are given by

$$\frac{1}{r^2}\frac{\partial}{\partial r}\left(r^2\frac{\partial T_w}{\partial r}\right)+\frac{1}{r^2 sin\theta}\frac{\partial}{\partial \theta}\left(sin\theta\frac{\partial T_w}{\partial \theta}\right)=0 \qquad \text{(I.33)}$$

and

$$\frac{1}{r}\frac{\partial}{\partial r}\left(r\frac{\partial T_v}{\partial r}\right)+\frac{\partial^2 T_v}{\partial x^2}=0 \qquad \text{(I.34)}$$

where the finite difference forms of Equations (I.33) and (I.34) are shown in Appendix I.F.

The corresponding boundary conditions are

$$-k_w\frac{\partial T_w}{\partial r}=k_{cd}\frac{dT_{cd}}{dz}, \quad 0\le\theta\le\theta_0, \quad r=R_1, z=0$$

$$-k_w\frac{\partial T_w}{\partial r}=q_{w,rad}, \quad \theta_0<\theta\le\pi/2, \quad r=R_1$$

$$-k_w\frac{\partial T_w}{\partial r}=h_L(T_w-T_L), \quad 0\le\theta\le\theta_1,\theta_3<\theta\le\pi/2, \quad r=R_2$$

$$-k_w\frac{\partial T_w}{\partial r}=h_a(T_w-T_{sat}), \quad \theta_1\le\theta\le\theta_2, \quad r=R_2$$

$$\frac{\partial T_w}{\partial r}=0, \quad \theta_2\le\theta\le\theta_3, \quad r=R_2$$

$$\frac{\partial T_w}{\partial \theta}=0, \quad \theta=0$$

$$T_w=T_v, \quad \theta=\pi/2, \quad x=0$$

$$k_w\frac{\partial T_v}{\partial r}=h_c(T_v-T_{sat}), \quad r=R_1$$

$$-k_w\frac{\partial T_v}{\partial r}=h_L(T_v-T_L), \quad r=R_2$$

$$\frac{\partial T_v}{\partial x}=0, \quad x=X$$

where

θ_1 = Angle of subtended by free surface of water in the vessel support

skirt.
θ_2, θ_3 = Angles between inner and outer walls of the vessel support skirt and the vessel outer wall.

Equations (I.10), (I.11), (I.12) and (I.13) for the average and local heat transfer coefficients can be used to calculate the equilibrium crust thickness and the rate of heat transfer in the vessel wall. The radiative heat fluxes from the upper surface of the pool to the unwetted vessel wall, the baffle plate, the core shroud and the upper structure are calculated by using the enclosure theory of the radiation heat transfer [21]. For the nucleate, transition and film boiling occuring on the cylindrical vessel inner wall, the appropriate correlations reported in references [24,25,26] are used.

Radiation Heat Transfer

Assuming that the surfaces are gray and using an arbitrary black surface along the top of the hemispherical vessel lower head as shown in Figure I.2, Equation (I.6) can be used for i, j = u, w, b, s, c and t where the subscript s stands for the arbitrary black surface along the top of the hemispherical vessel lower head.

Using T_w, T_b and T_c as the average temperatures along the unwetted vessel wall, the baffle plate, and the core shroud respectively, the desired radiation heat transfer rates and the shape factor are obtained as

$$Q_u = \frac{1}{\Delta_E}\left(A_1E_1 + A_2E_2 + A_3E_3\right) \tag{I.35}$$

$$Q_w = \frac{1}{\Delta_E}\left(A_4E_2 - A_5E_1 - A_6E_3\right) \tag{I.36}$$

$$Q_b = \frac{1}{\Delta_E}\left(A_7E_1 + A_8E_2 + A_9E_3\right) \tag{I.37}$$

$$Q_c = \frac{1}{\Delta_G}\left(B_1G_1 - B_2G_2\right) \tag{I.38}$$

and

$$F_{u-w} = 1 - \frac{1}{2}\left(Z - \sqrt{Z^2 - 4Y^2}\right) \tag{I.39}$$

where the expressions for A's, B's, E's, G's, Z and Y are listed in the Appendix I.G.

The values of Q_w, Q_b and Q_c can be used as the boundary conditions along the dry vessel wall, the baffle plate and the core shroud respectively, and Q_u can be used to determine the pool temperature for a certain set of values of ϵ_u, ϵ_w, ϵ_b, ϵ_c, ϵ_t and T_t.

Equilibrium Pool Temperature

The temperature of the pool bounded by the upper and lower crusts is obtained from an energy balance as

$$Q_{gen,p} = (A_d h_{d,av} + A_u h_{u,av})(T_p - T_m) \tag{I.40}$$

or

$$T_p = T_m + \frac{Q_{gen,p}}{A_d h_{d,av} + A_u h_{u,av}} \tag{I.41}$$

where

$$A_u h_{u,av}(T_p - T_m) = \frac{1}{\Delta_E}(A_1 E_1 + A_2 E_2 + A_3 E_3) \tag{I.42}$$

For a uniform temperature of the upper surface of the pool, T_u, the temperature of the pool without the upper crust is obtained as follows:

$$Q_{gen} = A_d h_{d,av}(T_p - T_m) + A_u h_{u,av}(T_p - T_u) \tag{I.43}$$

or

$$T_p = \frac{Q_{gen,p} + A_d h_{d,av} T_m + A_u h_{u,av} T_u}{A_d h_{d,av} + A_u h_{u,av}} \tag{I.44}$$

where

$$A_u h_{u,av}(T_p - T_u) = \frac{1}{\Delta_E}(A_1 E_1 + A_2 E_2 + A_3 E_3) \tag{I.45}$$

For a particular temperature of the vessel outer wall, the heat transfer coefficients in natural convection or nucleate and transition boiling can be used to calculate the heat loss to the subcooled water and the steam in the air pocket of the vessel support skirt.

Heat Transfer from the Vessel Outer Wall

Equations (I.20) and (I.21) for the nucleate and transition boiling heat transfer coefficients can be used to calculate the heat loss to the subcooled water. Water level in the BWR vessel support skirt is about 4.0 inches above the vessel bottom head when the drywell is flooded with subcooled water up to near the top of the recirculation nozzle. It is assumed that the pocket formed in the vessel support skirt contains mostly saturated steam generated from the nucleate boiling occuring on the bottom of the vessel outer wall. For the steam in the air pocket, the heat transfer coefficient is found to be

$$h_a = 0.00367(1.414 + 13.84(T_{wo} - T_{sat})^{1/6})^2 \qquad \text{(I.46)}$$

While a stationary water level in the vessel skirt is used in this study, the variations in the water level could occur because of chugging cycle established by the generation of steam within the skirt, the expulsion of water, the condensation of steam on the inner skirt surface, and the reentry of the water to again contact the bottom head [4]. A detailed analysis of the cyclic variations of the water level within the vessel skirt would require further investigations of the amount of steam generated, the rate of steam condensed, and the heat transport from the vessel outer wall to the skirt inner and water free surface through steam-air mixture.

Heat Transfer into Water in the Downcomer Region

Due to radiation heat transfer from the upper surface of the molten pool, the temperatures along the baffle plate and the lower core shroud become much higher than the saturation temperature of water in the downcomer region. The heat transfer coefficient for film boiling on the inner wall of the baffle plate and the inner wall of the lower core shroud are used to calculate the heat transfer to the saturated water in the downcomer region. In this study, the downcomer region is assumed to be filled with water up to the height of the recirculation outlet nozzle. Water is at the saturation temperature at one atmosphere pressure.

The correlation for the film boiling heat transfer coefficient on the flat

plate is obtained from Berenson [27]. The heat transfer coefficient excluding radiation is found to be

$$h_e = (451.4 + 0.3T_{ei})(T_{ei} - T_{sat})^{-1/4} \qquad \text{(I.47)}$$

where T_{ei} is the inner wall temperature of the baffle plate.

The correlations for the heat transfer coefficients in the nucleate, transition and film boiling on the vertical wall are obtained from the results of Dhir and Liaw [24] and Bui and Dhir [25,26]. The heat transfer coefficients in nucleate, transition and film boiling are determined to be

$$h_c = 4.881(T_{ci} - T_{sat})^{2.883}, \quad 373 \leq T_{ci} \leq 393K \qquad \text{(I.48)}$$

$$h_c = 4.512 \times 10^7 (T_{ci} - T_{sat})^{-2.503}, \quad 393 \leq T_{ci} \leq 517K \qquad \text{(I.49)}$$

and

$$h_c = (463.8 + 0.31T_{ci})(T_{ci} - T_{sat})^{-1/4}, \quad 517K \leq T_{ci} \qquad \text{(I.50)}$$

where T_{ci} is the inner wall temperature of the lower core shroud.

In writing the heat transfer correlations (I.47) and (I.50), the variations in vapor properties with temperature are included by using a least square linear fit.

I.4 STRESSES IN THE VESSEL SHELL

The temperature distribution obtained in the hemispherical (PWR and BWR) and cylindrical (BWR) vessel shells can be used to calculate the effective stresses at a given system pressure. In this work, linear elasticity theory is used as a first step in obtaining the distribution of the stresses and displacements in the vessel shell and no allowance is made for relaxation of stresses. The results of present analysis are accurate for the regions of vessel wall in which the stresses are lower than yield stress of steel. For regions in which stresses are above the elastic limit, the analysis only provides the possibility of plastic deformation. In order to get more reliable results, large deformation theory or plasticity analysis will be required.

Using the axial symmetry of the vessel shell, the equilibrium equations in spherical coordinates (r,θ,ϕ) are given by [28]

$$\frac{\partial \sigma_{rr}}{\partial r} + \frac{1}{r}\frac{\partial \sigma_{r\theta}}{\partial \theta} + \frac{1}{r}(2\sigma_{rr} - \sigma_{\theta\theta} - \sigma_{\phi\phi} + \sigma_{r\theta}cot\theta) = 0 \qquad (51)$$

and

$$\frac{\partial \sigma_{r\theta}}{\partial r} + \frac{1}{r}\frac{\partial \sigma_{\theta\theta}}{\partial \theta} + \frac{1}{r}[(\sigma_{\theta\theta} - \sigma_{\phi\phi})cot\theta + 3\sigma_{r\theta}] = 0 \qquad (52)$$

where σ_{ij} is the ij component of the stress tensor.

The linear stress-strain-temperature relations can be expressed as [28]

$$\sigma_{rr} = \lambda d + 2\mu e_{rr} - (3\lambda + 2\mu)\alpha T \qquad (53)$$

$$\sigma_{\theta\theta} = \lambda d + 2\mu e_{\theta\theta} - (3\lambda + 2\mu)\alpha T \qquad (54)$$

$$\sigma_{\phi\phi} = \lambda d + 2\mu e_{\phi\phi} - (3\lambda + 2\mu)\alpha T \qquad (55)$$

$$\sigma_{r\theta} = 2\mu e_{r\theta} \qquad (56)$$

where e_{ij} is the ij component of the strain tensor, d is the dilatation, T is the temperature increase, λ and μ are the Lame constants and α is the coefficient of thermal expansion of the material.

$$d = e_{rr} + e_{\theta\theta} + e_{\phi\phi}$$

The strain-displacement relations are given by [28]

$$e_{rr} = \frac{\partial u_r}{\partial r} \tag{57}$$

$$e_{\theta\theta} = \frac{1}{r}\left(\frac{\partial u_\theta}{\partial \theta} + u_r\right) \tag{58}$$

$$e_{\phi\phi} = \frac{1}{r sin\theta}(u_r sin\theta + u_\theta cos\theta) \tag{59}$$

$$e_{r\theta} = \frac{1}{2}\left(\frac{1}{r}\frac{\partial u_r}{\partial \theta} + \frac{\partial u_\theta}{\partial r} - \frac{u_\theta}{r}\right) \tag{60}$$

where u_i is the i^{th} component of the displacement vector.

Using stress-strain and strain-displacement relations given by Equations (I.53) - (I.60), stresses can be expressed in terms of displacements and temperature gradients. Substituting these in Equations (I.51) and (I.52), a system of coupled second-order differential equations for the displacement components u_r and u_θ are obtained.

$$\begin{aligned}(\lambda+2\mu)\frac{\partial^2 u_r}{\partial r^2} + \frac{2}{r}(\lambda+2\mu)\frac{\partial u_r}{\partial r} + \frac{\mu}{r^2}\frac{\partial^2 u_r}{\partial \theta^2} + \frac{\mu}{r^2}cot\theta\frac{\partial u_r}{\partial \theta} - \\ \frac{2}{r}(\lambda+2\mu)u_r + \frac{1}{r}(\lambda+\mu)\frac{\partial^2 u_\theta}{\partial\theta\partial r} + \frac{cot\theta}{r}(\lambda+\mu)\frac{\partial u_\theta}{\partial r} - \\ \frac{1}{r^2}(\lambda+3\mu)\frac{\partial u_\theta}{\partial\theta} - \frac{cot\theta}{r^2}(\lambda+3\mu)u_\theta - (3\lambda+2\mu)\alpha\frac{\partial T}{\partial r} = 0\end{aligned} \tag{61}$$

and

$$\begin{aligned}\frac{1}{r}(\lambda+\mu)\frac{\partial^2 u_r}{\partial r\partial\theta} + \frac{2}{r^2}(\lambda+2\mu)\frac{\partial u_r}{\partial\theta} + \mu\frac{\partial^2 u_\theta}{\partial r^2} + \frac{2\mu}{r}\frac{\partial u_\theta}{\partial r} + \\ \frac{1}{r^2}(\lambda+2\mu)\frac{\partial^2 u_\theta}{\partial\theta^2} + \frac{1}{r^2}(\lambda+2\mu)cot\theta\frac{\partial u_\theta}{\partial\theta} - \\ \frac{1}{r^2 sin^2\theta}(\lambda+2\mu)u_\theta - \frac{1}{r}(3\lambda+2\mu)\alpha\frac{\partial T}{\partial\theta} = 0\end{aligned} \tag{62}$$

The above equations can, in principle be solved for the displacements in the spherical shell once the temperature profiles are known. The obtained displacements can then be used to calculate the strains given by Equations (I.57) - (I.60) and the stresses given by Equations (I.53) - (I.56). However, it is difficult to obtain an analytical solution due to

the complexity of the temperature field. In this study a finite element code (NASTRAN) in conjunction with the linear elasticity theory is employed to calculate the displacement and stress fields in the spherical vessel shell. Large deformation theory or plasticity analysis are required to obtain more reliable results. Since at temperature near 1000 K, carbon steel undergoes a ferrite-to-austenite phase transformation [6] which affects the material properties considerably, the coefficient of thermal expansion is evaluated at 800 K. Axisymmetric analysis using a 6-node triangular element is used. In the FEM modeling, when the average temperature of an element exceeds the melting temperature of steel (1700 K), the corresponding element is eliminated.

The calculated principal stresses are used to determine the effective stress in accordance with the Von-Mises criterion that yielding occurs when the effective stress reaches a value that is equal to the yield stress,

$$\sqrt{\frac{1}{2}\left[(\sigma_{rr}-\sigma_{\theta\theta})^2+(\sigma_{\theta\theta}-\sigma_{\phi\phi})^2+(\sigma_{\phi\phi}-\sigma_{rr})^2\right]} \geq \sigma_Y \qquad (63)$$

In order to implement the finite element code it is necessary to specify the boundary conditions. The vessel inner wall is subjected to the system pressure. The vessel outer wall is assumed to be traction free, neglecting the atmospheric pressure. This assumption is not valid for the system pressure less than 1 MPa. Because of the geometric symmetry of the vessel shell, a roller type boundary condition is applied at the bottom of the hemispherical shell ($\theta = 0^o$). Since the upper portion of the hemispherical (PWR) vessel shell merges into the cylindrical vessel shell, it is difficult to obtain the exact boundary condition on the lower vessel head unless the upper cylindrical shell is included in this analysis. Because of this uncertainty, two types of boundary conditions are employed to estimate the extreme behavior of the vessel shell due to thermal stresses. The two extreme conditions are a clamped and a roller type boundary condition on the upper part of the vessel shell.

Figures I.3 and I.4 show the typical finite element modeling of the PWR and the BWR vessel shells respectively with the boundary conditions at the lower and at the upper parts of the vessel shell.

Clamped Boundary Condition
at $\theta = \pi/2$

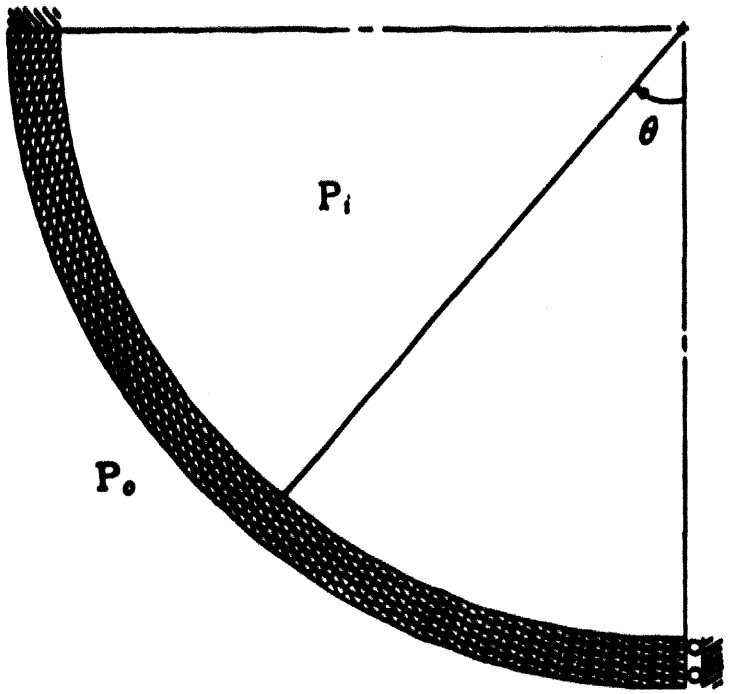

Roller Boundary Condition
at $\theta = \pi/2$

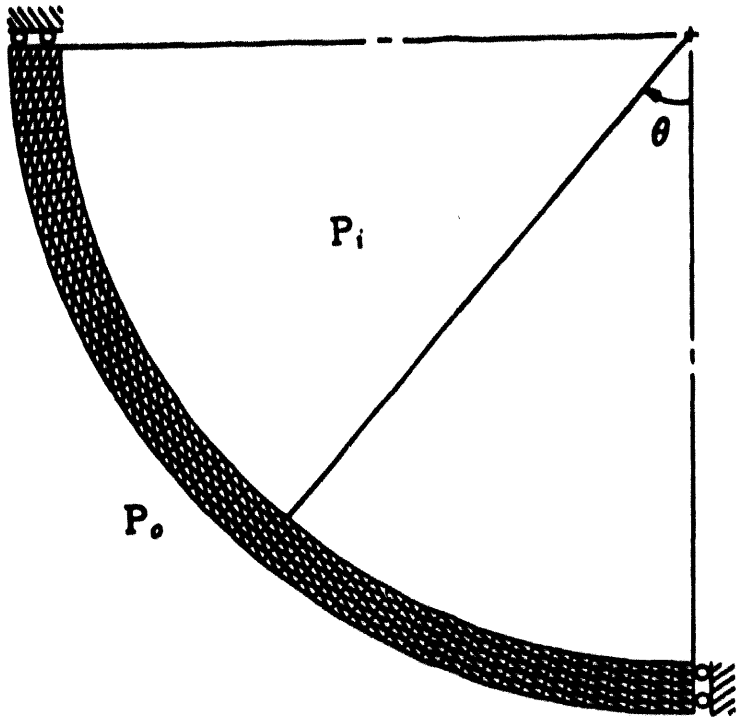

Figure I.3: Finite element modeling (PWR) with boundary condition

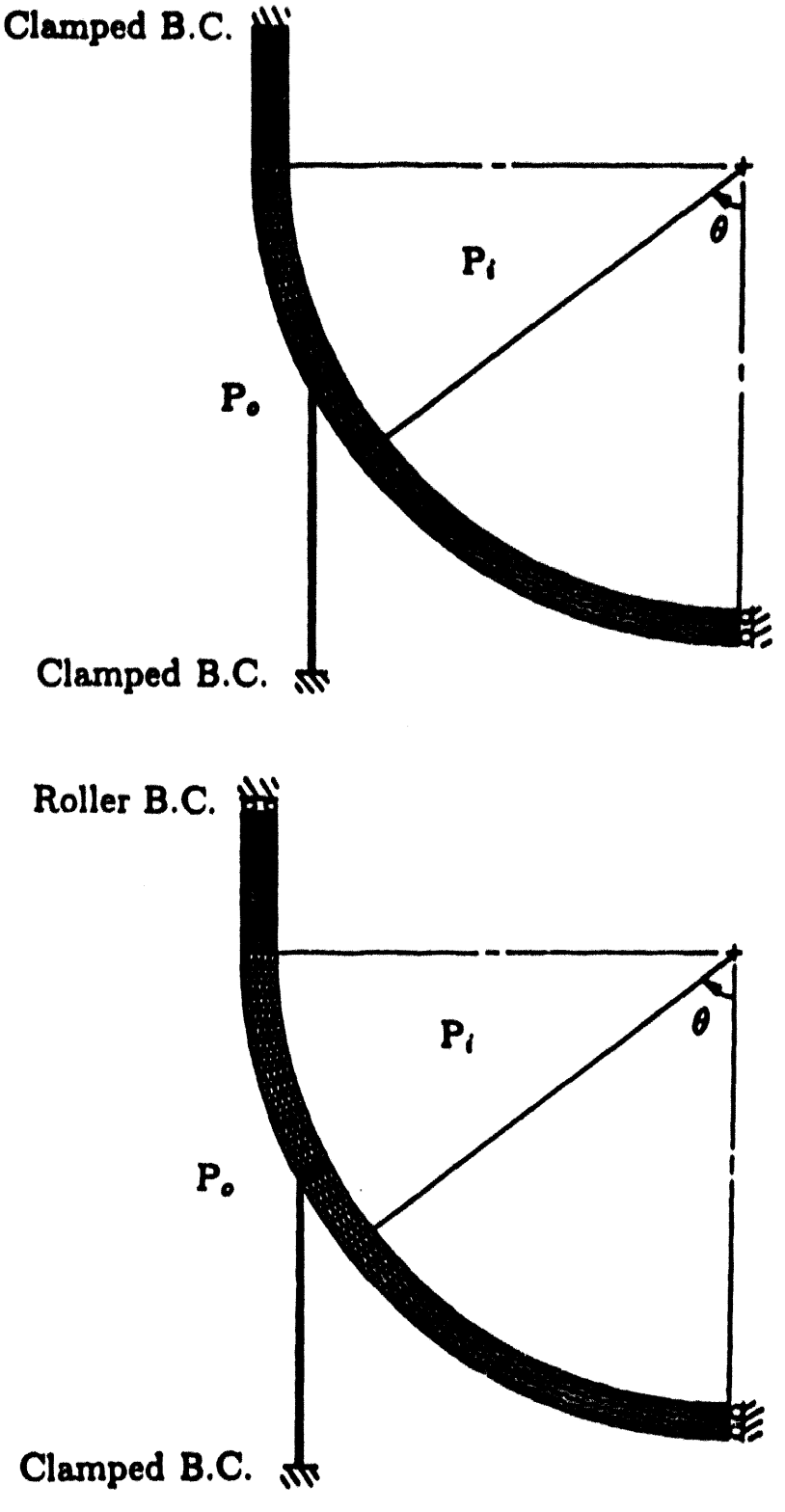

Figure I.4: Finite element modeling (BWR) with boundary condition

It should be noted that the roller boundary conditions are only approximately satisfied in the FEM model, due to the fact that the vanishing of the shear stress at the support is satisfied in a global sense. In the present problem, the FEM code yielded shear stresses at the boundary nodes whose magnitudes are of the order of 0.3 MPa. Since the other nonzero stress components in the vessel wall are significantly higher than this, the FEM solution is deemed to be satisfactory.

I.5 CREEP RUPTURE ANALYSIS

The effect of creep on the vessel shell is quite complex and is not easily quantified when the temperature varies in the vessel shell. Even though the temperature distribution used in reference [5] restricts the temperatures on the inside surface of the vessel lower head to a high value of 1255K, the transient is not really long enough to cause any significant creep in the wall which could in turn lead to rupture. For transients of short duration, creep only causes the high thermal compressive stresses on the inner surface to relieve rather quickly and in turn allows the wall to carry load on its outer portions.

The reactor vessel lower heads are generally fabricated from the plate material, SA533B1 Carbon Steel. The INEL [6] has performed isothermal creep tests up to 1423 K to extend the structural property database for vessel steel. For the SA533B1 Carbon Steel, the master creep curve shown in Figure I.5 was developed by employing a least-squares fit to the creep rupture data obtained in the INEL tests [6].

The rupture time for the reactor vessel lower head sujected to the given system pressure at several elevated temperatures are calculated. For a given stress, S(in ksi), the Larson-Miller [29] parameter is given by the equation

$$T(20 + logt_r) = 10^3[49.01 - 13.106logS] \tag{64}$$

where T is the absolute temperature in degrees Rankine and t_r is the rupture time in hours.

The hoop stress in the hemispherical shell is given by

$$\sigma_{\theta\theta} = \frac{P_i R_1}{2(R_2 - R_1)} \tag{65}$$

Since the hoop stress from the above equation is the principal stress, the equivalent stress in the hemispherical shell subjected to system pressure P_i is obtained by using the criterion that yielding occur when the maximum shear stress reaches a value that is equal to the yield stress in the tensile test, [30].

$$S = \sigma_{00} + P_i \tag{66}$$

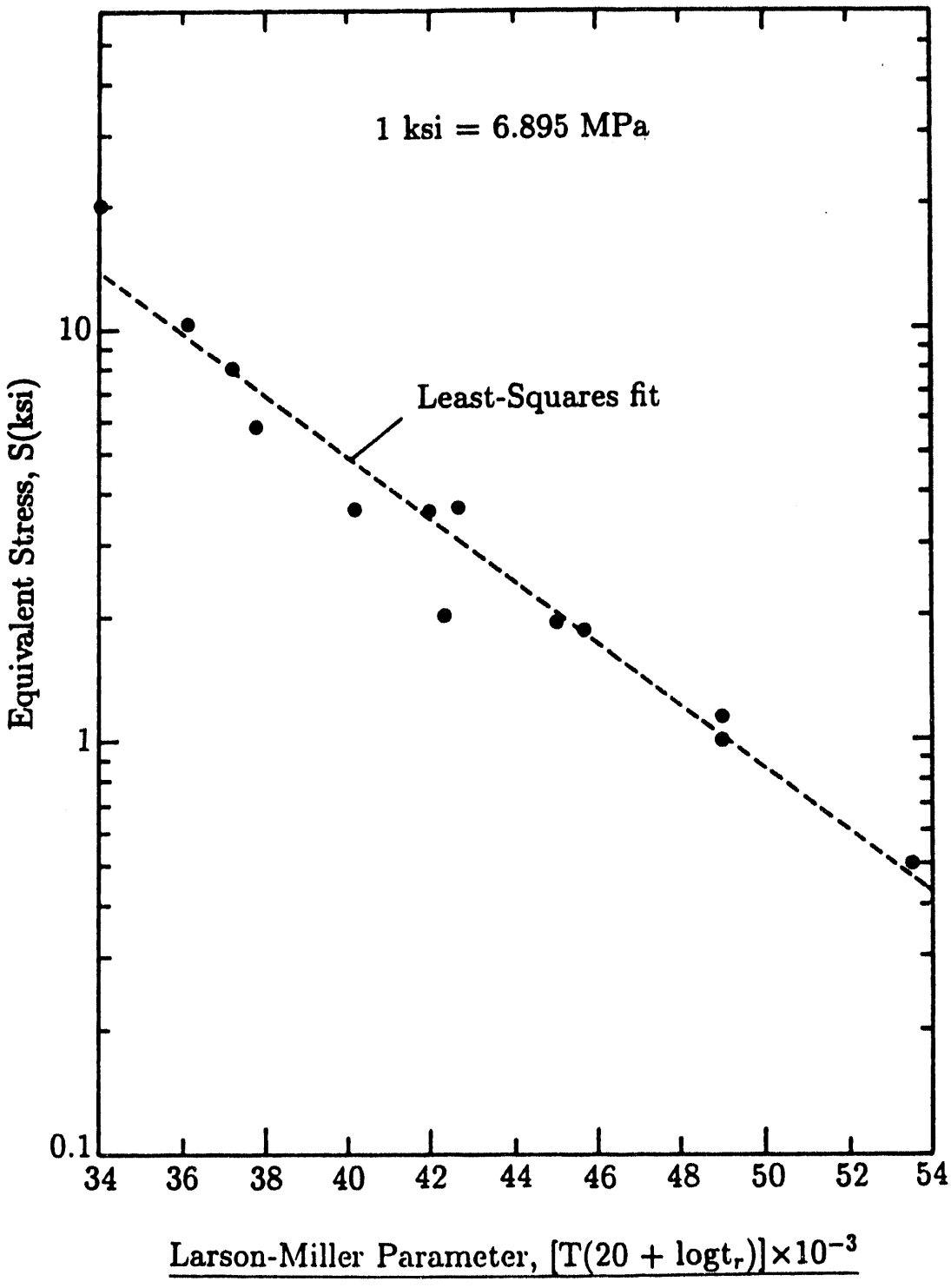

Figure I.5: Master creep rupture curve for SA533B1 carbon steel

where the stress value, in Pascals, is converted to ksi using the following relationship:

$$1 \text{ ksi} = 6.895 \text{ MPa}$$

For a given stress, the time to rupture is related to the average temperature in the vessel shell by the Larson-Miller parameter given by Equation (I.64).

It should be noted that a large uncertainty exists in the prediction of creep rupture times for situations in which large temperature gradients occur across a vessel wall. The calculated rupture times based on the properly chosen wall temperatures and accumulation of damage can be used to estimate the probability of vessel failure during flooding of the cavity of a PWR and the drywell of a BWR.

I.6 RESULTS AND DISCUSSION

I.6.1 FLOODING OF THE PWR CAVITY

Transient and steady state temperatures in the PWR vessel shell were obtained when half or full core was assumed to drop into the vessel lower head. Calculations were performed by varying between 0.1 and 0.8 the emissivity, ϵ_w, of the vessel, the emissivity, ϵ_s, of the upper structure and the emissivity, ϵ_u, of the free surface of the pool. The upper structure temperature was assumed to be either 800 or 1600 K. For the calculational convenience, the temperature of the upper structure is limited to 1600 K which is around the melting temperature of the structure. No subsequent melting or relocation of the core material are considered in this study. Results were obtained by using heat transfer coefficients for the lower part of the pool as given by Mayinger et al [12] and Gabor et al [13]. This was done to understand as to how uncertainties in the modeling of physical processes can influence the evaluation of accident management strategies.

Thermal Behavior of A PWR Vessel Shell

Figure I.6 shows the variation of the pool temperature and crust thickness with time when the molten pool contains full core and Mayinger et al's correlation is used. The results are plotted for the time period up to about 3 hours after relocation of the core material into the vessel lower head. According to the experimental correlations (shown in Appendix I.H), the time scales required to develop steady convection in the volumetrically heated pool are about $2 \sim 3$ hours. These heatup times are predicted by extending the correlations to large Rayleigh numbers encountered in this problem. The heatup of the pool begins at 2000 seconds after relocation of the core material. As stated earlier this is a result of the assumption that pool remains at the melting temperature of corium until heat loss rate from the pool equals the heat loss rate from the vessel outer wall. This duration is considered to be sufficient to allow solids contained in the molten material as it relocates to melt. Steady state condition is assumed to prevail at the start of the heatup period. This may be somewhat optimistic since much longer times may

be needed for convective flows to fully establish. Because initial heatup of the pool occurs very rapidly, the effect of use of steady state heat transfer coefficient on time to reach steady state will be small. The pool temperature is observed to increase asymptotically to the steady state value of 2865 K. The thickness of the crust at $\theta = 0^o$ increases with time up to about 2000 seconds. Thereafter a gradual remelting of the crust occurs. It appears that time periods much longer than 10000 seconds are needed for the crust to attain its steady state value of 4.7 cm. The upper crust, however, very quickly remelts after pool begins to heat up. Similar results were obtained for $V_p = 1/2\ V_{core}$.

Figure I.7 shows the variation of crust thickness around the vessel inner wall for different times when Mayinger et al's correlation is used. Prior to heatup of the pool, the thickness of the crust around the vessel is nearly uniform. However, after the pool heats up and convective motion sets in, the crust thins. Under steady state conditions the crust is the thickest at the lower stagnation point. The crust thickness decreases along the vessel inner wall. The variation of steady state crust thickness along the vessel is the reflection of the dependence of the magnitude of convective heat transfer coefficient on the angular position along the vessel wall.

The temperature along the vessel inner wall is plotted in Figure I.8 for several times after relocation of the core material when Mayinger et al's correlation is used. The predictions plotted in this figure are for full core when the upper structure temperature is chosen to be 1600 K. It is very difficult to determine apriori the temperature of the upper structure as it depends on several unknowns such as fractions of core and structural material that remain in their original location and the development of natural circulation between the the reactor vessel and the steam generator. It is seen that for the chosen set of emissivities, inner wall temperatures are predicted to exceed the melting temperature of steel over a wide region below and above the pool free surface. The highest vessel inner wall temperatures occur near the free surface of the pool because of the radiative heat transfer to the unwetted portion above the pool and the very high convective heat transfer coefficient just below the free surface.

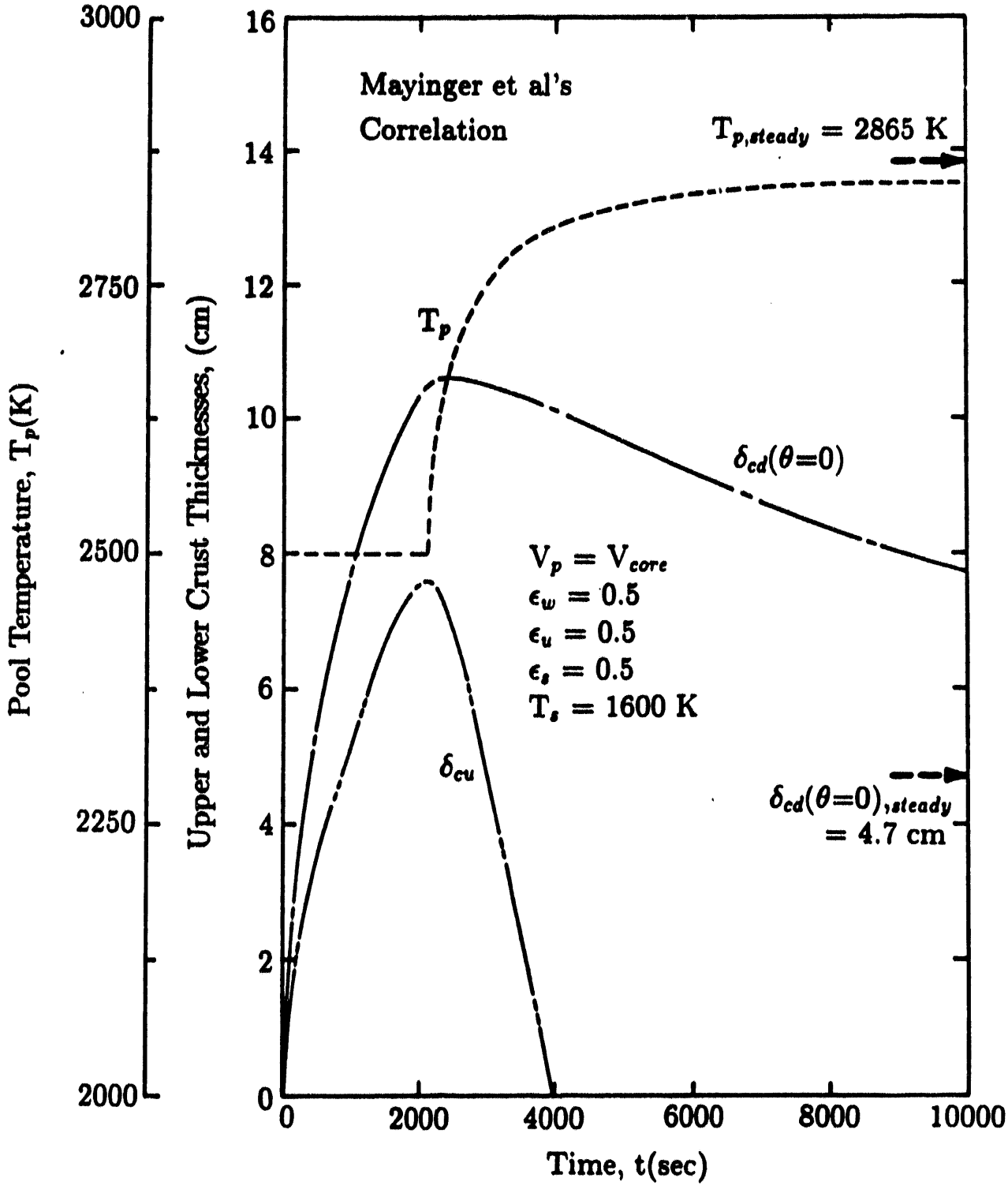

Figure I.6: Variation of pool temperature and crust thickness with time

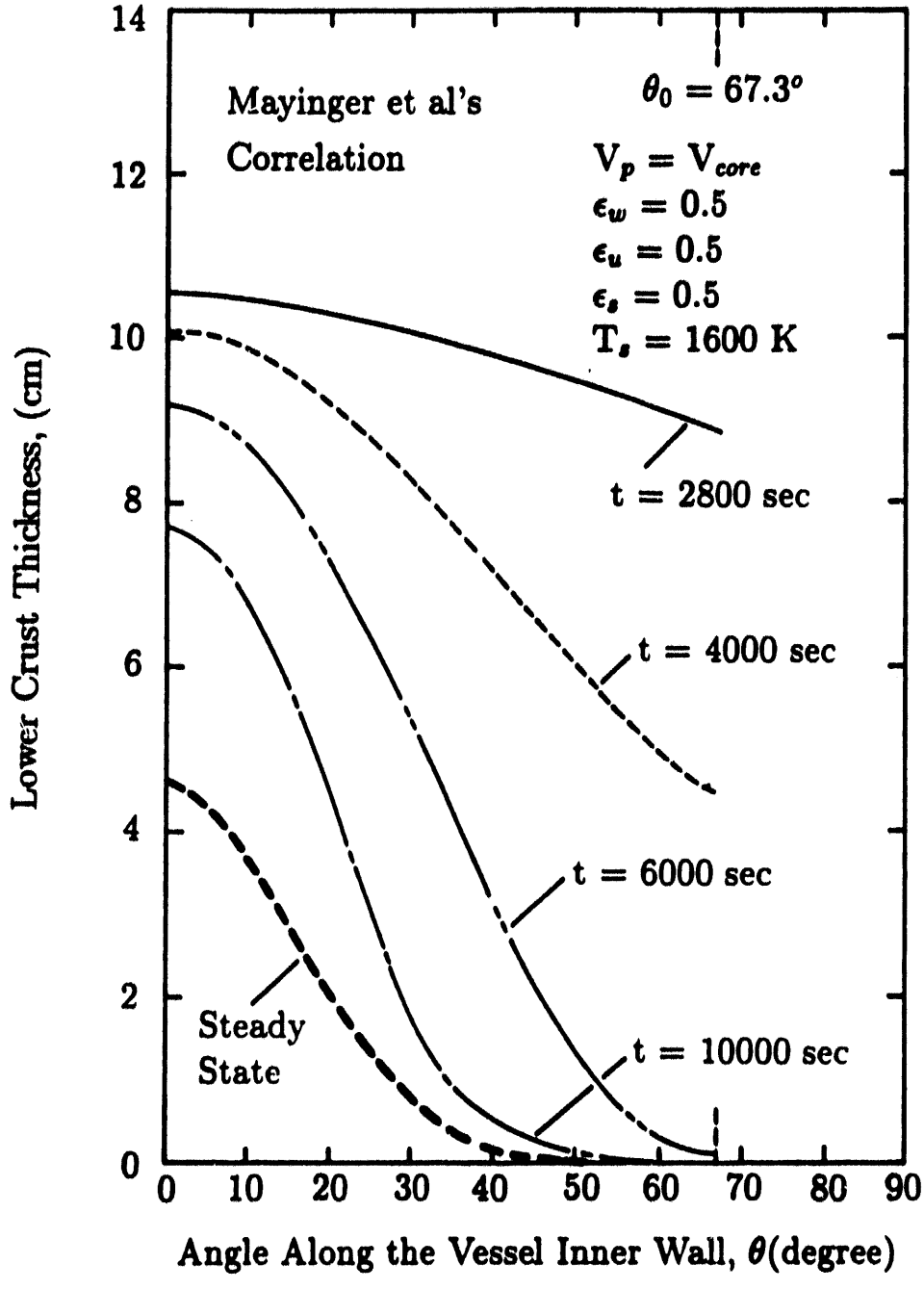

Figure I.7: Variation of lower crust thickness along the vessel inner wall with time

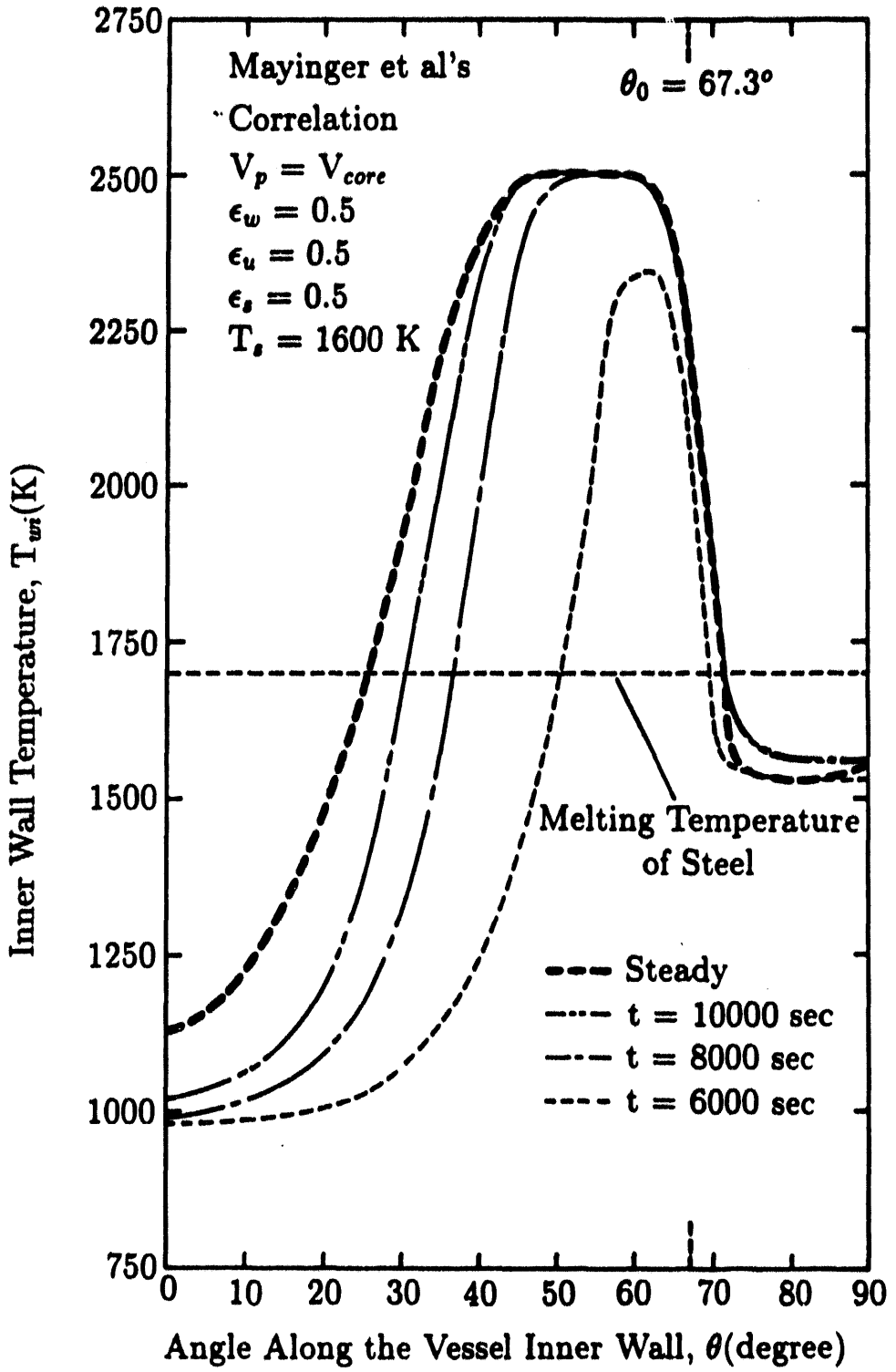

Figure I.8: Variation of inner wall temperature with time for $V_p = V_{core}$

Steady state pool temperatures when vessel lower head contains the full core or half of the core are plotted in Figure I.9 as a function of emissivity of the pool free surface. Since the correlation of Mayinger et al yields average downward heat transfer coefficients that are about 12 times (for $V_p = V_{core}$) and 19 times (for $V_p = 1/2\ V_{core}$) higher than those given by Gabor et al, the pool temperatures predicted by using the correlation of Mayinger et al are lower than those obtained by using the correlation of Gabor et al. The pool temperature decreases as the pool free surface emissivity increases or heat loss from the pool free surface increases. The pool temperature predicted by using Gabor et al's correlation shows a strong dependence on the pool surface emissivity. This is due to the higher radiative heat loss from the pool free surface. However, the pool temperature predicted by using Mayinger et al's correlation shows little effect of the pool surface emissivity. This is due to the higher heat loss to the vessel wall when Mayinger et al's correlation is used. The predicted pool temperatures are lower for $V_p = 1/2\ V_{core}$ mainly due to large reduction in pool volume in comparison to pool surface area. It was also found that the pool temperature increases as the structure temperature increases and as emissivity of the vessel wall decreases.

Figure I.10 shows the thickness of the crust along the vessel inner wall for a given set of parameters. For the correlation of Mayinger et al, the crust thickness profile shows an inverse dependence on the profile of the heat transfer coefficient along the pool boundary. The crust thickness for angular positions larger 40^o is very thin. However, when the heat transfer coefficient is small, a thicker crust is predicted to be present along the vessel inner wall.

The vessel inner wall temperature is plotted in Figure I.11 as a function of angular position. For higher internal heat transfer coefficients, circumferential conduction becomes important. Because of the much higher heat transfer rate into the wetted wall of the pool and the lower pool temperature when Mayinger et al's correlation is used, less heat is transferred by radiation to the unwetted portion of the vessel inner wall. This in turn, results in a large temperature drop in the unwetted wall of the vessel. It can be seen that the inner wall temperature increases sharply up to

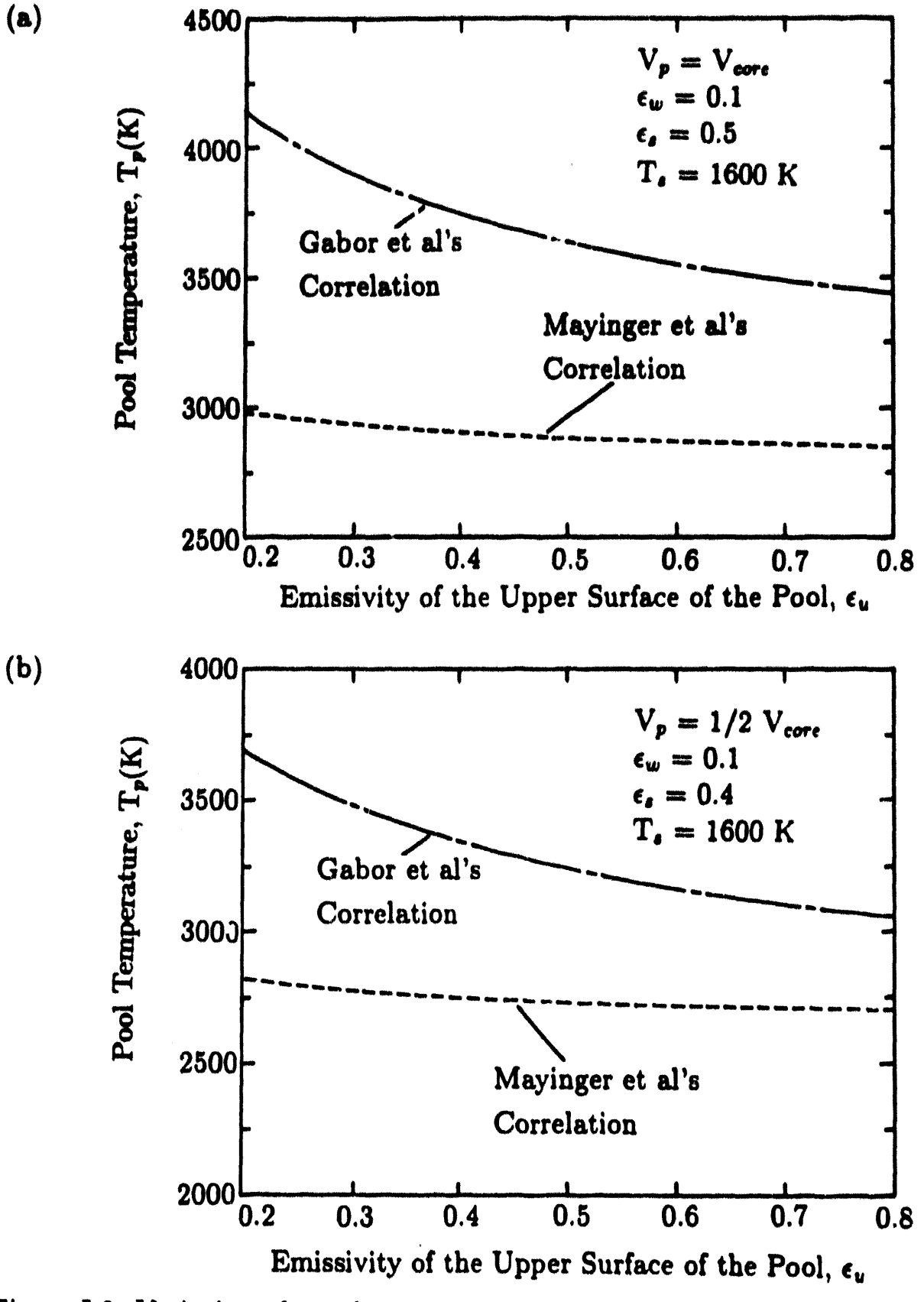

Figure I.9: Variation of steady state pool temperature with emissivity of the upper surface of the pool

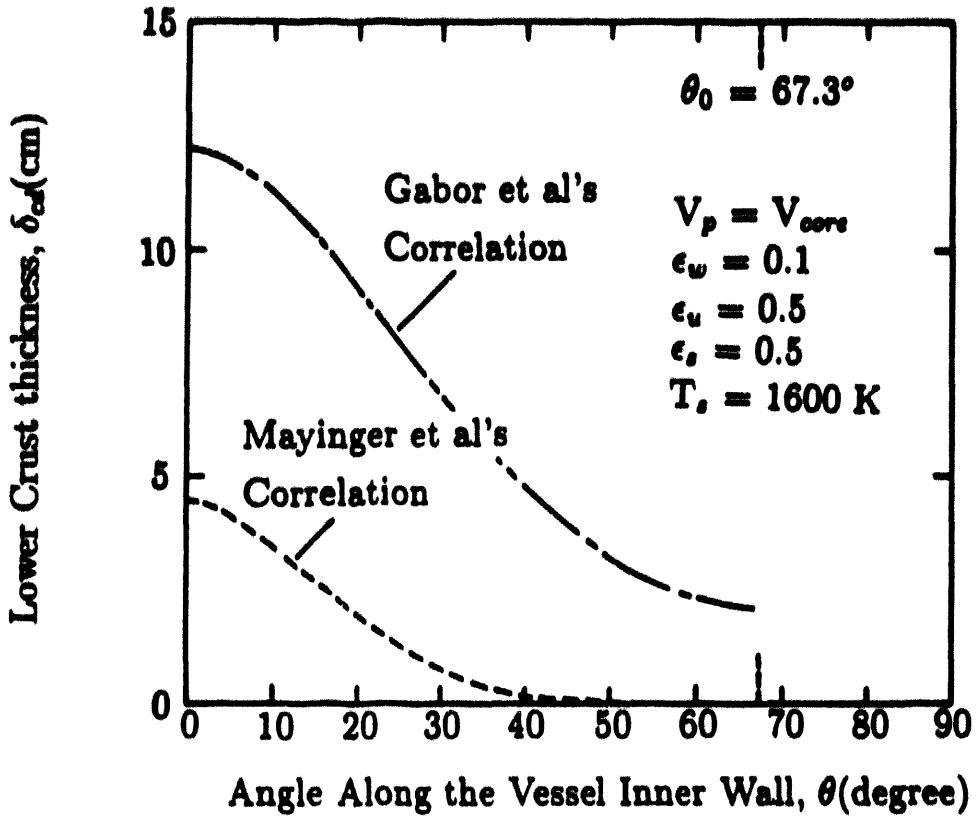

Figure I.10: Variation of the lower crust thicknes

about the melting temperature of the crust (2500 K) for angular positions larger than about 40° and remains at this high temperature near the pool free surface.

Under steady state conditions the fraction of generated energy that goes into structure, the unwetted and the wetted portion of the vessel wall are plotted in Figure I.12. It is seen that for Mayinger et al's correlation as much as 50-70 % of the total energy generated in the pool is lost to the wetted portion of the vessel. However, only about 10 - 20 % of the energy generated in the pool is lost to the wetted portion of the vessel when Gabor et al's correlation is used. It is noted that between 70 to 80 % of the decay heat is absorbed in the structure that does not relocate with the core and the vessel upper walls when Gabor et al's correlation is used. This energy must get redistributed in the remainder of the reactor coolant system (RCS) by natural circulation. As such this raises the possibitity of the failure of the hot leg or the steam generator tubes. Such a failure will open a new path for escape of radioactivity into the containment.

Isotherms in the reactor vessel wall when full or half core relocates are plotted in Figures I.13 - I.15. It is seen that significant variation of temperature occurs with radial and angular positions and it points to the shortcomings that may exist in predictions made by employing one dimensional analysis. The highest temperature occurs near the vicinity of the triple interface between wetted and unwetted portion of the vessel wall and the pool free surface. Figure I.13 shows the isotherms obtained by using the two heat transfer correlations for $V_p = V_{core}$. For the correlation of Mayinger et al which yields average downward heat transfer coefficients that are about 12 times higher than those given by Gabor et al, higher inner wall temperature and lower pool temperature are predicted to occur. The vessel inner wall temperature under the crust exceeds the melting temperature of steel (1700 K) over a wide area when Mayinger et al's correlation is used. However, the inner wall temperature when Gabor et al's correlation is used does not exceed the melting temperature of steel for the parameters considered.

Figure I.14 shows the isotherms for the same conditions as Figure I.13

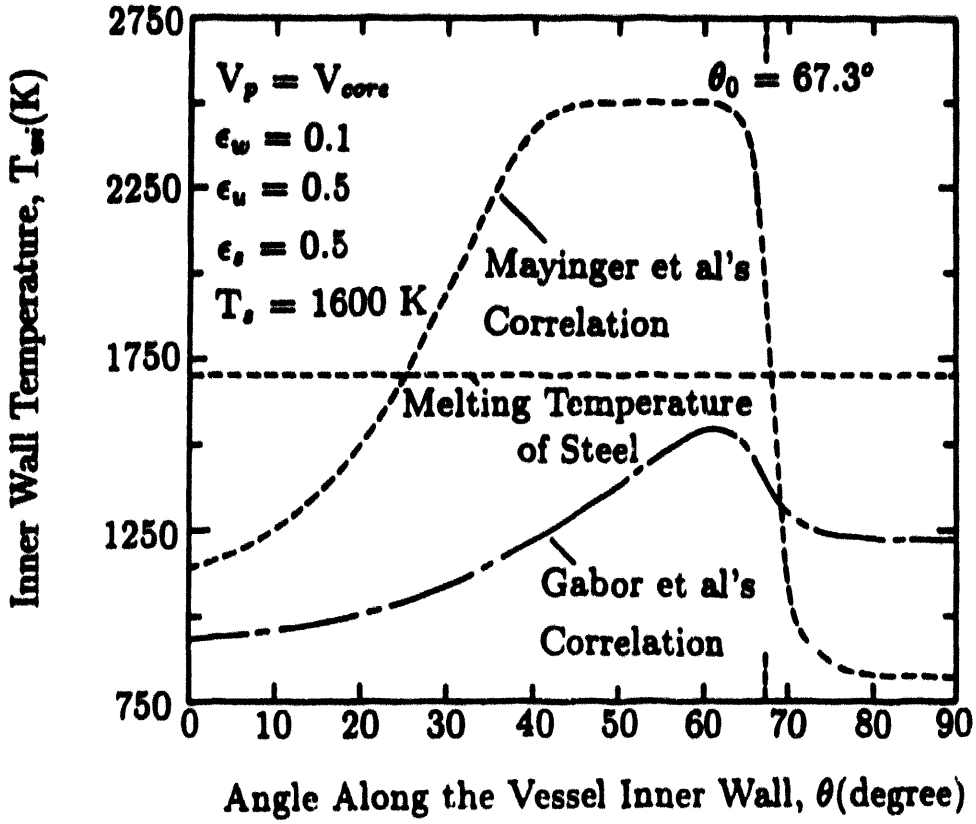

Figure I.11: Variation of the inner wall temperature

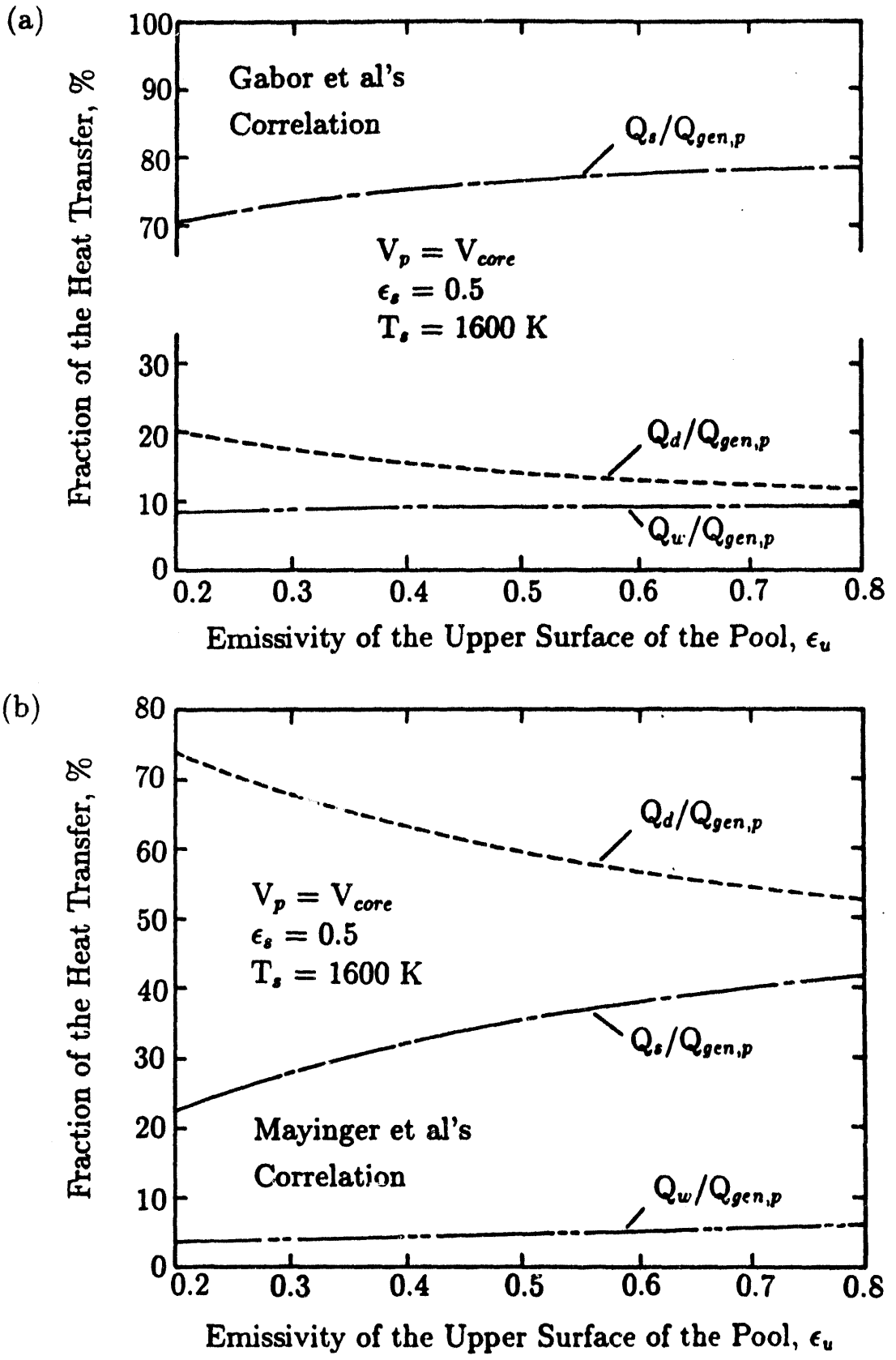

Figure I.12: Partition of the heat generated from the molten pool

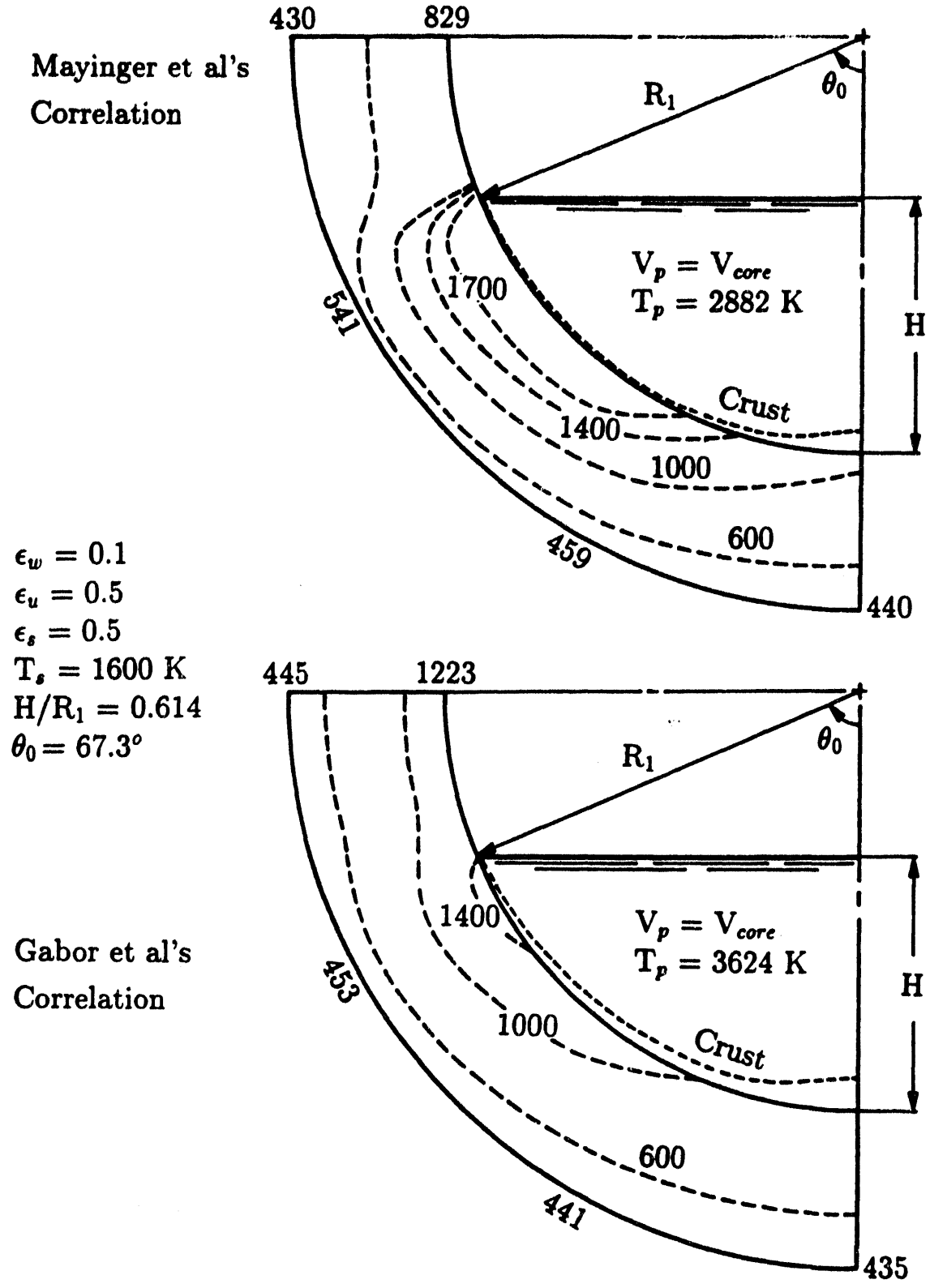

Figure I.13: Temperature distribution in the vessel shell

but with ϵ_w increased to 0.5. In this case melting of the unwetted portion of the vessel wall is predicted to occur when Gabor et al's correlation is used. The contour of the unwetted wall after melting has occured has been obtained from the steady state calculations. Although transient calculations were not carried out to precisely determine the contour of the unwetted vessel when melting stops i.e. the inner wall temperature drops below the melting temperature of steel. Simplified analysis, however, shows that melting will stop with further thinning of the vessel wall.

Figure I.15 shows the isotherms when only half of the core material is assumed to relocate into the vessel lower head. For the correlation of Mayinger et al which yields average downward heat transfer that are about 19 times higher than those obtained from the work of Gabor et al, higher inner wall temperature and lower pool temperature are predicted. The inner wall temperature under the crust in the upper portion of the vessel when Mayinger et al's correlation is used exceeds the melting temperature of steel over a region just below the pool free surface. However, the inner wall temperature with Gabor et al's correlation does not exceed the melting temperature of steel for all sets of parameters.

Simple calculations are performed to estimate the possible minimum vessel shell thickness if the molten steel along the vessel inner wall is mixed with the molten corium because of the instability of the very thin corium crust separating the molten corium from the molten steel as shown in Figures I.13 to I.15. After the trapped molten steel is allowed to mix with the molten corium, the melting of the vessel wall will not propagate further if the inner wall temperature falls below the melting temperature of steel. Using the one-dimensional heat conducton through the vessel wall, the heat flux is given by

$$q_w = \frac{k_w}{\delta_w}(T_{ms} - T_{wo}) = h_L(T_{wo} - T_L) \tag{I.67}$$

or

$$q_w = \frac{q_{gen,cd}}{2}\delta_{cd} + (T_m - T_{ms})\frac{k_{cd}}{\delta_{cd}} \tag{I.68}$$

where T_{ms} is the melting temperature of steel (1700 K), δ_w is the minimum wall thickness, h_L is given by Equations (I.20) and (I.21) and the equilibrium crust thickness is given by Equation (I.28) in which T_{ms} and

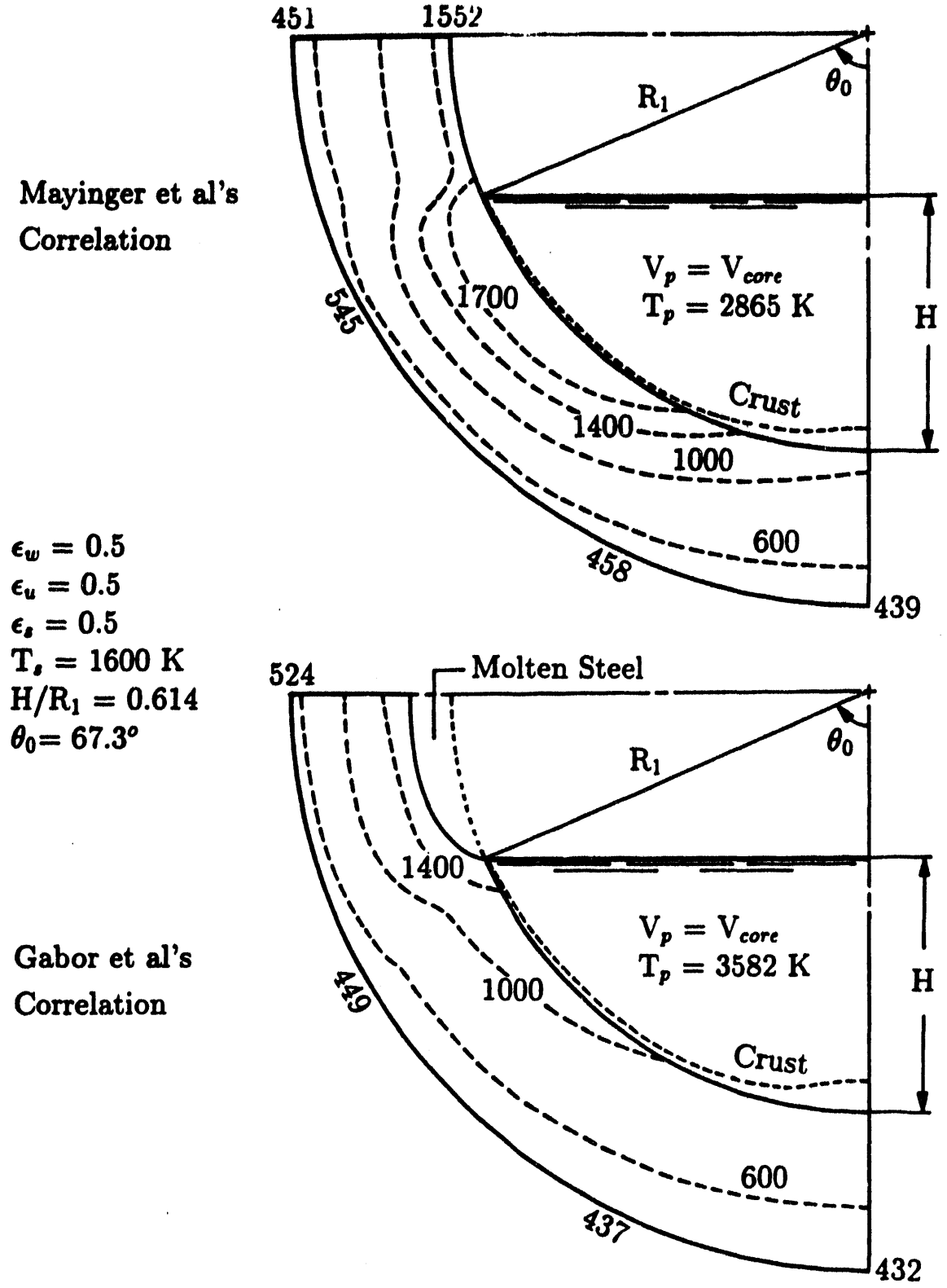

Figure I.14: Temperature distribution in the vessel shell

Mayinger et al's Correlation

$\epsilon_w = 0.1$
$\epsilon_u = 0.5$
$\epsilon_s = 0.5$
$T_s = 1600$ K
$H/R_1 = 0.418$
$\theta_0 = 54.4°$

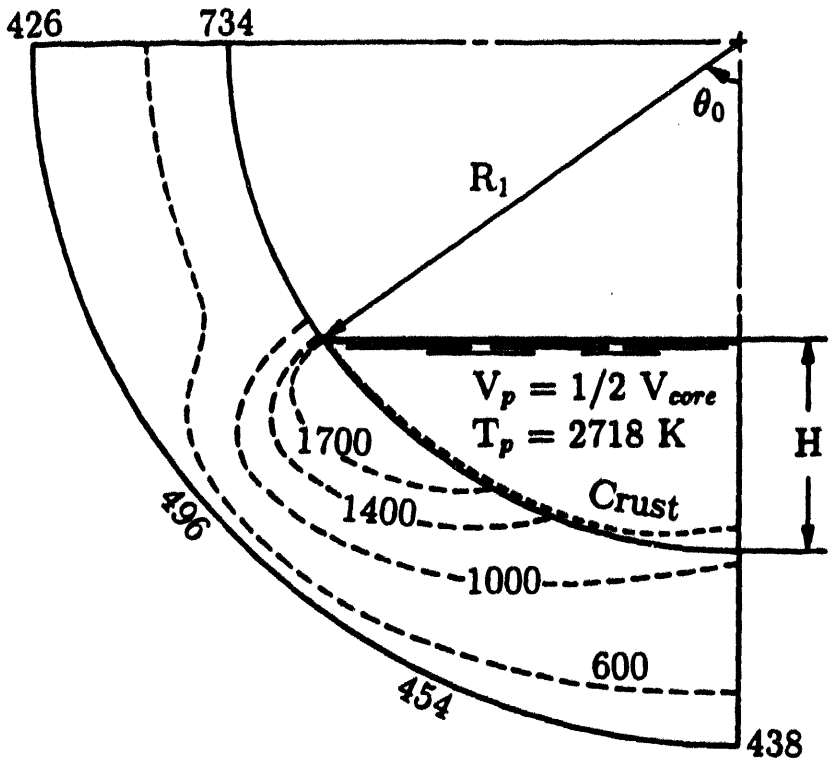

Gabor et al's Correlation

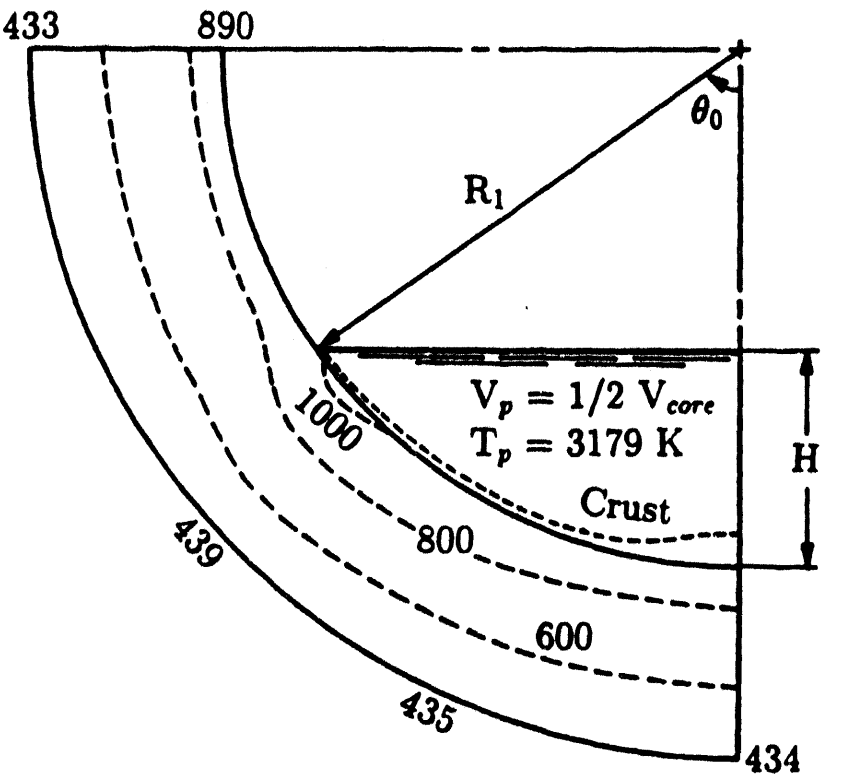

Figure I.15: Temperature distribution in the vessel shell

$h_{d,max}$ at $\theta = \theta_0$ can be used instead of T_{wi} and $h_d(\theta)$. Using $T_p = 2865$ K with the set of parameters as shown in Figure I.14, the maximum outer wall temperature T_{wo} of 770 K which is in transition boiling region, the crust thickness δ_{cd} of 4.5 mm and the minimum wall thickness δ_w of 3.3 cm are obtained. This small value of the wall thickness will not be able to sustain the thermal stresses which in turn will lead to vessel failure.

The effect of emissivity of pool free surface, of structure and of the unwetted region of vessel on the vessel inner wall temperature is shown in Figures I.16 and I.17 when Mayinger et al's correlation is used. The predictions are plotted for $V_p = V_{core}$. From Figure I.16a, it is seen that the vessel wall temperature over the region wetted by the pool increases as the emissivity of the free surface of the pool decreases. However, the effect on the unwetted portion of the wall is opposite in that the vessel wall temperature decreases with a reduction in the emissivity of the pool free surface. This is due to the fact that as the pool free surface emissivity decreases, the reduced heat loss to unwetted vessel wall and to the upper structure causes the pool temperature to increase. The results plotted in Figure I.16b show that the structure emissivity plays a role similar to that played by emissivity of the pool free surface. It is noted that the effects of emissivities of the pool free surface and the upper structure are small. This is due to the fact that large fraction of energy is transferred to the vessel inner wall when Mayinger et al's correlation is used. As shown in Figure I.17a, the effect of emissivity of the vessel on the temperature of the unwetted portion of the inner wall is opposite to the effect of emissivity of the structure. With increase in emissivity, the temperature of the unwetted wall increases. However, its effect on the temperature of the wetted wall is very small. As the emissivity increases, more radiative energy is intercepted by the unwetted wall. The effect of structure temperature on the vessel inner wall temperature is shown in Figure I.17b. It is found that increased structure temperature causes an increase in the temperature of both the wetted as well as the unwetted portion of the vessel wall. However, the effect is predicted to be small.

Reduction in the decay heat can occur due to the loss of volatile fission products from the fuel-clad gap and during subsequent fuel heatup,

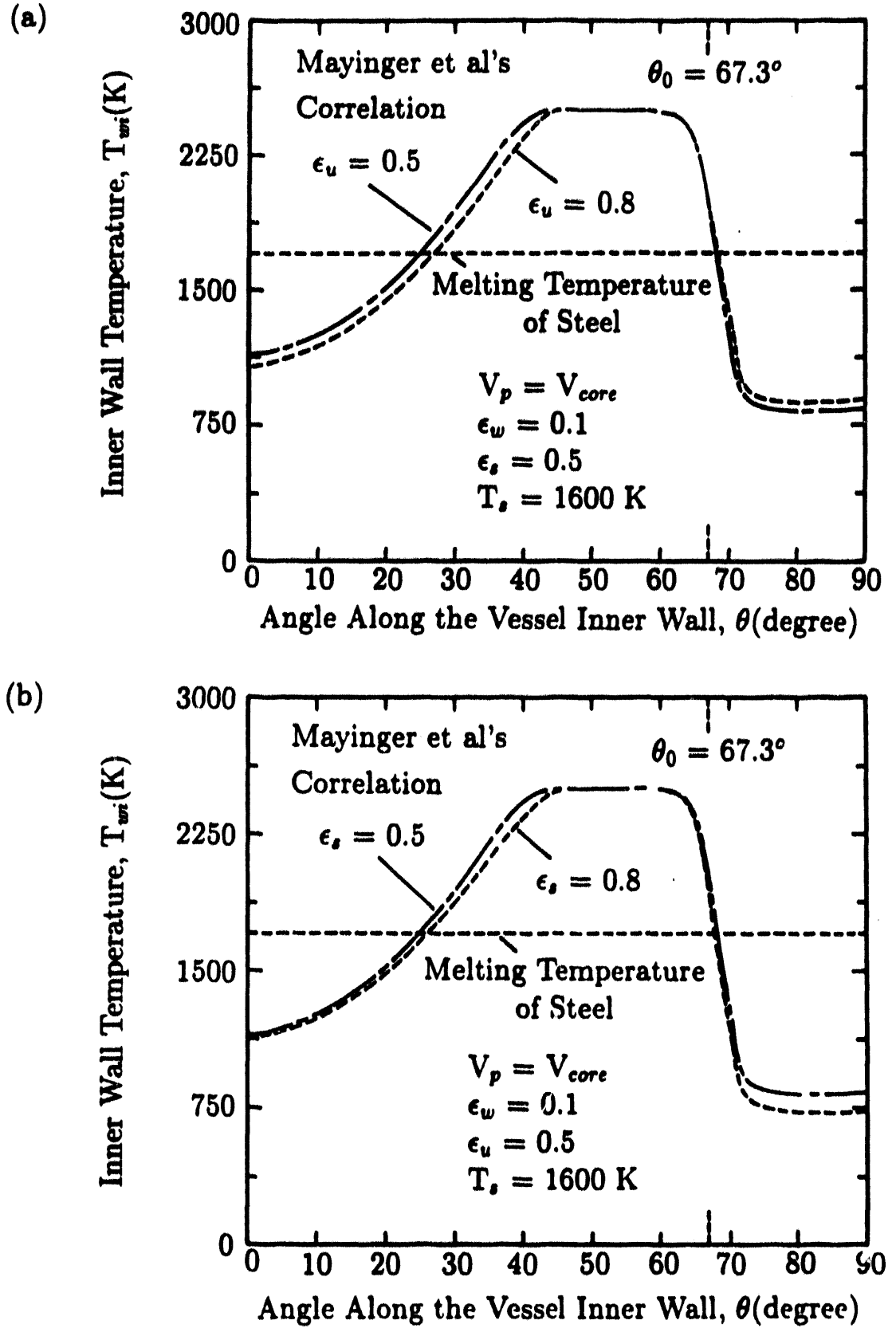

Figure I.16: Effects of the emissivities of the pool free surface (a) and the upper structure (b) on the inner wall temperature

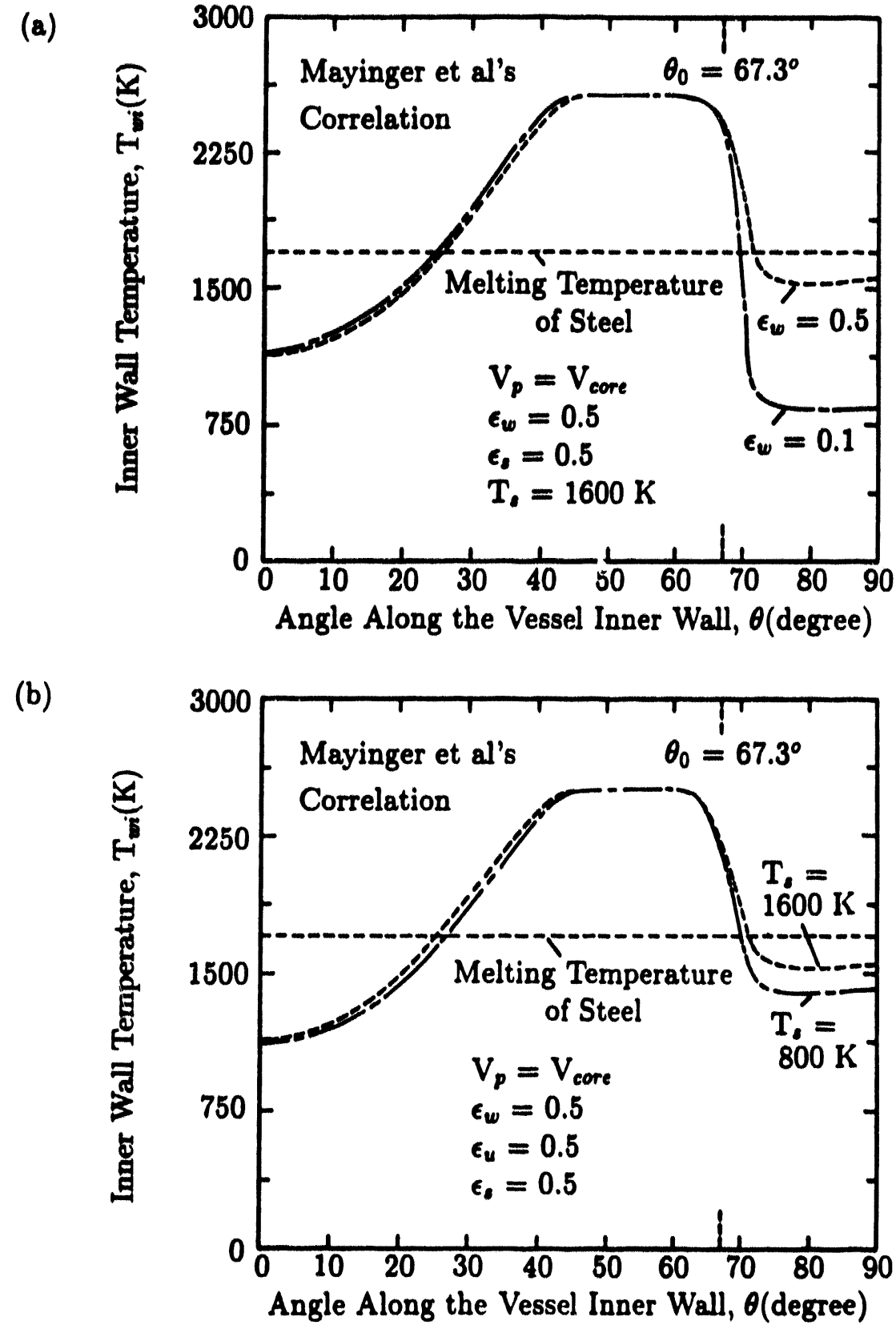

Figure I.17: Effects of unwetted wall emissivity (a) and the upper structure temperature (b) on the inner wall temperature

melting and relocation. Hodge et al [4] suggested that about 80.3 % of the total decay power at the time of lower plenum dryout is predicted to remain within the fuel in the debris bed. An additional release of gases (equivalent to about 3.5 % of the total decay power) from the fuel within the debris bed is predicted as a result of fuel melting within the bed. The effect of decay heat on the PWR vessel lower head was considered. Using the base case with the decay heat of 29.5 MW for full core, the decay heat after accounting the release of volatiles and noble gases (about 23 % reduction) is obtained as 22.66 MW. Figure I.18 shows isotherms obtained by using $Q_{gen,p}$ = 22.66 MW when Mayinger et al's correlation is used for $V_p = V_{core}$. It is seen that lower temperatures of the pool and vessel shell compared to those of the base case (shown in Figure I.14) are predicted. The inner wall temperature under the crust still exceeds the melting temperature of steel vessel over a region.

Since the thermal conductivity of the steel vessel (k_{vessel}) decreases as vessel temperature increases, the effect of the lower value of k_{vessel} (smaller than that for the base case with k_{vessel} = 50 W/mK) on the vessel shell temperature was considered. Figure I.19 shows isotherms obtained by using k_{vessel} = 30 W/mK (value of thermal conductivity of carbon steel at about 1000 K obtained from reference [6]) when Mayinger et al's correlation is used for $V_p = V_{core}$. It is seen that in comparison to the base higher temperatures for the pool and the inner wall and a lower temperature of the outer wall (shown in Figure I.14) are predicted. Also, as shown in Figure I.19, the temperature of unwetted wall is predicted to be about the melting temperature of steel vessel.

Mechanical Behavior of the PWR Vessel Shell

It appears that for the range of emissivities and structure temperatures studied in this work, molten core material can be contained in the reactor vessel indefinitely (from thermal considerations alone) if the reactor vessel is cooled from outside. In the absence of cooling with water, the simple calculations (not documented here) show that reactor vessel will fail even when V_p = 1/16 V_{core}. The temperature distributions in the vessel shell such as those shown in Figures I.13 - I.15 need to be used to calculate effective stresses in the reactor vessel shell and to determine the reponse

Mayinger et al's Correlation

$\epsilon_w = 0.5$
$\epsilon_u = 0.5$
$\epsilon_s = 0.5$
$T_s = 1600$ K
$H/R_1 = 0.614$
$\theta_0 = 67.3°$

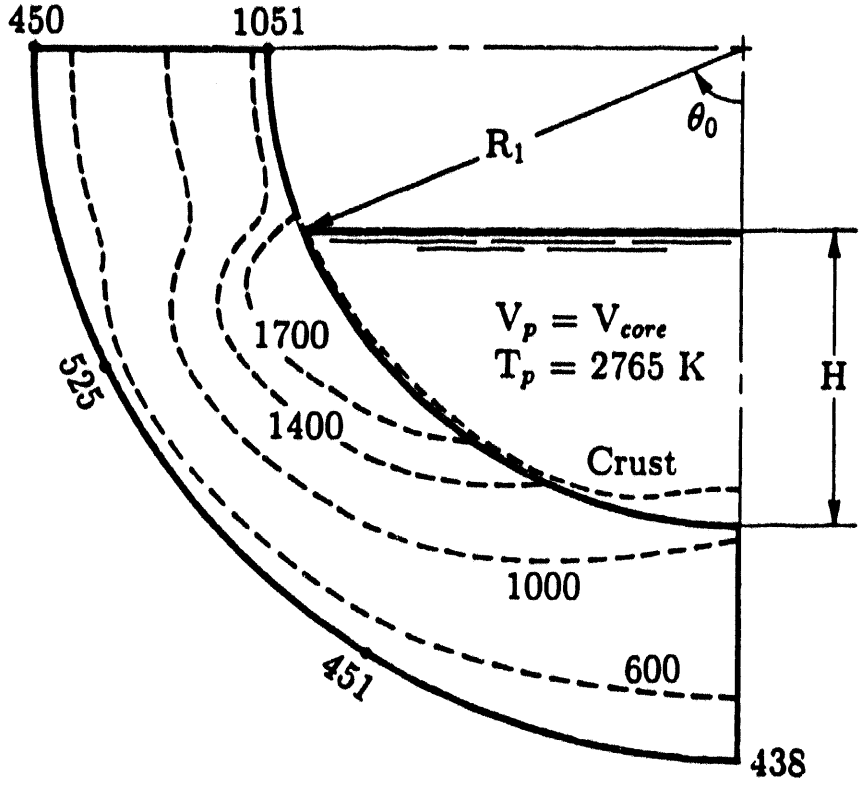

Figure I.18: Temperature distribution in the vessel shell for $Q_{gen,p} = 22.66$ MW

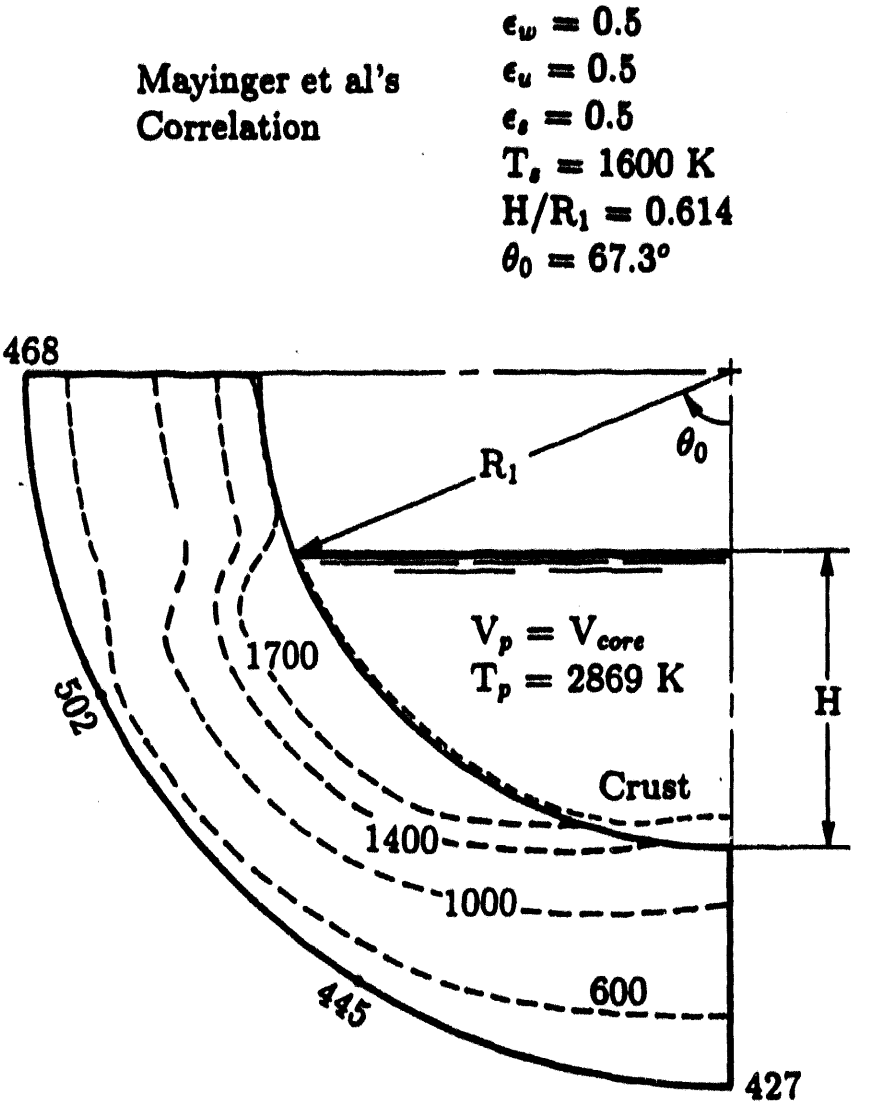

Figure I.19: Temperature distribution in the vessel shell for k_{vessel} = 30 W/mK

of the reactor vessel to creep rupture before an unequivocal conclusion with respect to indefinite retention of core material in the vessel can be drawn. Since the heat transfer correlation predicted from the work of Mayinger et al is more representative of the physical situation than that of Gabor et al as mentioned earlier, the temperature distributions in the vessel shell obtained by using Mayinger et al's correlation are used to predict the thermal stress distributions in the vessel shell and the creep rupture times.

Figure I.20 shows the stress distributions in the hemispherical vessel shell for the roller boundary condition on the top of the PWR vessel shell during the normal operation. Temperature of the vessel shell is taken to be 580 K which is about the mean temperature of the coolant of a PWR with the system pressure of about 15 MPa. The calculated stresses are uniformly distributed in the vessel shell (between 13 and 15 ksi) and much lower than the yield stress of the steel vessel (about 50 ksi). The primary stresses in the PWR vessel lower head (due to system pressures ranging from 4 to 15 MPa) are in the range of 35 (5.1 ksi) to 130 MPa (18.8 ksi) [30]. For a BWR the normal operating wall stress is 68.75 MPa (9.97 ksi) [4]. Therefore, the results obtained by using the NASTRAN code seem to be reliable in the prediction of the stress distributions in the vessel shell. Using the clamped boundary condition at $\theta = \pi/2$, the calculated stresses exceed the yield stress of the steel vessel near the area of the top of the hemispherical vessel shell. Therefore, use of the clamped boundary condition at $\theta = \pi/2$ seems to be conservative in predicting the stress distributions near the top of the vessel shell. In the absence of quantitative information as to how the vessel is restrained, the rigid boundary condition at $\theta = \pi/2$, can be considered as an extreme boundary condition that is used to predict the stress distributions in other regions of the vessel shell.

Based on the temperature distribution in the vessel shell, the effective stresses are determined for a given system pressure. Figure I.21 shows the distribution of the effective stresses in the vessel shell for the two types of boundary conditions on the top of the hemispherical shell when Mayinger et al's correlation is used and the system pressure is 15 MPa.

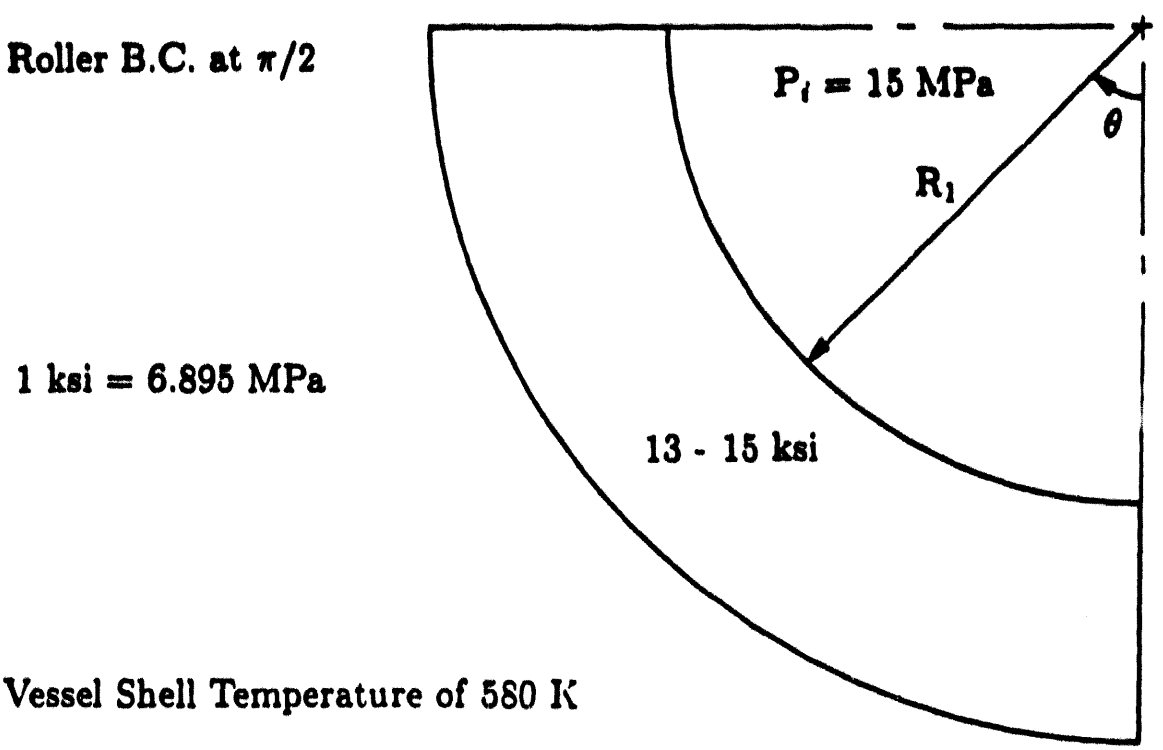

Figure I.20: Stress distribution in the PWR vessel shell during the normal operation

For the clamped boundary condition at $\theta = \pi/2$, the calculated stresses are predicted to exceed the ultimate stress of the steel vessel (about 100 ksi as an upper limit) over a wide region of the vessel shell. For the roller boundary condition at $\theta = \pi/2$, the stresses are predicted to exceed the ultimate stress over a relatively narrow region across the vessel shell. For both cases minimum stresses occur along the mid plane of the vessel shell because the inner half of the shell is in compression whereas the outer half is in tension. Because of the deformation of the vessel shell due to the large temperature gradient across the shell thickness, the stress distributions in the outer elements which are in tension are higher at some angular positons than those in the inner elements which are in compression. This can be explained by the fact that the tangential stress increases with the radial position when the temperature gradient exists across the spherical shell [31]. Since the minimum stresses along the mid plane of the vessel shell exceed the yield stress of the steel vessel for both types of boundary conditions imposed on the top of the vessel shell, a large plastic deformation is predicted to occur in that region. The survival of the vessel shell is in question unless it is proven otherwise when relaxation of stresses is considered.

In order to investigate the effect of the system pressure on the effective stresses, the effective stresses in the vessel shell are considered for the low system pressure. Figure I.22 shows the distribution of the effective stresses in the vessel shell with the roller boundary condition at $\theta = \pi/2$ for $V_p = V_{core}$ when Mayinger et al's correlation is used and the system pressures are assumed to be 5 and 1 MPa. Comparing the stresses with $P_i = 15$ MPa (shown in Figure I.21), it is seen that the system pressure does not play a dominant role on the effective stresses in the vessel shell. Most of the contribution to the stresses comes from temperature gradient across the vessel shell.

Figure I.23 shows the distribution of the stresses in the vessel shell with the roller boundary condition imposed on the top of the hemispherical shell with $V_p = 1/2\ V_{core}$. In obtaining the effective stresses Mayinger et al's correlation was used with system pressures of 15 and 5 MPa. Since the melting of the inner wall of the vessel shell when Mayinger et al's

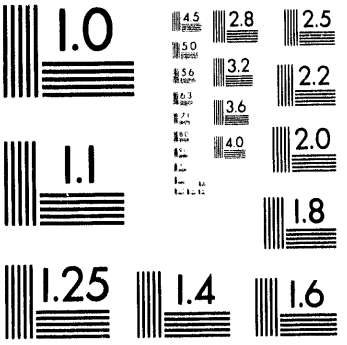
1.0
1.1
1.25
1.4
1.6
1.8
2.0
2.2
2.5
2.8
3.2
3.6
4.0
4.5
5.0
5.6
6.3

4 of 5

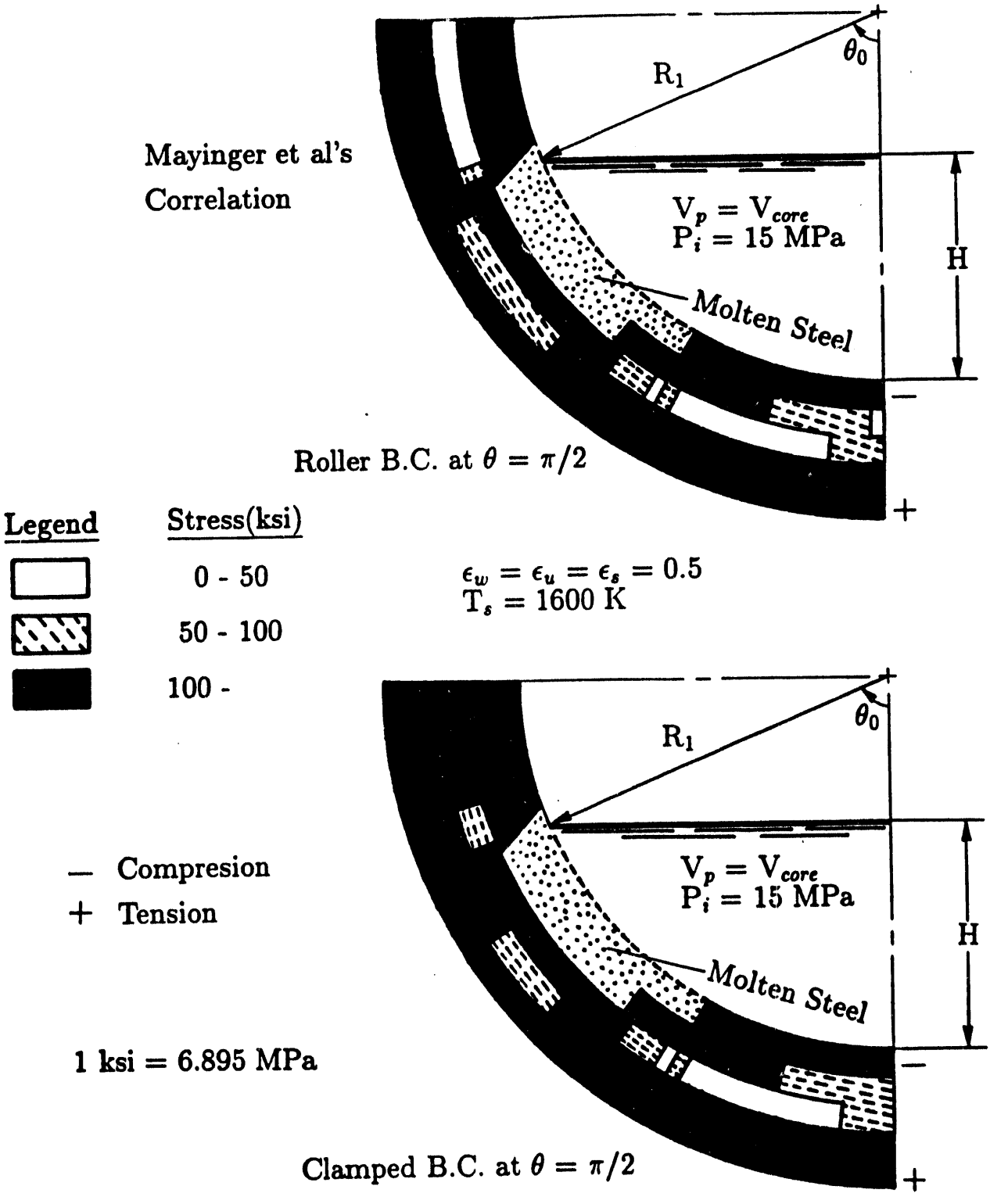

Figure I.21: Stress distribution in the PWR vessel shell

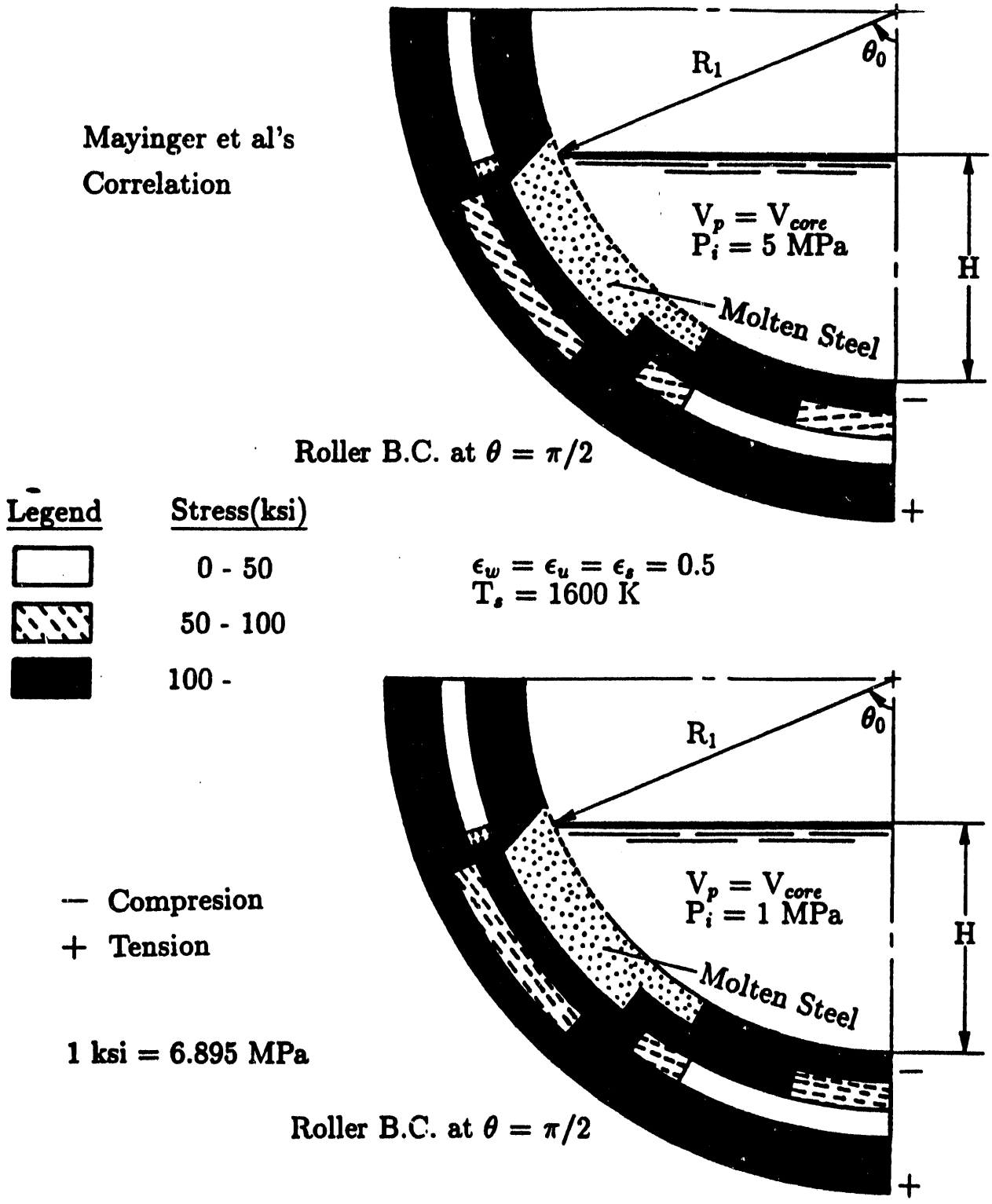

Figure I.22: Stress distribution in the PWR vessel shell

correlation is used occurs for all sets of parameters considered in this study, the effect of temperature distribution on stresses is dominant. For the roller boundary condition at $\theta = \pi/2$, the stresses are found to exceed the yield stress over the region just below the pool free surface. However, it is found that for the clamped boundary condition at $\theta = \pi/2$, the calculated stresses exceed the ultimate stress of the steel vessel over a wide region across the vessel shell. For both cases the minimum stresses occurring along the mid plane of the vessel shell are predicted to exceed the ultimate stress of steel, resulting in a large plastic deformation in that region. Hence, from the results in which relaxation of the stresses is not considered, the survival of the vessel shell cannot be guaranteed.

The total displacements of the outer wall of the vessel shell are plotted in Figure I.24 when Mayinger et al's correlation is used for $V_p = V_{core}$. It is seen that differences between displacements for different system pressures are very small.

Based on the results of the steady state temperature distribution in the vessel shell, a large plastic deformation in the vessel shell is predicted to occur due to excessive thermal stresses when Mayinger et al's correlation is used.

To assess the failure of the vessel due to creep rupture, the creep rupture times are calculated by using the relationship between the Larson-Miller parameter and the equivalent stress in the vessel shell. Figure I.25 shows the dependence of rupture time on the temperature of the vessel shell for system pressures of 15 and 5 MPa. The maximum steady-state average temperature across the vessel shell and the maxima of steady-state outer wall temperature of the vessel are obtained for $V_p = V_{core}$, $\epsilon_w = \epsilon_u = \epsilon_s = 0.5$ and $T_s = 1600$ K when Mayinger et al's correlation is used. It can be seen that much longer rupture times are predicted when the maximum steady-state outer wall tempearature of the vessel shell is used, but immediate creep rupture of the vessel shell would occur if the maximum value of steady-state average wall temperature across the vessel shell is used.

After slumping of the core material into the reactor vessel lower head, the pool temperature increases above the melting temperature of corium (2500 K) and the vessel shell temperature also increases and reaches a steady state value. From to the transient analysis of the thermal behavior of the PWR vessel lower head, time periods longer than 10000 seconds are needed for the vessel wall temperature to attain its steady state value. Since the average wall temperature across the vessel shell and the outer wall temperature at any time after slumping of the core are lower than the maximum steady-state temperature as shown in Figure I.25, the rupture times are predicted by using the highest average or outer wall temperature at any time. The isotherms and the rupture times are considered for system pressures of 15 and 5 MPa. Figure I.26 shows the isotherms in the vessel shell for $V_p = V_{core}$ and 1/2 V_{core} when Mayinger et al's correlation is used and the system pressure is assumed to be 15 MPa. The creep rupture times are determined by using the highest average wall temperature ($(T_{av})_{max}$), the highest mid plane temperature ($(T_{mid})_{max}$) and the highest outer wall temperature ($(T_{r=R_2})_{max}$) at any time after slumping of the core material into the vessel lower head. The creep rupture is predicted to occur within 2 and 3 hours after slumping of the core material into the vessel lower head for $V_p = V_{core}$ and $V_p = 1/2$ V_{core} when $(T_{av})_{max}$ and $(T_{mid})_{max}$ are used. However, much longer creep rupture times are predicted when $(T_{r=R_2})_{max}$ is used.

Figure I.27 shows the isotherms in the vessel shell when Mayinger et al's correlation is used for a system pressure of 5 MPa. Using the highest average temperature across the vessel shell at any time, creep rupture is predicted to occur in 3 hours for half core and in 2 hours for full core. Using the highest mid wall temperature at any time, creep rupture is predicted to occur in 11 hours for full core and in 231 hours for half core. However, much longer creep rupture times are predicted when the highest outer wall temperatures of the vessel shell ($(T_{r=R_2})_{max}$) are used instead of the average temperatures across the vessel shell.

Thus, the creep rupture times for the reactor vessel shell are dependent upon the average temperatures chosen for the calculations. The calculated rupture times based on those temperatures can be used to estimate the probability of vessel failure during flooding of the cavity of a PWR. No data on rupture time could be located in literature for situations in which large temperature gradients exist across a structure. It should also be noted that creep rupture times were not obtained by carrying out time dependent stress calculations and by evaluating time integrated damage to a particular element in the vessel wall.

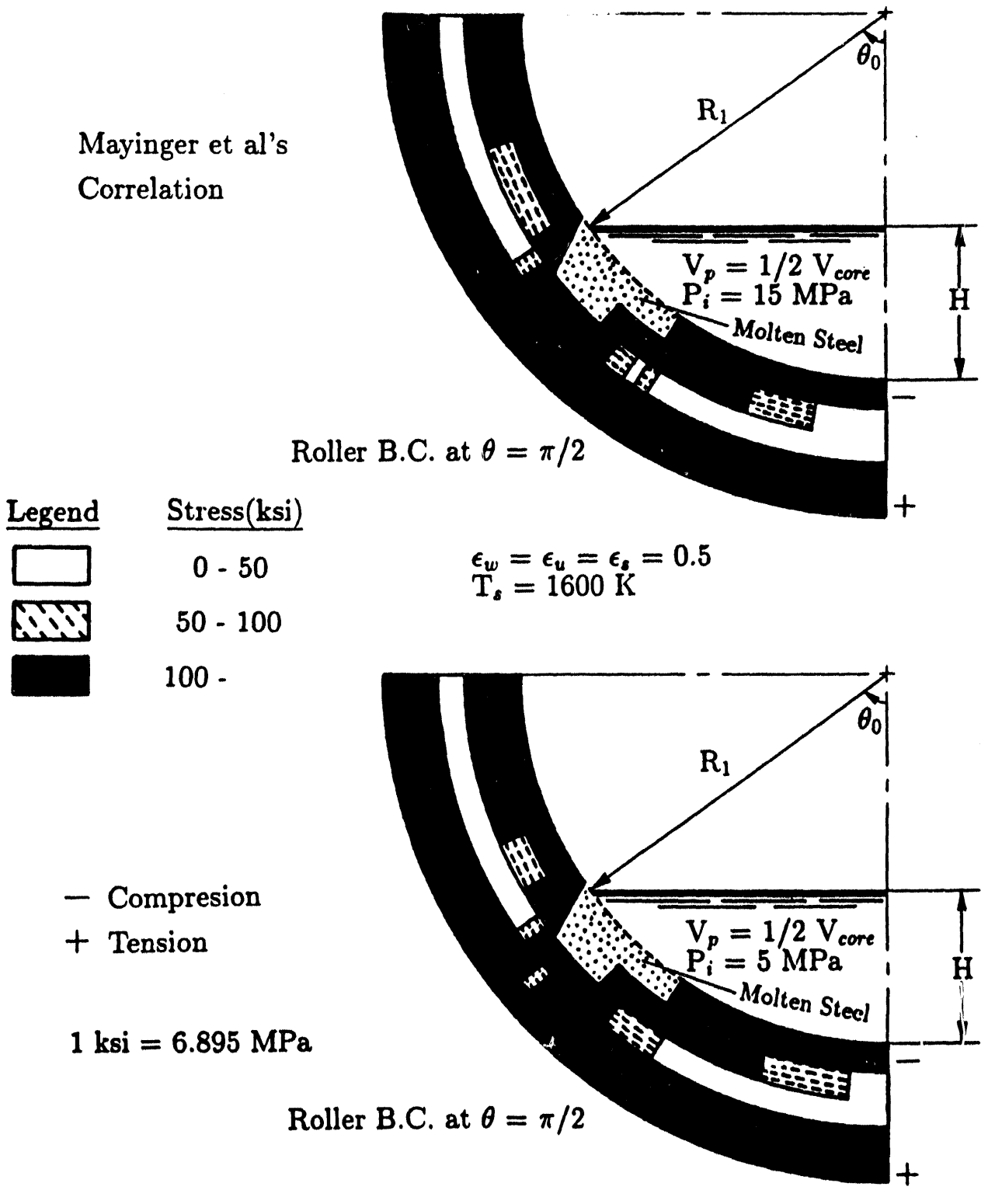

Figure I.23: Stress distribution in the PWR vessel shell

(a

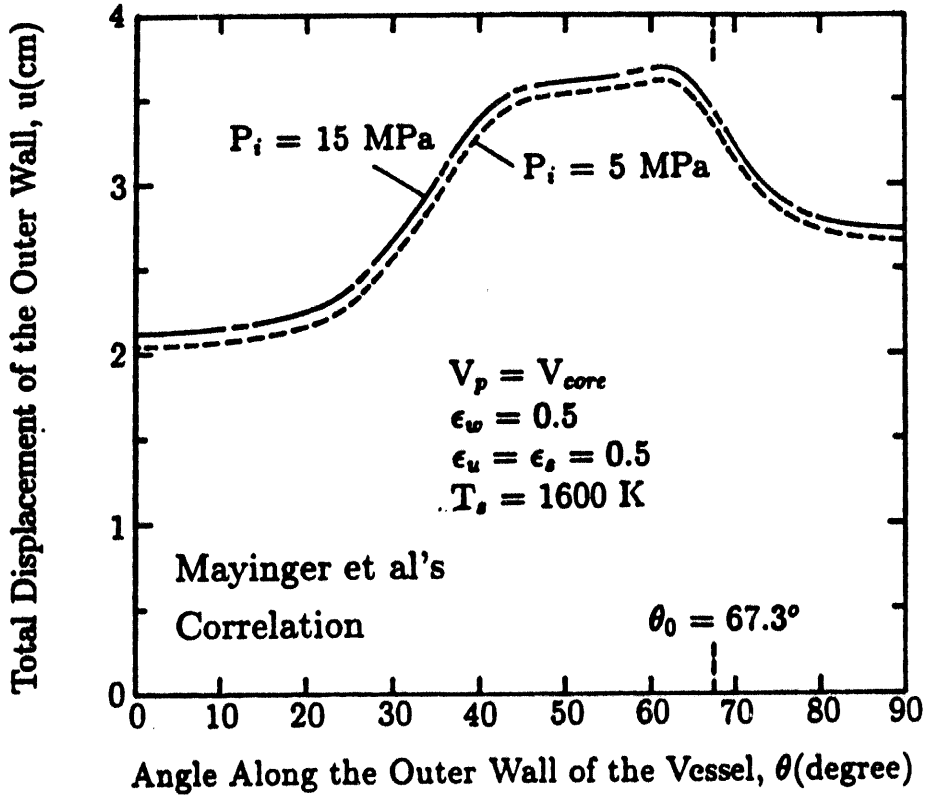

(b)

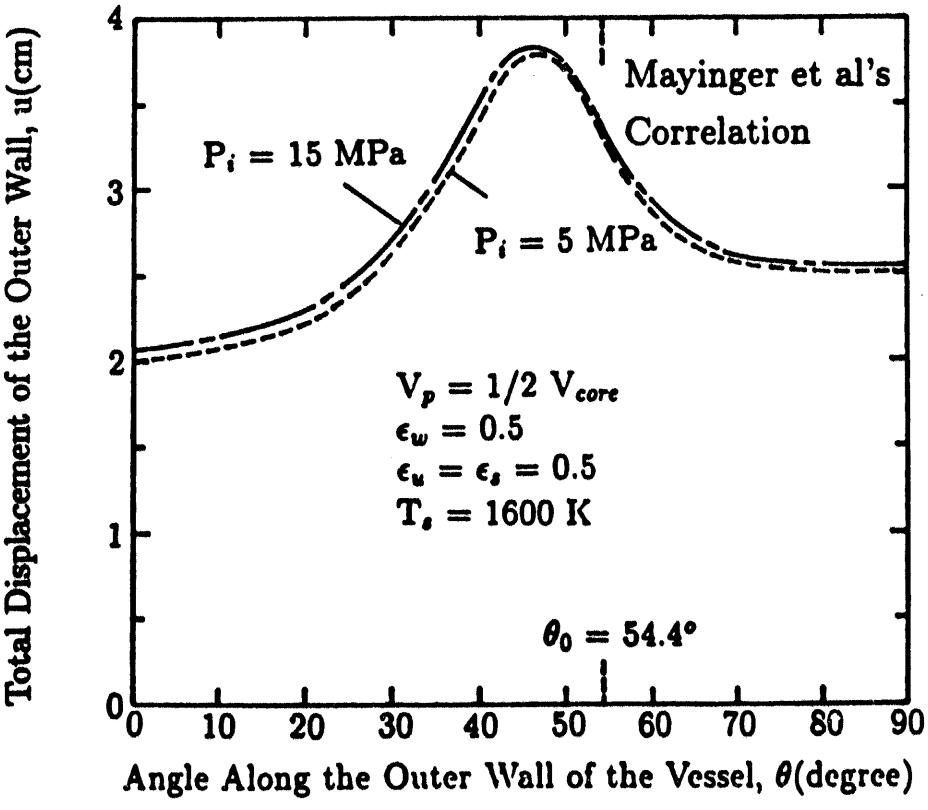

Figure I.24: Comparison of total displacement of the outer wall of the PWR vessel under different system pressure

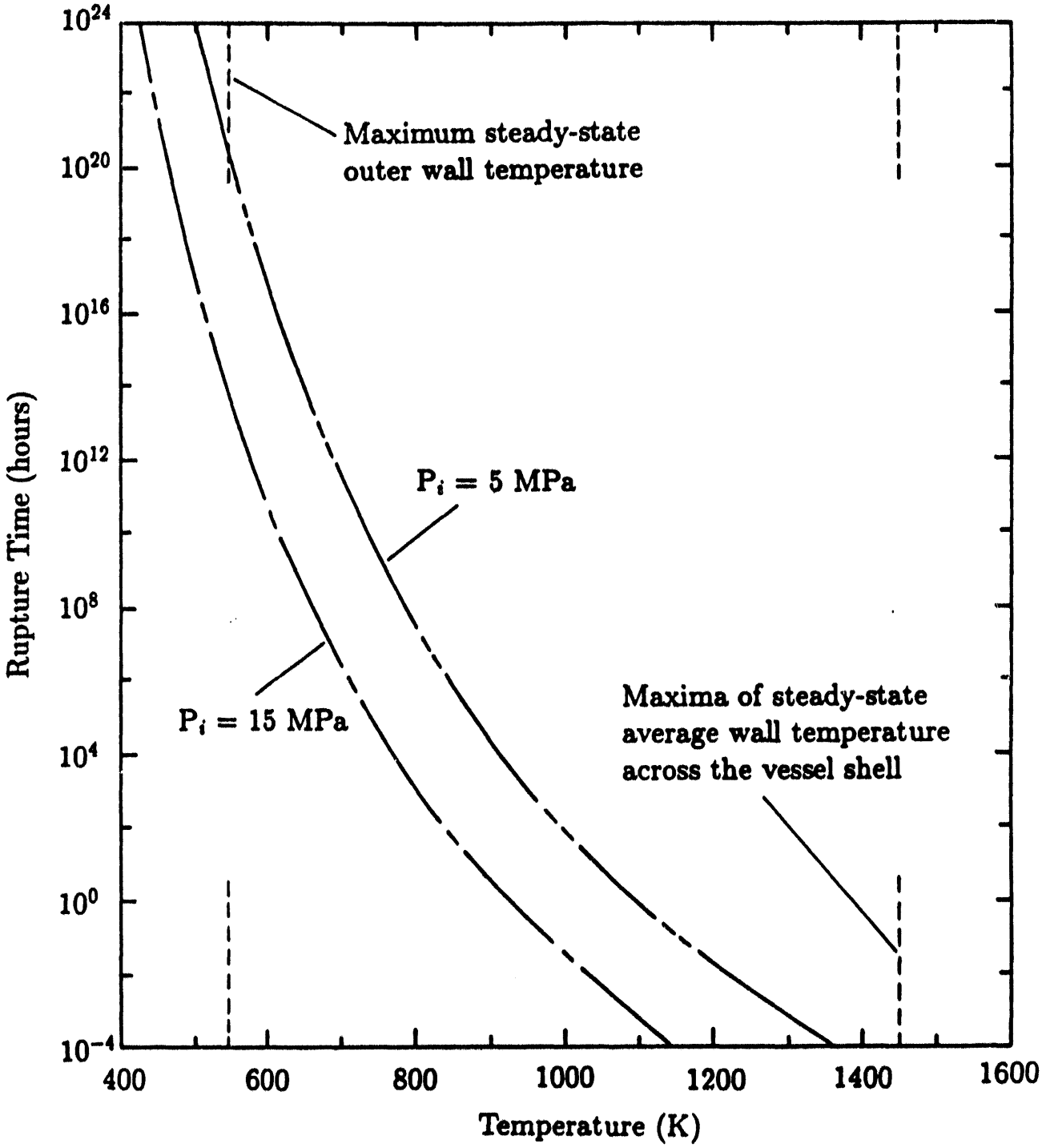

Figure I.25: Variation of the creep rupture time with vessel wall temperature

(a)

$\epsilon_w = 0.5$
$\epsilon_u = \epsilon_s = 0.5$
$T_s = 1600$ K

Creep Rupture at
$t_r = 5600$ sec.
Based on $(T_{av})_{max}$
$t_r = 1.43 \times 10^{21}$ hours
Based on $(T_{r=R_2})_{max}$
$t_r = 2.78$ hours Based on $(T_{mid})_{max}$

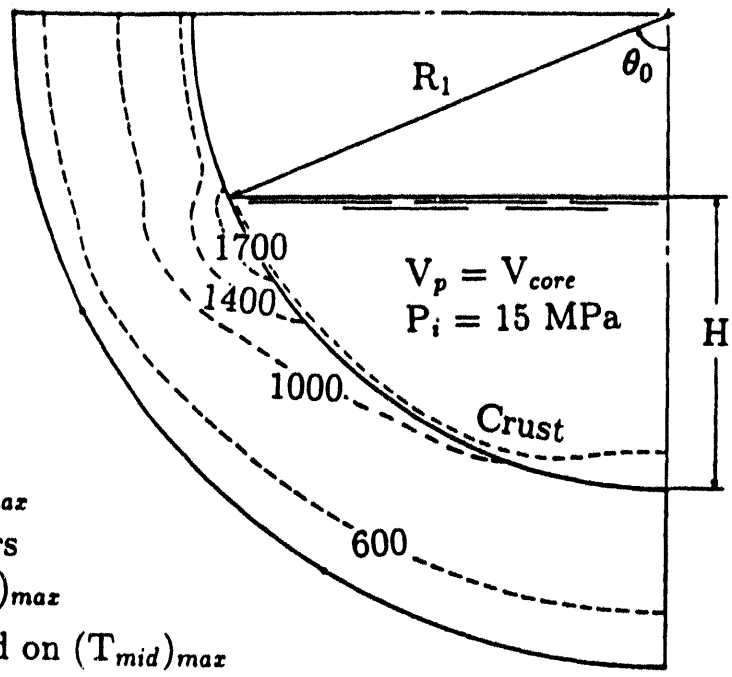

(b)

$\epsilon_w = 0.5$
$\epsilon_u = \epsilon_s = 0.5$
$T_s = 1600$ K

Creep Rupture at
$t_r = 8000$ sec.
Based on $(T_{av})_{max}$
$t_r = 1.48 \times 10^{20}$ hours
Based on $(T_{r=R_2})_{max}$
$t_r = 2.84$ hours Based on $(T_{mid})_{max}$

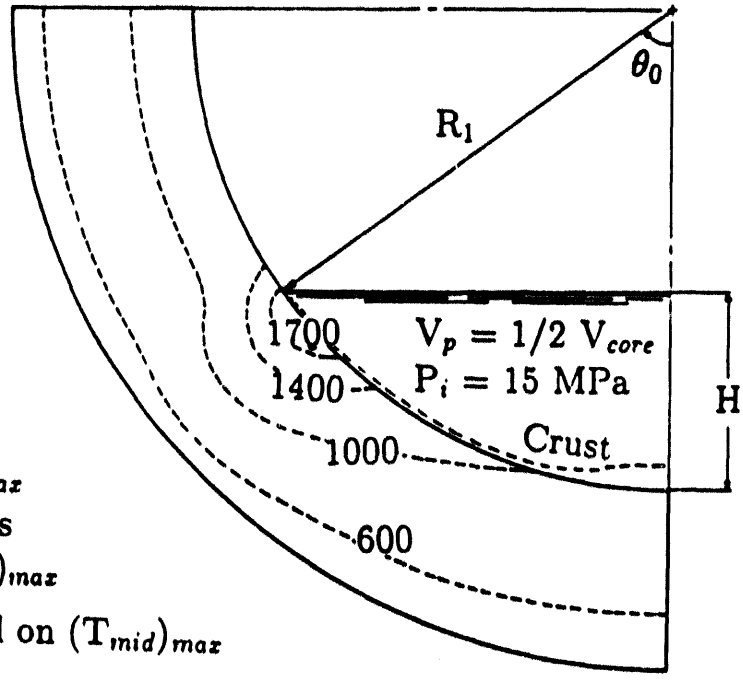

Figure I.26: Transient temperature distributions in the vessel shell using Mayinger et al's correlation

(a)

$\epsilon_w = 0.5$
$\epsilon_u = \epsilon_s = 0.5$
$T_s = 1600$ K

Creep Rupture at
$t_r = 6400$ sec.
Based on $(T_{av})_{max}$
$t_r = 3.4 \times 10^{27}$ hours.
Based on $(T_{r=R_2})_{max}$
$t_r = 11$ hours Based on $(T_{mid})_{max}$

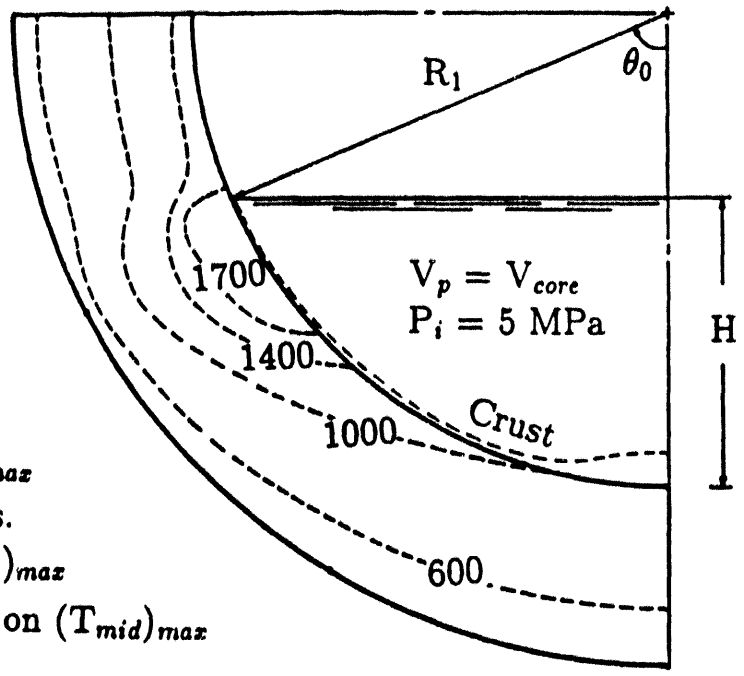

(b)

$\epsilon_w = 0.5$
$\epsilon_u = \epsilon_s = 0.5$
$T_s = 1600$ K

Creep Rupture at
$t_r = 9600$ sec.
Based on $(T_{av})_{max}$
$t_r = 8.32 \times 10^{26}$ hours
Based on $(T_{r=R_2})_{max}$
$t_r = 231.3$ hours Based on $(T_{mid})_{max}$

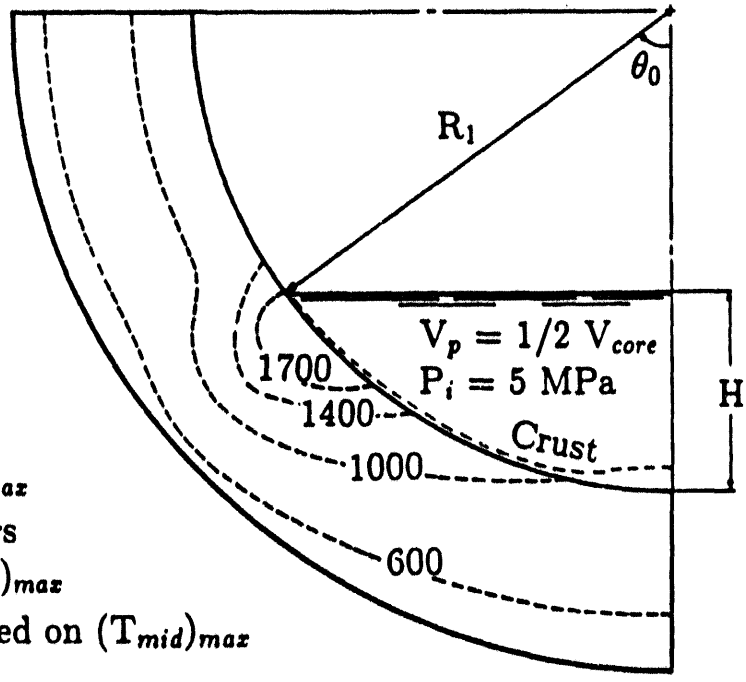

Figure I.27: Transient temperature distributions in the vessel shell using Mayinger et al's correlation

I.6.2 FLOODING OF THE BWR DRYWELL

Steady state temperatures in the BWR vessel shell were obtained when two-thirds of the core was assumed to be present in the vessel lower head. Calculations were performed by varying between 0.2 and 0.8 the emissivity, ϵ_w, of the vessel, the emissivity, ϵ_u, of the pool surface, the emissivity, ϵ_b, of the baffle plate, the emissivity, ϵ_c, of the core shroud and the emissivity, ϵ_t, of the upper structure. The upper structure temperature was assumed to lie between 1000 K and 1500 K. For the calculation purposes, the temperature of the upper structure is limited to 1500 K. Melting and subsequent relocation of the core material are not considered in this study.

Thermal Behavior of A BWR Vessel Shell

The thickness of the crust on the pool free surface is plotted in Figure I.28a as a function of the emissivity of the pool free surface. For the correlation of Gabor et al which yields average downward heat transfer coefficients that are about 10 times lower than those obtained from the expression of Mayinger et al, no upper crust is predicted to form for emissivities less than 0.3. However, as heat loss from the free surface becomes high enough, a crust forms and its thickness increases with emissivity. With the use of Mayinger et al's correlation, a much thicker crust is predicted to form at the pool free surface. Figure I.28b shows the dependence of pool temperature on the emissivity of the pool free surface. In the absence of a crust, the steady state pool temperature shows a strong dependence on the emissivity. The pool temperature decreases as the emissivity increases or heat loss from the pool free surface increases. However, in the presence of crust, the thermal resistance of the crust dominates and pool temperature is nearly insensitive to the emissivity of the pool free surface. In the presence of a crust, the pool temperature predicted by using the correlation of Mayinger et al is about 100 K less than that obtained by using the correlation of Gabor et al. This is due to the higher heat loss to the vessel predicted by using the correlation of Mayinger et al.

Figure I.29 shows the thickness of the crust along the vessel inner wall

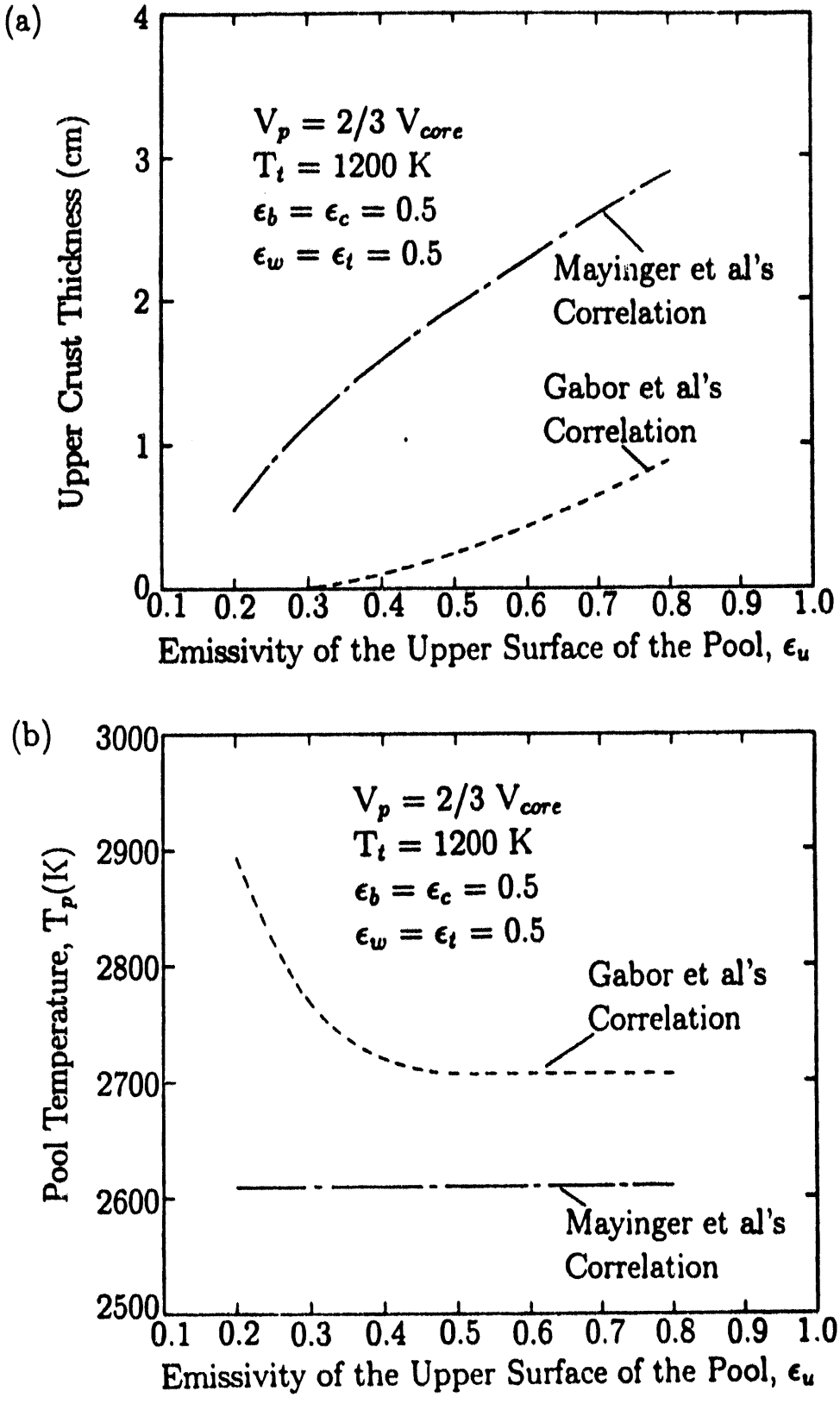

Figure I.28: Variation of upper crust thickness (a) and the pool temperature (b) with the pool surface emissivity

correlation of Mayinger et al, the crust thickness profile shows an inverse dependence on the variation of the heat transfer coefficient along the pool boundary. However, when the heat transfer coefficient is small, a thicker crust is predicted to be present along the vessel inner wall. Also, as is shown by the dotted line, for a low value of the internal heat transfer coefficient, the crust thickness increases as the cooling conditions on the outside wall improve. It can be seen that the crust thickness variations in the region of the vessel support skirt ($\theta_1 \leq \theta \leq \theta_2$) are different from those in the other regions.

The steady state vessel inner wall temperature is plotted in Figure I.30 as a function of angular position. Because of interuption by the air-steam pocket of good cooling conditions created by water, the temperature along the vessel wall shows oscillatory behavior. For higher internal heat transfer coefficients, conduction along the vessel wall becomes important and no distinct hot spot over the area covered by the steam pocket is observed. Since the pool temperature in the case of Gabor et al's correlation is higher, radiative heat transfer causes a rapid rise in temperature of the unwetted portion of the vessel wall. However, a drop in temperature is predicted when the correlation of Mayinger et al is used. Because of the much higher heat transfer rate into the lower part of the pool and the lower pool temperature when Mayinger et al's correlation is used, less radiation heat transfer into the unwetted portion of the vessel inner wall is predicted. This, in turn, results in a temperature drop along the unwetted wall of the vessel. It can be seen that the inner wall temperature increases sharply for angular positions greater than the angle θ_1. The large temperature oscillations in the vessel will lead to high thermal stresses.

The fractions of decay heat that are transferred downward, to the unwetted vessel wall, the upper structure, the core shroud and to the baffle plate are plotted in Figures I.31a and I.31b for the correlations of Gabor et al and Mayinger et al. It is seen that for Mayinger et al's correlation as much as 52 % of the total energy generated in the pool is lost to the wetted portion of the vessel. However, only about 10 - 20 % of the energy generated in the pool is lost to the wetted portion of the

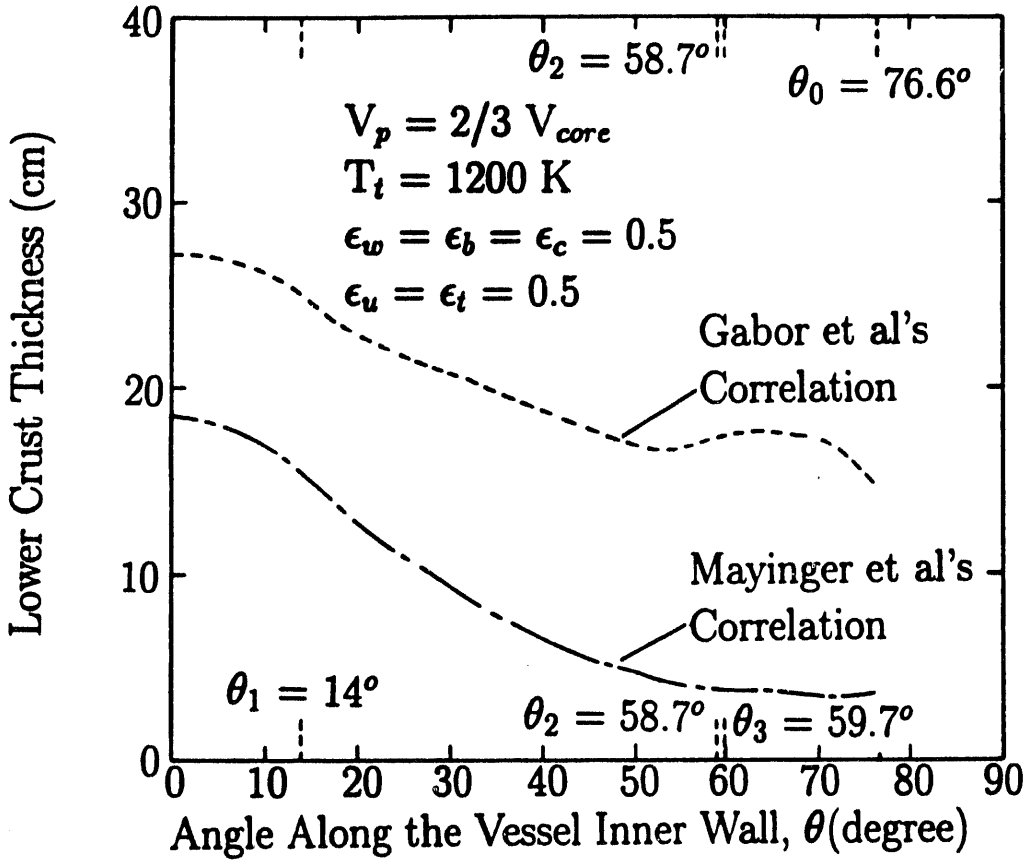

Figure I.29: Variation of lower crust thickness

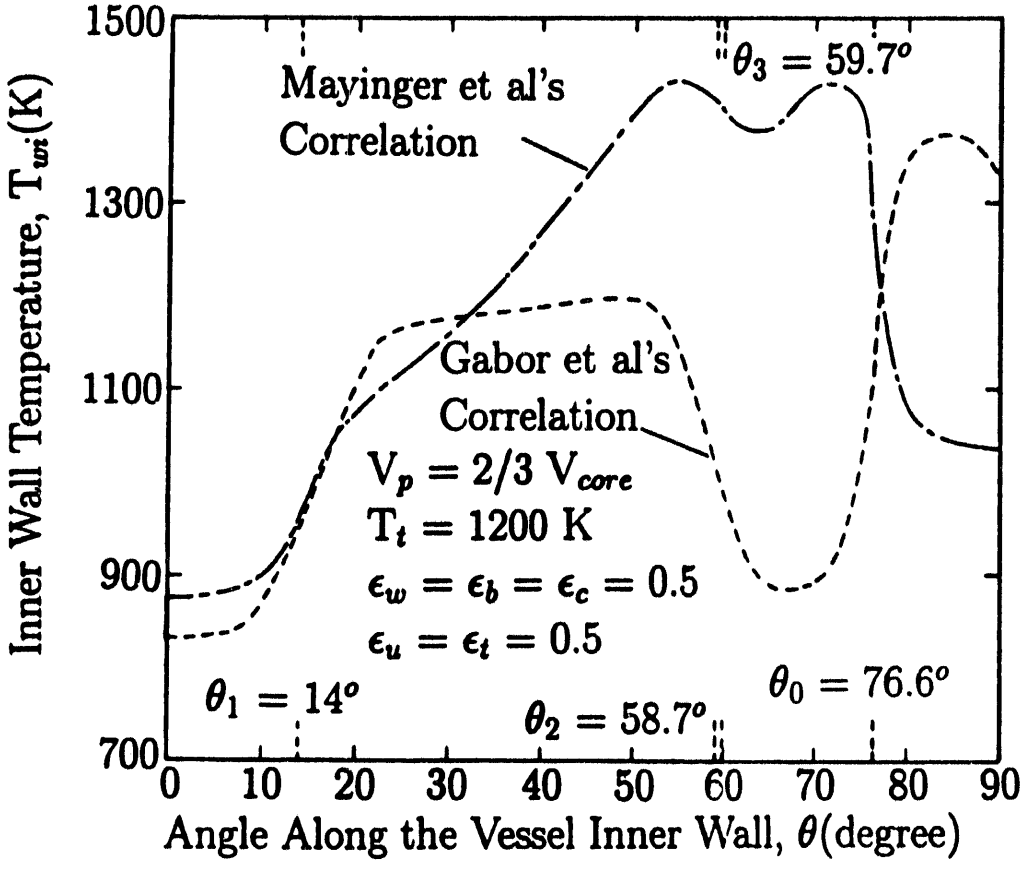

Figure I.30: Variation of the inner wall temperature

vessel when Gabor et al's correlation is used. It should be noted that these fractions do not include the energy that is generated in the crust but is also transferred to the vessel wall. Since the predicted crust is much thicker when Gabor et al's correlation is used, actual fraction of energy transferred downward can be as high as 40 % when Gabor et al's correlation is used.

Figures I.32a and I.32b show the effect of emissivity of the pool free surface on the vessel inner wall temperature. Comparison of the predictions plotted for the two correlations shows that emissivity of the pool free surface has little effect when a large fraction of decay heat is transferred to the vessel wall by natural convection in the pool.

The isotherms in the vessel wall and the temperature of the core shroud and baffle plate are shown in Figures I.33 and I.34 for the correlation of Gabor et al and Mayinger et al respectively. It is seen that in both cases the baffle plate temperature is predicted to be above the melting temperature of steel. As a result baffle will fail and any water left in the downcomer region will spill over the core debris. The failure will also lead to exposure of the recirculation pump seals to superheated steam. This failure of the seals will cause radioactivity to escape into the containment. The isotherms plotted in Figure I.34 show the two dimensionality of conduction heat transfer in the vessel wall.

The effect of the pool volumes on the thermal behavior of the BWR vessel lower head has also been considered. Figure I.35 shows the variation of the inner wall temperatures for different pool volumes in the vessel lower head. Since the total amount of heat generation in the pool decreases due to the reduction of the pool volume, the inner wall temperature decreases as the pool volume decreases. However, the inner wall temperatures in the skirt region, for $V_p = 1/3\ V_{core}$, are predicted to be higher than those for other pool volumes. This is due to the fact that the local heat transfer coefficient is high near the skirt region when the pool angle, θ_0, is approximately equal to the skirt angle, θ_2. Also, less heat is removed from the outer wall of the vessel in the skirt region.

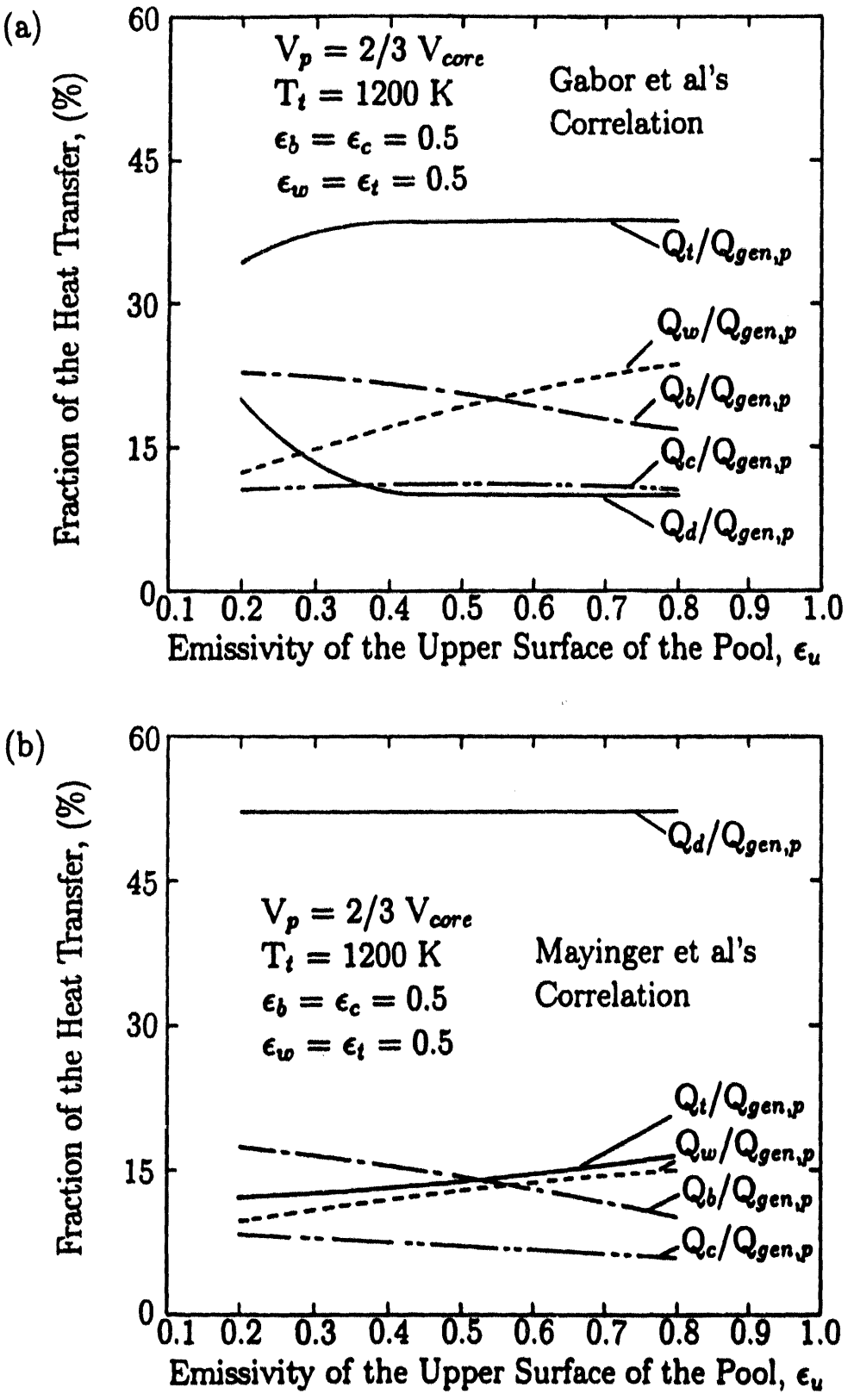

Figure I.31: Partition of the heat generated from the moltem pool

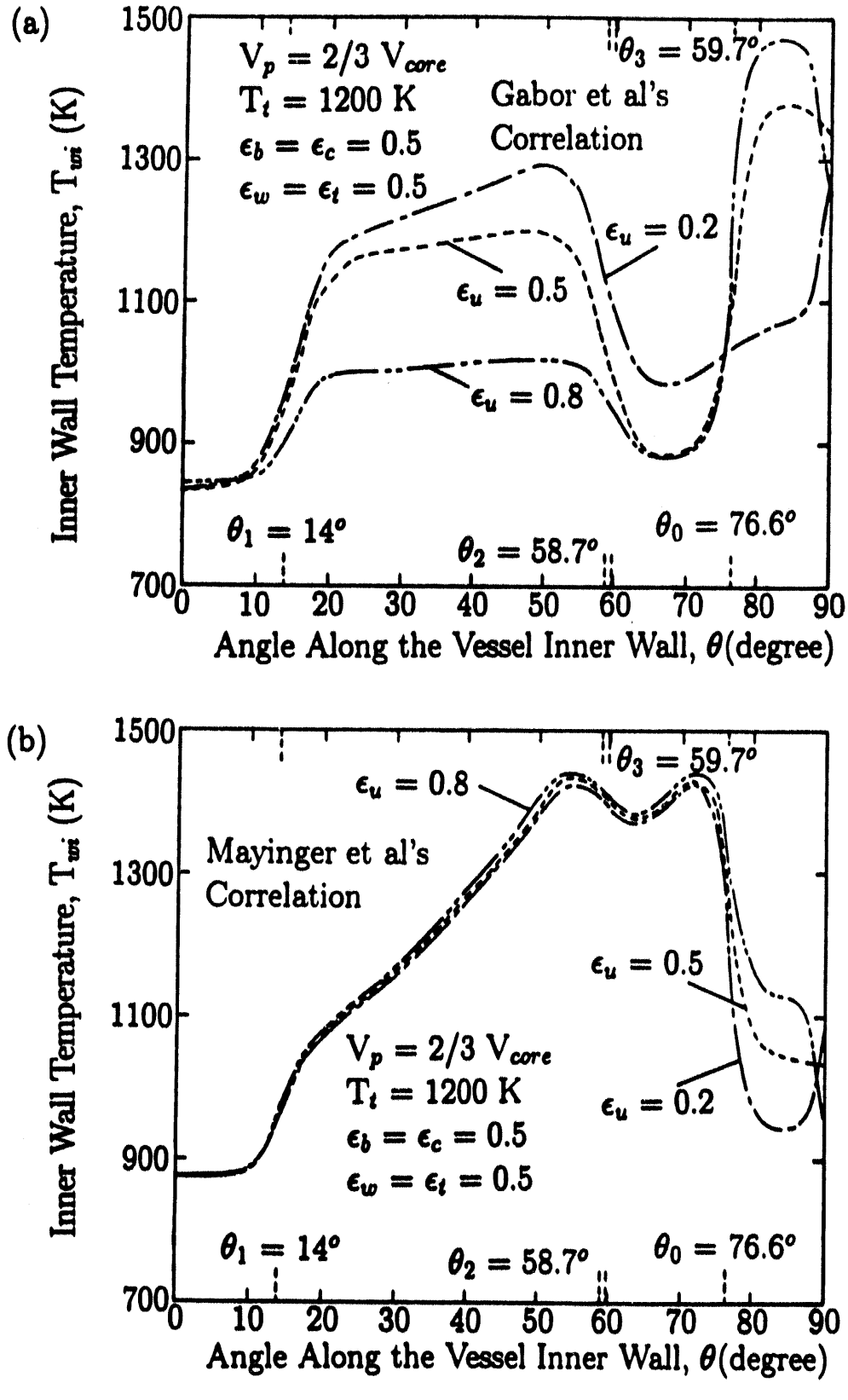

Figure I.32: Effect of the emissivity of the upper surface of the pool on the inner wall temperature

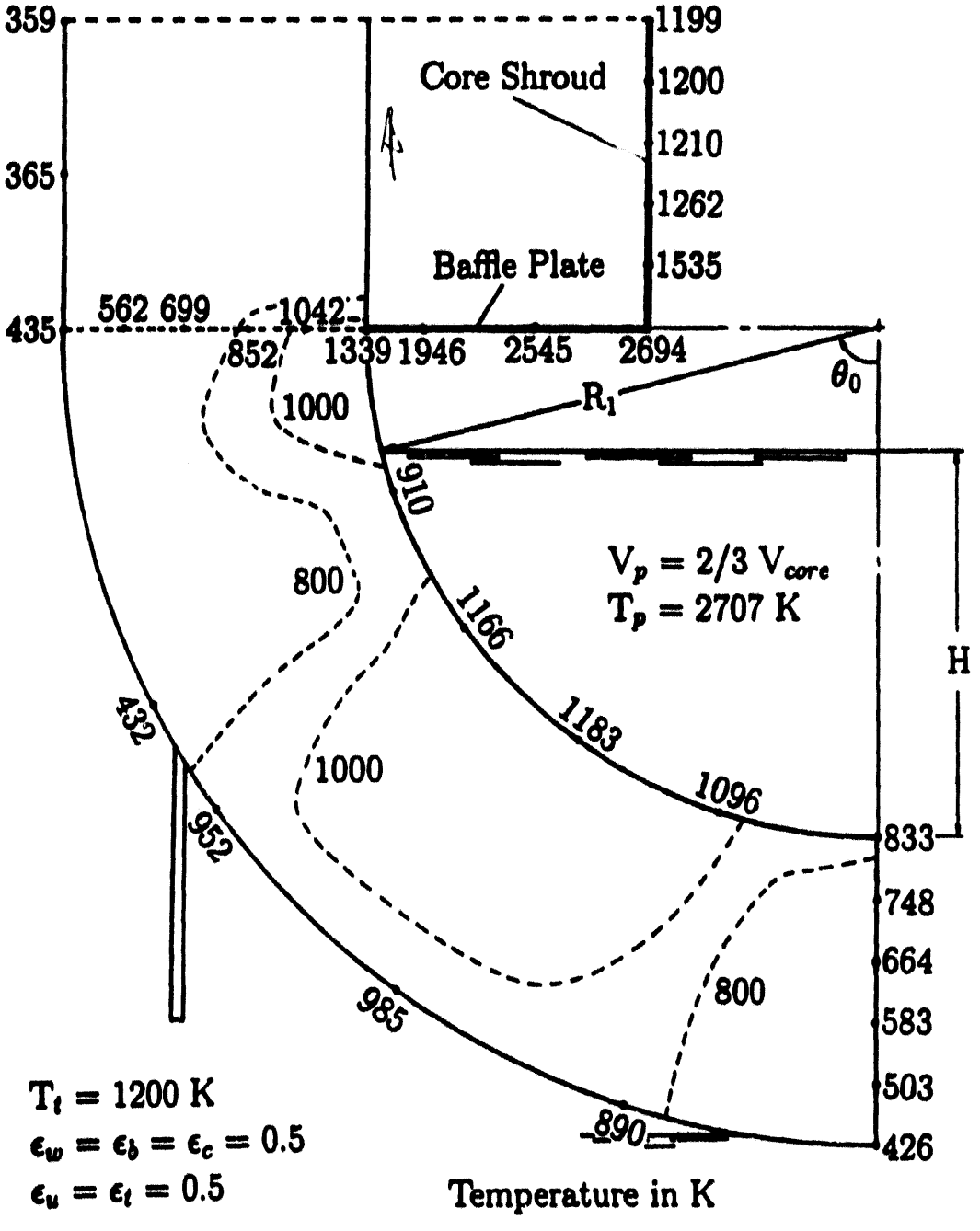

Figure I.33: Temperature distribution in the vessel shell based on Gabor et al's correlation

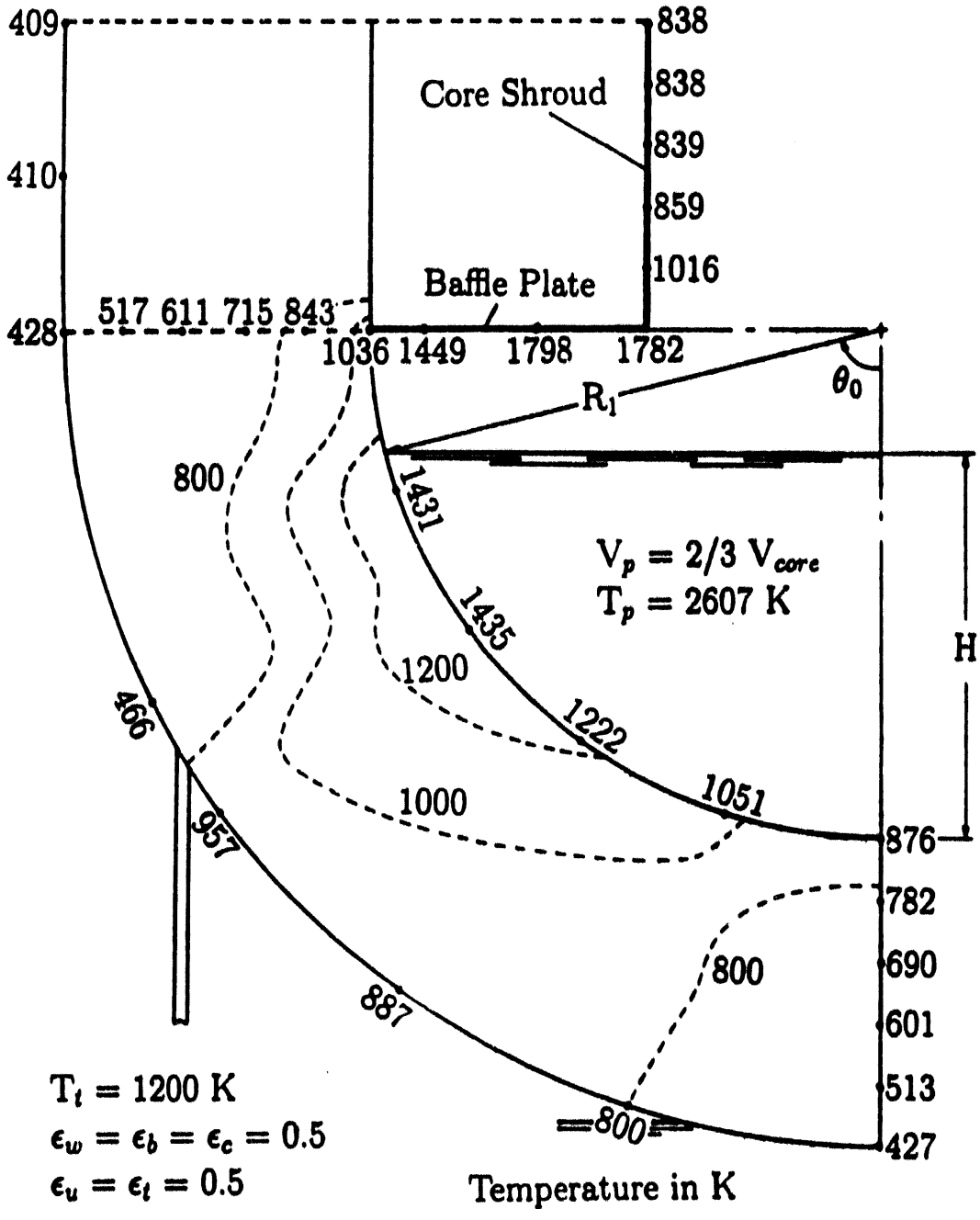

Figure I.34: Temperature distribution in the vessel shell based on Mayinger et al's correlation

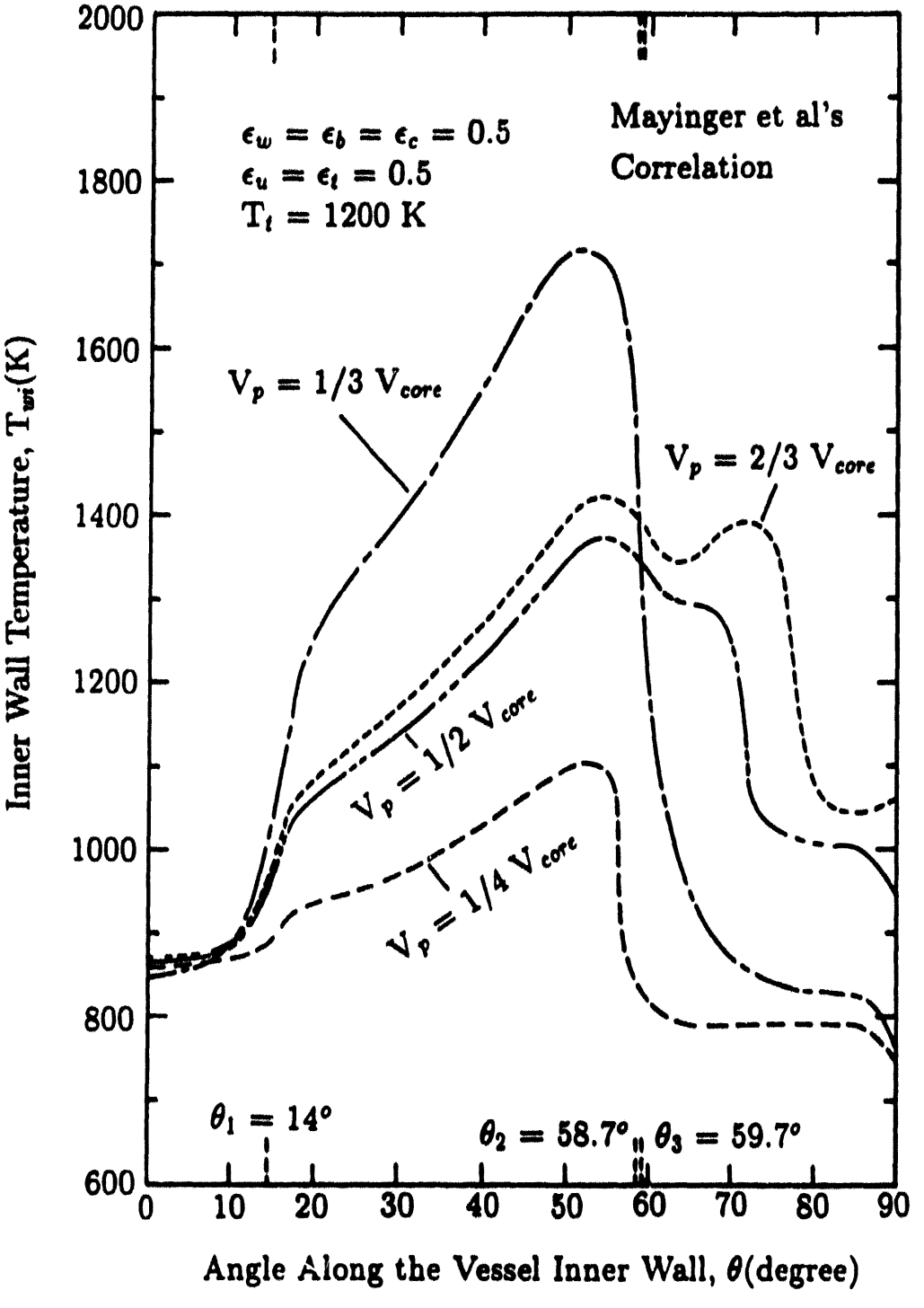

Figure I.35: Variation of the inner wall temperature with different pool volume

Figure I.36 shows the isotherm in the vessel shell for $V_p = 1/3\ V_{core}$. Highest inner wall temperature is seen to reach the melting temperature of steel vessel.

The flooded water within the skirt region is not well mixed with the water outside the skirt, especially the water near the vessel bottom and the free surface of water in the skirt. The subcooled water near the vessel bottom will be heated and eventually reach the saturation temperature of water. As water temperature near the vessel bottom reaches its saturation temperature, the vapor film will be formed on the outer wall of the vessel bottom head, resulting in increase of vessel wall temperature. Considering the water volume (V_l) between the vessel bottom head and the free surface of water in the skirt, the temperature increase of water volume (V_l) is determined by using a simple lumped-capacity method by

$$\rho_l c_{p,l} V_l \frac{dT_l}{dt} = Q_l \tag{69}$$

where Q_l is the amount of heat transfer rate from the wall to water volume and $T_l = T_L$ at $t = 0$.

The time required for the water volume to reach its saturation temperature is obtained by

$$t_{max} = \frac{(T_{sat} - T_L)\rho_l c_{p,l} V_l}{Q_l} \tag{70}$$

Assuming that a fraction of heat transferred from the vessel bottom wall during nucleate boiling is used to heat up the water volume, it is found that about 4 hours are needed to reach the saturation temperature of water volume (shown in Table I.2) when about 10 % of heat transfer rate from the vessel is used. Figure I.37 shows the isotherm in the vessel shell for $V_p = 2/3\ V_{core}$ with $T_L = T_{sat}$. It is seen that the wall temperatures around the vessel bottom and the skirt region are increased by a maximum of 170 K. With such an increase in temperature the vessel wall temperature is still much lower than the melting temperature of steel vessel (1700 K). This is due to the fact that the surface area of the bottom head submerged in water is very small.

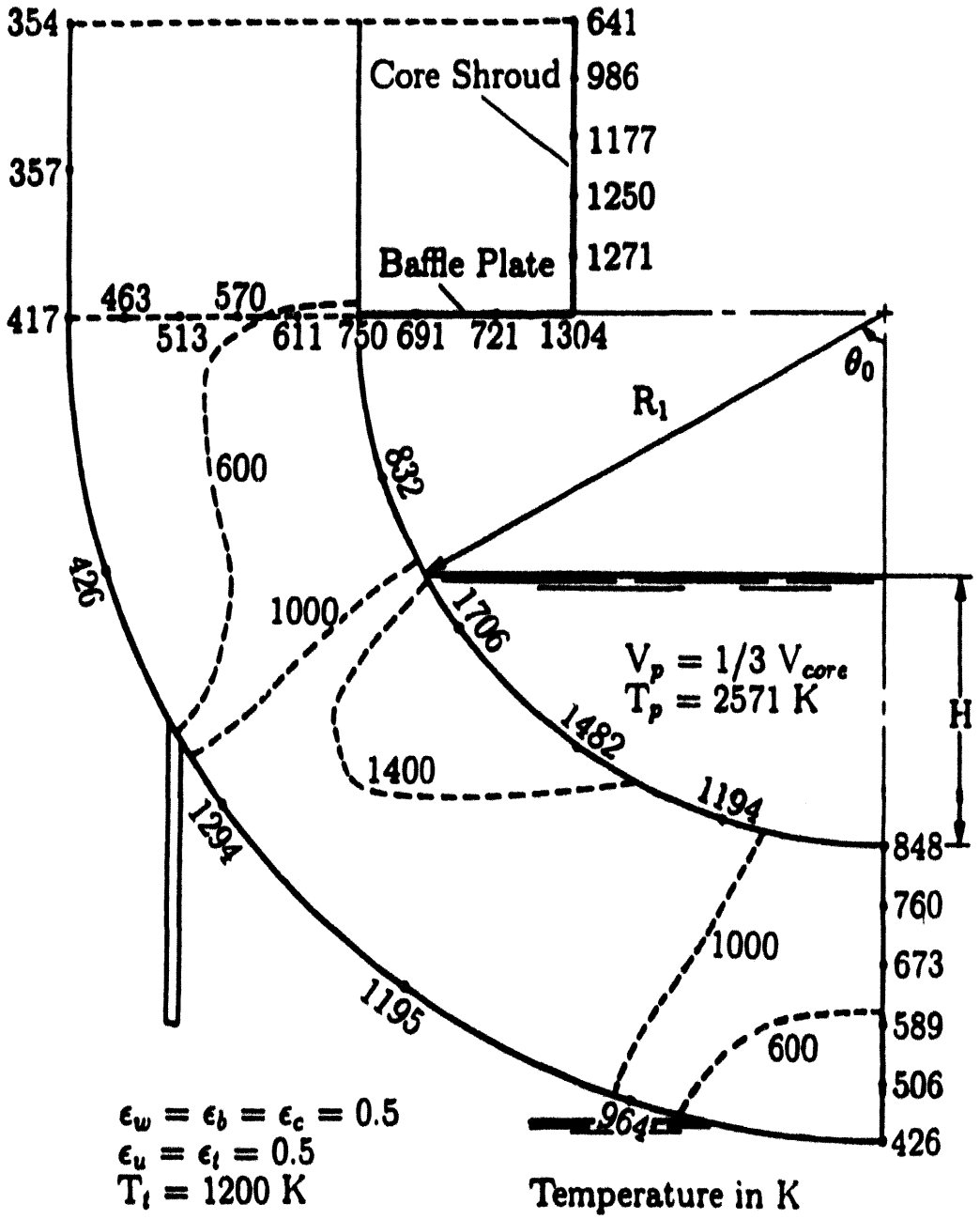

Figure I.36: Temperature distribution in the vessel shell based on Mayinger et al's correlation

Table I.2: Times required for water volume to reach its saturation temperature

V_p = 2/3 V_{core} ,ϵ_i's = 0.5, T_t = 1200 K
$Q_{boil,total}$ = 37.074× 10^4 W

Q_l/ $Q_{boil,total}$ (%)	t_{max} (sec./min./hrs.)
100	1440.8 / 24.01 / 0.40
80	1801.0 / 30.02 / 0.5
60	2401.3 / 40.02 / 0.67
40	3601.9 / 60.03 / 1.00
20	7203.8 / 120.05 / 2.00
10	14407.7 / 240.13 / 4.00

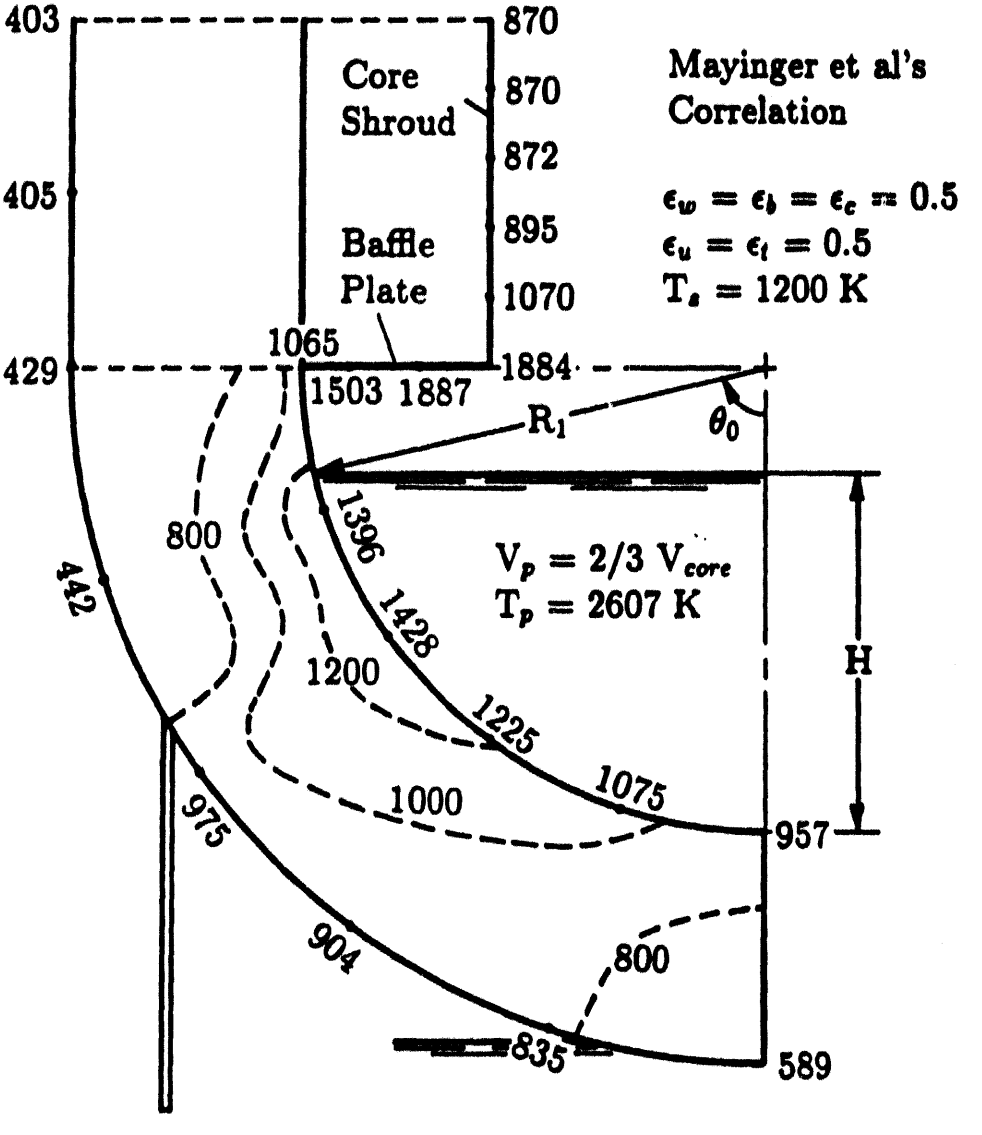

Figure I.37: Temperature distribution in the vessel shell for $T_L = T_{sat}$ in the skirt region

Effects of the decay heat in the corium pool and the thermal conductivities of the corium and the reactor vessel shell on the thermal behavior of the BWR vessel lower head are considered in Appendix I.I. It is found that the maximum inner wall temperature obtained by using the lower value of $Q_{gen,p}$ is predicted to be about 200 K lower than that of the base case (the upper bound of $Q_{gen,p}$ for $V_p = 2/3\ V_{core}$). The effects of k_{vessel} and k_p on the BWR vessel shell temperature are found to be not significant.

Mechanical Behavior of A BWR Vessel Shell

Based on the temperature distribution in the BWR vessel shell, the effective stresses are determined for a given system pressure. Figures I.38 and I.39 show the distribution of the stresses in the BWR vessel shell for the two types of boundary conditions on the top of the cylindrical shell when Mayinger et al's correlation is used and the system pressure is 7 MPa. The minimum stresses occuring along the mid plane of the hemispherical vessel shell are lower than the yield stress of steel vessel (about 50 ksi) except in the region near the vessel support skirt. However, the stresses in the cylindrical vessel shell are higher than the yield stress of the steel vessel over a wide region. Since the largest temperature gradients occur across the hemispherical vessel shell above the skirt attachment, the corresponding stresses in that region are high. Bending moment around the skirt attachment will result and affect the stress distribution in the cylindrical vessel shell connected to the hemisphere.

In order to investigate the effect of the system pressure on the thermal stresses, the thermal stresses in the vessel shell are considered for a low system pressure. Figure I.40 shows the distribution of the thermal stresses in the vessel shell with the roller boundary condition on the top of the cylindrical section when Mayinger et al's correlation is used and the system pressure is assumed to be 1 MPa. Comparing the thermal stresses with $P_i = 7$ MPa (shown in Figure I.38), it is seen that the system pressure does not play a dominant role on the thermal stresses in the hemispherical vessel shell. It is also noted that the bending effect on the cylindrical vessel shell is reduced as the system pressure decreases.

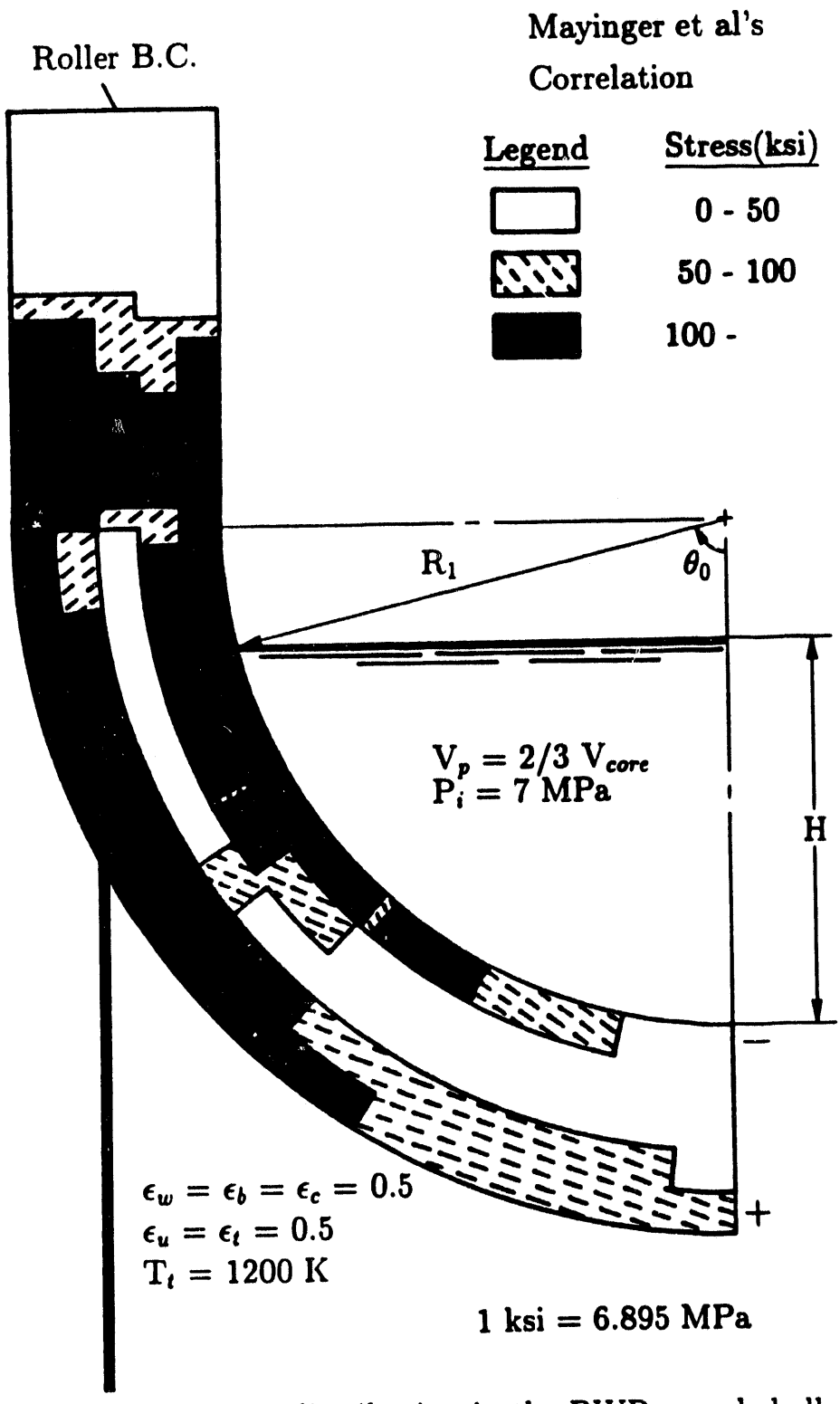

Figure I.38: Stress distribution in the BWR vessel shell

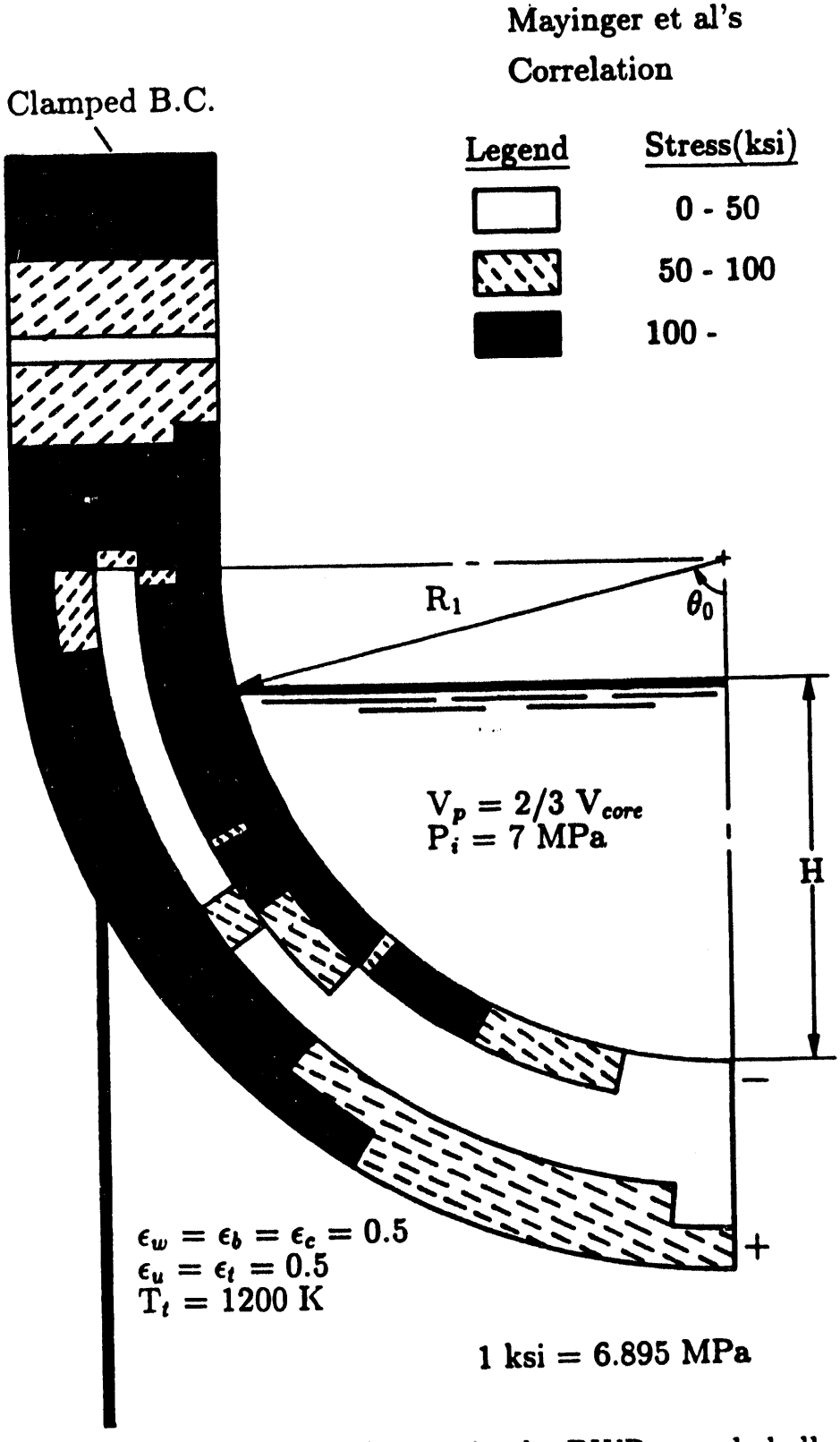

Figure I.39: Stress distribution in the BWR vessel shell

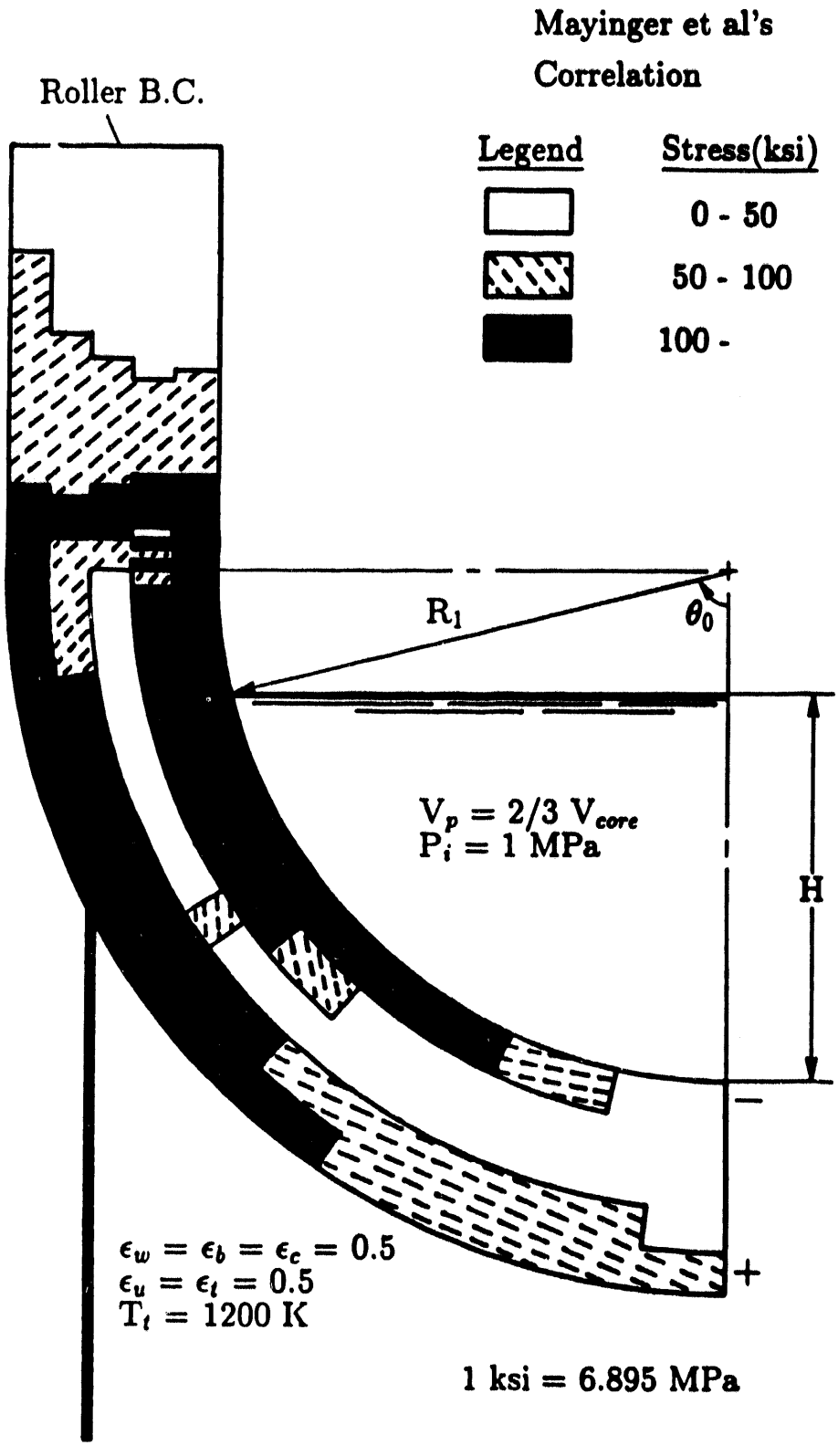

Figure I.40: Stress distribution in the BWR vessel shell

Figure I.41 shows the deformed shape of the vessel shell for the roller boundary condition on the top of the cylindrical section. Even though the severely deformed shape of the support skirt is obtained by using the elastic theory, it can be expected that the effective stresses in the skirt structure will be much higher than the yield stress of steel, especially near the armpit weld region. If the skirt armpit weld fails, water existing outside the skirt can flow into the skirt region and displace the trapped gas.

The total displacements of the outer wall of the vessel shell are plotted in Figure I.42 when Mayinger et al's correlation is used for $V_p = 2/3\ V_{core}$. It is seen that differences between displacements of the outer wall of the hemispherical vessel shell for different system pressures are very small.

Figure I.43 shows the distribution of the effective stresses in the vessel shell with the roller boundary condition imposed on the top of the cylindrical section for $V_p = 1/3\ V_{core}$. In obtaining the effective stresses Mayinger et al's correlation was used with a syatem pressure of 7 MPa. Since the vessel wall temperatures in the skirt region, for $V_p = 1/3\ V_{core}$, are higher than those for other pool volumes as shown in Figure I.35, the calculated stresses are predicted to exceed the yield and ultimate stresses of steel over a wide region across the hemispherical vessel shell. This raises the possibility of a large plastic deformation and the survival of the vessel is placed in question.

Figure I.44 shows the total displacements of the outer wall of the vessel shell for different pool volumes when Mayinger et al's correlation is used for $P_i = 7$ MPa. It is seen that larger displacements in the skirt region for $V_p = 1/3\ V_{core}$ are predicted to occur due to higher wall temperature distributions in that region.

A drywell flooding strategy to completely cover the BWR reactor vessel lower head with water in which a gas release pathway from the vessel skirt might be provided is obtained by drilling several small holes through the skirt at points just below the attachment weld [4]. From the standpoint of regulatory requirements, cost-benefit analyses, radiation exposure to personnel, etc., this is clearly not a practical proposal for existing

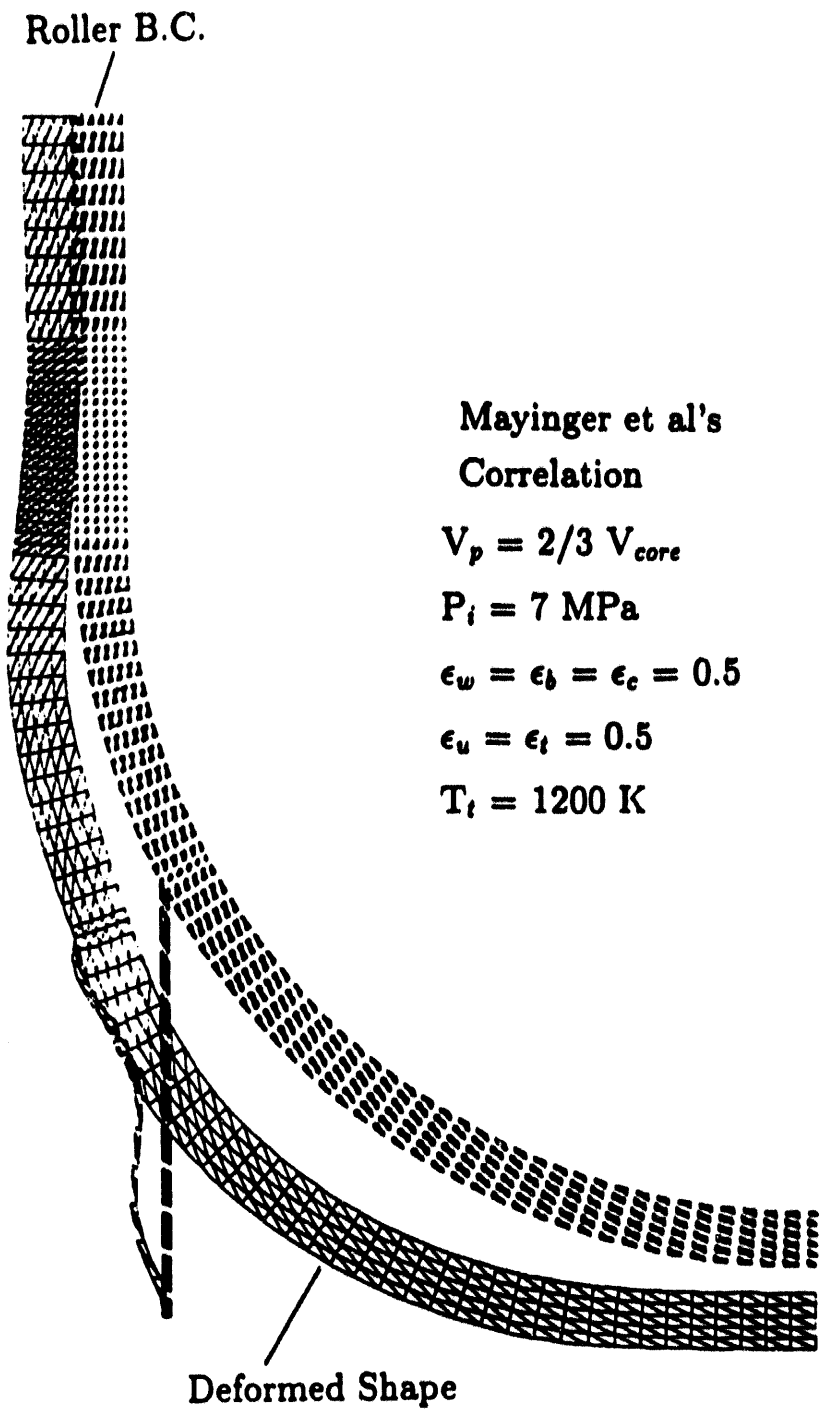

Figure I.41: Deformed shape of the BWR vessel shell

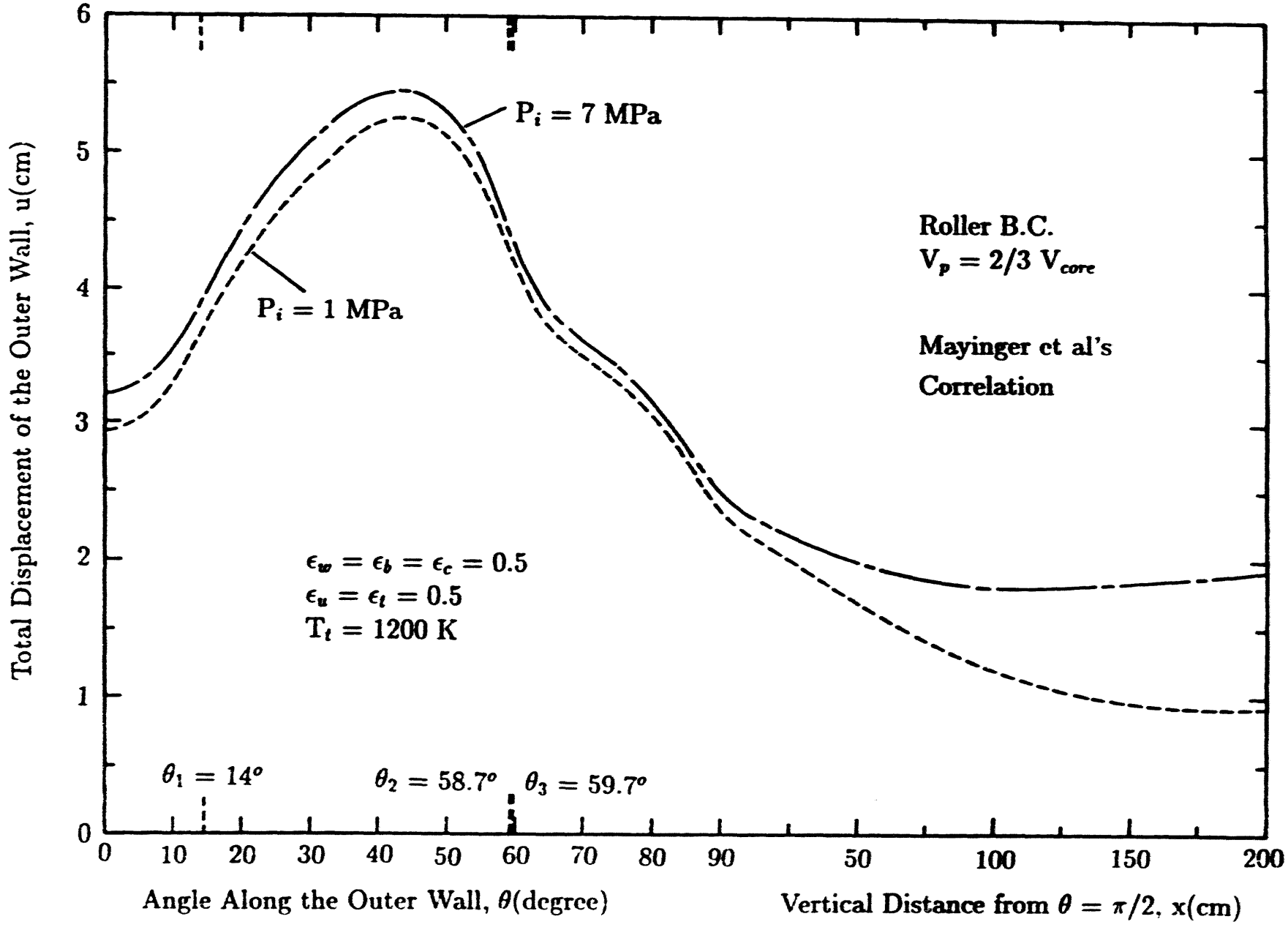

Figure I.42: Comparison of total displacement of the outer wall of the BWR vessel for different system pressures

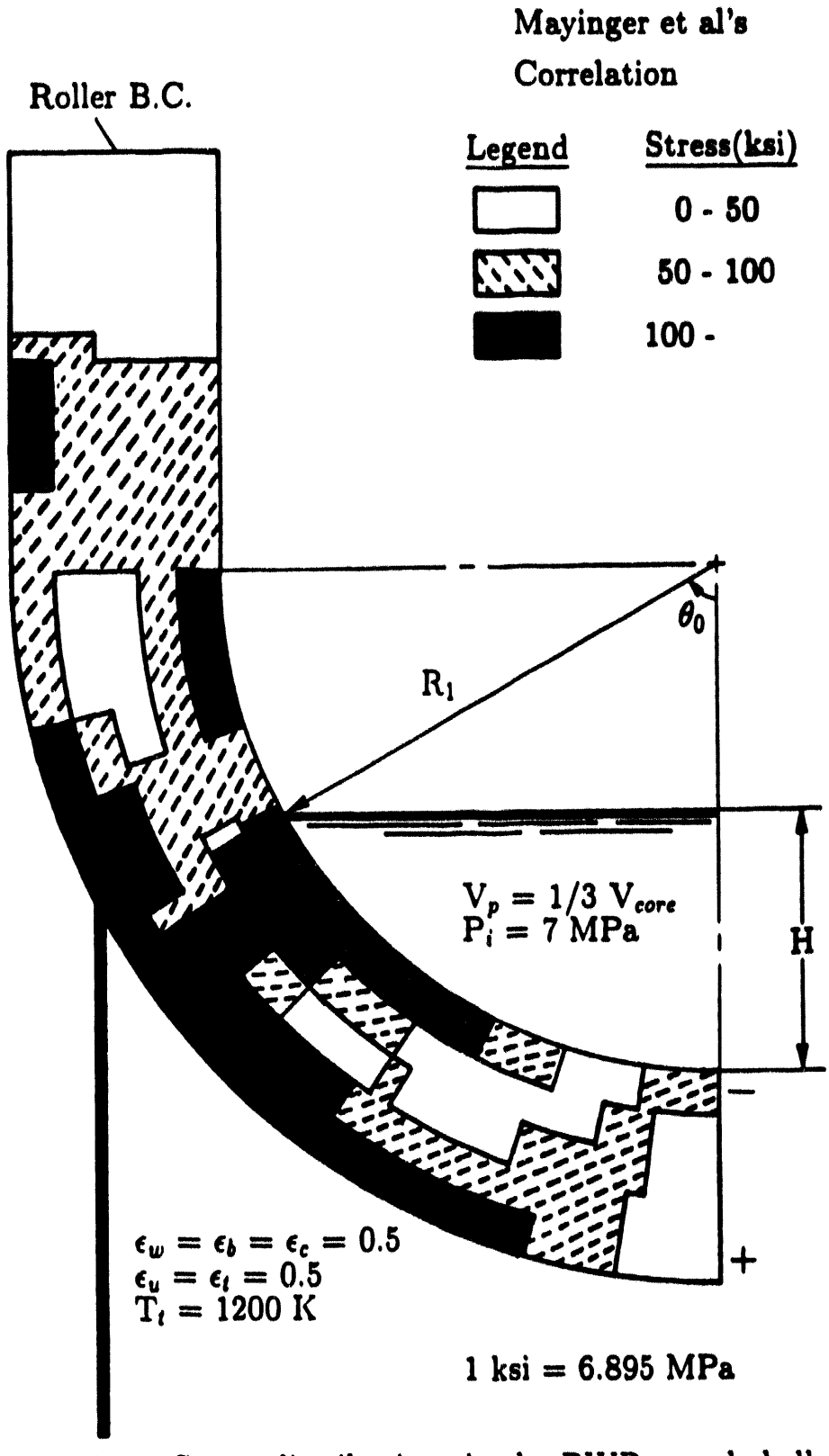

Figure I.43: Stress distributions in the BWR vessel shell

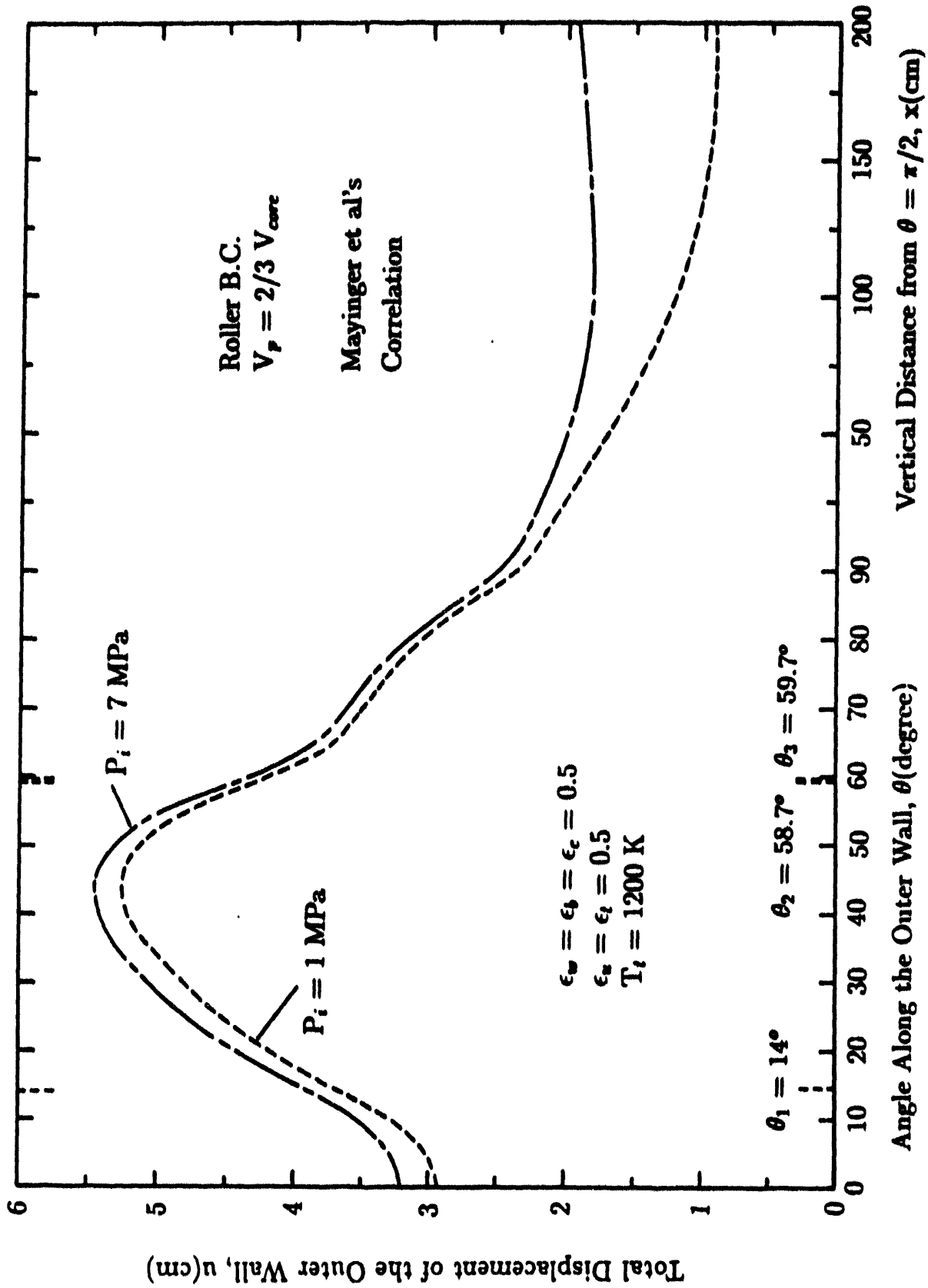

FIGURE I.44: Comparison of total displacement of outer wall of the BWR vessel under different pool volumes.

facilities; it might be considered, however, for advanced plant designs.

Figure I.45 shows the isotherms obtained by releasing the gas trapped in the support skirt when Mayinger et al's correlation is used for V_p = 2/3 V_{core}. It is seen that the outer wall temperatures in the skirt region are significantly lower than those without venting the trapped gas in the skirt.

An optimistic case for the distribution of the effective stresses in the vessel shell without the trapped gas in the skirt is considered. Based on the temperature distribution in the vessel shell as shown in Figure I.45, the thermal stresses are obtained for a system pressure of 1 MPa and V_p = 2/3 V_{core}. Figure I.46 shows the distribution of the thermal stresses in the vessel shell for the roller boundary condition on the top of the cylindrical section. The minimum stresses occur along the mid plane of the hemispherical vessel shell and are lower than the yield stress of the steel vessel. Because of a very large temperature difference across the hemispherical vessel shell above the skirt attachment and the high thermal stress distributions in that region, the bending effect on the cylindrical vessel shell is observed.

Figure I.47 shows the distribution of the stresses in the vessel shell without the support skirt attachment (assumed to be failed) on the outer wall of the vessel lower head for a system pressure of 1 MPa and V_p = 2/3 V_{core}. The minimum stress occuring along the mid plane of the hemispherical vessel lower head is lower than the yield stress of steel vessel except in the narrow region just below the pool free surface where the largest temperature differences occur across the vessel wall. Since there is no bending moment on the cylindrical vessel shell for this case, the stresses in the cylindrical vessel shell are lower than those obtained in the presence of the skirt.

From the results of the steady state temperature distribution in the BWR vessel shell for V_p = 2/3 V_{core} and when Mayinger et al's correlation is used, stresses across the hemispherical vessel shell are found not exceed the yield stress of steel except in the narrow region around the skirt. However, for V_p = 1/3 V_{core}, stresses in the hemispherical vessel

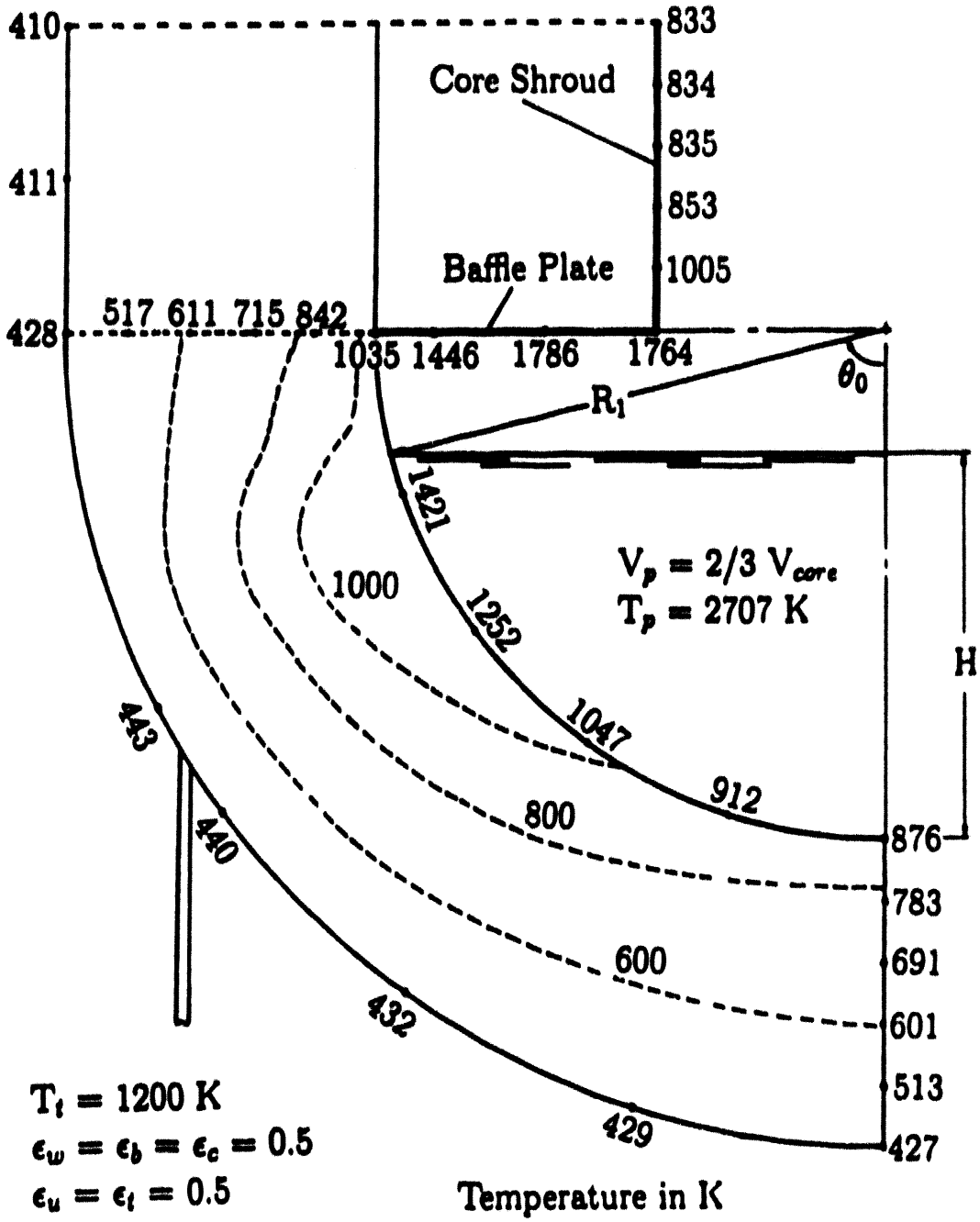

Without Air in the Support Skirt

Figure I.45: Temperature distribution in the vessel shell based on Mayinger et al's correlation

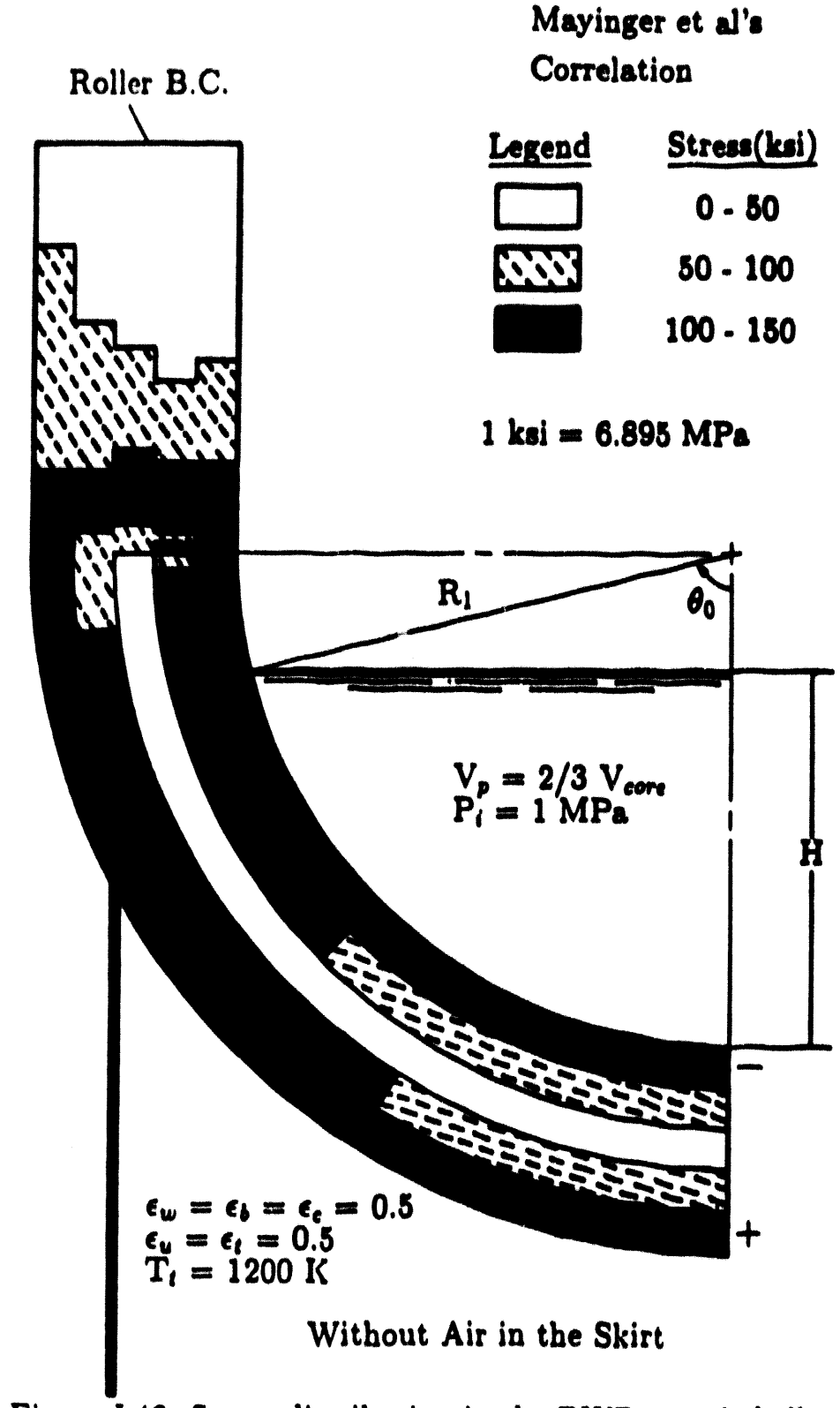

Figure I.46: Stress distribution in the BWR vessel shell

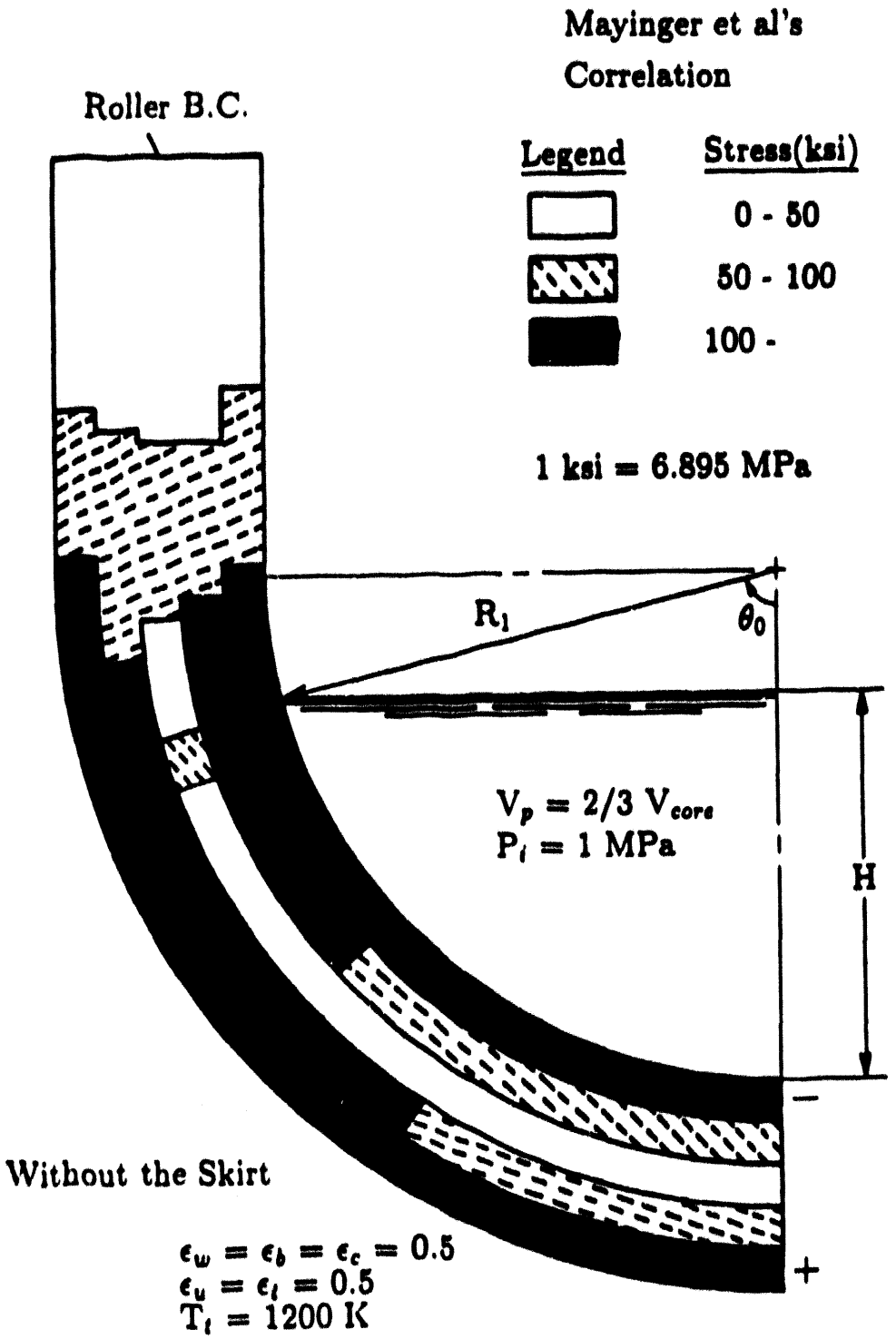

Figure I.47: Stress distribution in the BWR vessel shell

shell are predicted to exceed the yield stress over a wide region around the skirt and a large plastic deformation is predicted to occur. Large deformation theory or plasticity thoery needs to be applied before a conclusive statement with respect to failure of the vessel can be made.

To assess the failure of the BWR vessel shell due to creep rupture, rupture times are calculated by using the relationship between the Larson-Miller parameter and the equivalent stress in the vessel shell. The dependence of rupture times on various vessel shell temperatures is shown in Figure I.48 for different system pressures. From the transient analysis of the thermal behavior of the PWR vessel lower head, it was found that time period longer than 3 hours after slumping of the core material into the vessel lower head is needed for the vessel wall temperature to attain a steady state condition. Isotherms in the vessel shell for $V_p = 2/3\ V_{core}$ when Mayinger et al's correlation is used are shown in Figure I.34. The corresponding maximum steady-state inner wall temperature, the maximum steady-state mid plane temperature and the maximum steady-state outer wall temperature are obtained to calculate the creep rupture times for different system pressures. It is found that for system pressures of 4 and 7 MPa, immediate creep failure of the vessel shell will occur if the maximum steady-state inner wall temperature of the vessel lower head is used. However, about 1 hour of rupture time after quasi-steady conditions are obtained is predicted when the maximum steady-state outer wall temperature of the vessel lower head is used.

For a system pressure of 1 MPa, about 1 hour of rupture time after the pool attains its near steady state temperature is predicted when the maximum steady-state inner wall temperature is used. However, rupture time of the order of 10^6 hours is predicted when the maximum steady-state outer wall temperature is used.

If the trapped gas in the skirt region is vented by some means as mentioned earlier, the maximum steady-state outer wall temperature (shown in Figure I.45) is predicted to be lower than that without venting the trapped gas in the skirt. Using this outer wall temperature, much longer rupture times are calculated.

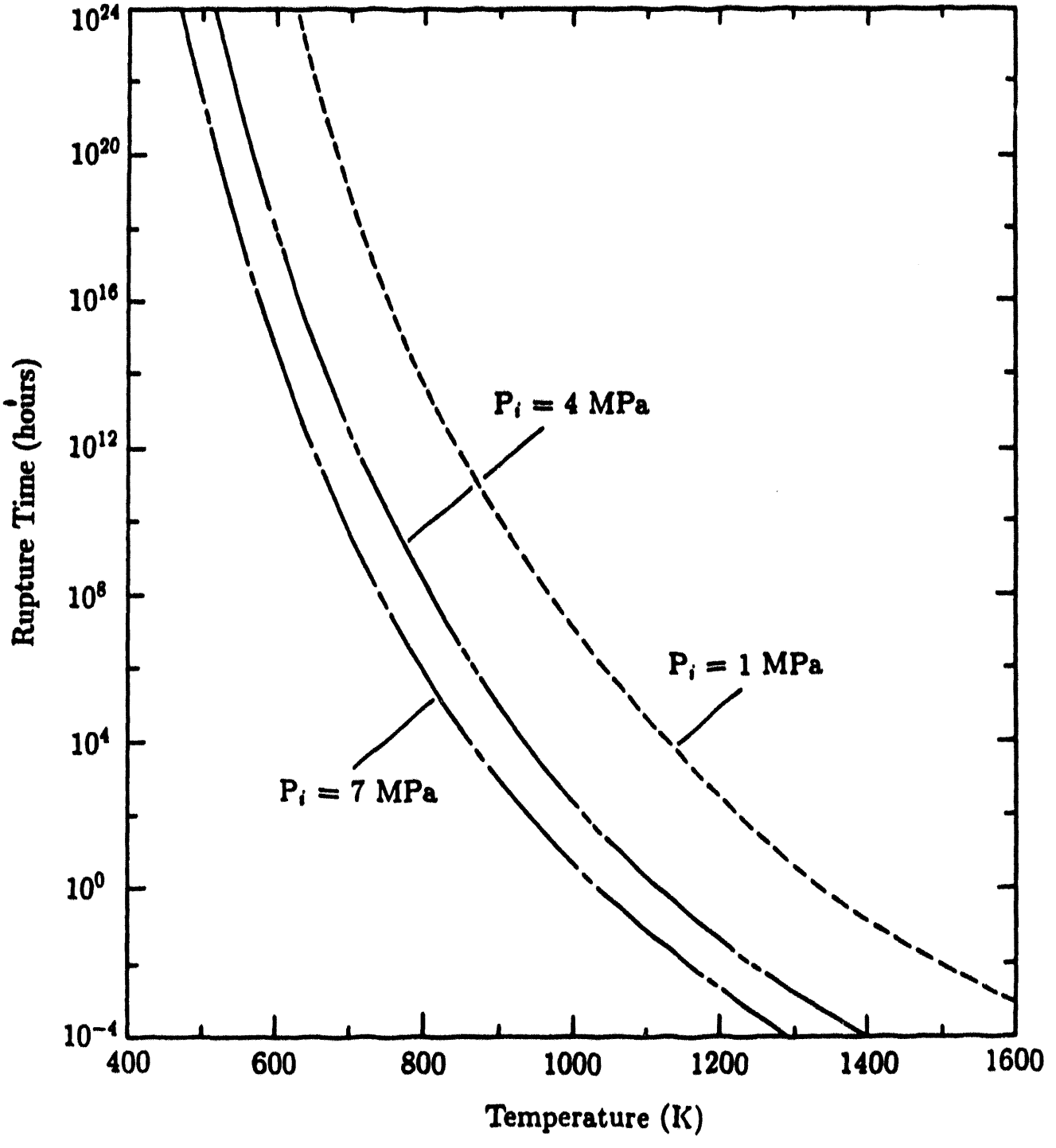

Figure I.48: Variation of the creep rupture time with vessel wall temperature

The creep rupture times are dependent upon the vessel wall temperature chosen for the calculations. The estimated rupture times can be used to assess the probability of vessel failure during flooding of the drywell of a BWR. It should again be noted that creep rupture times have not been calculated by carrying out time dependent stress calculations and by evaluating time integrated damage to a particular element in the vessel wall.

Calculations are performed in Appendix I.J to determine the effect of the water level in the drywell on the upper vessel wall temperature when complete venting of the support skirt occurs by some means. It is found that, for the attainable water level (about two-thirds vessel height) in the drywell, the upper vessel wall temperatures are predicted to be lower than the melting temperature of steel vessel. This is valid as long as heat loss rate from debris to the upper vessel wall is less than 10 MW. Therefore, if the water level in the drywell is kept high enough and the support skirt is vented, indefinite retention of core material in the vessel lower head can be achieved.

I.7 CONCLUSIONS

Two dimensional transient (PWR) and steady (PWR and BWR) state thermal analysis of the reactor vessel shell have been performed after core material relocates into the vessel lower head with cavity (or drywell) already flooded with water. Results were obtained by using two different heat transfer correlations for the natural convection in the molten pool. In the analysis, the emissivities of pool free surface, the vessel wall, the upper structure, the baffle plate (BWR) and core shroud (BWR) were varied parametrically. Calculations were performed for structure temperature between 800 and 1600 K (PWR) and between 1000 and 1500 K (BWR).

Effecitve stresses and displacements in the reactor vessel shell were investigated by using the numerically calculated steady state temperature distributions in the vessel shell when the cavity (or the drywell) is flooded. An axisymmetric finite element scheme was implemented by means of the computer code, NASTRAN. The clamped and the roller boundary conditions on the top of the vessel shell were employed as extreme cases. For the given system pressure, the creep rupture times after slumping of the core material into the vessel lower head were determined by using the relatonship between the Larson-Miller parameter and the equivalent stress. It was found that:

- It may take several hours before quasi-steady state conditions are established in the PWR vessel lower head. During the transient period the pool temperature will increase accompanied by remelting of the crust.
- Some melting of the PWR vessel inner wall is predicted to occur. The thickness of the vessel wall after mixing of the molten steel with the molten corium is allowed is small and may not be able to sustain the imposed stresses. This in turn may lead to vessel failure.
- Melting of the BWR baffle plate is predicted to occur and this may open a new path for the release of superheated steam and fission products.
- The effect of emissivities of the pool surface, structure, the vessel

wall, the baffle plate (BWR) and the core shroud (BWR), and the structure temperature on the vessel inner wall is predicted to be small when Mayinger et al's correlation is used. However, the emissivity of the unwetted wall has a larger effect on the unwetted wall temperature.

- The effect of variation in the decay heat in the molten corium on the vessel shell temperature is predicted to be small when Mayinger et al's correlation is used. However, the thermal conductivity of the vessel shell has a large effect on the unwetted wall temperature.

- From thermal analysis, it is found that for the range of parameters studied, some melting of the vessel inner wall will occur, hence flooding of the cavity of a PWR may not provide an effective means of retaining the core material in the reactor vessel lower head. However, flooding of the drywell of a BWR may provide sufficient cooling of the reactor vessel lower head to maintain the molten core within the vessel lower head.

- Significant deviations in the predicted temperatures can occur because of uncertainties in the internal natural convection correlations. At present no data are available at very high Rayleigh number encountered in the calculation of natural convection in the molten pool.

- The effective stresses in the PWR vessel shell are predicted to exceed the yield stress of vessel steel for both the roller and clamped boundary conditions and for pool volumes considered in this paper when Mayinger et al's correlation is used. The effect of temperature variation on the stresses is found to be much more pronounced than that of system pressure. Therefore, a large plastic deformation of the vessel shell is predicted to occur. The present calculations in which plastic deformation and relaxation of stresses was not considered suggest a high probability of the PWR vessel failure.

- For $V_p = 2/3\ V_{core}$ thermal stresses in the BWR vessel lower head are predicted to be lower than the yield stress of steel except in a narrow region in the support skirt when Mayinger et al's correlation is used. However, for $V_p = 1/3\ V_{core}$, the stresses are predicted to

be much higher than the yield stress of steel and the survival of the vessel lower head is in question. Again no plastic deformation or relaxation of thermal stresses have been included in the analysis.

- Venting of the trapped gas in the BWR vessel support skirt is found to lower the stress distributions in the BWR vessel lower head and in turn increases creep rupture times.

- The boundary conditions used in the effective stress calculations are only approximate. Further refinement of the model can be achieved through a more detailed analysis including the upper cylindrical portion of the vessel.

- Large deformation theory or plasticity analysis needs to be applied to predict more reliable displacement and stress distributions in the vessel shell. However, the plastic behavior of the vessel material at high temperature is not yet clearly understood.

- A large uncertainty exists in the prediction of creep rupture times. Creep rupture times of only a few hours are predicted if highest average wall temperature is used. However, rupture times are very long if vessel outer wall temperature is used. Creep rupture times have not been obtained by carrying out time dependent stress calculations and by evaluating time integrated damage to a particular element in the vessel.

I.8 REFERENCES

1. BWR Owners' Group Emergency Procedure Guidelines, Revision 4, General Electric Topical Report NEDO-31331, March 1987.

2. W. A. CONDON, S. R. GREENE, R. M. HARRINGTON AND S. A. HODGE, "SBLOCA Outside Containment at Browns Ferry Unit One - Accident Sequence Analysis," NUREG/CR-2672, Vol. 1, p. 197, ORNL/TM-8119/V1, 1982.

3. J. E. O'BRIEN AND G. L. HAWKES, "ARSAP AP 600 In-Vessel Coolability Thermal Analysis Final Report," DOE/ID-10369, December 1991.

4. S. A. HODGE, J. C. CLEVELAND, T. S. KRESS AND M. PETEK, "Identification and Assessment of BWR (In-Vessel) Severe Accident Mitigation Strategies," NUREG/CR-5869, ORNL/TM-12080, 1992.

5. G. L. THINNES, "TMI-2 Lower Head Creep Rupture Analysis," EGG-TMI-8133, August, 1988.

6. J. L. REMPE, S. A. CHAVEZ, G. L. THINNES, C. M. ALLISON, G. E. KORTH, R. J. WITT, J. J. SIENICKI, S. K. WANG, C. H. HEATH AND S. D. SNOW, "Light Water Reactor Lower Head Failure Analysis," NUGER/CR-5642, EGG-2618, 1992.

7. H. PARK AND V. K. DHIR, "Steady State Analysis of External Cooling of A PWR Vessel Lower Head", AIChE Symposium Series, No. 283, Vol. 87, p. 1, 1991.

8. H. PARK AND V. K. DHIR, "Effect of Outside Cooling on the Thermal Behavior of A Pressurized Water Reactor Vessel Lower Head," To appear in Nuclear Technology, 1992.

9. H. PARK AND V. K. DHIR, "Effect of External Flooding on Retention of Core Material in A BWR Lower Head", 7th Proceedings of Nuclear Thermal Hydraulics, p. 315, ANS Winter Meeting, 1991.

10. R. M. OSTMEYER, "An Approach to Treating Radionuclide Decay Heating for Use in the MELCOR Code System," NUREG/CR-4169, 1985.

11. J. METZINGER AND H. V. KLAPDOR, "New Results on the Decay Heat of Nuclear Reactors," Max-Planck-Institute fur Kernphysik, Heidelberg, Germany, 1985.

12. F. MAYINGER, M. JAHN, H. REINEKE AND V. STEINBRENNER, "Examination of Thermohydraulic Processes and Heat Transfer in a Core Melt," BMFT RS 48/1. 1976, Institute fur Verfanhrenstechnic der T.U., Hanover, Germany, 1976.

13. J. D. GABOR, P. G. ELLISON AND J. C. CASSULO, "Heat Transfer from Internally Heated Hemispherical Pools," Presented at the 19th National Heat Transfer Conference, Orlando, FL, 1980.

14. B, FRANTZ AND V. K. DHIR, "Experimental Investigation of Natural Convection in Spherical Segments of Volumetrically Heated Pools," presented at the 28th National Heat Transfer Conference, San Diego, August, 1992.

15. G. W. PARKER, L. J. OTT AND S. A. HODGE, "Small Scale BWR Core Debris Eutectics Formation and Melting Experiment," Nuclear Engineering and Design, Vol. 121, p. 341, 1990.

16. S. NAZARE, G. ONDRACEK AND B. SCHULZ, "Properties of Light Water Reactor Core Melts," American Nuclear Technology, Vol. 32, p. 239, 1977.

17. S. S. DOSANJH, "Melt Propagation in Dry Core Debris Beds," Nuclear Technology, Vol. 88, p. 30, 1989.

18. S. W. CHURCHILL AND R. U. CHURCHILL, "A Comprehensive Correlating Equation for Heat and Component Transfer by Free Convection," AIChE Journal, Vol. 21, No.3, p. 604, 1975.

19. V. K. DHIR, "Study of Transient Transitional Boiling Heat Fluxes from Spheres Subjected to Forced Vertical Flow," International Heat Transfer Conference, Toronto, Canada, 1978.

20. V. K. DHIR AND G. P. PUROHIT, "Subcooled Film-Boiling Heat Transfer from Spheres," Nuclear Engineering and Design, Vol. 47, p. 49, 1978.

21. R. SIEGEL AND J. R. HOWELL, Thermal Radiation Heat Transfer, McGraw-Hill Book Company, NY, 1981.

22. F. A. KULACKI AND A. A. EMARA, "High Rayleigh Number Convection in Enclosed Fluid Layers with Internal Heat Sources," U.S. Nuclear Regulatory Commission Report NUREG-75/065, July, 1975.

23. M. JAHN AND H. H. REINEKE, "Free Convection Heat Transfer with Internal Heat Sources," Proceedings of the Fifth International Heat Transfer Conference, Vol. 3, p. 74, 1974.

24. V. K. DHIR AND S. P. LIAW, "Framework for a Unified Model for Nucleate and Transition Pool Boiling," Journal of Heat Transfer, Vol. 111, p. 739, 1989.

25. T. D. BUI AND V. K. DHIR, "Transition Boiling Heat Transfer on a Vertical Surface," ASME Journal of Heat Transfer, Vol. 107, p. 756, 1985.

26. T. D. BUI AND V. K. DHIR, "Film Boiling Heat Transfer on a Isothermal Vertical Surface," ASME Journal of Heat Transfer, Vol. 107, p. 764, 1985.

27. P. J. BERENSON, "Transition Boiling Heat Transfer from a Horizontal Surface," Journal of Heat Transfer, Vol. 83c(3), p. 351, 1961.

28. A. K. MAL AND S. J. SINGH, Deformation of Elatic Solids, Prentice-Hall, Inc., NJ, 1991.

29. F. R. LARSON AND J. MILLER, "A Time-Temperature Relationship for Rupture and Creep Stress," Transaction of ASME, p. 765, July, 1952.

30. V. N. SHAH, "Creep Rupture Failure of Reactor Pressure Vessel Lower Head During Severe Accidents," EGG-M-06886, September, 1986.

31. S. P. TIMOSHENKO AND J. N. GOODIER, Theory of Elasticity, McGraw-Hill Book Company, p. 455, NY, 1982.

Appendix I.A
Finite Difference Form of the Transient Energy Equation for the Vessel Shell (PWR)

Using central differences for the spatial derivatives and the forward difference for the time derivative in Equation (I.1) and defining $\Delta r=(R_2-R_1)/M$, $\Delta\theta=\pi/2N$, $r=R_1+i\Delta r$ for i=0, 1, 2,..., M and $\theta=j\Delta\theta$ for j=0, 1, 2,..., N, $t_m=m\Delta t$ for m=0, 1, 2,... and $T_{i,j}^{(m)}=T_w(r,\theta,t_m)$, the finite difference form of Equation (I.1) becomes

$$T_{i,j}^{(m+1)} = (1-2U_1)T_{i,j}^{(m)} + U_2T_{i-1,j}^{(m)} + U_3T_{i+1,j}^{(m)} + U_4T_{i,j-1}^{(m)} + U_5T_{i,j+1}^{(m)}$$

where

$$U_1 = \alpha_w\Delta t\left(\frac{1}{\Delta r^2}+\frac{1}{r^2\Delta\theta^2}\right)$$

$$U_2 = \alpha_w\Delta t\left(\frac{1}{\Delta r^2}-\frac{1}{r\Delta r}\right)$$

$$U_3 = \alpha_w\Delta t\left(\frac{1}{\Delta r^2}+\frac{1}{r\Delta r}\right)$$

$$U_4 = \alpha_w\Delta t\left(\frac{1}{r^2\Delta\theta^2}-\frac{cot\theta}{2r^2\Delta\theta^2}\right)$$

$$U_5 = \alpha_w\Delta t\left(\frac{1}{r^2\Delta\theta^2}+\frac{cot\theta}{2r^2\Delta\theta^2}\right)$$

and the superscripts in the above equation denote the time step.

Appendix I.B
Effect of the Steam on the Radiative Heat Transfer

A simple calculation is performed to estimate the effect of the steam on the radiative heat transfer from the upper surface of the pool. Two parallel plates are considered to simulate the upper structure and the pool free surface as shown in Figures I.1 and I.2.

It is assumed that scattering is coherent and isotropic and that the steam temperature distribution is associated with the condition of radiative equilibrium. For the radiative equilibrium condition, equation of transfer is given by

$$\mu \frac{\partial J(z,\mu)}{\partial z} + \sigma J(z,\mu) = \frac{\sigma}{2} \int_{-1}^{1} J(\tilde{\mu}) d\tilde{\mu} \tag{I.71}$$

where $\mu = \cos\theta$, z is the distance from plate 1 having temperature T_1, σ is the aborption coefficient and J(z,μ) is the radiative intensity which is indendent of frequency.

The corresponding boundary conditions are

$$J(0,\mu) = \epsilon_1 \frac{acT_1^4}{4\pi} + 2(1-\epsilon_1) \int_{-1}^{0} J(0,\tilde{\mu}) \mid \tilde{\mu} \mid d\tilde{\mu}, \quad \mu > 0 \tag{I.72}$$

$$J(L,\mu) = \epsilon_2 \frac{acT_2^4}{4\pi} + 2(1-\epsilon_2) \int_{0}^{1} J(L,\tilde{\mu}) \tilde{\mu} d\tilde{\mu}, \quad \mu < 0 \tag{I.73}$$

where $\tilde{\sigma} = ac/4$, c is the speed of light, $\tilde{\sigma}$ is the Stefan-Boltzmann constant, L is the distance between two parallel plates, ϵ_1 and ϵ_2 are the surface emissivities, and T_1 and T_2 are surface temperatures.

Using the definition of the radiative flux of energy in terms of the solid angle, $\vec{\Omega}$, given by

$$\vec{F}(\vec{r}) = \int_{4\pi} \vec{\Omega} J(\vec{r},\vec{\Omega}) d\vec{\Omega} \tag{I.74}$$

and integrating (I.71) over all μ, we get

$$\frac{\partial F}{\partial z} = 0 \tag{I.75}$$

The classical diffusion theory states

$$F(z) = -\frac{1}{3\sigma} \frac{d}{dz}(cE) \tag{I.76}$$

where E is the radiative energy density defined as

$$E(\vec{r}) = \frac{1}{c}\int_{4\pi} J(\vec{r},\vec{\Omega})d\vec{\Omega} \tag{I.77}$$

Combining Equations (I.75) and (I.76), we find the following

$$\frac{d^2}{dz^2}(cE) = 0 \tag{I.78}$$

or

$$cE(z) = A + B\sigma z \tag{I.79}$$

To determine the constants A and B, we need the Marshak boundary condition corresponding to (I.72) and (I.73). In diffusion theory, we have

$$J(z,\mu) = \frac{1}{4\pi}\left[cE(z) + 3\mu F(z)\right] \tag{I.80}$$

Using Equation (I.80) in (I.72), multiplying by $2\pi\mu$ and integrating over $0 \leq \mu \leq 1$, we have for z = 0,

$$\epsilon_1\tilde{\sigma}T_1^4 = \left[\epsilon_1\frac{cE}{4} - \frac{(2-\epsilon_1)}{6\sigma}\frac{d}{dz}(cE)\right]_{z=0} \tag{I.81}$$

Similarly, at z = L, we have

$$\epsilon_2\tilde{\sigma}T_2^4 = \left[\epsilon_2\frac{cE}{4} + \frac{(2-\epsilon_2)}{6\sigma}\frac{d}{dz}(cE)\right]_{z=L} \tag{I.82}$$

Using Equation (I.79) in (I.81) and (I.82), we get

$$\epsilon_1\tilde{\sigma}T_1^4 = \frac{\epsilon_1}{4}A - \frac{(2-\epsilon_1)}{6}B \tag{I.83}$$

and

$$\epsilon_2\tilde{\sigma}T_2^4 = \frac{\epsilon_2}{4}A + \left[\frac{\epsilon_2}{4}\sigma L + \frac{(2-\epsilon_2)}{6}\right]B \tag{I.84}$$

Solving the above two equations simultaneously, the constants A and B can be obtained as

$$A = \frac{1}{\Delta}(h_1 g_4 + h_2 g_2) \tag{I.85}$$

and

$$B = \frac{1}{\Delta}(h_2 g_1 - h_1 g_3) \tag{I.86}$$

where

$$\Delta = g_1 g_4 + g_2 g_3$$

$$g_1 = \frac{\epsilon_1}{4}$$

$$g_2 = \frac{(2 - \epsilon_1)}{6}$$

$$g_3 = \frac{\epsilon_2}{4}$$

$$g_4 = \frac{\epsilon_2}{4}\sigma L + \frac{(2 - \epsilon_2)}{6}$$

$$h_1 = \epsilon_1 \tilde{\sigma} T_1^4$$

$$h_2 = \epsilon_2 \tilde{\sigma} T_2^4$$

Using Equations (I.85) and (I.86) in (I.79), the radiative energy density becomes

$$E(z) = \frac{a}{4\tilde{\sigma}\Delta}[(h_1 g_4 + h_2 g_2) + (g_1 h_2 - h_1 g_3)\sigma z] \tag{I.87}$$

From Equations (I.76) and (I.87), the radiative flux of energy becomes

$$F(z) = -\frac{1}{3\Delta}[g_1 h_2 - h_1 g_3] \tag{I.88}$$

The temperature distribution associated with the condition of radiative equilibrium becomes

$$T^4(z) = \frac{E(z)}{a} = \frac{1}{4\tilde{\sigma}\Delta}[(h_1 g_4 + h_2 g_2) + (g_1 h_2 - h_1 g_3)\sigma z] \tag{I.89}$$

If the radiation heat transfer between two parallel plates without the participating media is considered, the radiative heat flux from surface 1 to surface 2 is obtained as

$$F = \frac{\tilde{\sigma}(T_1^4 - T_2^4)}{1/\epsilon_1 + 1/\epsilon_2 - 1} \tag{I.90}$$

Using the participating media as steam between plates, the radiative heat flux is calculated, in which the emissivities of each surface are taken to be 0.5. The corresponding surface temperatures are taken to be T_1 = 2500 K which is the melting temperature of the molten pool and T_2 = 1600 K which is close to the melting temperature of vessel structure. Absorption coefficient of steam is about 0.7 m^{-1} at $T_{steam} \simeq$ 2200 K and 1 atmospheric pressure. This value is obtained from the reference listed below.

The calculated heat fluxes reaching the surface 2 with and without the participating steam between two parallel surfaces are F(with steam) = 0.6393 MW/m^2 and F(without steam) = 0.7344 MW/m^2. It can be seen that about 13 % of the radiative heat is absorbed by the participating steam. Therefore, this small amount of the radiative heat abosorbed by the participating steam does not affect significantly the calculated vessel inner wall temperature.

Reference for Appendix I.B

E. M. SPARROW AND R. D. CESS, Radiation Heat Transfer, McGraw-Hill Book Company, NY, 1978.

Appendix I.C
Radiative Heat Transfer Parameters (PWR)

The expressions for f's, Z and Y used in Equations (I.7), (I.8) and (I.9) are listed below :

$$f_1 = F_{u-w}(1-\epsilon_w)\frac{\epsilon_u A_u}{\epsilon_w A_w}$$

$$f_2 = F_{u-s}(1-\epsilon_s)\frac{\epsilon_u A_u}{\epsilon_s A_s}$$

$$f_3 = \epsilon_u A_u \sigma (T_u{}^4 - F_{u-w}T_w{}^4 - F_{u-s}T_s{}^4)$$

$$f_4 = F_{w-u}(1-\epsilon_u)\frac{\epsilon_w A_w}{\epsilon_u A_u}$$

$$f_5 = 1 - F_{w-w}(1-\epsilon_w)$$

$$f_6 = F_{w-s}(1-\epsilon_s)\frac{\epsilon_w A_w}{\epsilon_s A_s}$$

$$f_7 = \epsilon_w A_w \sigma ((1-F_{w-w})T_w{}^4 - F_{w-u}T_u{}^4 - F_{w-s}T_s{}^4)$$

$$f_{11} = (f_2 - f_1)f_4 + (f_2+1)f_5 + (f_1+1)f_6$$

$$Z = 1 + \frac{1+cos^2\theta_0}{sin^2\theta_0}$$

$$Y = \frac{1}{sin\theta_0}$$

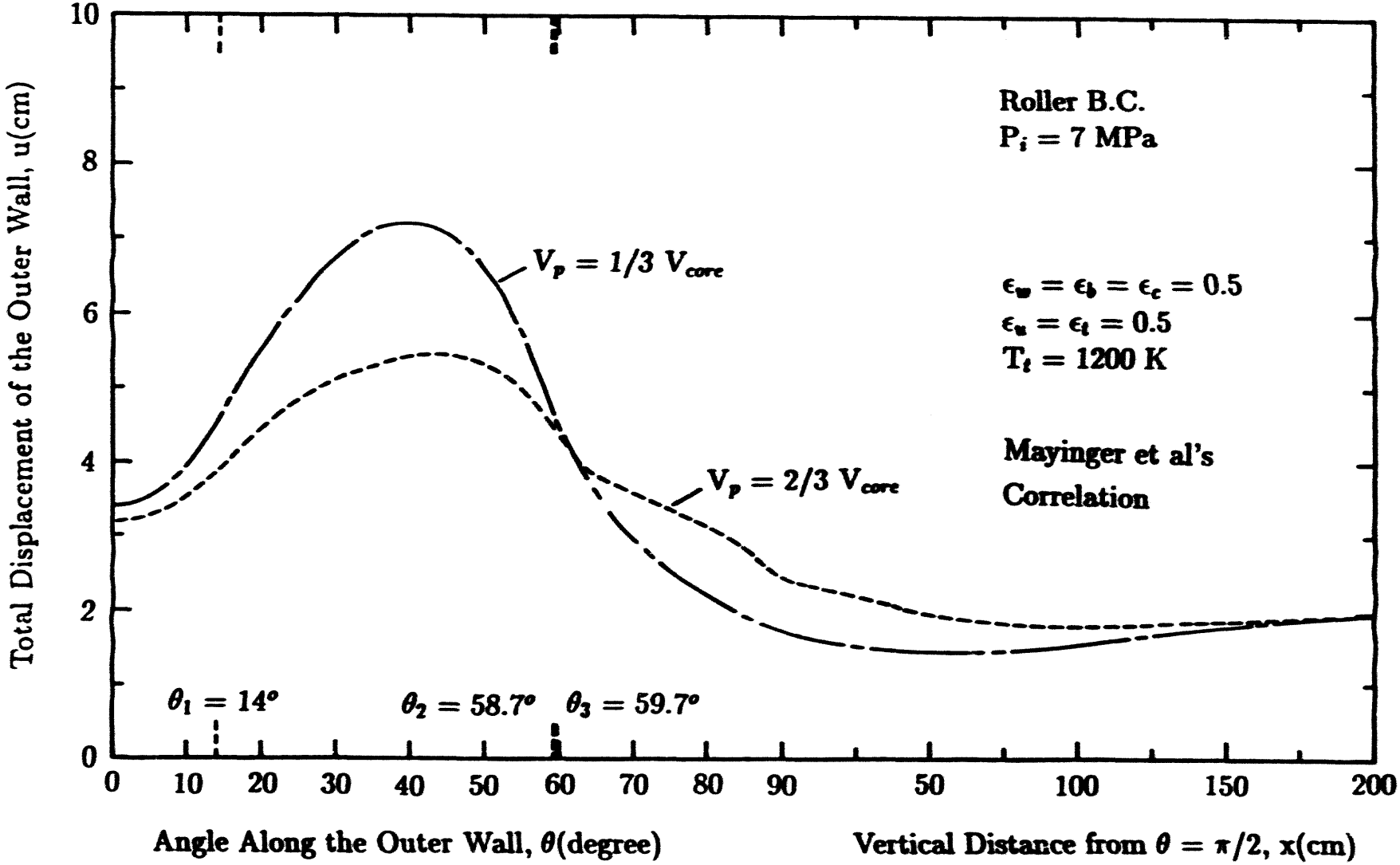

Figure I.44: Comparison of total displacement of the outer wall of the BWR vessel under different pool volumes

Appendix I.D
Comparison of the Heat Fluxes in Film Boiling

Simple calculations are performed to determine as to how much the vessel wall during film boiling increases and to compare to that during nucleate boiling occuring on the vessel bottom outer wall.

Heat fluxes are calculated by using the following expressions:

$$q_{nucleate} = 0.55\Delta T_{wo}, 409 \leq T_{wo} \leq 633K$$

$$q_{rad} = \epsilon\sigma(T_{wo}^4 - T_{sat}^4), \qquad q_{film} = h_{film}\Delta T_{wo}$$

$$q_{total} = q_{film} + q_{rad}$$

where $\epsilon = 0.5$, $\Delta T_{wo} = T_{wo} - T_{sat}$ and the film boiling heat transfer coefficient for the liquid subcooling of 50 K is obtained from the reference listed below.

$$h_{film} = 0.45\left[\frac{k_v^3 g\rho_v(\rho_l - \rho_v)h_{fg}}{\mu_v\Delta T_{wo}D_f}\right]^{0.25} + 0.7\left[\frac{k_l^3 g\beta\rho_l^3\Delta T_{sub}c_{pl}}{\mu_l D_f}\right]^{0.25}\frac{\Delta T_{sub}}{\Delta T_{wo}}$$

where

$$D_f = \sqrt{\frac{\sigma}{g(\rho_l - \rho_v)}}$$

and

$$\Delta T_{sub} = T_{sat} - T_{liquid}$$

Since even with the radiative contribution included the total amount of heat transfer in film boiling region is much less (by a factor of 10) that than in the nucleate boiling region as shown in Table I.3, the outer wall temperature in the film boiling region is found to exceed the melting temperature (1700 K) of the steel vessel.

Reference for Appendix I.D

R. VIJAYKUMAR, "Hydrodynamics and Heat Transfer Aspects of Subcooled Film Boiling on a Vertical Surface," Ph.D. Thesis at UCLA, 1991.

Table I.3: Heat fluxes under different outer wall temperature

T_{wo}	q_{film} (MW/m^2)	q_{rad} (MW/m^2)	q_{total} (MW/m^2)
1000	0.2969	0.0280	0.3249
1200	0.3388	0.0586	0.3974
1500	0.4021	0.1437	0.5458
1700	0.4463	0.2375	0.6838

T_{wo} (K)	$q_{nucleate}$ (MW/m^2)
450	0.2494
500	1.1226
550	3.0421
600	6.4207

Appendix I.E
Effects of Liquid Subcooling and Downward-Facing Orientation of the Vessel Bottom Head

The flooded water in the cavity will be heated during cooling of the reactor vessel lower head through the nucleate boiling occuring on the outer wall. The increase of water temperature around the vessel outer wall can be anticipated if the cooling process takes long enough time. A simple calculation is performed in this Appendix to estimate the increase of vessel wall temperature when water is heated up to its saturation temperature. Under such conditions, the result as shown in Figure I.49 indicates that the temperatures in most of the vessel shell exceeded the melting temperature of steel vell (1700 K) and complete failure of vessel shell will occur.

Concerns have been raised about the applicability of the nucleate boiling at the very bottom of the hemispherical vessel lower head. Due to the downward-facing orientation of the hemisphere, vapor film may form on the wall. A simple calculation is performed by applying the insulation boundary condition on the bottom wall for the angular position (θ) from 0 to 4.5° in order to determine the temperature increase at the bottom head. Figure I.50 shows the isotherms obtained by using the insulation boundary condition at the bottom wall when Mayinger et al's correlation is used for $V_p = V_{core}$. It is seen that the highest outer wall temperature at the stagnation point is less than the minimum film boiling temperature (about 926 K). Therefore, the formation of vapor film at the very bottom of the hemisphere is expected to be rare due to the high degree of liquid subcooling.

References for Appendix I.E

V.K. DHIR AND G.P. PUROHIT, "Subcooled Film Boiling Heat Transfer from Spheres," Nuclear Engineering and Design, Vol. 47, p. 49, 1978.
R. VIJAYKUMAR, "Hydrodynamics and Heat Transfer Aspects of Subcooled Film Boiling on a Vertical Surface," Ph.D. Thesis at UCLA, 1991.

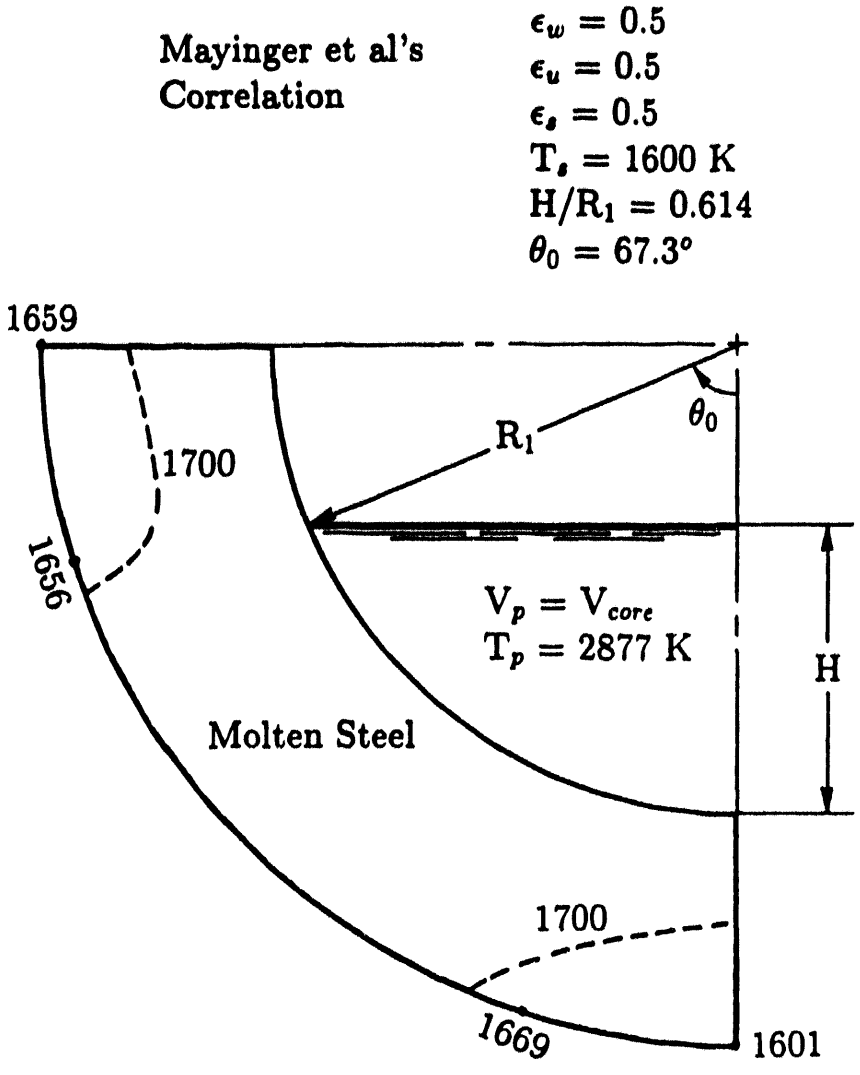

Figure I.49: Temperature distribution in the vessel shell for $T_{water} = T_{sat}$

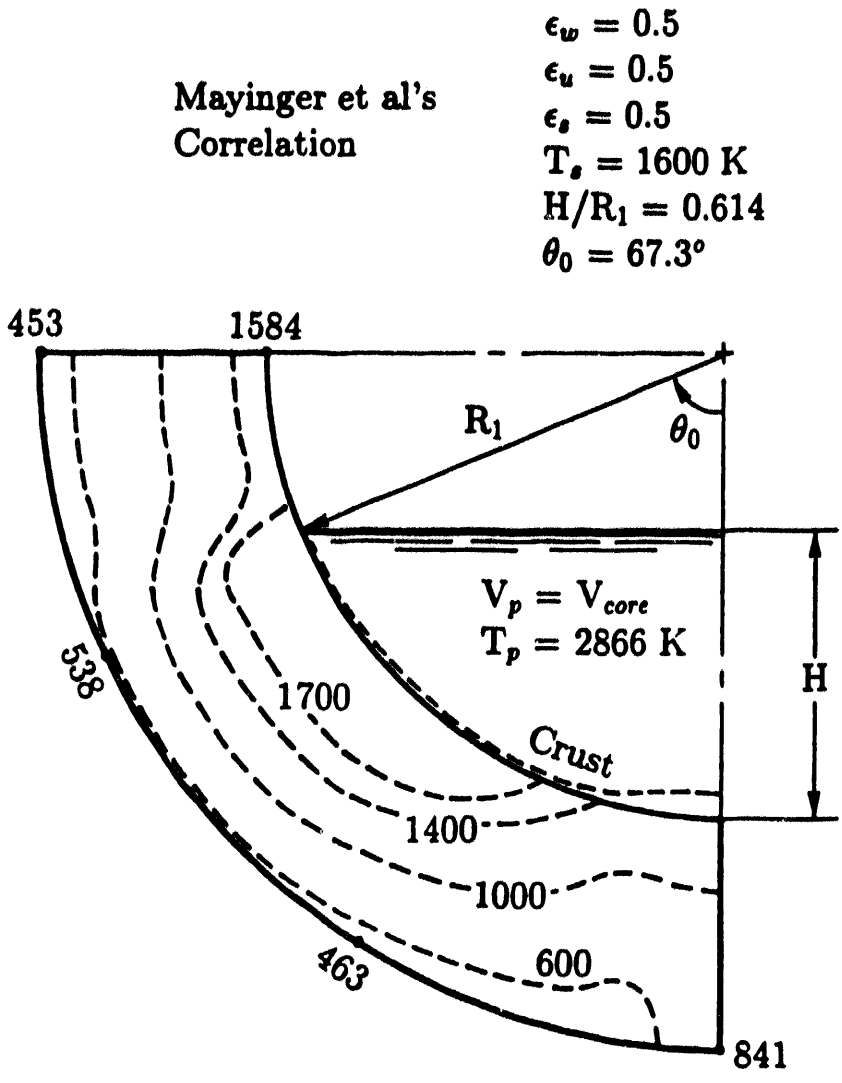

Figure I.50: Temperature distribution in the vessel shell obtained by using the insulation B.C. for $\theta = 0 \sim 4.5°$

Appendix I.F
Finite Difference Form of the Steady-State Energy Equations for the Vessel Shells

Gauss-Seidel iterative method in conjunction with central-difference approximations for the derivatives in Equations (I.22), (I.33) and (I.34) are used to solve the partial differential equations. Defining $\Delta r=(R_2-R_1)/M$, $\Delta\theta=\pi/2N$, $\Delta x=X/L$, $r=R_1+i\Delta r$, $\theta=j\Delta\theta$ and $x=k\Delta x$ for i=0, 1, ..., M, j=0, 1, ..., N, and k=0, 1, ..., L, and $T_{i,j}^{(n)}=T_w(r,\theta)$ and $T_{i,k}^{(n)}=T_v(r,x)$, the finite difference form of Equations (I.22), (I.33) and (I.34) become

$$C_1T_{i,j}^{(n+1)} = C_2T_{i-1,j}^{(n+1)} + C_3T_{i,j-1}^{(n+1)} + C_4T_{i+1,j}^{(n)} + C_5T_{i,j+1}^{(n)}$$

and

$$D_1T_{i,k}^{(n+1)} = D_2T_{i+1,k}^{(n)} + D_3T_{i-1,j}^{(n+1)} + D_4\left(T_{i,k+1}^{(n)} + T_{i,k-1}^{(n+1)}\right)$$

where

$$C_1 = 2\left(\frac{r^2}{\Delta r^2} + \frac{1}{\Delta\theta^2}\right)$$

$$C_2 = \frac{r^2}{\Delta r^2} - \frac{r}{\Delta r}$$

$$C_3 = \frac{1}{\Delta\theta^2} - \frac{cot\theta}{2\Delta\theta}$$

$$C_4 = \frac{r^2}{\Delta r^2} + \frac{r}{\Delta r}$$

$$C_5 = \frac{1}{\Delta\theta^2} + \frac{cot\theta}{2\Delta\theta}$$

$$D_1 = 2\left(\frac{1}{\Delta r^2} + \frac{1}{\Delta x^2}\right)$$

$$D_2 = \frac{1}{\Delta r^2} + \frac{1}{2r\Delta r}$$

$$D_3 = \frac{1}{\Delta r^2} - \frac{1}{2r\Delta r}$$

$$D_4 = \frac{1}{\Delta x^2}$$

Initial values $T_{i,j}^{(0)}$ and $T_{i,k}^{(0)}$ are assumed to be given for all variables and the superscripts in the above equations denote the iteration number.

Appendix I.G
Radiative Heat Transfer Parameters (BWR)

The expressions for Δ's, A's, B's, E's, G's, Z and Y used in Equations (I.35), (I.36), (I.37), (I.38) and (I.39) are listed below :

$$A_1 = f_F + f_H(f_L + 1)$$

$$A_2 = f_A - f_C(f_L + 1)$$

$$A_3 = -f_A f_H - f_C f_F$$

$$A_4 = -f_C(f_K + 1) - 1$$

$$A_5 = f_E - f_H(f_K + 1)$$

$$A_6 = -f_C f_E - f_H$$

$$A_7 = f_E(f_L + 1) + f_F(f_K + 1)$$

$$A_8 = f_A(f_K + 1) + f_K + 1$$

$$A_9 = f_F - f_A f_E$$

$$B_1 = g_F - g_E$$

$$B_2 = g_B + 1$$

$$\Delta_E = (f_C+1)(f_F-1)+f_H(f_A+f_L+1)+f_E(f_L f_C+f_L-f_A)+f_K(f_A f_H+f_F f_C)$$

$$\Delta_G = g_D(g_B + 1) + g_F(g_A + 1)$$

$$f_A = F_{u-w}(1 - \epsilon_w)\frac{\epsilon_u A_u}{\epsilon_w A_w}$$

$$f_C = F_{u-b}(1 - \epsilon_b)\frac{\epsilon_u A_u}{\epsilon_b A_b}$$

$$f_E = F_{w-u}(1 - \epsilon_u)\frac{\epsilon_w A_w}{\epsilon_u A_u}$$

$$f_F = 1 - F_{w-w}(1 - \epsilon_w)$$

$$f_H = F_{w-b}(1 - \epsilon_b)\frac{\epsilon_w A_w}{\epsilon_b A_b}$$

$$f_K = F_{s-u}(1 - \epsilon_u)\frac{A_s}{\epsilon_u A_u}$$

$$f_L = F_{s-w}(1-\epsilon_w)\frac{A_s}{\epsilon_w A_w}$$

$$E_1 = \epsilon_u A_u \sigma \left(T_u^4 - F_{u-w}T_w^4 - F_{u-s}T_s^4 - F_{u-b}T_b^4\right)$$

$$E_2 = \epsilon_w A_w \sigma \left((1-F_{w-w})T_w^4 - F_{w-u}T_u^4 - F_{w-s}T_s^4 - F_{w-b}T_b^4\right)$$

$$E_3 = A_s \sigma \left(T_s^4 - F_{s-u}T_u^4 - F_{s-w}T_w^4\right)$$

$$g_A = F_{s-c}(1-\epsilon_c)\frac{A_s}{\epsilon_c A_c}$$

$$g_B = F_{s-t}(1-\epsilon_t)\frac{A_s}{\epsilon_t A_t}$$

$$g_C = 1 - F_{c-c}(1-\epsilon_c)$$

$$g_F = F_{c-t}(1-\epsilon_t)\frac{\epsilon_c A_c}{\epsilon_t A_t}$$

$$G_1 = A_s \sigma \left(T_s^4 - F_{s-c}T_c^4 - F_{s-t}T_t^4\right)$$

$$G_2 = \epsilon_c A_c \sigma \left((1-F_{c-c})T_c^4 - F_{c-s}T_s^4 - F_{c-t}T_t^4\right)$$

$$Z = 1 + \frac{1+cos^2\theta_0}{sin^2\theta_0}$$

$$Y = \frac{1}{sin\theta_0}$$

Appendix I.H
Heatup period of Volumetrically heated pool

Measurements of the transient thermal responses of the fluid layer bounded from below by a segment of a sphere were performed by Min and Kulacki to determine the time scales of developing convection when volumetric heating is suddenly started. The thermal boundary conditions imposed on the convection chamber were zero heat flux on the lower surface and sidewall and constant temperature on the upper surface. In an effort to determine the time scale of developing convection, measurements of time-dependent temperature profiles within the fluid were made for a step change in Rayleigh number from zero to a certain value. According to their experiments, an over-shoot, or excess, in the temperature profile was predicted in the upper portion of the layer in the early stage of flow development when volumetric heating is suddenly started. This behavior was to be expected in their experiments owing to the influence of conduction near the upper surface in the early period of flow development. However, in the remainder of the layer, buoyant forces and mixing effects were expected to be strong enough even at the start of volumetric heating to produce the well mixed isothermal core characteristic of turbulent convection. This was believed to be due to a dominance of strong mixing and eddying effects and possibly strong secondary flows in early period of flow development. The time scales required for the temperature at any vertical positions of z/H =0 and 0.5 within the fluid layer to reach its steady-state value, t_{max}, were correlated in terms of the Fourier number (Fo = $\alpha t/H$) of the fluid layer with the Rayleigh number ($Ra_H = g\beta q_{gen} H^5/\alpha\nu k$) by

$$Fo_{max} = \frac{\alpha t_{max}}{H^2} = 23.577 Ra_H{}^{-0.223} \qquad \text{(I.91)}$$

where z/H = 0 for $1.266 \times 10^8 \leq Ra_H \leq 2.90 \times 10^{13}$ and

$$Fo_{max} = \frac{\alpha t_{max}}{H^2} = 58.055 Ra_H{}^{-0.266} \qquad \text{(I.92)}$$

where z/H = 0.5.

Frantz has investigated the natural convection in spherical segments of volumetrically heated pool. The transient pool temperatures were

Table H.4: Heatup time required for the pool to reach steady state

Correlations by	z/H	Heatup time (hours)
Min & Kulacki	z/H = 0.0 z/H = 0.5	3.24 1.62
Frantz	z/H = 0.0 z/H = 1.0	1.86 2.57

measured for different sizes of the hemispherical bell jar. Based on the experimental results, the time scales for obtaining steady convection is correlated in terms of Fo with Ra_H by

$$Fo_{max} = \frac{\alpha t_{max}}{H^2} = 8.20 Ra_H^{-0.2096} \qquad \text{(I.93)}$$

where z/H = 0 for $1.38 \times 10^9 \leq Ra_H \leq 2.74 \times 10^{12}$ and

$$Fo_{max} = \frac{\alpha t_{max}}{H^2} = 5.350 Ra_H^{-0.1893} \qquad \text{(I.94)}$$

where z/H = 1.0.

Assuming that these correlations for the time scales for obtaining steady convection in the volumetrically heated pool can be extended to large Rayleigh numbers encountered in this problem, the heatup times can be determined as shown in the Table H.4. It can be seen that the shorter heatup time of the pool at the bottom is predicted when the correlation by Frantz is used. This is due to the fact that the conduction near the pool boundary plays a role in developing the natural convection

in the volumetrically heated pool.

References for Appendix I.H

J.H. MIN AND F.A. KULACKI, "Steady and Transient Natural Convection with Volumetric Energy Sources in a Fluid Layer Bounded from Below by a Segment of a Sphere," NUREG/CR-0006, 1977.
B. FRANTZ, "An Experimental Investigation of Natural Convection in Spherical Segments of Volumetrically Heated Pools," Master's Thesis at UCLA, 1992.

Appendix I.I
Effects of $Q_{gen,pool}$, k_{pool} and k_{vessel}

Reduction in the decay power can occur due to the loss of volatile fission products from the fuel-clad gap during subsequent fuel heatup, melting and relocation. Hodge et al suggested that about 80.3 % of the total decay power at the time of lower plenum dryout is predicted to remain within the fuel in the debris bed. An additional release of volatile gases (equivalent to about 3.5 % of the total decay power) from the fuel within the debris bed is predicted as a result of fuel melting within the bed.

The effect of decay heat on the BWR vessel shell temperature was considered here. Using the full power of 3293 MW for Peach Bottom or Browns Ferry Plant, the predicted decay heat based on SANDIA-ORIGEN is about 20.72 MW at 10 hours after reactor scram. The decay heat after accounting the release of valatiles and noble gases (about 23 % reduction) is obtained as 15.91 MW. Taking the base case with the decay heat of 25.14 MW for full core as the upper limit and the case with the release of the volatiles and noble pases as the lower limit, vessel shell temperatures are obtained. Figure I.51 shows the variation of inner wall temperatures obtained by using the upper and lower values of $Q_{gen,p}$ in the pool when Mayinger et al's correlation is used for $V_p = 2/3\ V_{core}$. It is seen that the predicted inner wall temperatures obtained by using the lower value of $Q_{gen,p}$ are about 200 K lower than those obtained by using the value of the base case. The reduced vessel shell temperatures in the skirt region will produce the reduced thermal stresses in the vessel and the longer creep rupture times.

Since the large content of metals exists in BWR debris, the higher value of corium thermal conductivity can be predicted. Since the composition of the moltem corium relocated in the reactor vessel lower head is not known, an increase in the thermal conductivity of corium by a factor of 2 compared to the base case (k_{pool} = 3.6 W/mK) is used to predict the vessel shell temperature. Figure I.52 shows isotherms obtained by using k_{pool} = 7.2 W/mK when Mayinger et al's correlation is used for $V_p = 2/3\ V_{core}$. Since the average heat transfer coefficient based on the correlation

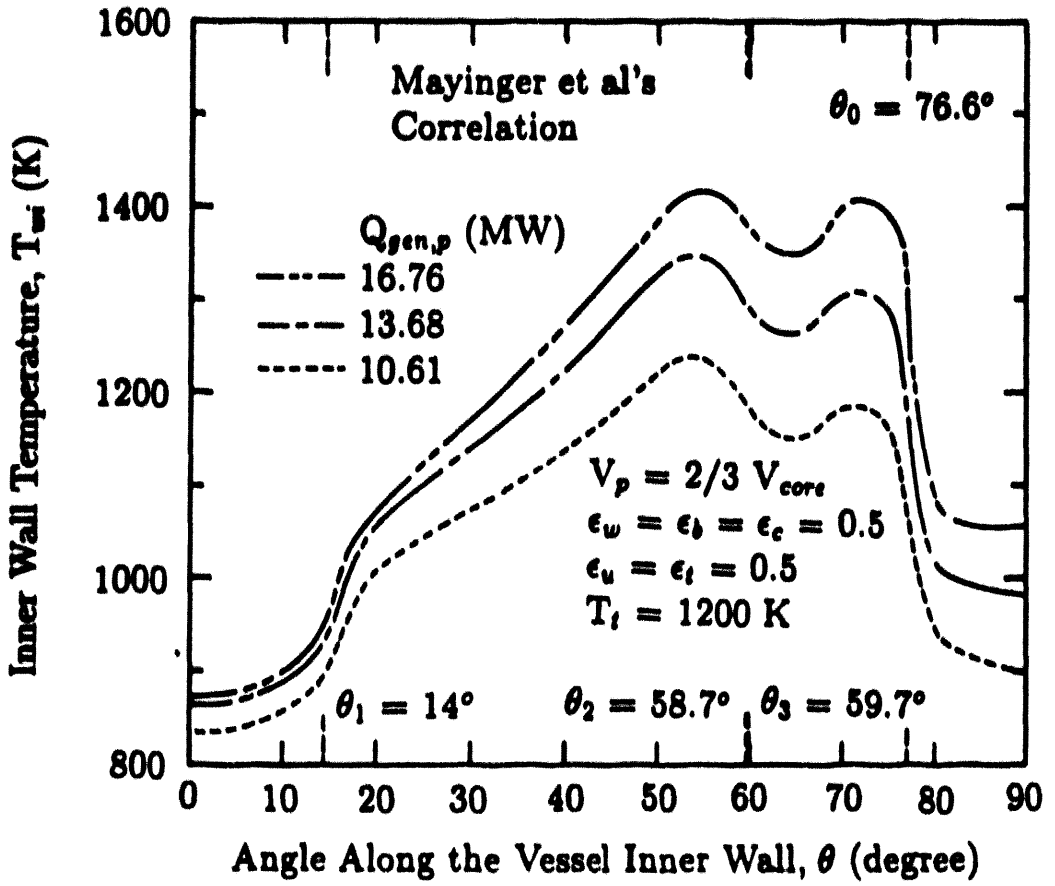

Figure I.51: Variation of the BWR inner wall temperature for different decay heat values in the pool

of Mayinger et al for the lower curved surface is enhanced by a factor of 1.74 compared to the base case, the higher vessel wall temperatures are predicted, especially in the skirt region.

Since the thermal conductivity of the steel vessel shell decreases as its temperature increases, the effect of the lower value of k_{vessel} on the vessel shell temperature is considered. Figure I.53 shows isotherms obtained by using k_{vessel} = 30 W/m K (value of thermal conductivity of carbon steel at about 1000 K obtained from Rempe et al's work) when Mayinger et al's correlation is used for $V_p = 2/3\ V_{core}$. It is seen that the reduction of thermal conductivity of vessel shell produces higher inner wall temperatures and lower outer wall temperatures in the skirt region compared to the base case with k_{vessel} = 50 W/mK. The large temperature vaiation across the vessel shell in the skirt region would result in the high thermal stresses in that region.

References for Appendix I.I

R.M. OSTMEYER, "An Approach to Treating Radionuclide Decay Heating for Use in the MELCOR Code System." NUREG/CR-4169, 1985.
J. METZINGER AND H.V. KLAPDOR, "New Results on the Decay Heat of Nuclear Reactors,' Max-Planck-Institute fur Kernphysik, Heidelberg, Germany, 1985.
S.A. HODGE, J.C. CLEVELAND, T.S. KRESS AND M. PETEK, "Identification and Assessment of BWR (In-Vessel) Secere Accident Mitigation Strategies," NUREG/CR-5869, ORNL/TM-12080, 1992.
J.L. REMPE, S.A. CHAVEZ, G.L. THINNES, C.M. ALLISON, G.E. KORTH, R.J. WITT, J.J. SIENICKI, S.K. WANG, C.H. HEATH AND S.D. SNOW, "Light Water Reactor Lower Head Failure Analysis," NUREG.CR-5642, EGG-2618, 1992.

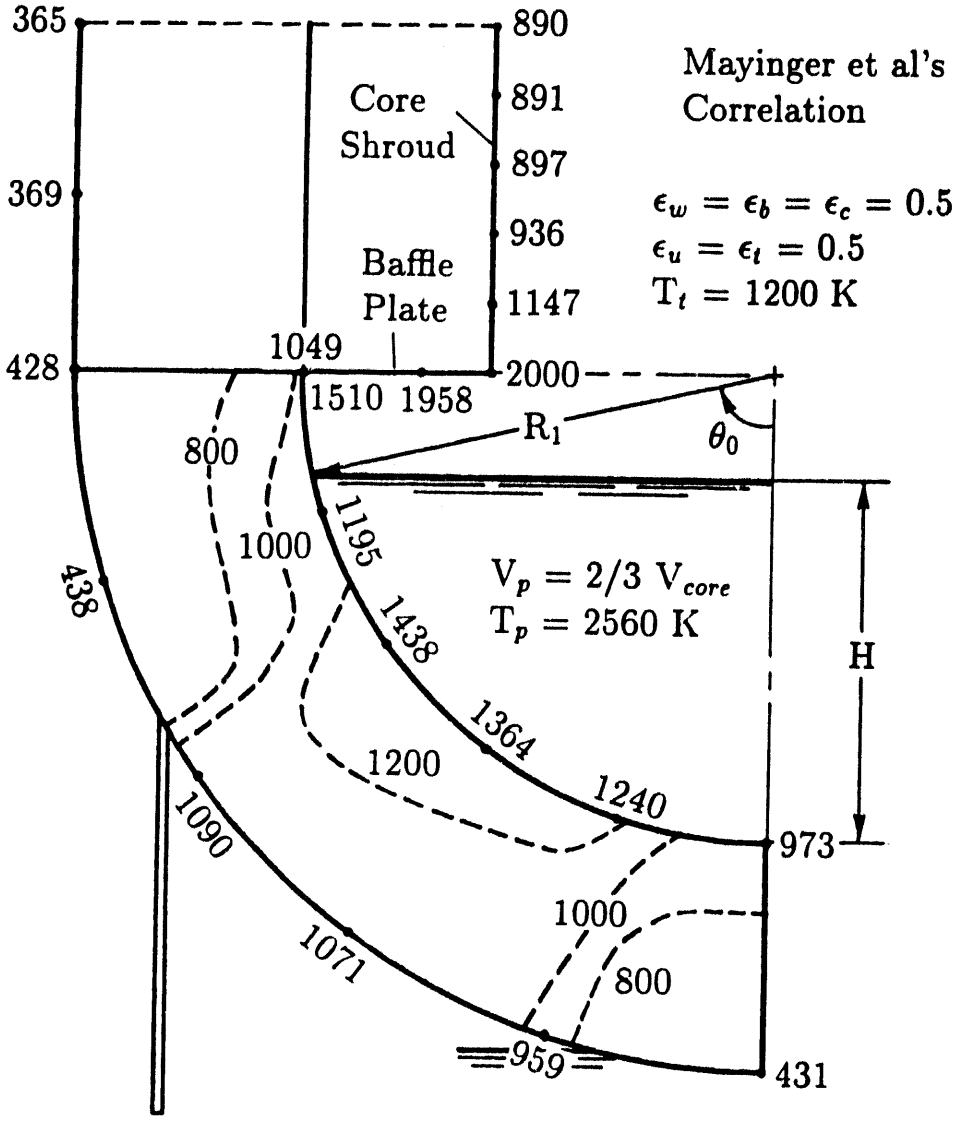

Figure I.52: Temperature distribution in the BWR vessel shell for k_{pool} = 7.2 W/m K

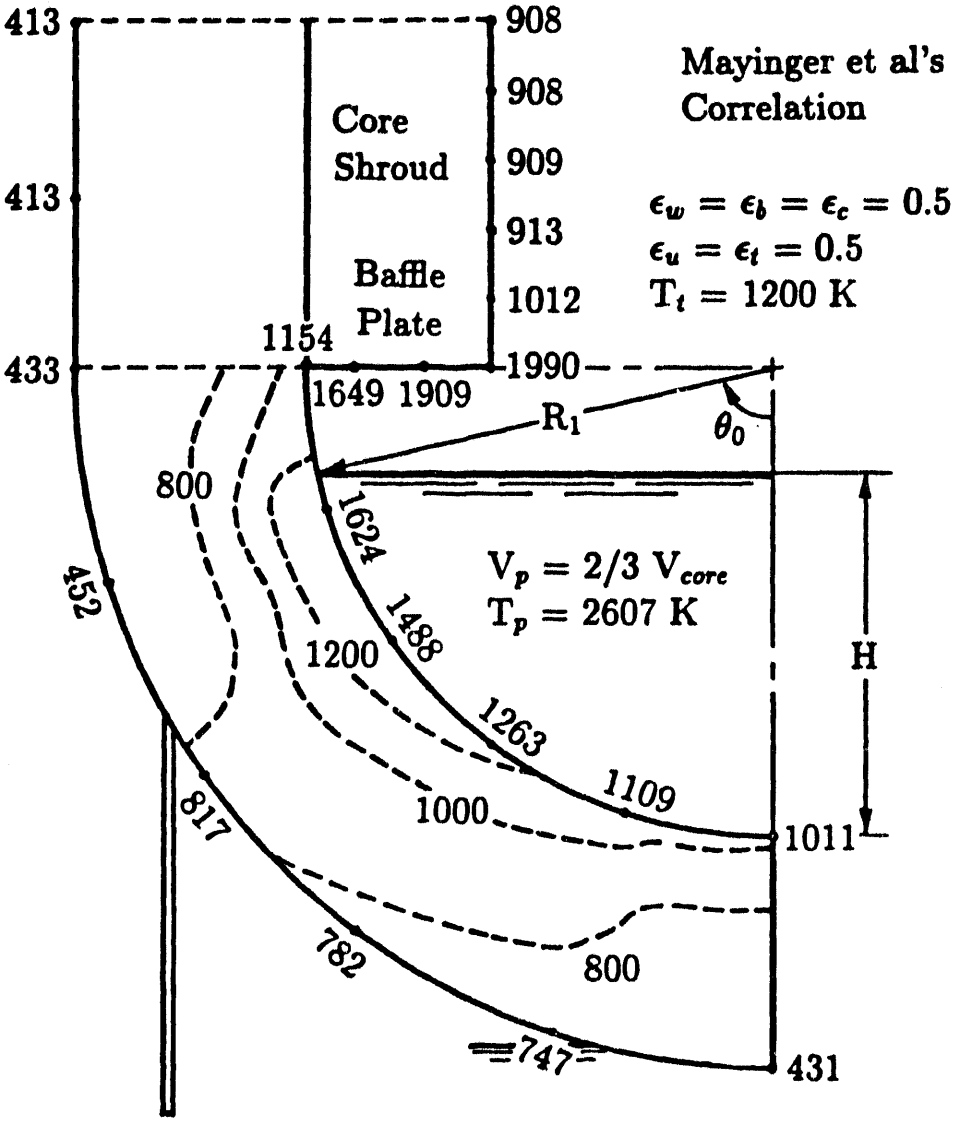

Figure I.53: Temperature distribution in the BWR vessel shell for k_{vessel} = 30 W/m K

Appendix I.J
Thermal Response of the Upper Reactor Vessel Wall Above the Water Level in the Drywell

Drywell flooding with complete venting of the BWR vessel support skirt by some means would maintain the core and structural material relocated subsequently in the vessel lower plenum. Since the water level in the drywell can not rise above the elevation of the drywell vents, at about two-thirds vessel height, the upper portion of the reactor vessel can not be covered by water. Due to the thermal loading applied by radiation from the upper debris bed surface, any possible failure of the upper vessel wall above the waterline in the drywell may occur.

Simple calculations are performed to see how the upper wall temperature varies with different water levels in the drywell and various amounts of radiative heat transfer from the relocated debris upper surface. It is assumed that the structural material in the vessel relocates into the vessel lower plenum as shown in Figure I.54. Because the time required to collect all the relocated structural material in the vessel lower plenum is not known, arbitrary values of the decay heats from the relocated debris bed were taken.

Assuming that the surfaces are diffuse and gray and that steam above the debris upper surface is totally transparent to radiative transfer of energy, the relationships for radiative heat exchange using the enclosure theory can be written as

$$Q_i - \sum_{j=1}^{n} F_{ij}(1-\epsilon_j)\frac{\epsilon_i A_i}{\epsilon_j A_j} Q_j = \epsilon_i A_i \sigma \left(T_i^4 - \sum_{j=1}^{n} F_{ij} T_j^4 \right) \qquad \text{(I.95)}$$

where i, j = 1, 2, 3.

Using T_2 and T_3 as the average temperatures along the vessel inner wall and T_1 as the temperature along the arbitrary black surface as shown in Figure I.54, the desired radiation heat transfer rates and the shape factors are obtained as

$$Q_1 = \frac{a(C+D) + b(A-B)}{\Delta_1} \qquad \text{(I.96)}$$

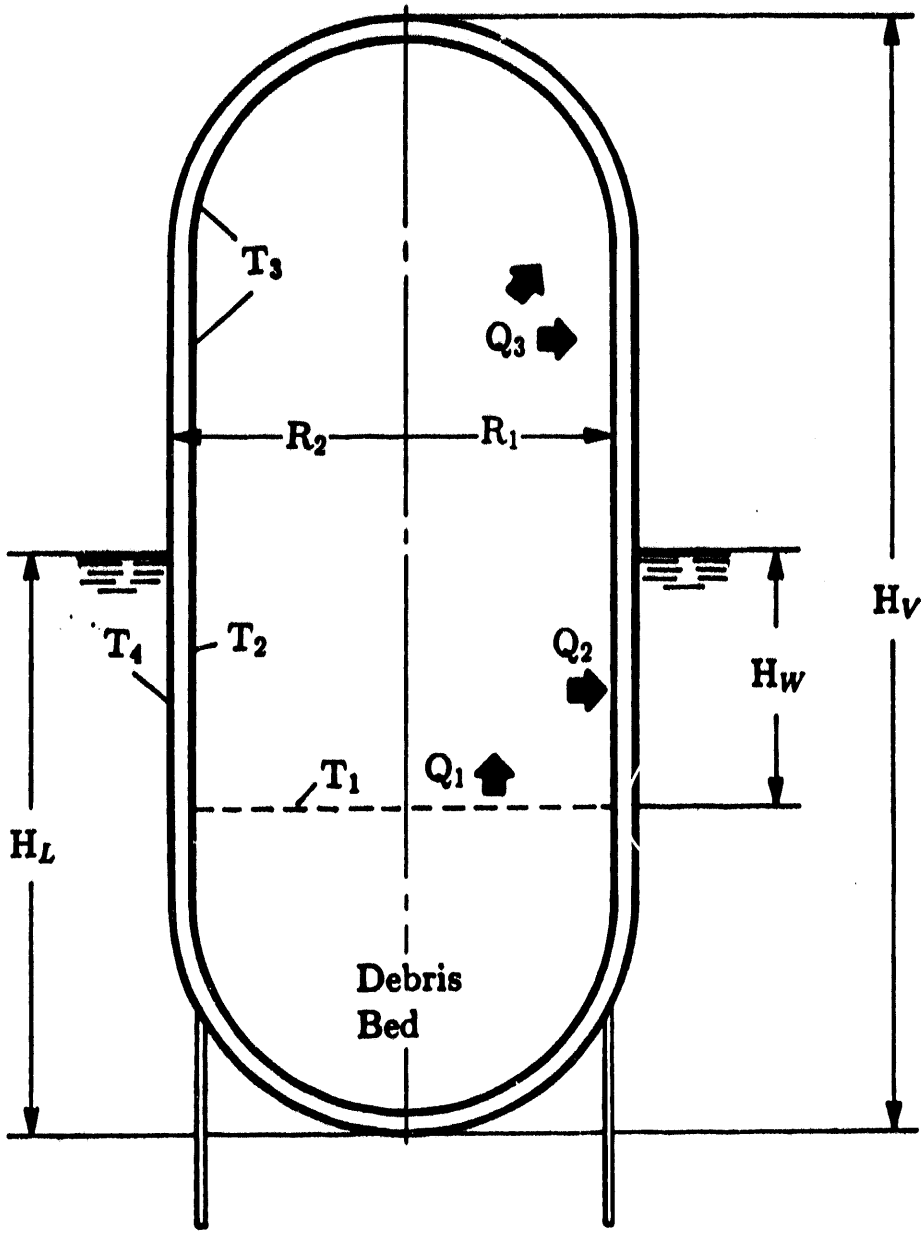

Figure I.54: Schematic of reactor vessel wall exposed to radiation heat from the upper surface of debris bed

$$Q_2 = \frac{aD - b(B+1)}{\Delta_1} \tag{I.97}$$

$$Q_3 = \frac{aC + b(A+1)}{\Delta_1} \tag{I.98}$$

and

$$F_{12} = 1 - \frac{1}{2}\left(Z - \sqrt{Z^2 - 4}\right) \tag{I.99}$$

where

$$A = F_{12}(1-\epsilon_2)\frac{A_1}{\epsilon_2 A_2}$$

$$B = F_{13}(1-\epsilon_3)\frac{A_1}{\epsilon_3 A_3}$$

$$C = 1 - F_{22}(1-\epsilon_2)$$

$$D = F_{23}(1-\epsilon_3)\frac{\epsilon_2 A_2}{\epsilon_3 A_3}$$

$$a = A_1\sigma(T_1^4 - F_{12}T_2^4 - F_{13}T_3^4)$$

$$b = \epsilon_2 A_2\sigma((1-F_{22})T_2^4 - F_{21}T_1^4 - F_{23}T_3^4)$$

$$\Delta_1 = C(B+1) + D(A+1)$$

$$Z = 2 + (\frac{H_W}{R_1})^2$$

Using a one-dimensional heat conduction through the vessel wall, the vessel shell temprature below the water line is given by

$$T(x) = T_2 + (T_2 - T_4)\frac{x}{\Delta R} \tag{I.100}$$

where $\Delta R = R_2 - R_1$ and x is the distance from the vessel inner wall.

The heat loss to the outside water is given by

$$q_L = h_L(T_4 - T_L) \tag{I.101}$$

where the natural convection heat transfer coefficient on the vertical plate is given by

$$h_L = \frac{k_L}{H_W}\left[0.825 + \frac{0.387Ra^{1/6}}{(1+(0.492/Pr)^{9/16})^{8/27}}\right]^2$$

where

$$Ra = \frac{g\beta(T_4 - T_L)H_W{}^3}{\nu\alpha}$$

For the upper vessel wall above the water level, the insulation boundary condition on the outer wall is used as an extreme case.

Table I.5 and Figure I.55 show the variation of the upper vessel wall temperatures for different heat transfer rates from the upper debris surface. The upper vessel wall temperature increases monotonically with the amount of heat transfer rate from the debris bed and exceeds the melting temperarature of steel vessel (1700 K) for the lower water levels, even for the low heat transfer rates as shown in Figure I.55. The vessel inner wall temperature (T_2) below the water level increases monotonically as the heat transfer rate increases and approach the upper wall temperature (T_3). However, the outer wall temperatures below the water level are not sensitive to the heat transfer rate and are much lower than the melting temperature of vessel shell. It can be seen that, for the maximum attainable water level ($H_L = 2/3\ H_V$) in the drywell, the upper wall temperatures are lower than the melting temperature of steel vessel even though the heat transfer rate is high enough as shown in Figure I.55. Therefore, for the higher water levels in the drywell, the integrity of the reactor vessel can be guaranteed as long as the energy transfer rate from the debris does not exceed 10 MW.

References for Appendix I.J

R. SIEGEL AND J.R. HOWELL, Thermal Radiation Heat Transfer, McGraw-Hill Book Company, NY, 1981.

S.W. CHURCHILL AND R.U. CHURCHILL, "A Comprehensive Correlating Equation for Heat and Component Transfer by Free Convection," AIChE Journal, Vol. 21, No. 3, p. 604, 1975.

Table I.5: The upper vessel wall temperatures above the debris upper surface

Water Level = 2/3 of Vessel Height

Q_1 (MW)	T_2 (K)	T_3 (K)	T_4 (K)
5	847	995	348
6	950	1083	351
7	1053	1171	355
8	1156	1261	358
9	1259	1353	361
10	1361	1446	364
11	1464	1539	366
12	1566	1634	367
13	1668	1730	371
14	1771	1827	374
15	1873	1924	376

Table H.1 contd.

Water Level = 1/2 of Vessel Height

Q_1 (MW)	T_2 (K)	T_3 (K)	T_4 (K)
5	1187	1323	359
6	1360	1472	363
7	1527	1624	368
8	1697	1779	372
9	1866	1937	376
10	2035	2097	379

Water Level = 1/3 of Vessel Height

Q_1 (MW)	T_2 (K)	T_3 (K)	T_4 (K)
1	834	1066	347
2	1335	1480	362
3	1834	1925	375
4	2331	2392	385
5	2826	2870	394

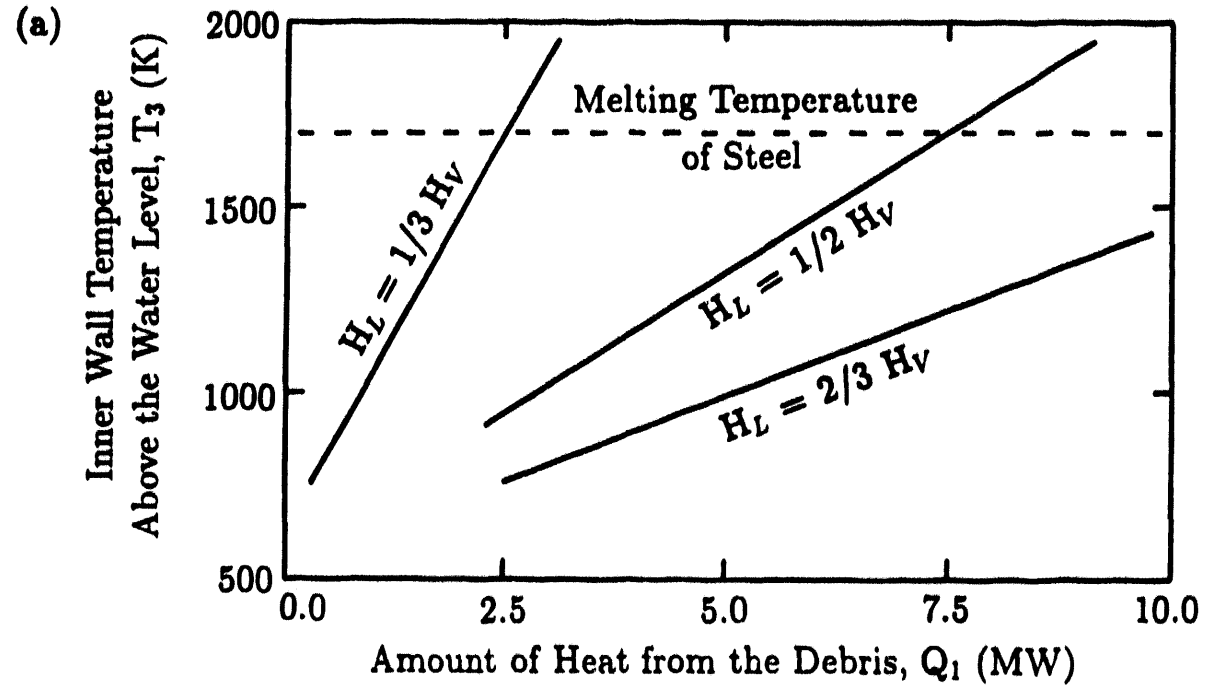

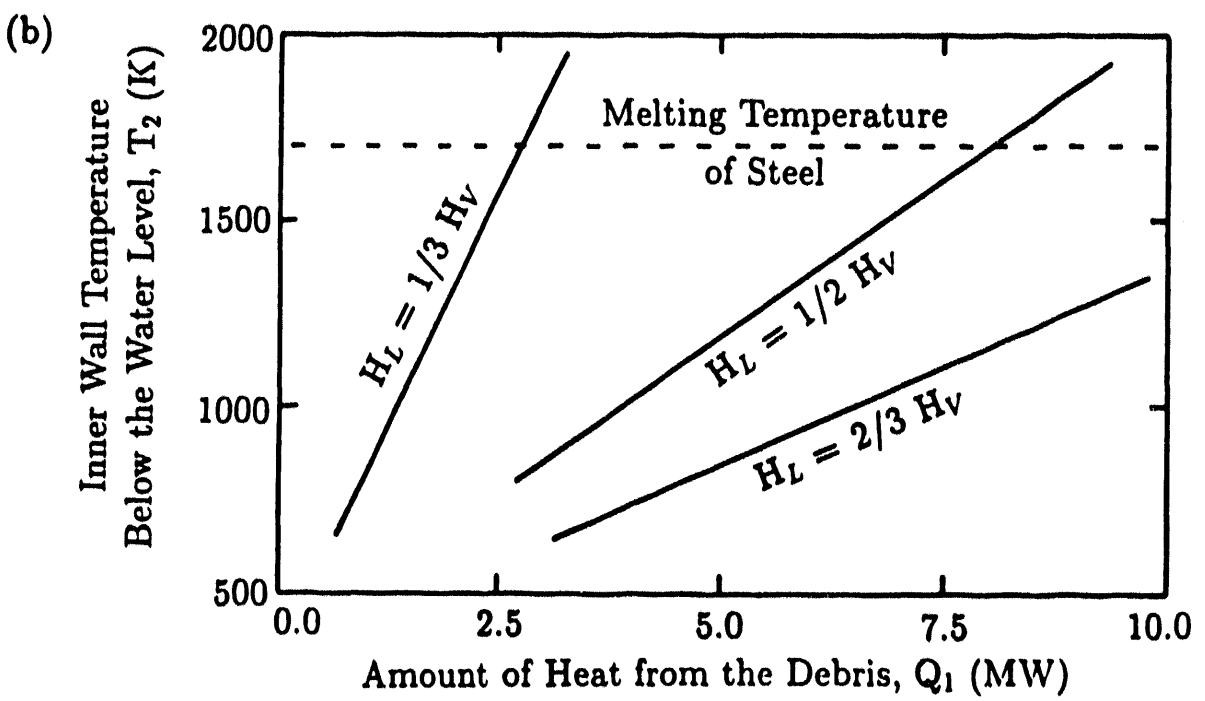

Figure I.55: Variation of the upper vessel wall temperature above the debris bed relocated in the vessel lower part

APPENDIX II

EARLY CONTAINMENT FAILURE DUE TO EX-VESSEL STEAM EXPLOSIONS

II.1 Introduction

A steam explosion occurs when the time scale for heat transfer from a hot liquid to water is smaller than the time scale for pressure wave propagation and expansion in a local region of the hot liquid-water mixture. Industrial and natural experience has revealed that such explosions are an important or at least potentially important class of damaging explosion accidents.

When water is present in the reactor cavity (for PWR) or the pedestal region (for BWR) at the time of vessel failure, the contact of molten core debris with water may result in a steam explosion. This is called an ex-vessel steam explosion and may result not only in an impulse load, but also in a quasistatic pressure load on containment structures. If the consequences of a steam explosion can result in impairment of the containment function, such as containment failure, then such an explosion could conceivably contribute significantly to the risk associated with core melt accidents in light water reactors. Currently, flooding the drywell or the reactor cavity with the aim of cooling the vessel from the outside and possibly preventing vessel failure is considered as one of the severe accident management strategies. Ex-vessel steam explosions may be the most serious adverse effect of this strategy. The purpose of the present study is the investigation of the consequences of an ex-vessel steam explosion when flooding the drywell or the reactor cavity strategy is used.

II.2 Issue Definition and Technical bases for PWR

There are three possibilities for the mode of failure of the lower reactor vessel head (penetration, gravity pour and gross failure) and two conditions at which it might happen (low and high pressure). At high pressure, no vessel failure (no VB) may lead to failure somewhere else in the primary system. If the failure is in the steam generator, then early containment failure or bypass is the result. Alternatively, the hot leg or surge line failure may occur first. All locations result in primary system depressurization and possible actuation of the accumulators leading to possible in-vessel steam explosions. A penetration failure requires consideration of direct containment heating (DCH) and gross failure

requires consideration of upward loads on the vessel. The gravity pour is not probable at high pressure.

At low pressure, one must consider in-vessel steam explosions prior to loss of primary system integrity. The probability of its occurrence and its consequences are, however, part of the base case considered in Chapter 3 and will not be considered further in this appendix. Again there are three possibilities: 1) no vessel failure, 2) penetration failure, and 3) gross bottom head failure. The first is the result of successful accident management, whereas the second and third require consideration of ex-vessel steam explosions. These two lead to a corium pour to the reactor cavity by gravity. For large dry containments, however, only hydrogen production will be a concern. The presence of water will most likely preclude basemat penetration.

A penetration failure at high pressure could result in DCH even though water exists in the cavity. At least two scenarios are conceivable [1]. One scenario is that one or more steam explosions will occur after only a fraction of the debris has been injected into the cavity and the cavity water will then be dispersed ahead of the bulk of the injected debris. The other scenario is that the cavity water will be co-dispersed with the debris, exiting the cavity region as small droplets intermixed with the transported debris, steam, and hydrogen. Experiments with water-filled cavities have been inconclusive, in part because of the tendency of the experimental facilities to be destroyed by the debris-water interactions. Reality may involve some combination of these two scenarios.

A gross failure at high pressure could result in upward loads on the vessel. The lower head separated from the vessel would impact with high velocity on the lower concrete bottom structure of the containment when it fails. The two-phase water and steam mixture together with the core melt would flash out of the RPV downwards into the containment space. The impact forces acting on the upper support structures of the RPV would be a dynamic force of about 300 MN over about 100 ns [2].

Experimental results [3] show that 32 out of 37 tests (86%) involving the release of molten thermite at ambient pressure and water temperature resulted in spontaneously triggered steam explosions. The probability of ex-vessel steam

explosions which occur under ambient pressure and water temperature can then be assumed to be approximately, 0.86. The expected explosion expansion would be truly three dimensional and there are many paths through which the explosion can expand. The amount of water needed to flood the reactor cavity was estimated to be about 245 metric tons which corresponds to equivalent volume of the reactor cavity volume and 4.54 m in depth from the vessel zero. If the explosion occurs, the expansion would be more hemispherical in nature and the pressure pulse generated from the explosion would travel to the containment walls through atmosphere, not through water. The early time pressure pulse travelling through water might damage the reactor cavity wall, but it is below ground level and separated from the containment walls, therefore, leakage is not likely. This pressure pulse would expel large quantities of water through the cavity exit into the containment and fragment water and debris into fine droplets. The late time explosion expansion could relieve itself in one of three ways; up to the refueling pool, through the outlet nozzle clearance or out to the personnel access door. The strength of the late time expansion would be reduced rapidly because the expansion moves hemispherical and interacts with the structures inside the containment. However, how the explosion could efficiently couple its energy to some solid material to form a missile is very uncertain. The ex-vessel steam explosion probably could not cause containment failure by dynamic pressure pulses since water in the cavity would not directly contact structures that are both vulnerable and essential to the containment function [1], whereas containment failure by missile generation is uncertain and should be studied.

II.3 Issue Definition for BWR

According to NUREG-1150, the containment design assessed to display the most significant vulnerabilities to ex-vessel steam explosions was Grand Gulf since the likelihood of a deep water pool in the drywell is high during the course of a severe accident. The threat to the Peach Bottom containment from ex-vessel steam explosions was not considered significant because of the shallow pool of water in the drywell. However, if the drywell is flooded in the Peach Bottom plant, the same consequences as those of the Grand Gulf plant should be considered.

The scenario of concern in the Grand Gulf containment design is that a steam explosion impulse is delivered to the reactor pedestal through water on the drywell floor. The same scenario can be considered for the Peach Bottom containment. Upon receiving the explosion impulse, the pedestal collapses, resulting in failure of the drywell wall due either to impact by the unsupported vessel or damage by the penetrating steam line and feedwater pipes. Another scenario of concern in the Peach Bottom containment is that the drywell is overpressurized by the rapid vaporization of water. The shock waves generated from the explosion can fragment molten debris into fine droplets. The fragmentation creates a large surface area of the molten debris and makes the rapid vaporization of water possible. When the strategy of flooding the drywell is used, the remaining free volume in the drywell is less than one third of the drywell free volume. Because of the small free volume, the pressure rise can become more serious.

The ex-vessel steam explosion issue is expressed in terms of four parameters or probabilities:

* The likelihood of an ex-vessel steam explosion with the presence of water in the pedestal at vessel breach, P_1.
* The likelihood of pedestal failure when a steam explosion occurs, P_2.
* The likelihood of drywell wall failure due to collapse of the pedestal, P_3.
* The likelihood of drywell failure due to the overpressurization by rapid vaporization of water, P_4.

The likelihood of containment failure due to a steam explosion (P_{ev}) can be calculated by the equation, $P_{ev} = P_1 \times \{ P_2 \times P_3 + (1 - P_2 \times P_3) \times P_4 \}$. Figure II.1 shows an event tree for early containment failure due to ex-vessel steam explosion.

II.4 Technical Bases for BWR

The scenario of concern at Peach Bottom is that molten debris is released from the breached vessel into a deep water pool (about 9 meters) on the drywell floor when the strategy of flooding the drywell is used. The accident progression models developed for this study decompose the ex-vessel steam explosion scenario into four phases: (1) occurrence of the steam explosion, (2) subsequent failure of

the pedestal, (3) subsequent failure of the drywell wall, and (4) failure of the drywell due to the overpressurization.

Initial Conditions

If the drywell is flooded before slumping of the core, the vessel failure time becomes much longer than that of the no flooding case. For the Browns Ferry short-term station blackout, the amount of debris accumulated in the vessel lower head before vessel breach was calculated at about 80% of the core mass (UO_2 + Zirconium) and large masses of top guide, fuel support pieces, core plate, and control rod guide tubes [4]. In the case of the Surry plant (this is a pressurized water reactor), about 80% of total core mass of the Surry plant would be accumulated in the vessel lower head before vessel breach. This calculation for Surry is based on low primary system pressure and that the vessel failure time is about 10 hours after the station blackout accident initiation [5]. For a boiloff accident starting at the same decay time, the BWR and PWR core meltdown results are quite similar; for instance, the time required to achieve 80% of the core melting is almost the same. Differences in the calculations are primary attributable to differences in the core power density, pressure vessel water inventory at the start of the accident, and the fuel element design (open lattice versus shrouded) [6]. So, the amount of debris accumulated in the lower head is assumed to be about 80% of the total core mass because vessel breach is assumed to occur at about 10 hours [7] after station blackout. It can be also assumed that all the debris accumulated in the vessel lower head melts due to the decay heat except the upper and lower crust of molten debris [7].

As the bottom head debris reaches high temperature, several challenges to the vessel pressure boundary would be introduced simultaneously. Penetration failures can occur by weakening of the stub tube welds supporting the control rod drive mechanism assemblies or by failure of the instrument tube welds at the reactor vessel wall. The subsequent failure i.e., complete detachment of the tubes from the vessel or creep rupture of the tubes just outside the wall would not occur because the water outside the vessel cools the tubes.

Failure of a stub tube weld would only cause a small downward motion of the control rod drive mechanism assembly and therefore, although gas blowdown would be initiated by such a failure, gross release of debris from the vessel would not [8]. For the instrument tube, although there is nothing to prevent its complete detachment from the vessel given weld failure at the vessel wall, the subsequent continuous spillover of molten debris into the tube is difficult because the tube outside the vessel remains cool.

Gross failure of the portion of the reactor vessel bottom head underneath the vessel support skirt would be expected to occur long after the penetration failures discussed above. The reactor vessel bottom head wall is thick, and there is relatively little wall stress after the vessel is depressurized due to the penetration failures [8]. So, the failure mechanism for the BWR vessel bottom head when the drywell is flooded is expected to be gross failure of the vessel wall, no matter whether the vessel pressure is high or not. If gross failure occurs, a large pour of molten debris drops into the water pool because the vessel lower head may not melt uniformly along the circumference of the lower head and because there are control rod drive mechanism assemblies under the lower head.

A steam explosion is expected to be triggered at some time inside the pedestal after slumping of the melt into the pedestal. The total amount of water needed for flooding the drywell up to the expected level is about 1.5 million gallons [4]. However, it is expected that only the water inside the pedestal can participate in the steam explosion. The amount of water inside the pedestal is 225,000 kg (equivalent volume inside the pedestal). Since there exists control rod drive mechanism assemblies and many structures supporting the assemblies inside the pedestal which help the melt mix with water, all the water inside the pedestal can be assumed to participate in the explosion. The water may be highly subcooled (20-30^{o}C). Heat released from the vessel lower head to water inside the pedestal before vessel breach may be small because natural convection cannot be expected inside the pedestal and because the part of the lower head which contacts with water, is small. The ambient pressure is assumed to be about one atmosphere because the drywell is vented for flooding.

The fraction of core involved in an ex-vessel steam explosion is estimated for the penetration failure and gross failure at low pressure by expert opinions in reference [9]. The results are illustrated in Figure II.2. These results can be used for Peach Bottom because the geometries and the specifications of the vessel and pedestal of the Peach Bottom plant is similar to those of the Grand Gulf plant. The dispersed premixtures are not a necessary condition for strong explosions because the necessary prefragmentation can be achieved by precursor or weak explosions or mixing waves and there may be no limit of the melt amount in mixing with water. The mean of the level assignments on the gross failure is 16.5% of the core. The initial temperature of melt is assumed 2700 K [7].

During the explosion, thermal energy from Zirconium oxidation is not considered because water is highly subcooled. Hydrogen burning is not considered because the Peach Bottom containment is maintained in an inerted state i.e., nitrogen filled.

Occurrence of the Steam Explosion

The probability evaluated for this phase of the scenario is the fraction of occasions upon which a steam explosion would be triggered when molten debris is released from the vessel to an underlying water pool. The water temperature and ambient pressure are the most important factors in this phase. As mentioned above, even though the water near the vessel lower head may be saturated, most of water inside the pedestal remains in a highly subcooled state (20-30^{o}C). An estimate of the probability, 0.86, was based upon the same experimental results [3] that were used for the PWR case.

Subsequent Failure of the Pedestal

The estimation of the Grand Gulf pedestal impulse capacity can be used for Peach Bottom because the pedestal region geometry and composition of each are very similar. According to NUREG-1150, the potential failure impulse levels for the Grand Gulf pedestal extends from 3.5 to 18 psi-s based on the assumption of the similarity in the impulse duration between steam explosion and gas detonation loads (typically millisecond). Estimation of the impulse delivered to the pedestal

was based on the similitude equation for an impulse from the underwater explosion [10] modified by Berman [11], as follows:

$$I = 4.0\ W^{1/3}\ (\ W^{1/3} / R\ )^{.89}\ \text{kPa-s} \qquad \text{(II.1)}$$

where I = impulse at distance R in kilopascal-second,
W = mass of corium in kilograms, and
R = distance from explosion center to load in meters.

This equation was adopted to determine the relationship between the mass of debris participating in the steam explosion and the impulse to the pedestal. Calculations revealed that, with less than 0.5 percent of the total core (UO_2 + Zirconium) participating in the explosion, the impulse to the pedestal would reach the upper edge (18 psi-s) of the uncertainty range over pedestal failure loads. Failure of the pedestal is credible when a steam explosion is triggered in the Peach Bottom pedestal.

The impulse generated from the explosion can directly reach the drywell wall through the door, which exists on the pedestal wall. The door size is about 7.2 feet high and 3.4 feet wide. The maximum energy reaching the door is 1.167% of the melt energy participating in the explosion by assuming the kinetic energy travels along all the directions equally. The impulse reaching the drywell wall can be calculated by the equation above. The distance from the door to the wall is 3.0 m and the corium mass is assumed to be 1.167% of the melt participating in the explosion. The impulse to the drywell wall is only 11.8 psi-s when the total core participates in the explosion. The failure of the drywell wall due to the direct impulse generated from the explosion is incredible.

For the Grand Gulf plant assessed in NUREG-1150, this probability of failure of the pedestal when a steam explosion is triggered in the pedestal (P_2) is calculated at 0.5 by a Monte Carlo analysis with a uniform distribution assigned to the interval between the fraction zero and fraction 1.

Subsequent Failure of the Drywell Wall

According to NUREG-1150 (for Grand Gulf), engineering judgement was used and this probability of failure of the drywell wall when the pedestal fails due

to the impulse from ex-vessel steam explosion, was taken to be 0.17. This estimate cannot be used for Peach Bottom directly because the Peach Bottom containment structure is very different from the Grand Gulf containment structure. At Grand Gulf, there are many structures inside the drywell and the distance between the vessel and the drywell wall is longer than that of the Peach Bottom containment. It can be assumed that these differences make "failure of the drywell wall" at Peach Bottom more probable than that at Grand Gulf. As mentioned above, the mechanisms of subsequent drywell wall failure due to steam explosions are the impact to the drywell wall by the unsupported vessel and the damage by the penetrating pipes through the drywell wall. The impact to the wall by the vessel and the damage by the pipes due to the vessel movement may more easily occur when the distance between the vessel and the drywell wall is short. The value of $P_3 = 0.17$ for Grand Gulf may be considered as the lower bound probability for Peach Bottom.

Failure of the Drywell Wall due to Overpressurization

This probability, P_4, is the fraction of occasions that the quasistatic overpressurization due to the rapid vaporization of water results in failure of the drywell wall when the drywell wall does not fail due to the impulse generated from the given steam explosion. The potential static failure pressure levels for the Peach Bottom drywell wall extends from 120 to 174 psig (mean value is 148 psig) [1]. The primary containment venting system at Peach Bottom is used to prevent containment pressure limits from being exceeded. It is probable that the venting system would be operable or open. (It has to be open to flood.) The venting capability should be considered. If the vessel fails at high vessel pressure, gas (steam+hydrogen) blowdown from the vessel to the containment would contribute to the pressure rise.

Estimation of the containment pressure rise was performed by two approaches; simple mechanistic calculation and scaling of the experimental results. The probability, P_4, could be assigned based on the results of two approaches with the initial conditions as mentioned above. The first approach is an energy balance calculation of the core debris quench in the water pool assuming that the drywell is adiabatic and isolated. It is assumed that all the sensible and latent heat of the debris is transferred into heating and vaporizing

water, and the debris and water reach thermal equilibrium consequently. For the calculation, the droplet diameter of the debris is assumed to be 0.001, 0.01 or 0.1 m. A part of the steam bubbles generated around the debris droplets might condense before they rise to the surface of water. The amount of steam generated around the debris droplets that condenses is a very uncertain factor in this approach. The ratio ('fc') of condensed steam to the total generated is assumed from 0 to 1.0. After the water is saturated (the saturation temperature is assumed constant, T_l = 373 K), steam cannot condense any more. The steam and the gas in the vessel are treated as ideal gases. The containment pressure with respect to time can be calculated by the following equations.

Debris Droplet Energy Equation

$$-\rho_p V_p C_p \frac{dT}{dt} = A_p (hc + 0.88hr)\,(T(t) - T_l(t)) = q(t) \qquad \text{(II.2)}$$

Coolant Energy Equation

$$C_l M \frac{dT_l}{dt} = fc\; n_p q(t) \qquad \text{(II.3)}$$

Steam Generation Rate

$$\dot{m}_v = \frac{n_p q(t)\,(1-fc)}{h_{fg}} \qquad \text{(II.4)}$$

Steam/Air Energy Equation

$$\frac{V}{r-1}\frac{dP}{dt} = -Wh + \dot{m}_v h - \dot{m}_v \frac{P}{\rho_l (r-1)} + W_v h \qquad \text{(II.5)}$$

Containment Vent Rate

$$W = C_d A_d \sqrt{\frac{2(P-P_a)}{\rho_v}} \qquad \text{(II.6)}$$

Vessel to Containment Vent Rate

$$W_v = C_{dv} A_{dv} \sqrt{\frac{2(P_v - P)}{\rho_v}} \qquad \text{(II.7)}$$

Vessel Gas Space Energy Equation

$$\frac{V_v}{r-1}\frac{dP_v}{dt} = -W_v h \qquad \text{(II.8)}$$

The properties of water and steam are assumed to be constant. Figure II.3 represents the containment pressure with respect to time. When venting is available, the pressure increases up to the maximum pressure and decrease to the ambient pressure, whereas the pressure increases continuously up to the maximum pressure when venting is not available. However, at the initial state, there is no big difference in the containment pressure between venting and no venting. Venting might not be effective for mitigation of the threat from rapid vaporization. Figure II.4, II.6 and II.7 represent the effects of fc, droplet size and melt mass, respectively. Assuming the water inside the pedestal and 16.5% of the core (about 40 tons) participate in the explosion, which corresponds to the initial conditions, the containment pressure would rise up to over 10 MPa when fc is 0.5. Except for high fc (near 1.0), the maximum containment pressures exceed the containment failure pressure. When fc is 1.0, the containment pressure does not increase under any circumstances. Figure 5 shows a containment failure criterion as a function of fc and vent diameter, that the containment fails if the maximum containment pressure exceeds the mean containment failure pressure, 148 psig. Figure II.8 shows that the effect of the vessel pressure is not significant because there is no big difference of the pressures of two cases when the pressures are over the containment failure pressure.

The second approach [9] is an empirical scaling of the results from the Sandia Fully Instrumented Test Series (FITS) [3]. Almost fifty FITS experiments were performed with the molten debris masses between 2 to 20 kg in the 5.6 m^3 test chamber. Figure 9 illustrates the quasistatic gas phase pressurization from a steam explosion in the FITS chamber for the FITS A, B, and G series. If one makes the assertion that the FITS test can be considered a scaled test reflecting the behavior in the Peach Bottom drywell, it is possible to predict pressurization for Peach Bottom from the experimental data. There are potential problems with this assumption: (1) the tests represent approximately a one-seventh linear scale of free volume, and the surface area/volume effects influence the results and tend to underpredict the pressure rise at full scale; and (2) the scaling of microscopic phenomena is not actually known. Assuming that the scaling laws are one-seventh

for the linear geometry scale and all other scale factors are zero, then the observed pressure rises in the FITS tests would be the same as those predicted for full scale. Using the graph in Figure II.9, the quasistatic pressure rise would be less than 2 bars (29 psia) for as much as 15% of the core (about 36 metric tons) interacting with the available water in the pedestal (225 metric tons) i.e., when the coolant fuel mass ratio is about 6.

The first approach showed that the maximum containment pressures obtained exceed the containment failure pressure in most cases so that containment failure due to the overpressurization is probable. On the contrary, the second approach showed that the pressure rises are not high enough to fail the containment, even in the low coolant fuel mass ratio case, so that containment failure due to the overpressurization does not seem to be probable. The inconsistent results of the two approaches were caused by uncertainties and assumptions of the approaches mentioned above. In the first approach, the most significant uncertainty is how much heat transfers from the debris to water for sensible heating. In the second approach, the scaling laws are not well known and have many uncertain factors. If the two results of each approach are considered to be equally weighted, the probability, P_4, can be assigned as 0.5, which gives the maximum uncertainty.

With uncertainties mentioned above, P_1, P_2, P_3 and P_4 are assumed 0.86, 1.0, 0.17 and 0.5, respectively if water inside the pedestal and 16.5% of the core are assumed to participate in the explosion. Based upon the technical bases, the likelihood of early containment failure due to the ex-vessel steam explosion is calculated at approximately 0.5 by $P_{ev} = P_1 \times \{ P_2 \times P_3 + (1 - P_2 \times P_3) \times P_4 \}$, $0.86 \times (1.0 \times 0.17 + 0.83 \times 0.5)$, in this study.

Nomenclature

A : area (or surface area)
C : specific heat
C_d : discharge coefficient for venting (0.9)
C_{dv} : discharge coefficient for gas discharge from the vessel (0.6)
fc : the ratio of heat used for heating water to total transferred heat from the debris
h : enthalpy of steam (2700 kJ/kg)
h_c : convective heat transfer coefficient
h_{fg} : latent heat of water (2100 kJ/kg)
hr : radiative heat transfer coefficient
M : amount of water participating in the explosion (225 tons)
m_v : amount of steam generated per second
n_p : number of droplets
P : containment pressure
P_a : ambient pressure (0.101 MPa)
P_v : vessel pressure (initial pressure 7.03 MPa)
q : heat transferred from a debris droplet to water
r : specific heat ratio (1.4)
V : remaining containment free volume after flooding(1415.5 m^3)
V_v : vessel volume (585.1 m^3)
W : discharge mass rate from containment
W_v : discharge mass rate from vessel to containment
ρ : density

Subscripts

d : for venting
dv : for discharge from vessel
l : water
p : debris droplet
v : steam

References

[1]. U.S. Nuclear Regulatory Commission (USNRC), "Severe Accident Risks: An Assessment for Five U.S. Nuclear Power Plants," NUREG-1150, Vol. 1 and 2, (Dec. 1990).

[2]. J. Eible, F.H. Schulter, H. Cuppers, H.H. Hennies and G. Kesseler, "Containment for Future PWR-Reactors," SMiRT 11 Transactions Vol. A, 57-68, (1991).

[3]. M. Berman, "LWR Safety Quarterly," SAND80-1304, Sandia National Laboratories; see also SAND81-1216; SAND82-0006; SAND82-1572; SAND83-1576; SAND84-1072; SAND85-1606.

[4]. S. Hodge, "External Flooding of a BWR Reactor Vessel as a Late Accident Mitigation Strategy," presentation at UCLA, (Mar. 25, 1991).

[5]. S. Levy, "An Integrated Structure and Scaling Methodology for Severe Accident Technical Issue Resolution, Appendix G Amount of Material involved in Direct Containment Heating During a Pressurized Water Reactor Station Blackout (Draft)," (May 1991).

[6]. U.S. Nuclear Regulatory Commission(USNRC), "Reactor Safety Study, Appendix VIII," NUREG 75/014 (WASH-1400), (Oct. 1975).

[7]. H. Park and V. K. Dhir, "Effect of External Flooding on Retention of Core Material in a BWR Lower Head," (to be published).

[8]. S.A. Hodge, "Boiling Water Reactor Severe Accident Models for MELCOR," ORNL/NRC/LTR-90/13, (May 1990).

[9]. U.S. Nuclear Regulatory Commission (USNRC), "Evaluation of Severe Accident Risks and the Potential for Risk Reduction: Grand Gulf, unit 1 (Draft for Comment)," (Feb. 1987).

[10]. R.H. Cole, Underwater Explosions, Princeton University Press, (1948).

[11]. M. Berman, private communication with George A. Green at Oct. 26, 1988.

EVENT TREE FOR ECF DUE TO STEAM EXPLOSION

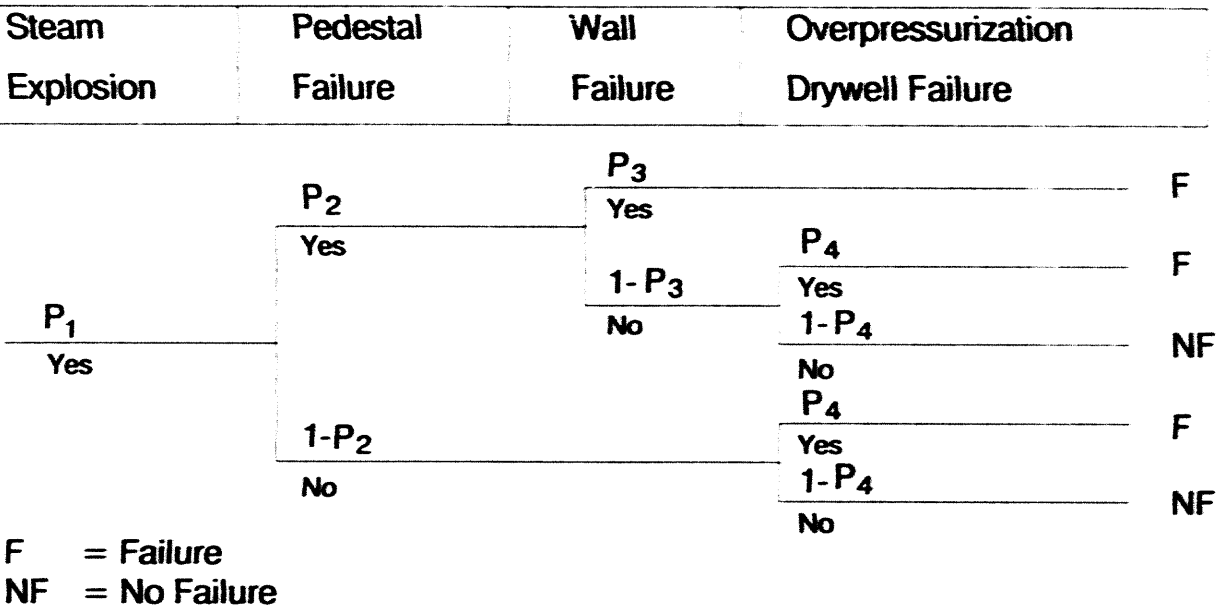

Figure II.1. Event tree for early containment failure due to ex-vessel steam explosion

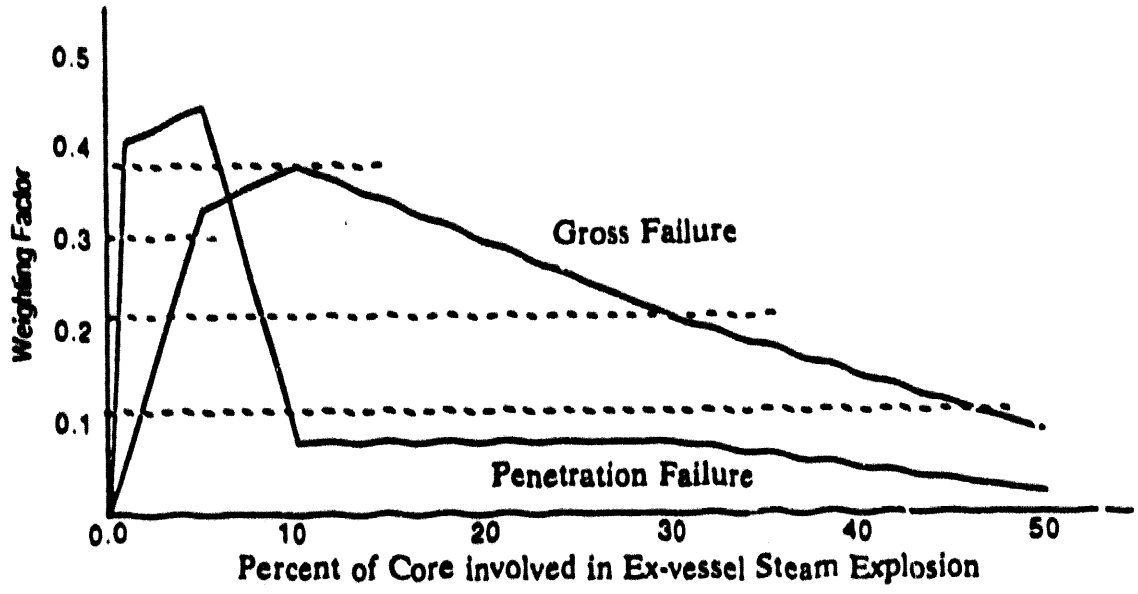

Figure II.2. Combined expert opinion for the ex-vessel steam explosion issue [9].

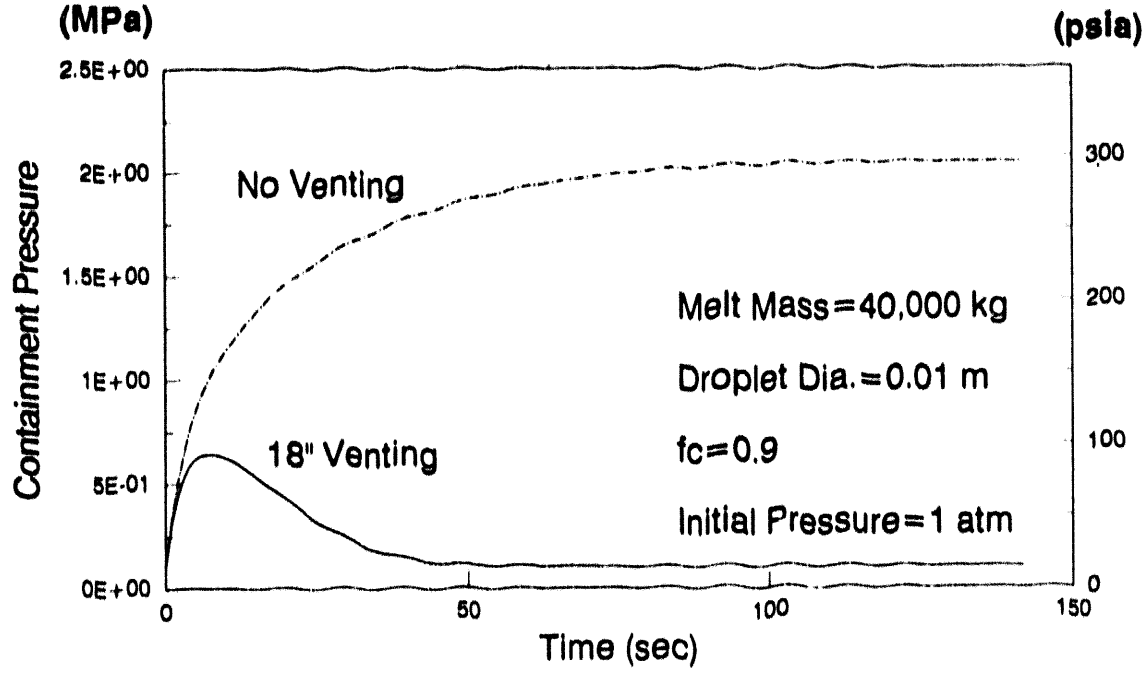

Figure II.3. Containment pressure rise.

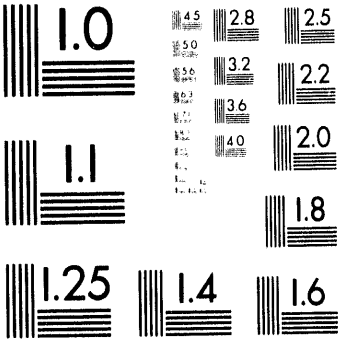
1.0
1.1
1.25
1.4
1.6
1.8
2.0
2.2
2.5
2.8
3.2
3.6
4.0
4.5
5.0
5.6

5 of 5

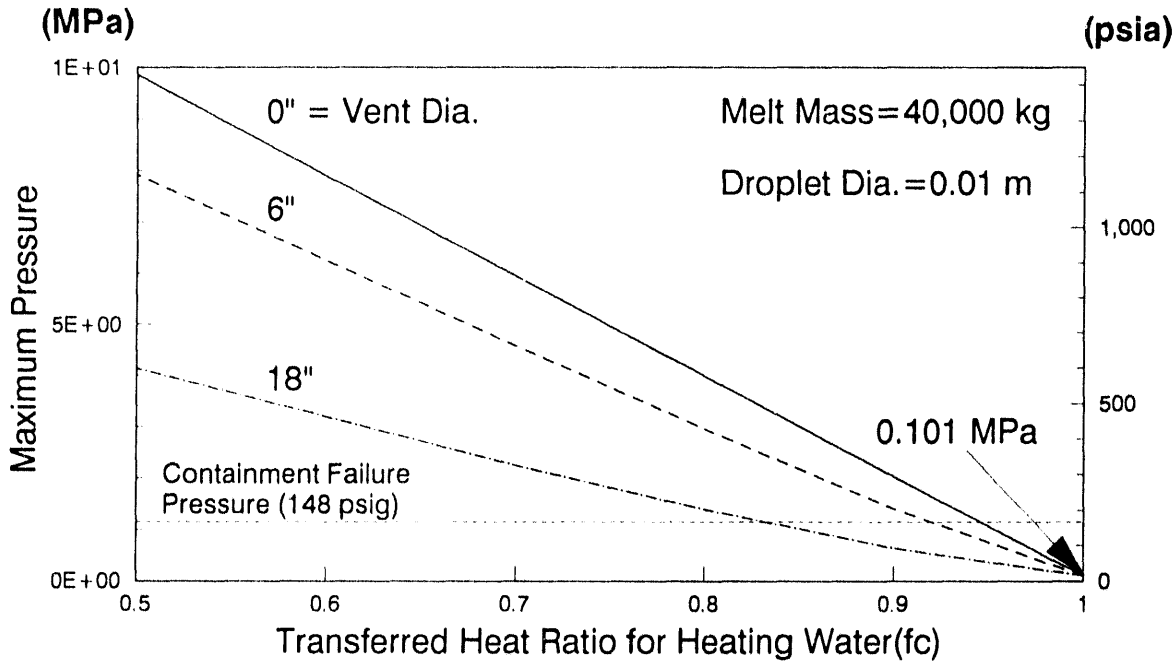

Figure II.4. Maximum containment pressure as a function of fc.

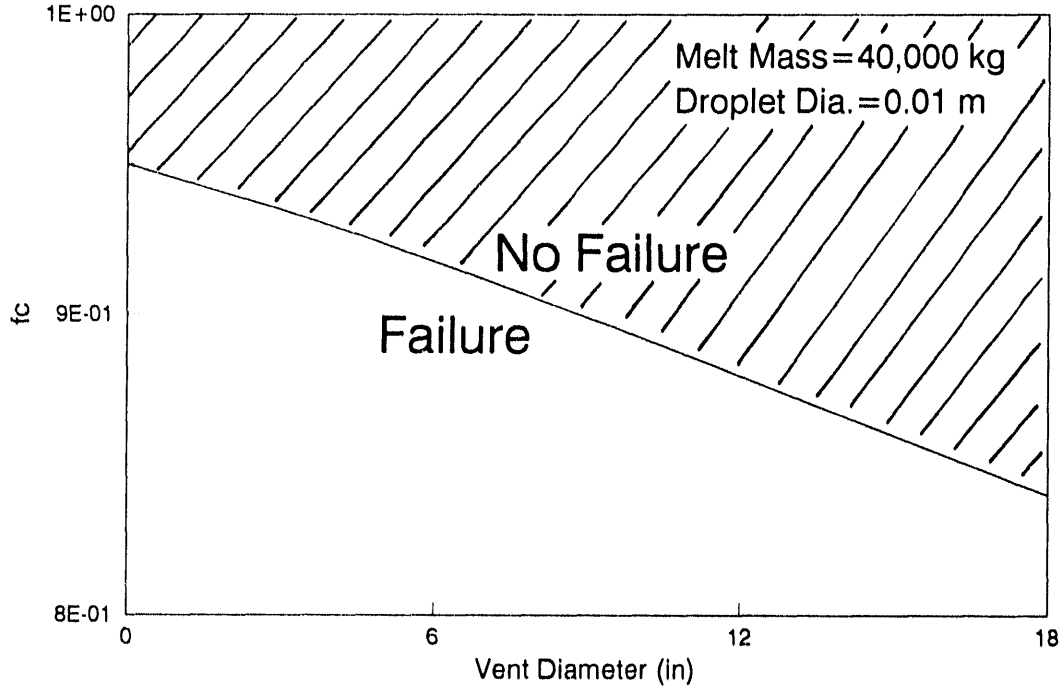

Figure II.5. Containment failure criterion as a function of fc and vent diameter.

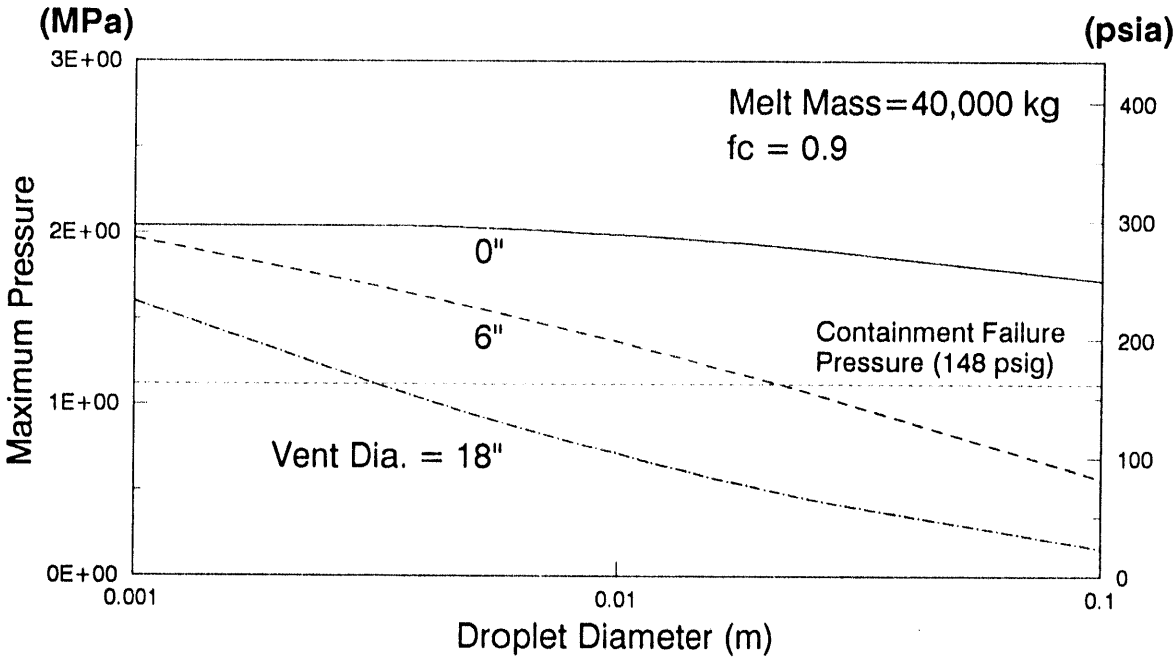

Figure II.6. Maximum containment pressure as a function of droplet diameter.

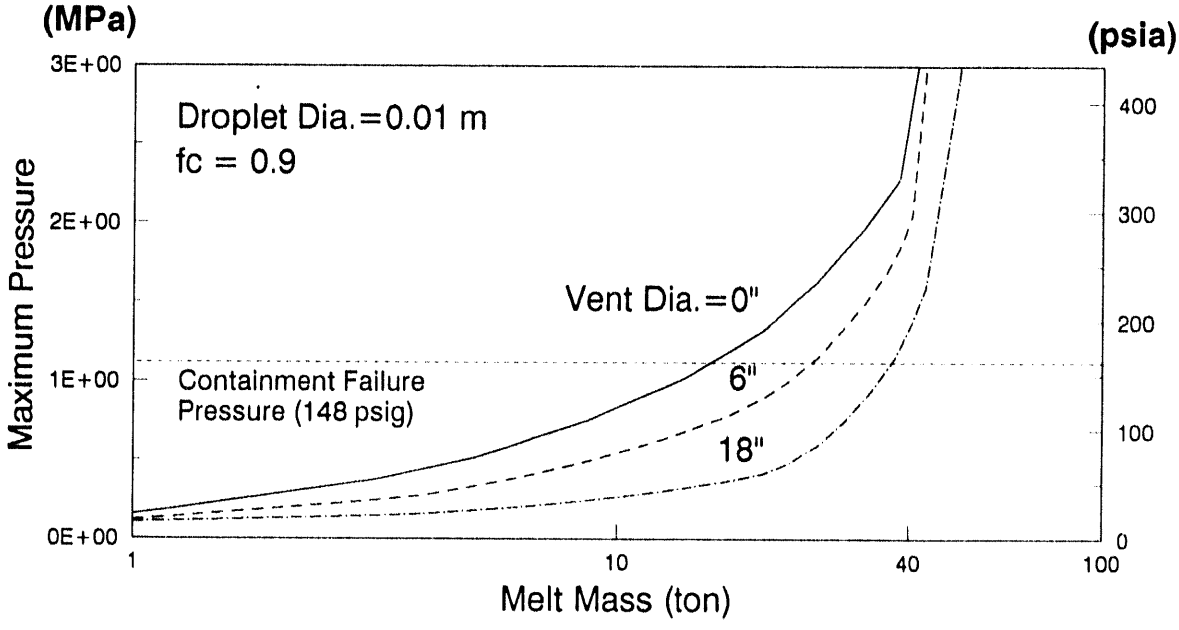

Figure II.7. Maximum containment pressure as a function of melt mass participating in the explosion.

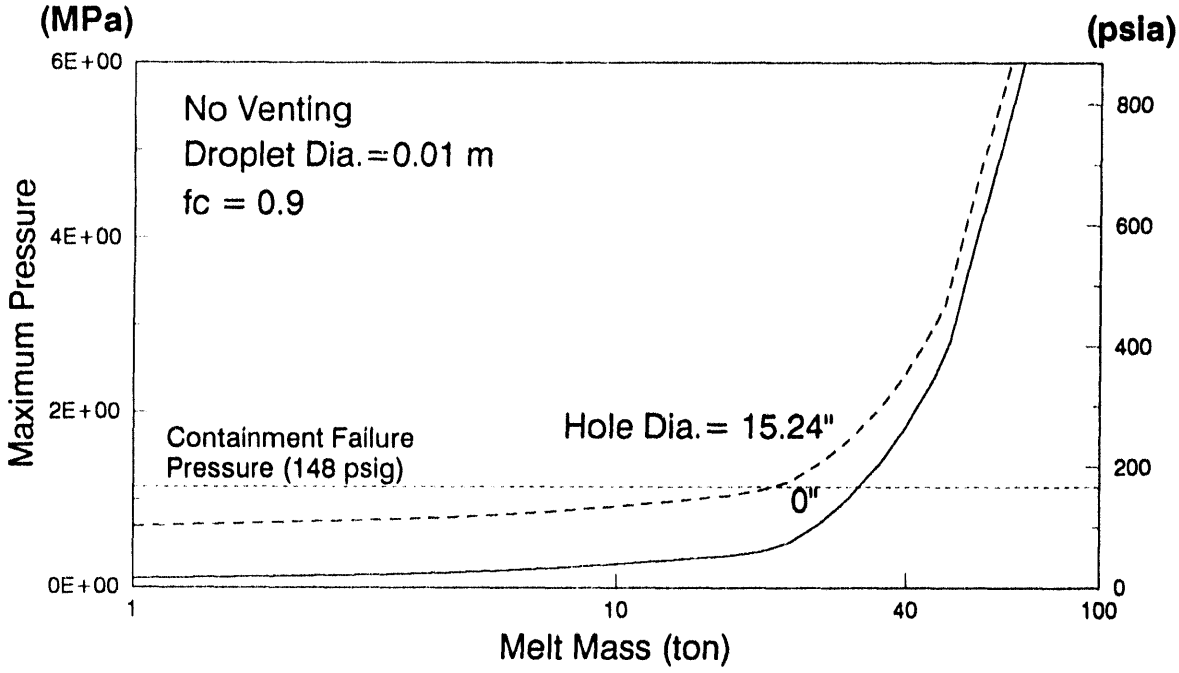

Figure II.8. Maximum containment pressure as a function of melt mass at high vessel pressure.

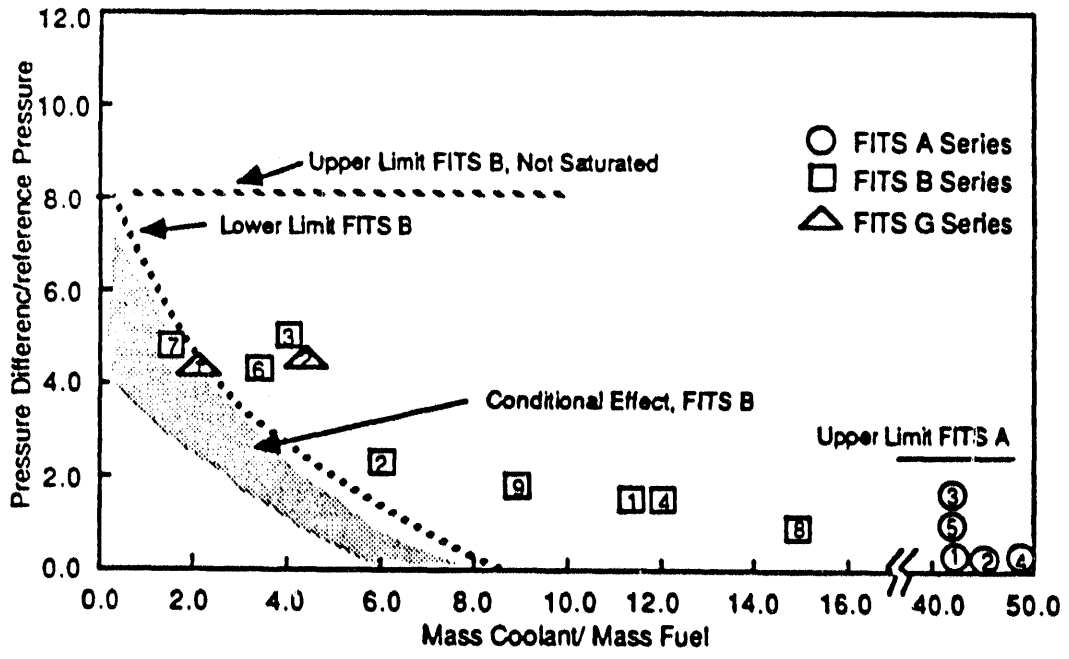

Figure II.9. FITS data analysis for steam generation [9]

APPENDIX III

THE ASSESSMENT OF PROBABILITY DISTRIBUTIONS FROM EXPERT OPINION

Introduction

The need to work with rare events and limited data about severe accidents have led analysts to use expert opinion extensively. This application is for the estimation of a containment pressure distribution curve from expert-supplied percentiles.

General Formulation

In a Bayesian framework, expert opinions are treated as evidence which is incorporated into the analyst's state of knowledge via Bayes' Theorem, i.e.,

$$\pi(x|E) = K^{-1} L(E|x) \pi_0(x) \qquad \text{(III.1)}$$

where

$\pi_0(x)$ = the analyst's prior state of knowledge about the unknown quantity x (prior to receiving the opinions of the experts),

E= the set of expert opinion regarding the value of x,

L(E|x) = the likelihood of evidence E given that the true value of the unknown quantity is x,

$\pi(x|E)$ = the analyst's posterior state of knowledge about the unknown quantity x given that he has received the set of expert opinion and

K^{-1} = normalization factor.

The problem of expert opinion is reduced to the assessment of $\pi_0(x)$ and L(E|x) by the analyst. Especially, for the situation that we have unknown prior knowledge, the key element is how to obtain the posterior from the likelihood supplied by experts. In other word, the objective is to obtain an estimate for an unknown posterior distribution using the assumption that the likelihood function (L) can be quantitative judgement about the value of the unknown value. And, these opinions are usually expressed by three percentiles such as the 5th, 50th and 95th.

The evidence here is

$$E = \{ x_{ij}, j=1,3; i = 1,.., N\} \qquad \text{(III.2)}$$

where x_{ij} is the estimate of expert i for the jth percentiles, and we have the opinions of N experts on three percentiles.

Model

Reference [1] used the following assumptions to develop the model:

1) the unknown distribution is a member of a parametric family of distributions. With this assumption, the problem of estimating the unknown distribution is equivalent to that of estimating its parameters.

2) A log-normal with parameter $\underline{\alpha} = (\theta, \omega)$ is used for the unknown distribution.

Therefore, Eq (III.1) is written as

$$\pi(\underline{\alpha}|E) = K^{-1} L(E|\underline{\alpha}) \pi_0(\underline{\alpha}) \qquad \text{(III.3)}$$

Assuming that experts are independent and one has a uniform distribution for $\pi_0(\underline{\alpha})$ (i.e., we have unknown prior distribution), then the posterior log-normal distribution becomes :

$$\pi(\theta, \omega \mid E) = K^{-1} \exp\{-\frac{1}{2}[(\frac{\omega-\omega_m}{\sigma_\omega})^2 + (\frac{\theta-\theta_m}{\sigma_\theta})^2]\}$$

where

θ, ω = parameters of a log-normal distribution.

$$(\sigma_\theta)^2 = (3 \sum_{i=1}^{n} \sigma_i^{-2})^{-1}$$

$$(\sigma_\omega)^2 = (2 Z^2_3 \sum_{i=1}^{n} \sigma_i^{-2})^{-1}$$

$$\theta_m = \frac{1}{3} \sum_{i=1}^{n} w_i (\ln x_{Z_1} + \ln x_{Z_2} + \ln x_{Z_3})$$

$$\omega_m = \frac{1}{2 Z_3} \sum_{i=1}^{n} w_i (\ln x_{Z_3} - \ln x_{Z_1})$$

w_i = weighting factor of each expert, $\sum_{i=1}^{n} w_i = 1.0$

K^{-1} = normalization factor

Z_1, Z_2, and Z_3 = three percentiles

E = evidence (i.e., expert opinions) (III.3)

"Most probable distribution" (i.e., the one that has the largest probability of being the true distribution) is used for the analysis. This is done by maximizing the posterior distribution with respect to (θ, ω) as follows:

$$\frac{\partial \pi(\omega,\theta|E)}{\partial \omega}|\omega_m = 0$$

$$\frac{\partial \pi(\omega,\theta|E)}{\partial \theta}|\theta_m = 0 \quad \text{(III.4)}$$

and using the resulting θ_m and ω_m as set of parameters of the final distribution. In other words, the most probable log-normal curve has the parameters θ and ω with θ_m and ω_m, respectively, which are obtained from Eq (III.4).

Reference

[1] Mosleh, A. and Apostolakis, G., "The Assessment of Probability Distributions from Expert Opinions with an Application to Seismic Fragility Curves," Risk Analysis, Vol. 6 (1986), 447 - 461

DATE
FILMED
11/16/93
END